Southern Methodist University
SMU Scholar

Physics Theses and Dissertations | Physics

Spring 5-19-2018

An Analysis of Frenkel Defects and Backgrounds Modeling for SuperCDMS Dark Matter Searches

Matthew Stein
Southern Methodist University, alkusoittow@gmail.com

Follow this and additional works at: https://scholar.smu.edu/hum_sci_physics_etds

Part of the Condensed Matter Physics Commons, Cosmology, Relativity, and Gravity Commons, Nuclear Commons, Other Astrophysics and Astronomy Commons, Other Physics Commons, and the Theory and Algorithms Commons

Recommended Citation
Stein, Matthew, "An Analysis of Frenkel Defects and Backgrounds Modeling for SuperCDMS Dark Matter Searches" (2018). *Physics Theses and Dissertations*. 3.
https://scholar.smu.edu/hum_sci_physics_etds/3

This Dissertation is brought to you for free and open access by the Physics at SMU Scholar. It has been accepted for inclusion in Physics Theses and Dissertations by an authorized administrator of SMU Scholar. For more information, please visit http://digitalrepository.smu.edu.

AN ANALYSIS OF FRENKEL DEFECTS AND BACKGROUNDS MODELING FOR SUPERCDMS DARK MATTER SEARCHES

Approved by:

Dr. Jodi Cooley
Associate Professor of Experimental Physics

Dr. Ryszard Stroynowski
Professor of Experimental Physics

Dr. Roberto Vega
Associate Professor of Theoretical Physics

Dr. Bernard Sadoulet
Professor of Physics
University of California, Berkeley

AN ANALYSIS OF FRENKEL DEFECTS AND BACKGROUNDS MODELING FOR SUPERCDMS DARK MATTER SEARCHES

A Dissertation Presented to the Graduate Faculty of the

Dedman College

Southern Methodist University

in

Partial Fulfillment of the Requirements

for the degree of

Doctor of Philosophy

with a

Major in Physics

by

Matthew Stein

B.S., Physics, University of North Texas
M.S., Physics, Southern Methodist University

May 19, 2018

Copyright (2018)

Matthew Stein

All Rights Reserved

ACKNOWLEDGMENTS

It has been my privilege to work with the SuperCDMS collaboration, and especially with my adviser Jodi Cooley. Though already quite busy with other students and projects, Jodi made room for me to join her group. Over the past several years, she has given me the advice, guidance and example I needed to accomplish my goals. Jodi has helped me find meaningful ways to contribute to science and our collaboration, and she has supported me in pursuing my own ideas as well. Additionally, she has given me incredible flexibility to balance my studies with family life. For this I am profoundly grateful. I have her to thank for all that I have been able to accomplish while at SMU.

My wife, Erin, has stood by me every year as I have slowly ground through the educational system. The personal sacrifice and level of patience she has shown through these years still baffles me. Without her, I would never have pursued a PhD or come so close to realizing my childhood dreams. Someday, somehow, I hope to repay all that she has done for me.

I would like to extend my sincere gratitude to Ryszard Stroynowski and Roberto Vega for their time and feedback as members of my thesis committee. They have patiently watched as I planned and progressed through my research program, giving useful feedback along the way.

I would like to thank Randy Scalise and John Fattaruso for the inspiration and assistance with my computational physics project. This work would not have been possible without their guidance.

I would like to thank Ray Bunker for all the time he has spent working with me on our various projects, and the invaluable feedback provided in analysis and documentation. Mike Kelsey has contributed large quantities of time and brain power in assisting me with code and simulations. Ben Loer and Jon Wilson have also given essential feedback and guidance on multiple projects. The shield design, plate-out study, and Frenkel defects analysis have

all significantly improved as a result of these four individuals. Thanks are owed to Alan Robinson who provided valuable perspective and evaluation of the Frenkel defects paper we worked on together.

Rob Calkins has taught me more about scientific analysis than I ever thought I needed to learn. I cannot imagine how any student gets through a graduate program without a post-doc like Rob to help them. Dan Jardin and Hang Qiu have been my fellow students at SMU and I am grateful for the privilege of working with them. Whether through weekly meetings, collaboration activities or otherwise, I am thankful for their input, opinions, and friendship.

Stein, Matthew

B.S., Physics, University of North Texas
M.S., Physics, Southern Methodist University

An Analysis of Frenkel Defects and Backgrounds Modeling for SuperCDMS Dark Matter Searches

Advisor: Dr. Jodi Cooley
Doctor of Philosophy degree conferred May 19, 2018
Dissertation completed April 23, 2018

Years of astrophysical observations suggest that dark matter comprises more than ∼80% of all matter in the universe. Particle physics theories favor a weakly-interacting particle that could be directly detected in terrestrial experiments. The Super Cryogenic Dark Matter Search (SuperCDMS) Collaboration operates world-leading experiments to directly detect dark matter interacting with ordinary matter. The SuperCDMS Soudan experiment searched for weakly interacting massive particles (WIMPs) via their elastic-scattering interactions with nuclei in low-temperature germanium detectors.

During the operation of the SuperCDMS Soudan experiment, ^{210}Pb sources were installed to study background rejection of the Ge detectors. Data from these sources were used to investigate energy loss associated with Frenkel defect formation in germanium crystals at mK temperatures. The spectrum of ^{206}Pb nuclear recoils was examined near its expected 103 keV endpoint energy to extract the first experimentally determined average displacement threshold energy of $19.7 \pm 0.5(\text{stat}) \pm 0.1(\text{syst})$ eV for germanium. This has implications for the sensitivity of future germanium-based dark matter searches including the SuperCDMS SNOLAB experiment.

The SuperCDMS SNOLAB experiment will employ germanium and silicon detectors to improve current WIMP-search results by at least one order of magnitude for masses $\leq$10 GeV/c^2. This will require substantial shielding against cosmogenic and radiogenic backgrounds. The SuperCDMS SNOLAB passive shield will be permanent for the

duration of the experiment so extensive simulations were undertaken to optimize the shield design. This resulted in a design of an outer layer of 60 cm of water, a middle layer of 20 cm of lead, and 30 cm of polyethylene which limits the background rate to that required for the primary physics goals of the experiments.

The experiment will begin operations in 2020 and care must be taken during the construction phase to limit exposure to the $\sim$135 Bq/m^3 radon activity in the laboratory. The daughter products of ^{222}Rn can attach to nearby surfaces leaving long-lived ^{210}Pb in place for the duration of the experiment. For non-line-of-sight surfaces of the polyethylene shield, the maximum allowable ^{210}Pb activity is 10,000 nBq/cm^2. A study was conducted to experimentally determine the contamination rate of polyethylene and copper by exposing samples for 83 days at SNOLAB. From the resulting surface activities, obtained from high-sensitivity measurements of alpha emissivity using the XIA UltraLo-1800 spectrometer, the average ^{210}Pb plate-out rate was determined to be 249 and 423 atoms/day/cm^2 for polyethylene and copper, respectively. A time-dependent model of alpha activity was developed leading to a maximum exposure time of 39 days in the SNOLAB environment.

TABLE OF CONTENTS

LIST OF FIGURES

LIST OF TABLES

For my sons, Lucas & Ethan.

Part I

Introduction

Chapter 1

THE MYSTERY OF MATTER

The field of dark matter physics is a lively and active area of research. There are many individuals and collaborations working on cutting-edge experimental and theoretical frontiers, all with the aim of detecting or defining the nature of what is believed to be a highly elusive particle undefined by the standard model of particle physics. There are still others who attempt to find theories in which observations can be explained through new mathematical tools or modifications of existing theories.

The "darkness" of the matter that scientists hope to find today is the same as that of the Atomists of the 5^{th} century BCE who theorized that all matter is made of the same building block: the atom. They had no way to prove this, nor was it proven for another $\sim$ 2,400 years. Other "dark" predictions include the existence of Neptune, which was required to explain Uranus' orbital motion.

History is rife with examples of dark mysteries like these. When Galileo first made observations of the night sky with his telescope, an entire new perspective of the universe came into view: Jupiter had moons, Venus had phases, and there were many more stars than could be seen with the naked eye. With the telescope, it was possible to see previously hidden parts of the universe and to make further predictions on other potential mysteries. For example, Galileo's observations gave further evidence to the heliocentric model of the solar system put forth by Copernicus.

So it is through clever predictions, new technology, or a combination of both that scientists have been able to define more clearly the nature of the universe.

The current search for dark matter will be yet another stepping stone, and the 21^{st} century is an exciting time to conduct research on the frontier of human knowledge. Scientists invent new technologies, work in international collaborations, and conduct research with the support

of local communities and governments. Perhaps in searching for the contemporary form of "dark" matter, scientists will find something even more surprising along the way.

1.1. The Missing Matter Problem

As early as 1904, there was talk of unseen matter that must be present to explain otherwise inexplicable motion of stars. The physicist Lord Kelvin treated the stars in the galaxy as a gas of particles interacting gravitationally [1]. Taking into account the velocity dispersion of stars observed, he attempted to predict the total number of stars in the Milky Way and determined that there must be as many as a billion stars, many of which are completely dark or beyond the current power of observation. Nevertheless, Kelvin set an upper limit on the local (stellar neighborhood) matter density noting that anything higher was in conflict with observation.

Two years later, Henry Poincaré claimed that Kelvin's predicted "matière obscure" (dark matter) either did not exist, or was no greater than visible matter [2]. It was at this time that the term "dark matter" first appeared, contrary to some sources that claim it was Fritz Zwicky who first used the term in 1933.

Expanding on these local matter density estimates, Jan Oort published his own estimate of 0.092 $M_\odot/pc^3$ ($M_\odot \equiv 1$ Solar Mass $= 2\times10^{30}$ kg; pc $\equiv 1$ parsec $= 3.1\times10^{13}$ km) [3], a refinement of work previously performed by Oort's former professor Jacobus Kapteyn [4]. Previous estimates made by James Jeans and Bertil Lindbald had been 0.143 $M_\odot/pc^3$ and 0.217 $M_\odot/pc^3$ respectively [5, 6]. Using his local density estimate, Oort calculated that at most approximately half of the local density could be attributed to dark matter. Oort posited gaseous or meteoric matter as potential dark matter constituents.

These preliminary estimates on helped lay the ground work for what has become the modern search for dark matter. The local density of dark matter continues to be a key value in predictions for direct detection experiments (Fig. 1.1).

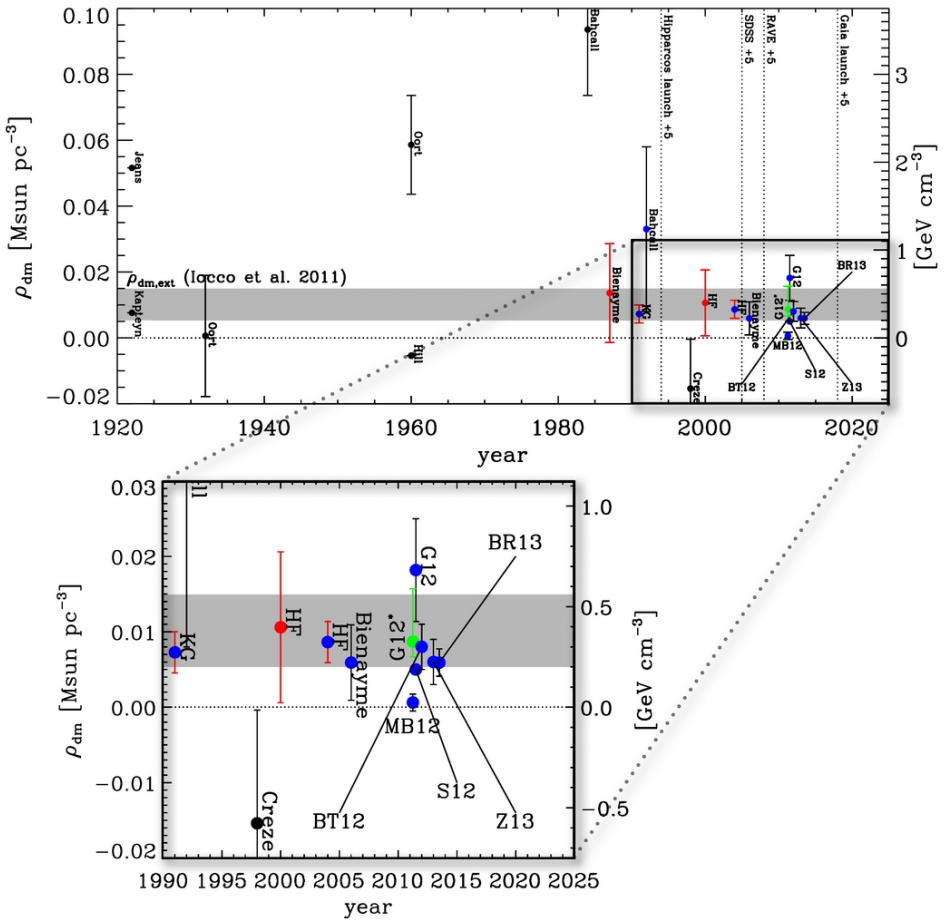

Figure 1.1. Local dark matter density estimates (vertical axis) since 1920. Kapteyn and Oort's estimates appear surprisingly close to that of modern measurements (shown in expansion). All estimates assume a baryonic matter density of 0.0914 $M_\odot/pc^3$ from Ref. [7]. Exact values and associated references are available in Table 4 of Ref. [8].

1.1.1. Additional Dynamical Evidence

Historically, Fritz Zwicky was one of the best-known researchers in the field of dark matter. He provided a different set of arguments for the case of missing matter from extragalactic observations. From the redshift of galaxies in the Coma cluster, Zwicky found a variance in the recessional velocities of >2000 km/s and applied the virial theorem to deduce the mass of the system [9].

Zwicky also estimated the expected velocity dispersion for the observed ∼800 galaxies in the cluster, assuming that each galaxy was 10^6 ly across (ly ≡ 1 light-year = 9.46×10^{15} m) and contained 10^9 stars, as predicted by Edwin Hubble [10]. For this system, he predicted an average velocity dispersion of 80 km/s, much lower than the average observed value of 1000 km/s for the Coma Cluster [9]. He concluded that only the presence of a significant amount of unseen matter could explain the discrepancy between observation and his mathematical model that only accounted for the luminous matter.

The Coma Cluster was only one of many clusters examined for its unusual velocity dispersion. In 1936, the Virgo Cluster was examined by Sinclair Smith who found an average mass of 2×10^{11} $M_\odot$ per galaxy [11]. Zwicky's own estimate from his 1937 paper was 4.5×10^{10} $M_\odot$ per galaxy, still remarkably higher than Hubble's estimate of 10^9 $M_\odot$ as was expected from luminous matter alone. Of this huge discrepancy, Hubble prophetically stated:

> The investigations are beset with uncertainties, and the numerical results are mainly estimates which will be revised when more elaborate techniques and larger telescopes have been applied to the problem [10].

It was not long before the next evidence of missing mass emerged, this time from a different type of measurement. World War II, however, created a long pause in many fields of research, including astronomy.

1.1.2. Andromeda

The Andromeda galaxy (M31) played an especially important role in the evidence of dark matter, examined time and again throughout much of the 20$^{\text{th}}$ century. In 1939,

astronomer Horace Babcock measured the rotational velocities of stars orbiting the nucleus out to 100 arcminutes as illustrated in Fig. 1.2. Babcock pointed out that only by the presence of additional unobserved mass could the so-called rotation curve take on such high values at high distances from the center. The values he calculated were high compared to modern measurements, but as Hubble had pointed out a few years earlier, better equipment and telescopes were required to improve the estimates.

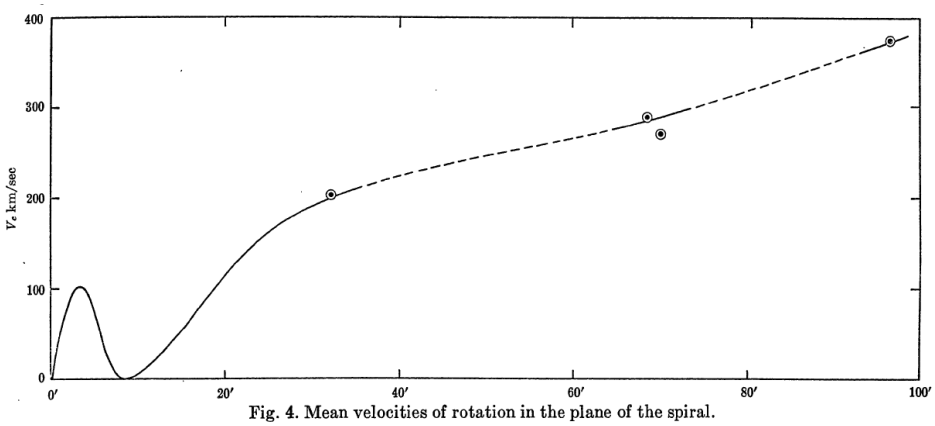

Fig. 4. Mean velocities of rotation in the plane of the spiral.

Figure 1.2. Rotational velocities for luminous matter in M31, from Ref. [12]. Horizontal units are given in arcminutes from the center. 100' is approximately 20 kpc.

The Second World War and subsequent Korean and Cold Wars put a lengthy pause on many fields of non-military research, but there were some unexpected technological advances as well. Abandoned radar sites from Nazi installations were repurposed for astronomical use. The 21 cm hydrogen line[1] was first observed in 1951 by Harold Ewen and Edwin Purcell [14] from one such radar station. This feature was crucial to many astronomical discoveries and advances, not least of which was the observation by Franz Kahn and Lodewijk Woltjer that the combined mass of M31 and the Milky Way was six times larger than previously thought [15].

Despite the mounting evidence for missing matter, there was not a clamor to resolve the mystery and it was another decade before Vera Rubin and Kent Ford famously measured the

[1]This refers to the wavelength of electromagnetic radiation from hydrogen as it changes between the two levels of the 1s ground state [13].

rotation curves of M31 [16]. The results, illustrated in Fig. 1.3, presented a large increase in precision from Babcock's earlier measurement. This precision was achieved thanks in part to Ford's image-tube spectrograph which was a remarkable step forward in imaging technology. Rubin won many awards for her work including the Gold Medal of the Royal Astronomical Society. Ford won the 1985 James Craig Watson Medal for his own contributions.

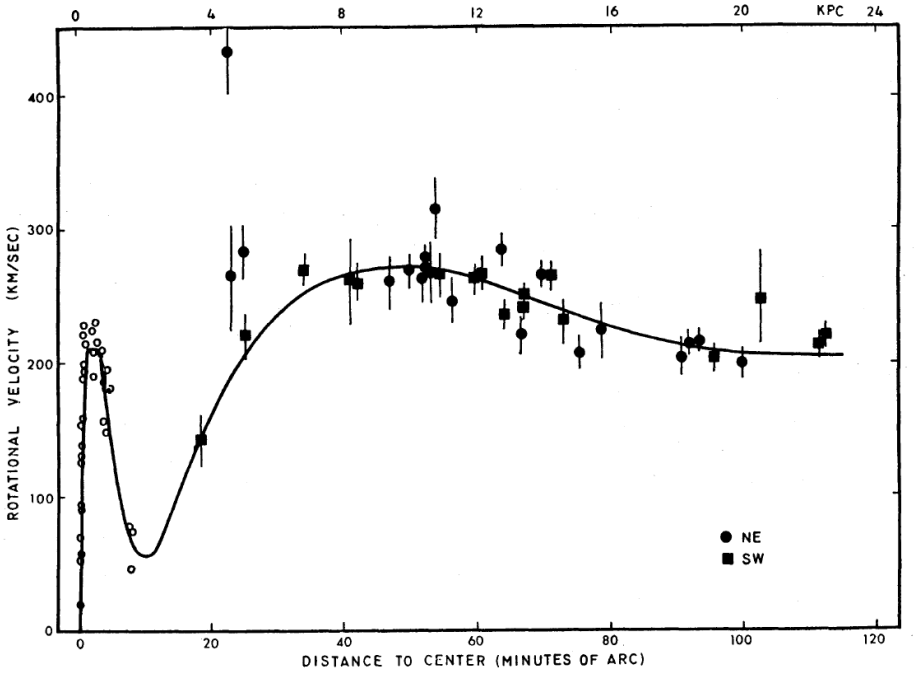

Figure 1.3. Rotation curve for M31 as measured by Vera Rubin in 1970 [16]. Solid black line represents a polynomial fit to the data. The rotational velocity at high distances cannot be explained from the dynamics of luminous matter alone.

In 1970, Ken Freeman used the 21 cm line to measure rotation curves of M33 and NGC 300 [17], extending observations to radii beyond the optical disk. This showed, once again, a large discrepancy between the predicted mass and that which must account for the flat rotation curves at the outer regions of galaxies. His work was later confirmed by several other astronomers.

In 1978, Albert Bosma produced rotation curves for 25 galaxies in his thesis [18] showing flat curves for various Hubble types[2]. That same year, Norbert Thonnard worked with Rubin and Ford to add another 10 spiral galaxies to the list of those with flat rotation curves. Over the following decades, a wide variety of theoretical models have attempted to explain the various observations as discussed in Section 1.2.

1.1.3. Cosmological Evidence

The cosmic microwave background (CMB) is a radiation emitted during the recombination era of the universe, approximately 380,000 years after the Big Bang [21]. Photons from this period have been streaming freely across the universe and are now shifted to the microwave part of the electromagnetic spectrum by the expansion of the universe. At all observable angles, the CMB appears nearly uniform at ∼2.73 K with point-to-point variations of less than one part in 100,000. The small anisotropies that do exist correlate to the quantum fluctuations of matter in a very small volume. The peaks in the power spectrum of these anisotropies, illustrated in Fig. 1.4, give meaningful information about the structure, formation and fate of the universe [22].

Moreover, information can be obtained about the baryonic and dark matter components of the universe. The Planck collaboration measured the polarization and temperature fluctuations of the CMB. For different positions in the sky at $\mathbf{n} \equiv (\theta, \phi)$, the measured fluctuations yield $\delta T/T(\mathbf{n}) \equiv \delta_T(\mathbf{n})$. The temperature fluctuations $\delta_T(\mathbf{n})$ are expressed in terms of spherical harmonics[3]

$$\delta_T(\mathbf{n}) = \sum_{l=1}^{\infty} \sum_{m=-l}^{l} a_{lm} Y_{lm}(\mathbf{n}) \tag{1.2}$$

[2]This is a morphological classification scheme for galaxies developed by Edwin Hubble, also known as the tuning fork diagram (see Refs. [19] and [20]).

[3]Spherical harmonics are given by

$$Y_{lm}(\mathbf{n}) = \sqrt{\frac{2l+1}{4\pi} \frac{(l-m)!}{(l+m)!}} P_l^m \cos(\theta) e^{im\phi} \tag{1.1}$$

with P_l^m the Legendre polynomials.

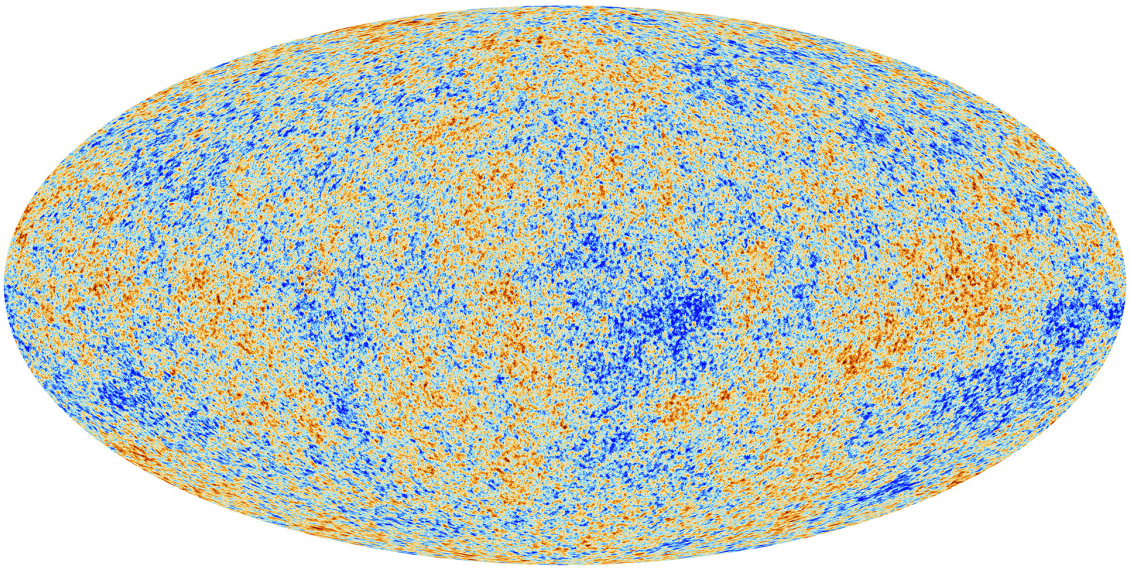

Figure 1.4. The anisotropies of the Cosmic microwave background (CMB) as observed by *Planck*, the satellite observatory [23]. The CMB is a snapshot of the oldest light in the Universe, imprinted on the sky when the Universe was just 380,000 years old. It shows tiny temperature fluctuations that correspond to regions of slightly different densities, representing the seeds of all future structure: the stars and galaxies of today. Adapted from Ref. [24].

where a_{lm} is

$$a_{lm} = \int_{\theta=-\pi}^{\pi} \int_{\phi=0}^{2\pi} \delta_T(\mathbf{n})\, Y_{lm}^*(\mathbf{n}) d\Omega \tag{1.3}$$

For two points in the sky $\mathbf{n}$ and $\mathbf{n}'$, the two-point correlation function is given by

$$\langle \delta_T(\mathbf{n}), \delta_T(\mathbf{n}') \rangle = \frac{1}{4\pi} \sum_{l=1}^{\infty} (2l+1)\, C_l P_l(\cos\theta) \tag{1.4}$$

where $\theta = \mathbf{n} \cdot \mathbf{n}'$. The power spectrum of the fluctuations C_l is

$$C_l = \frac{1}{2l+1} \sum_{m=-l}^{l} \langle |a_{lm}|^2 \rangle \tag{1.5}$$

and the variance of the $\langle |a_{lm}|^2 \rangle$ term is a predictor of cosmological models which can specify, among other things, the baryon matter density Ω_b and cold matter density Ω_c [25]. Figure 1.5 illustrates the power spectrum, shown as $l(l+1)C_l/2\pi$, for various multipole moments l.

The fluctuations in the power spectrum are called acoustic peaks. These arise from plasma oscillations moving at the speed of sound in the early universe. The physics of the oscillations are defined by cosmological parameters such as the values of Ω_b and Ω_c. Peaks in the power spectrum correspond to favored scales of matter density and associated fluctuations. These fluctuations would grow throughout the universe being observable today in the large scale structure observed such as galactic clusters. The 2015 results of the Planck collaboration indicate dark matter contributes 26.8% of the matter-energy density of the universe whereas ordinary matter contributes 4.9% with dark energy filling in the remaining 68.3%.

1.2. Theories & Predictions

1.2.1. MOND

If the observations of the last hundred years could be explained by a significant modification in the theories of nature, it would not be the first time. The motion of the planets in

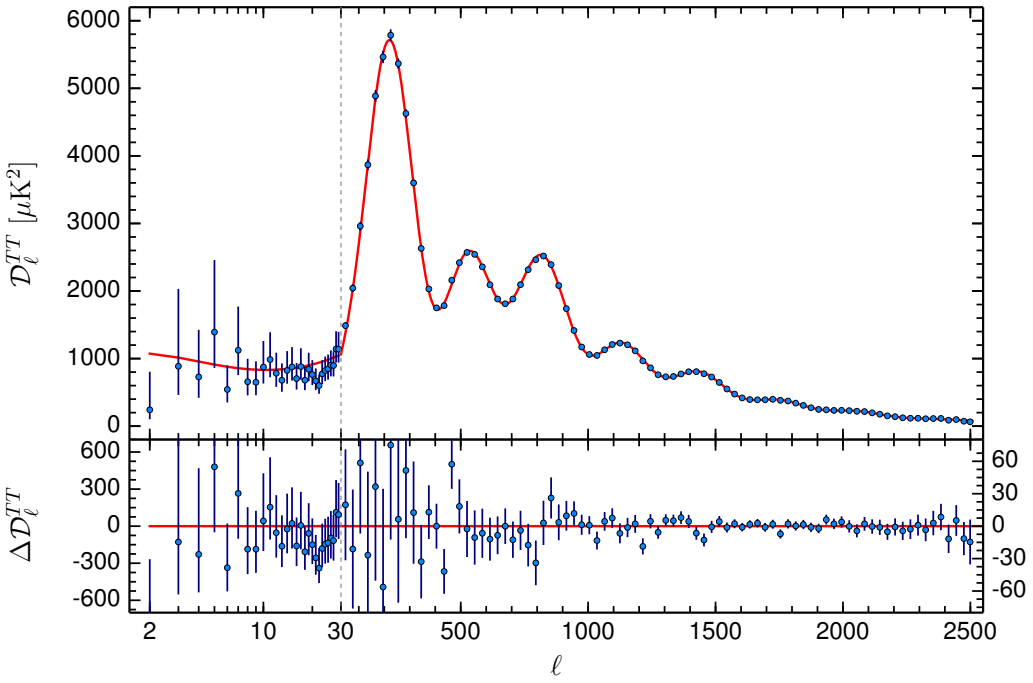

Figure 1.5. Temperature power spectrum of the CMB taken from data from the Planck Collaboration as of February 2015. Vertical axis is given as $l\,(l+1)\,C_l/2\pi$ with C_l defined from Equation 1.5 for different multiple moments l. Adapted from Ref. [25].

the night sky was once interpreted by a model of circular motion. The so-called Ptolemaic model was continuously modified to account for minor discrepancies, leading to a theory in which there were circles within circles (equants, epicycles, etc). The predictions were so good, however, that the model was not seriously challenged for nearly 1,300 years. In the 17^{th} century, Johannes Kepler forever enlightened humanity with the knowledge of the ellipse, shattering the idea of circular motion of planets.

In the same spirit, many theorists and astronomers have tried to identify new models and theories to explain the observation of the "missing mass" without introducing new objects or particles. The most prevalent theory is referred to as Modified Newtonian Dynamics or MOND. In 1982, Mordehai Milgrom presented an adjustment to Newton's second law [26–28]

$$\mathbf{F} = m\mathbf{a}(a/a_o) \tag{1.6}$$

This equation reduces to the more familiar $F = ma$ when $a \ll ao \sim 10^{-10}\text{m/s}^2$. Though not intended to be a complete theory, this treatment of the second law did not conserve energy. However, it helped open the door on ways to modify mechanical theories to fit observation.

Other theories started by first modifying the Lagrangian of Newtonian mechanics, among them the AQUAdratic Lagrangian theory (AQUAL) [29], Relativistic AQUAL (RAQUAL) [30], and Tensor-Vector-Scalar gravity (TeVeS) [31], all authored by Jacob Berkenstein and Milgrom. The last of these (TeVeS) has proven to be the most realistic of all MOND theories, now being potentially compatible with galactic rotation curve, gravitational lensing, and CMB observations.

Difficulty remains, however, with galactic cluster observations. While reducing the overall amount of missing mass, TeVeS still requires a substantial amount of unobserved mass in the form of neutrinos. If neutrinos have a mass of ∼1-2 eV, TeVeS might still be a workable theory, but this pushes the masses near the Mainz-Troitsk upper bound of 2.3 eV for the electron antineutrino [32]. This limit will be measured by the KATRIN experiment [33] with

the fate of TeVeS potentially hanging in the balance, especially if the neutrino mass is found to be significantly less than 1 eV.

A greater challenge came with the observation of the Bullet Cluster in which one cluster appeared to have passed through another as shown in Fig. 1.6. In the wake of the merger, hot gas was detected from x-ray observations indicating the areas of greatest "normal" matter [34]. The cluster was also observed for gravitational lensing effects where the mass in the cluster enhanced the luminosity of background galaxies. The greatest lensing effect corresponds to the location of greatest mass and is illustrated by the blue highlighted regions in Fig. 1.6. There is a greater than 8σ significance spatial separation between the location of greatest mass and the location of greatest *luminous* mass. A theory of particle dark matter fits this observation well, where dark matter particles would pass through without interaction, whereas the hot plasma and gas would interact and emit Bremsstrahlung radiation.

1.2.2. Neutrinos

Neutrinos, of course, seem a likely candidate for dark matter. They interact only through gravitational and weak forces, making them invisible to astronomical observation except by lensing effects. With the exception of TeVeS, all theories that considered neutrinos as dark matter candidates required masses much higher than the previously mentioned current limit of $\sim$2 eV, some even theorizing GeV scale masses [35, 36]. As discussed in Section 1.2, the neutrino mass will be explored by KATRIN, but whatever the result, neutrinos seem an unlikely candidate for dark matter.

1.2.3. MACHOs

More than 100 years ago, Kelvin theorized that perhaps the vast majority of stars in the Milky Way were either completely dark, or beyond the present ability to observe them [1]. In 1986, Bohdan Paczyński proposed a similar theory which extended the idea to include brown dwarfs, failed stars, and Jupiter-sized bodies moving freely throughout the galactic halo. He proposed that such objects could be indirectly detected by watching for microlensing

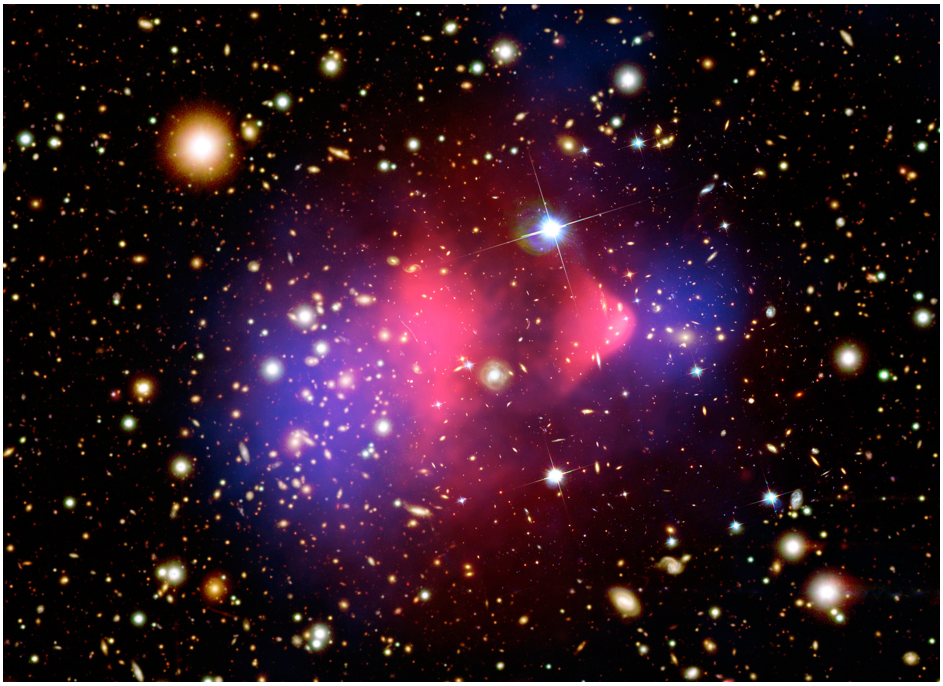

Figure 1.6. The Bullet Cluster image from Hubble with overlaid highlights. The pink highlights indicate the observed hot gas from Chandra, while blue highlights are correlated to the areas of greatest mass, determined from lensing effects. Credit: X-ray: NASA/CXC/M.Markevitch et al. Optical: NASA/STScI; Magellan/U.Arizona/D.Clowe et al. Lensing Map: NASA/STScI; ESO WFI; Magellan/U.Arizona/D.Clowe et al.

of stars in the Large Magellanic Cloud (LMC) [37]. Kim Griest later coined the phrase "Massive Astrophysical Compact Halo Object" (or MACHO) in his 1991 paper re-examining Paczyński's work with updated models on the galactic halo [38].

The MACHO collaboration (among others) aimed to test the theory that the halo was comprised mostly of these dark objects. Under such an assumption, lensing events are expected for one out of every two million observed stars. After an observation period of 5.7 years covering 11.9 million stars in the LMC, the MACHO collaboration reported between 13 and 17 candidate lensing events [39]. Though the number of events observed was higher than predicted, the mass of each lensing object was low enough to set a predicted halo mass fraction of 20% for MACHOs. They claimed a 95% confidence interval of 8-50% of total mass being that coming from MACHOs.

Seven years later, the EROS collaboration (Expèrience pour la Recherche d'Objets Sombres), also looking for MACHOs, reported on their 6.7 years of observation covering 33 million stars. Their upper limit was 8% for MACHO halo mass fraction [40]. While both collaborations produced significant advances in lensing astronomy, the results indicated that MACHOs could not alone solve the missing mass problem.

1.2.4. WIMPs

While some theories attempt to explain the missing mass with known objects or particles, others focus on entirely new particles outside the standard model of physics. One of the most studied theories has been the Weakly Interacting Massive Particle, or WIMP. Like neutrinos, WIMPs are expected to interact only via the weak and gravitational forces, but theories continue to vary as to the mass and probability of interaction with ordinary matter. There are, however, cosmological constraints to consider.

While considering the age, structure, and evolution of the universe, Gary Steigman and Michael Turner set limits on the masses and lifetimes of Weakly Interacting Massive Particles (WIMPs) in their 1985 paper [41]. Other considerations have included early abundances, freeze-out, annihilation cross sections and more [38,42,43] which have collectively contributed

to the Lambda Cold Dark Matter (ΛCDM) model, often referred to as the standard model of cosmology as it reasonably correlates with observations of the CMB, large scale structure of the universe, atomic abundances, and a flat, expanding universe.

1.2.4.1. The WIMP Miracle

During the radiation era, heavier and lighter particles were in thermodynamic equilibrium. Dark matter could self-annihilate to create standard model particles and vice versa. The reaction rate per unit particle Γ is given by

$$\Gamma = n\sigma v$$

where n is the number density of particles, σ is the interaction cross section, and v the relative velocity of the particles. As the universe continued to expand, n decreased such that interactions occurred less frequently. Additionally, lighter particles no longer had the kinetic energy required to create heavier particles as emitted photons were more free to stream across the universe. Eventually, the particles are said to "freeze-out" with their comoving number density remaining relatively constant from that time on as illustrated in Fig. 1.7. This occurs when Γ is equal to the Hubble rate [44]. The particle density at this point is called the relic density.

By using the Boltzmann equation with entropy conservation, the number density of particles over time can be estimated as

$$\frac{dn}{dt} = -3Hn - \langle \sigma_A v \rangle \left(n^2 - n_{eq}^2 \right)$$

where t is time, H is the Hubble parameter, σ_A is the effective annihilation cross section, and n_{eq} is the equilibrium number density. The number density at freeze-out can be calculated by setting $n\langle \sigma_A v \rangle = H$ [46] yielding

$$n_f \sim \frac{T_f^2}{M_{Pl}\langle \sigma_A v \rangle}$$

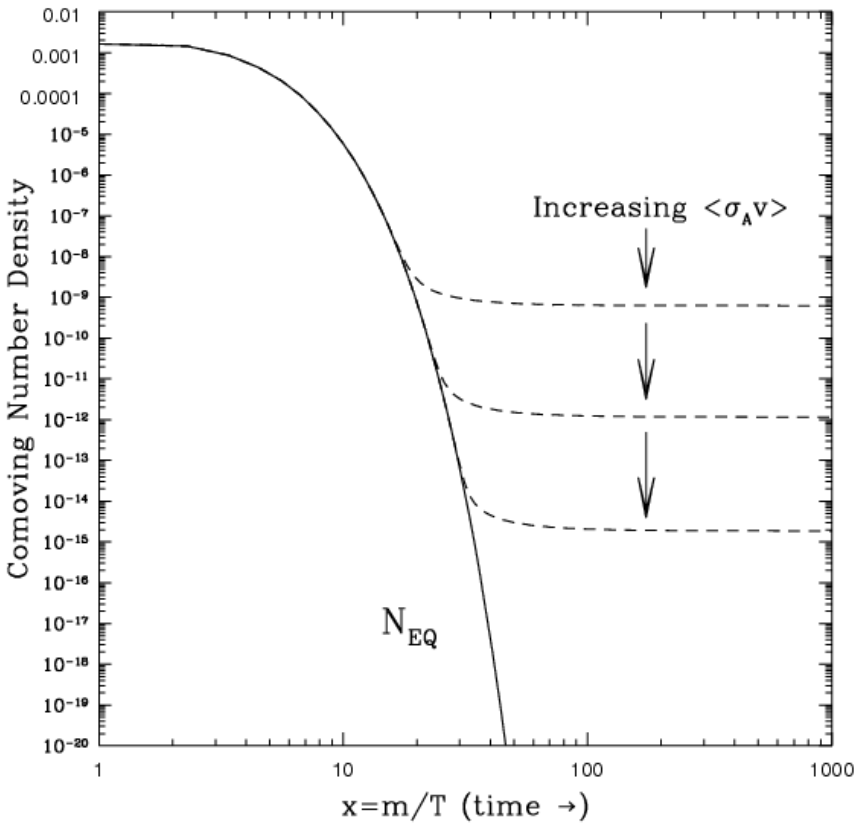

Figure 1.7. A schematic of the comoving number density of a stable species as it evolves through the process of thermal freeze-out. The vertical arrows indicate increasing self-annihilation interaction cross sections $\langle \sigma_A v \rangle$ with dashed lines indicating associated freeze-out densities. Adapted from Ref. [45].

where T_f is the freeze-out temperature and M_{Pl} is the Planck mass ($\sim 1.2 \times 10^{19}$ GeV). The thermal relic density Ω_χ is

$$\Omega_\chi = \frac{m_\chi T_0^3}{\rho_c M_{Pl} T_f} \frac{1}{\langle \sigma_A v \rangle}$$

where m_χ is the dark matter particle mass, T_0 is the present temperature, and ρ_c is the critical density[4]. Importantly, the relic density is inversely proportional to the annihilation cross section which, for a weakly-interacting particle, can be written

$$\sigma_A v \propto \frac{g_{\text{weak}}^4}{m_\chi^2}$$

where $g_{\text{weak}} \sim 0.65$ is the weak interaction gauge coupling. With the relic density Ω_χ being a function of m_χ, one can inspect the ratio of relic density to that measured by the CMB ($\Omega_{DM} \sim 0.23$ is the CMB measured dark matter density). A band of allowable dark matter masses is illustrated in Fig. 1.8.

Given these assumptions, dark matter particles have mass between 100 GeV and 1 TeV if it comprises 100% of all dark matter. If the particle comprises only 10%, the mass falls between 30 and 300 GeV. This is the essence of the WIMP miracle: a stable weak-scale particle that adequately constitutes the dark matter density measured by the CMB.

1.2.4.2. Halo Model

As discussed in Section 1.1.2, the rotation curves of galaxies indicated that the missing mass was present in large quantities outside of the core region of the galaxy, and was distributed spherically as opposed to the disc distribution of ordinary matter. This distribution is referred to as a three-dimensional halo around the galaxy, with the following predicted density function [47]

$$\rho(r) = \rho_0 \left(1 + \frac{r}{r_c}\right)^{-1} \tag{1.7}$$

[4]The critical density is the density of matter required for the universe to stop expanding but only after an infinite amount of time (i.e. the condition required for a "flat" universe).

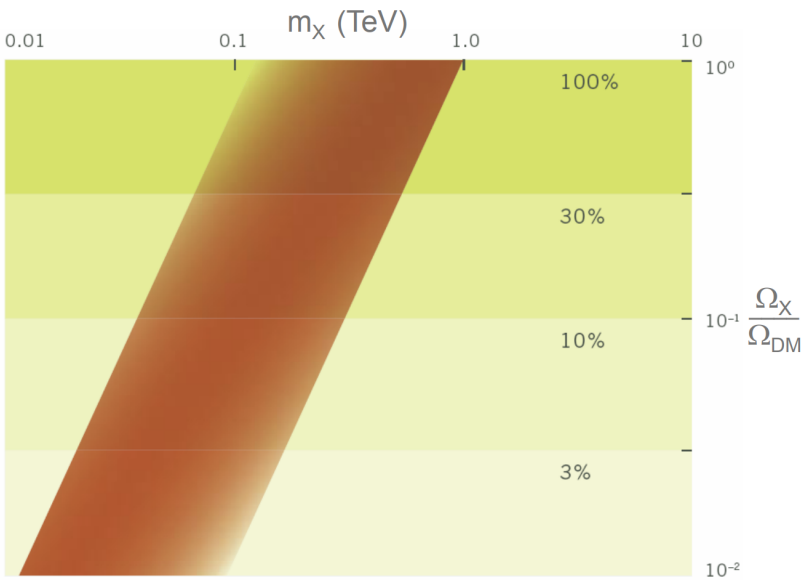

Figure 1.8. The ratio of relic and current densities of dark matter versus the dark matter particle mass. The width of the band comes from varying parameters in the annihilation cross section.

where ρ_0 is the density at the core region of the galaxy, r_c is the core radius, and r is the distance from the center of the galaxy. While this is a commonly cited density function, there are other forms based on numerical simulation such as the Navarro-Frenk-White profile [48] or the Einasto profile [49] which better agree with data. In the solar neighborhood ($r \approx 25.8$ kpc from the center of the Milky Way), the local density is assumed to be $\rho \approx 0.3$ GeV/cm^3 and a mean WIMP velocity of $\sim$230 km/s [50, 51].

1.2.4.3. Light Dark Matter

Years of attempts to directly detect WIMPs, there is still an absence of evidence of TeV-scale dark matter [52]. Recent focus has been given to dark matter particles with mass on the order of keV to GeV. Progress has been made in recent years supporting models for "light" dark matter that also gives the correct relic abundance in the universe [53–57]. For example, if dark matter is not a single particle but part of larger dark sector which includes

multiple particle species and mediators, it is simple to have sub-GeV masses and maintain the correct relic abundance [52, 58].

Dark matter may also exhibit the same particle-antiparticle asymmetry exhibited by ordinary matter. Given that the baryonic matter density is approximately on the order of dark matter, $\rho_{\text{baryon}} \sim 4.5\rho_{DM}$, an asymmetric dark matter model predicts that the number of dark matter particles is also on the order of baryonic matter, or $n_{baryon} \sim n_{\text{DM}}$. This gives $\Omega_{\text{DM}} \sim (m_{\text{DM}}/m_{\text{B}})\,\Omega_{\text{B}}$. A dark matter particle of mass $m_{\text{DM}} \sim 5$ GeV fits the observed relic abundance model [59]. However, the model allows for masses from keV to GeV scales for varying mechanisms driving the asymmetry [60].

If dark matter interacts very feebly with standard model particles (i.e. a Feebly Interacting Massive Particle, or FIMP), it may never have been in thermal equilibrium in the early universe. Moreover, if standard model particles can annihilate or decay into dark matter, the dark matter abundance can "freeze-in" through this mechanism. Depending on couplings and interaction probabilities, this can fully account for the dark matter relic abundance [61].

Dark may also interact strongly with itself, but not ordinary matter. Such a particle, known as a Strongly Interacting Massive Particle (SIMP), may account for the correct relic abundance if there exists a process for which three SIMPs interact and form only two others [62]. These particles would have been in thermodynamic equilibrium in the early universe, and would be detectable today having sub-GeV scale masses [63].

1.3. WIMP Detection Methods

1.3.1. Direct Detection

In 1985, Mark Goodman and Edward Witten suggested that the experimental methods proposed to detect neutrino scattering [64] could also be employed for WIMP searches [65] as both particles interact with only the weak and gravitational forces. The detection relies on the following interaction

$$\chi + p \rightarrow \chi + p$$

where χ is the dark matter particle, and p is a nucleon (proton or neutron). During this interaction, phonons and free charges are generated, both of which could be detected in terrestrial detectors.

Predicted values for the interaction cross section of WIMPs with nucleons have been greatly modified over the years in response to experimental measurements (Fig. 1.9). It is worth noting, however, the initial estimates Goodman and Witten put forward.

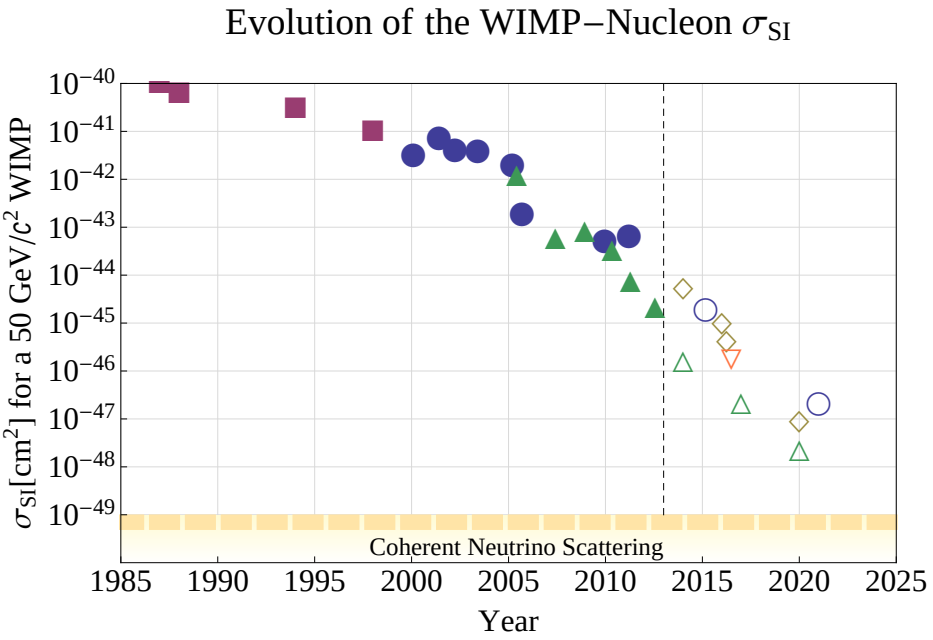

Figure 1.9. History and projected evolution with time of spin-independent WIMP-nucleon cross section limits for a 50 GeV WIMP. The shapes correspond to technologies: cryogenic solid state (blue circles), crystal detectors (purple squares), liquid argon (brown diamonds), liquid xenon (green triangles), and threshold detectors (orange inverted triangle). Below the yellow dashed line, WIMP sensitivity is limited by coherent neutrino-nucleus scattering. Reproduced from Ref. [66].

The initial rate estimates for coherent scattering of WIMPs off nuclei were 50-1,000 and less than 10,000 events per kg per day for WIMPs of 2 GeV/c^2 and 100 GeV/c^2 mass, respectively, with recoil energies of 10-100 keV for both cases. Spin-dependent interaction rates are approximately three orders of magnitude lower for the same masses. Additionally, the authors detail experimental methods that could be employed to directly detect these

interactions. This work, among others, helped pave the way to developing modern experimental techniques including the use of germanium and silicon detectors to probe interactions in the 10-100 keV recoil regime.

In 1996, J.D. Lewin and P.F. Smith published their seminal paper updating dark matter rate predictions in modern detectors [50]. They calculated that WIMPs of mass 10–10,000 GeV/c^2 yield recoil energies in the 1–100 keV range. In 2004, Alexander Kurylov and Marc Kamionkowski published a detailed explanation of WIMP-nucleon interaction field theory, including calculations of cross sections and invariant amplitudes [67]. The event rate R for direct-detection experiments is given by

$$\frac{dR}{dE_R} = \frac{\sigma_0 \rho_0}{2 m_\chi \mu} F^2 (E_R) \int_{v_{min}}^{\infty} \frac{f(v)}{v} dv \tag{1.8}$$

where σ_0 is the interaction cross section for zero momentum transfer, ρ_0 is the local WIMP density, m_χ is the mass of the WIMP, μ is the reduced mass of a nucleus of mass m_N and a WIMP of mass m_χ, E_R is the nuclear recoil energy, $F^2 (E_R)$ is the nuclear form factor, $v_{min} = \sqrt{E_R m_N / 2\mu^2}$ (the minimum velocity to create a recoil of energy E_R), and $f(v)$ is the WIMP velocity distribution relative to Earth.

Assuming the standard halo model predictions and a theoretical dark matter particle mass of 100 GeV, millions of particles pass through a disc the size of a DVD every second. However, the probability for interaction is so low (σ <10^{-45} cm^2 for m$_\chi$ = 100 GeV/c^2) that modern predictions expect less than 1 event per year for a spin-independent interaction in 10 kg of germanium. Predicted event rates for various detector materials is illustrated in Fig. 1.10.

With such low predicted rates, it is clear that any detector with an energy sensitivity to 10-100 keV recoils needs to operate nearly background free. A direct detection experiment requires substantial shielding and excellent background rejection. Cosmic rays can be shielded against by placing an experiment deep underground. However, radiogenic impuri-

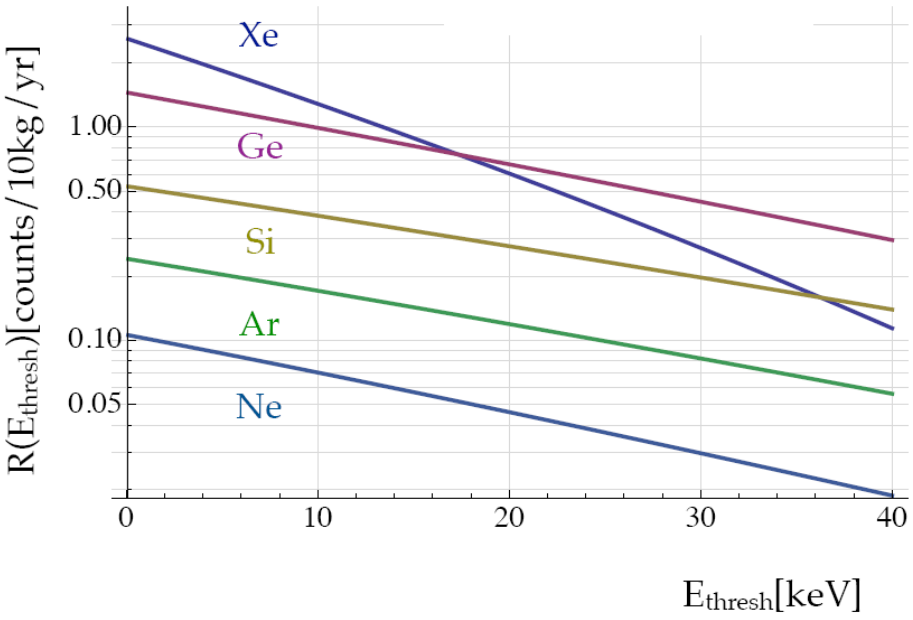

Figure 1.10. Predicted event rates found by integrating Eq. 1.8 for various detector elements at different minimum threshold energies, E_{thresh}. Here it is assumed that the dark matter particle mass is 100 GeV/c^2 and the interaction cross section is 10^{-45} cm^2.

ties in materials and contamination from radon plate-out remain a concern. These will be discussed in greater detail in Chapters 5 and 7.

Despite these challenges, considerable work continues to be done to push the known limits of the mass and interaction probability of WIMPs, including a focus on sub-GeV mass candidates. These particles are more difficult to detect as instruments need to be sensitive to nuclear recoils as low as a few tens of eVs. Within a few more years, the parameter space will be pushed by more than an order of magnitude further by SuperCDMS SNOLAB (see Chapter 4 and Ref. [68]), among others [69–77].

1.3.2. Indirect Detection

Another method of detecting WIMPs may come from observation of the self-annihilation of dark matter particles [78, 79]

$$\chi + \chi \rightarrow p + p$$

where χ represents a dark matter particle and p is either a gamma, neutrino or other particle as illustrated in Fig. 1.11. Dark matter may also decay:

$$\chi \rightarrow p + p$$

These interactions are more likely to be observed in high dark matter density areas such as the centers of galaxies. Dwarf spheroid galaxies are particularly promising objects for observation as they are predicted to be high in dark matter density and low in other gamma emitting sources. The Fermi-LAT collaboration has set upper limits on the dark matter self-interaction cross section through observations of 25 dwarf spheroid galaxies [80], and observations of galaxy clusters [81].

The AMS detector, located in orbit around Earth, can directly detect cosmic rays [82]. If dark matter self-annihilates or decays into charged particles, it may explain any excess of positrons, anti-protons or gamma rays detected by the AMS detector [83]. Data from the AMS experiment has placed constraints on self-annihilating dark matter for candidates

with mass $M_{\rm DM} \lesssim 100$ GeV [84]. Dark matter lifetimes have been constrained to greater than 10^{26} s for masses in the range of 400 MeV to $\sim 10^7$ GeV [85] by data from the AMS experiment [82, 86, 87], *Fermi* [88, 89], the Pierre Auger Observatory [90], KASCADE [91], and CASA-MIA [92].

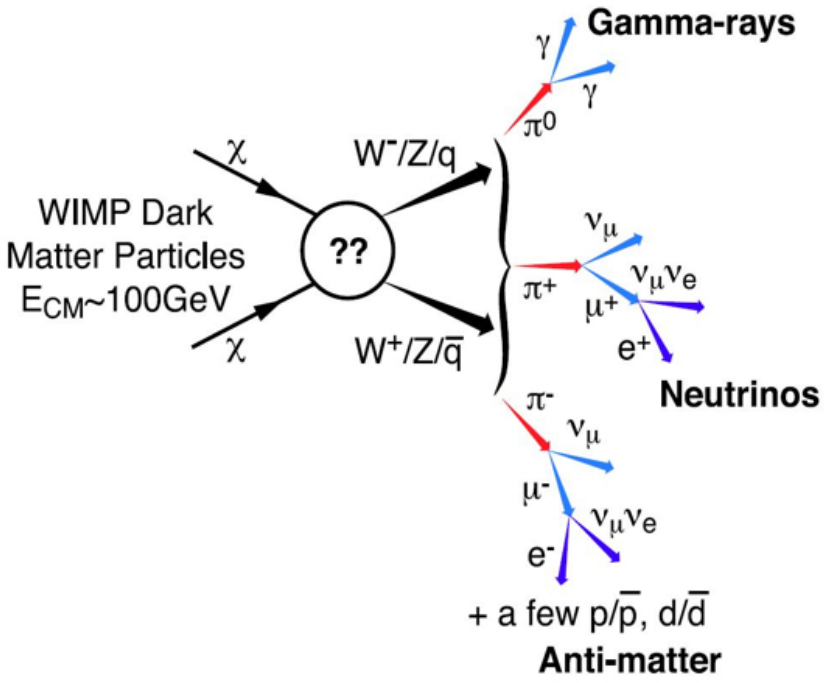

Figure 1.11. Theorists have speculated that the strong gravitational effects caused by the presence of dark matter may mean these particles are very massive. If so, their self-annihilation would likely result in a signature visible in the gamma-ray regime. Adapted from Ref. [93].

1.3.3. Collider Searches

Particle colliders are able to probe all basic interactions of ordinary matter. Dark matter might be produced as another undetected by-product of the interaction of ordinary matter

$$p + p \rightarrow \chi + \chi + p' + p' + \ldots$$

where p' indicates "ordinary" particles generated in the collision. Finding dark matter in collider data relies on searching for missing mass from an event. Colliders also have different systematic uncertainties and can provide complementarity to the field of direct and indirect searches.

More modern searches predict that dark matter interacts with the Higgs boson via a mediator (i.e. the Higgs portal) [94]. This can be probed in multiple ways including exotic Higgs decays [95]. Both ATLAS [96] and CMS [97] are actively searching for dark matter [98–100].

1.4. The SuperCDMS Collaboration

The Super Cryogenic Dark Matter Search (SuperCDMS) collaboration is searching for WIMPs via their elastic-scattering interactions with nuclei. The SuperCDMS Soudan experiment employed low-temperature Ge detectors and was located deep underground in the Soudan Underground Laboratory in Minnesota, USA [101]. The collaboration's next generation experiment will be located at SNOLAB (Vale Inco Mine, Sudbury, Canada), a much deeper facility, and will begin operations in 2020. The experimental configuration and hardware for both experiments is detailed in Chapters 3 and 4.

The use of underground facilities provide shielding from cosmogenic events and as a result reduces background events. This increases the chances of having a positive identification of a WIMP or will allow much more stringent limits to be placed on the WIMP-nucleon interaction cross-section. Chapter 5 describes the cosmogenic and radiogenic background sources for these experiments.

1.4.1. Recent Results from SuperCDMS Soudan

The SuperCDMS Soudan experiment operated in two distinct modes: the normal iZIP operation described in Section 3.1.3, and another mode called CDMSlite [101, 102]. Results from the former set an upper limit for the WIMP-nucleon interaction cross section: $\sigma \leq 1.4 \times 10^{-44}$ cm^2 for a WIMP of mass 46 GeV/c^2 [103] and is illustrated in Fig. 1.12.

This result was from a combined 1690 kg days of exposure at Soudan and set the strongest limit for WIMP-germanium-nucleus interactions for WIMP masses ≥ 12 GeV/c^2.

The CDMSlite mode involved a single detector at a bias voltage of 69 V on one side, and grounded on the other. The objective was to strongly amplify the phonon signal by taking advantage of the Neganov-Trofimov-Luke (NTL) effect: Charge carriers liberated from recoil events gain momentum from the the applied electric field as they drift through the crystal. When the charge carriers collide with Ge atoms, energy is released in the form of additional phonons, thus amplifying the phonon signal [115, 116]. This resulted in a lower-mass reach than for standard iZIP operation as illustrated in Fig. 1.13.

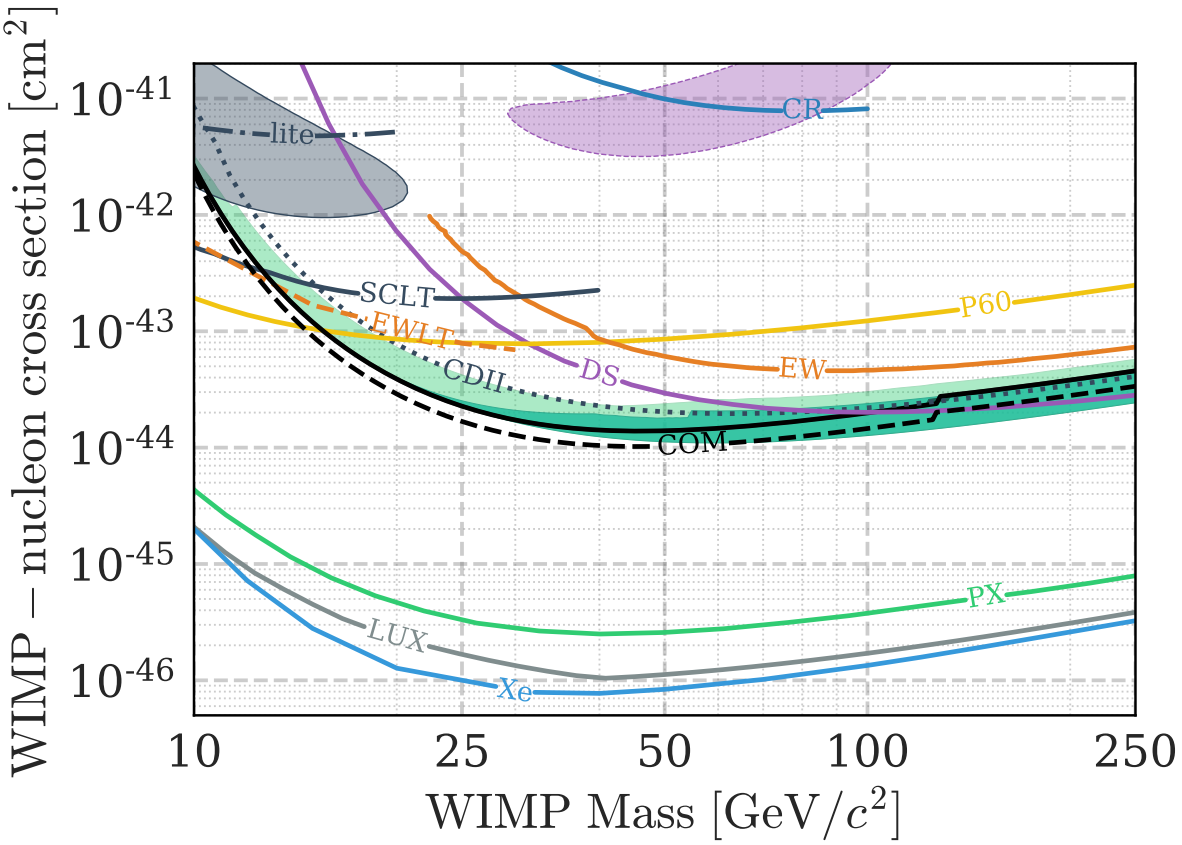

Figure 1.12. The 90% confidence upper limit on the DM-nucleon cross section (solid black) based on a single observed event. The range of the pre-unblinding 68% (95%) most likely expected upper limits are shown as dark green (light green) bands. Closed contours shown are CDMS II Si [104] (solid gray, 90% C.L.) and DAMA/LIBRA [105] (dotted purple, 90% C.L.). The remaining 90% C.L. exclusion limits shown are, in order of increasing sensitivity at 25 GeV/c^2, CRESST (CR) [77], CDMSlite Run 2 (lite) [106], EDELWEISS (EW) [107], SuperCDMS Soudan low threshold (SCLT) [108], DarkSide (DS) [109], PICO-60 (P60) [71], EDELWEISS low mass (EWLT) [110], CDMS II Ge alone (CDII) [111] as well as a combined limit with this result (COM), PandaX-II (PX) [112], LUX (LUX) [113], and XENON1T (Xe) [114]. Adapted from Ref. [103]

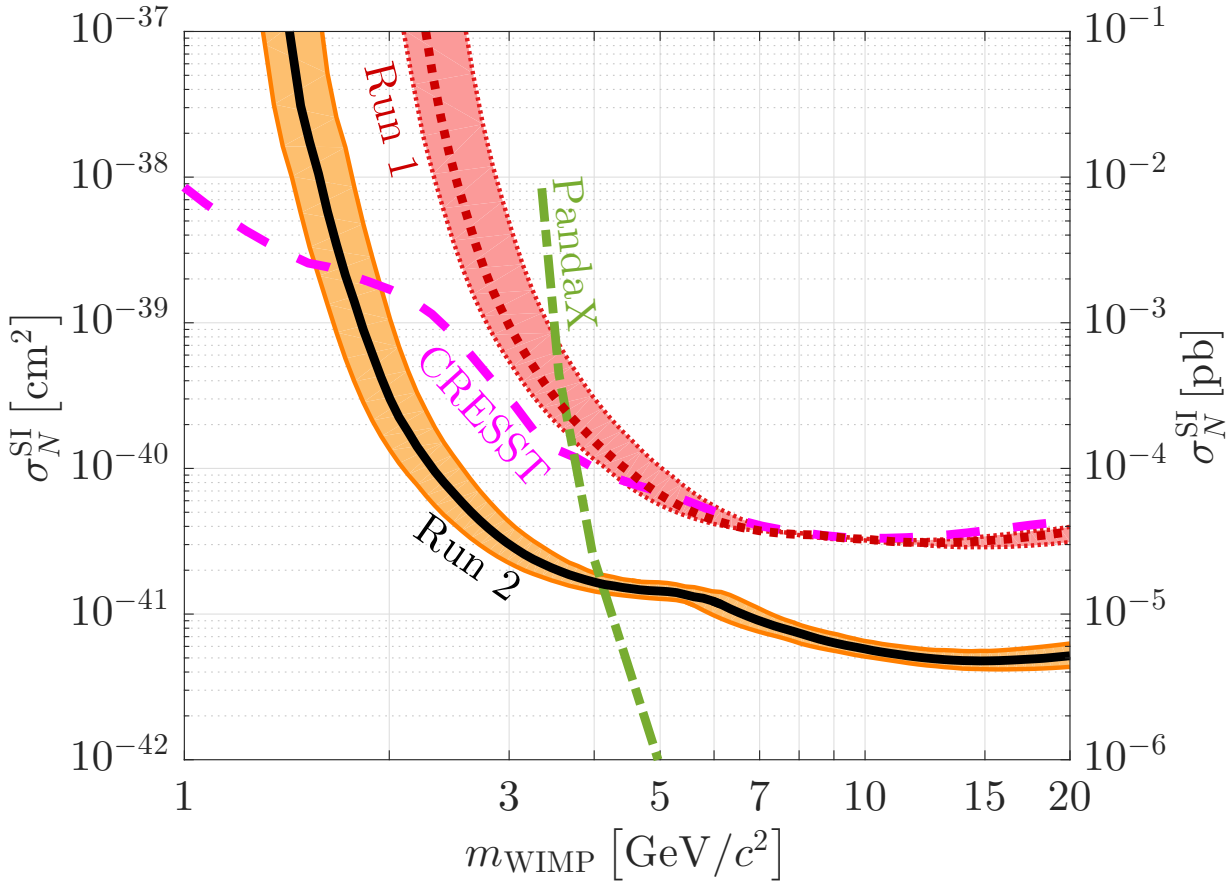

Figure 1.13. Spin-independent WIMP-nucleon cross section 90 % upper limits from CDMSlite Run 1 (red dotted curve with red uncertainty band) [108] and Run 2 (black solid curve with orange uncertainty band) [106] compared to the other (more recent) most sensitive results in this mass region: CRESST-II (magenta dashed curve) [77], which is more sensitive than CDMSlite Run 2 for $m_{\mathrm{WIMP}} < 1.7$ GeV/c^2, and PandaX-II (green dot-dashed curve) [112], which is more sensitive than CDMSlite Run 2 for $m_{\mathrm{WIMP}} > 4$ GeV/c^2. The Run 1 uncertainty band gives the conservative bounding values due to the systematic uncertainty in the nuclear-recoil energy scale. The Run 2 band additionally accounts for the uncertainty on the analysis efficiency and gives the 95 % uncertainty on the limit. Adapted from Ref. [102]

Chapter 2

Defect Formation in Solid State Detectors

As WIMPs do not interact via the electromagnetic force, nuclear recoils with atoms in solid state detectors are of primary interest. When an incident particle scatters off atomic nuclei in a crystal, there exists the possibility that the primary knocked-on atom (PKA) will have enough kinetic energy to leave its lattice site creating a vacancy. The PKA can carry enough kinetic energy that it recoils from multiple atoms. Each knocked-on atom may leave its site with enough energy to create further dislocations.

Energy is released during defect formation in the form of phonons and ionization. Ionization related to recoil energies $\gtrsim$10 keV can be modeled by standard Lindhard theory [117]. This theory, however, overestimates ionization below this point when compared to data [118, 119]. As solid state direct detection experiments begin to search for sub-GeV WIMP candidates, the ionization process from sub-keV nuclear recoils and associated defect formation become a key area of interest.

2.1. Frenkel Defects

The energy required for dislocation is dependent on the bond strength of the crystal and the direction of the recoiling nuclei. If a displaced atom remains elsewhere in the crystal, it is referred to as an interstitial atom. The combination of the interstitial atom and the vacancy are referred to as a Frenkel pair [120] and is illustrated in Fig. 2.1.

The interstitial atom occupies a site that has a higher potential energy than a normal lattice site, but is still a local potential well. In a diamond lattice crystal such as Ge or Si, the conventional lattice is viewed as a face-centered cubic lattice with four additional basis atoms in the tetrahedral positions as illustrated in Fig. 2.2. An interstitial atom can

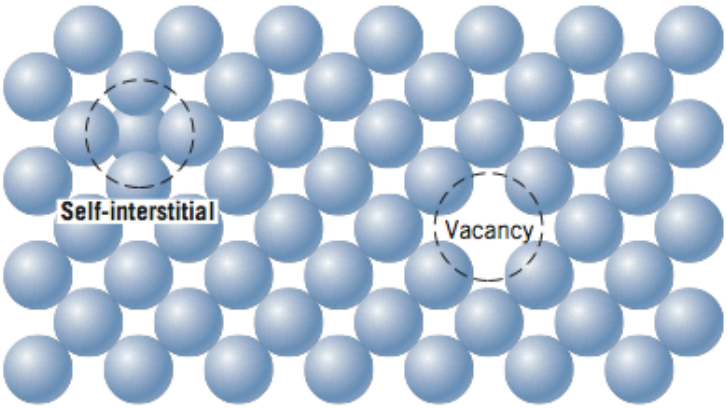

Figure 2.1. A Frenkel pair is the combination of a vacancy and an interstitial atom in a crystal. The interstitial atom occupies a non-lattice site.

be visualized as being located in what would otherwise be a tetrahedral site if the view was rotated 90 degrees.

The probability of creating a Frenkel defect is dependent on the energy of an incoming particle, the atomic numbers of each atom, and the mass of each atom. Consider the incoming atom as having mass m_1 and the target atom, which is at rest in the lab frame, as having mass m_2. The atomic numbers are Z_1 and Z_2 respectively. The incoming atom's energy and momentum as measured in the lab frame are E_1 and p_1 respectively.

When computing the interaction cross section, it is useful to introduce an "effective particle" whose mass (μ_r) and momentum (p_r) are defined as

$$\mu_r = \frac{m_1 m_2 c^2}{E_{cm}} \tag{2.1}$$

$$p_r = p_1 \frac{m_2 c^2}{E_{cm}} \tag{2.2}$$

with E_{cm} taken as the center of mass energy of the system

$$E_{cm} = \sqrt{(m_1 c^2)^2 + (m_2 c^2)^2 + 2E_1 m_2 c^2} \tag{2.3}$$

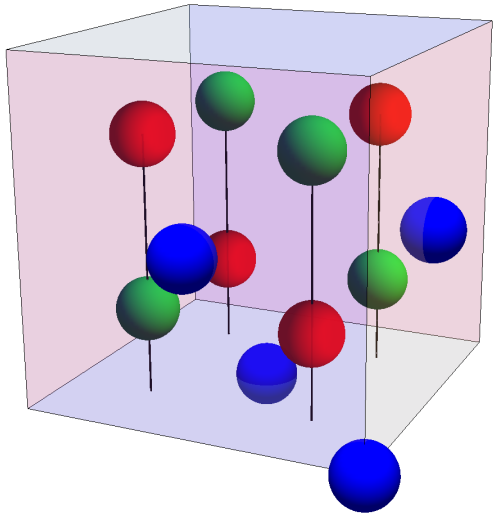

Figure 2.2. The conventional diamond lattice is composed of a face-centered cubic lattice (blue spheres) with four atoms in the tetrahedral positions (green or red spheres depending on orientation). Black lines are visible as posts to clarify atoms at a tetrahedral position. An interstitial atom would occupy a fifth tetrahedral position akin to four green atoms plus one red atom or vice-versa.

The effective particle's velocity (v_r) is then

$$v_r = \frac{1}{\sqrt{1 + \left(\frac{\mu_r c}{p_r}\right)^2}} \tag{2.4}$$

The cross section can be computed as a modified form of Wentzel's cross section [121,122]

$$\frac{d\sigma(\theta_r)}{d\Omega} = \left(\frac{Z_1 Z_2 e^2}{p_r c v_r}\right)^2 \frac{1}{(2A_s + 1 - \cos\theta_r)^2} \tag{2.5}$$

with θ_r the scattering angle of the effective particle in the lab frame, and A_s the screening coefficient as defined in Eq. (6.73) in Ref. [121]. The kinetic energy (T) of the PKA is

$$T = m_2 c^2 \left(\frac{p_1 c}{E_{cm}}\right)^2 (1 - \cos\theta_r) \tag{2.6}$$

It is this final energy, T, that must cross the displacement energy threshold (E_d) in order to create a defect. It can take any value from E_d to the maximum energy of the incoming atom, T_{max}. The total energy loss to defects can be calculated using the Wentzel-Moliere differential cross-section $\sigma^{WM}(T)$ (see Eq. 6.75 in Ref. [121]) and the Lindhard partition function $L(T)$ [123] as

$$-\frac{dE}{dx} = n_A \int_{E_d}^{T_{max}} T L(T) \frac{d\sigma^{WM}(T)}{dT} dT \tag{2.7}$$

where n_A is the number of atoms per unit volume. The non-ionizing energy loss scales with the mass of the particle as shown in Fig. 2.3.

2.2. Angular Dependence

The defect formation energies discussed thus far involved single defects, or the total energy lost from many defects. More explicitly, it is the *average* energy. The defect threshold energy, E_d, depends strongly on the angle of the recoiling nucleus. For example, in silicon, the defect

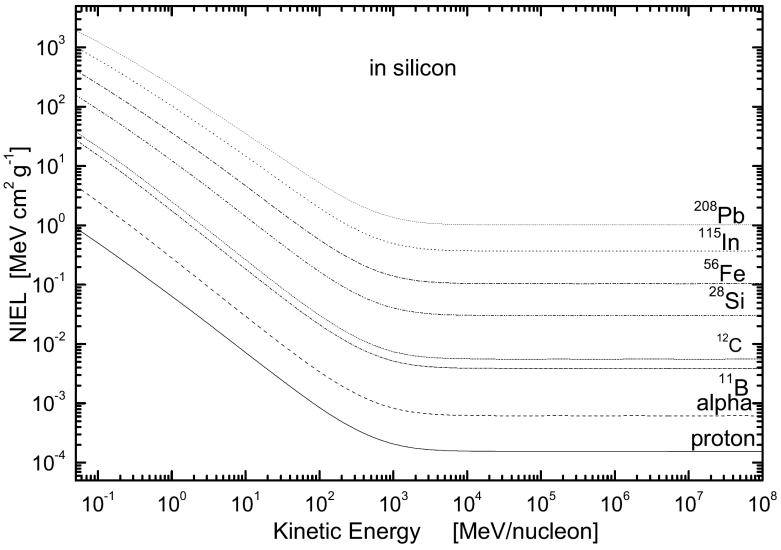

Figure 2.3. Non-ionizing energy loss (NIEL, Equation 2.7) in MeV·cm^2·g^{-1} calculated for silicon is shown as a function of the kinetic energy per nucleon from 50 keV/nucleon up 100 TeV/nucleon for protons, α-particles and ^{11}B, ^{12}C, ^{28}Si, ^{56}Fe, ^{115}In, and ^{208}Pb nuclei. The threshold displacement energy for Si is ∼24 eV [124]. Adapted from Ref. [121].

formation energy in the ⟨111⟩ direction is ∼12.5 eV while the ⟨100⟩ exhibits a minimum of ∼20 eV [124]. The average defect formation energy over all directions is ∼24 eV.

To determine displacement threshold energies, molecular dynamics simulations are employed that simulate shooting a particle at an atom in a lattice repeatedly with increasing energy until a stable defect is formed. These simulations are carried out over many directions until sufficient fineness is achieved to model an angular dependence on the displacement threshold energy, $E_d(\theta, \phi)$. Such simulations are computationally costly and typically involve crystals with atoms numbering only in the thousands, a potential trade-off of speed versus fineness of the determined values for $E_d(\theta, \phi)$. The average displacement threshold energy [125] over all angles is then

$$E_d^{avg} = \frac{\int_0^{2\pi} \int_0^{\pi} E_d^l(\theta, \phi) \sin\theta d\theta d\phi}{\int_0^{2\pi} \int_0^{\pi} \sin\theta d\theta d\phi} \tag{2.8}$$

The average energy as described in Equation 2.8 uses a lower-limit of the displacement threshold energy, E_d^l [126]. When determining the displacement threshold energy from experiment, as opposed to simulation, it is E_d^{avg} that is measured. From this, one can also check and perform a fit of the chosen potential energy formulation. For example, the Stillinger-Weber potential [127] is used to model the total potential energy of the diamond lattice (useful for carbon, silicon, or germanium)

$$
\begin{aligned}
U_{tot} &= \epsilon \left[\sum_{i<j} f_2(r_{ij}/\sigma) + \sum_{\substack{i\neq j \\ j<k}} f_3(r_{ij}/\sigma, r_{ik}/\sigma, \theta_{ijk}) \right] \\
f_2(r) &= \begin{cases} A\left(Br^{-p} - r^{-q}\right) exp\left[(r-a)^{-1}\right], r < a \\ 0, r \geq a \end{cases} \\
f_3(r_{ij}, r_{ik}, \theta_{ijk}) &= \lambda \left(\cos\theta_{ijk} + \frac{1}{3}\right)^2 \exp\left(\frac{\gamma}{r_{ij}-a}\right) \\
&\quad \times \exp\left(\frac{\gamma}{r_{ik}-a}\right)
\end{aligned}
\tag{2.9}
$$

where U_{tot} is the combination of two-body and three-body functions, $f_2(r)$ and $f_3(r)$. The term r_{ij} is the distance between two atoms i and j, and θ_{ijk} is the angle formed between atoms i, j and k. The remaining nine terms $(\epsilon, \sigma, A, B, p, q, a, \lambda, \gamma)$ are the floating parameters (see Table 1 of Ref. [128] for an example parameterization). This potential is commonly used for diamond lattice calculations as it takes into account the bond angles which is especially useful for simulation of the tetrahedral bonds.

Working backwards from an experimentally determined value for E_d^{avg}, it is possible to fit parameters to Equation 2.9. To improve precision, it is useful to increase the cut-off parameter a. This cut-off value effectively discards contributions of atoms further than a to the potential energy calculation. Lowering a speeds up simulations which is useful when very high precision is not anticipated to be required. Increasing a allows for more realistic modeling of the crystal which is useful when higher precision is required or when simulating processes in which atoms move closer and further away (such as defect formation). Increasing

the cut-off value, however, comes at significant computational cost that is proportional to a^3. Thus a fast algorithm needs to be employed, such as that found in Ref. [129].

With potential fitted to an experimentally determined value for E_d^{avg}, it is possible to perform more accurate simulations of the angular dependence of defect formation, or to determine $E_d^l(\theta, \phi)$. This result is useful for a proposed directional search for light dark matter [130] which depends on a strong understanding of the angular dependence of defect formation.

2.3. Prior Ge Threshold Value Calculations

Several past studies attempted to calculate the threshold value for displacing a Ge atom from its lattice site. Displacement threshold values from these studies have varied from seven to 30 eV as illustrated in Fig. 2.4. Early studies did not consider isotopic composition of the crystal, and some studies relied on data from electron beam experiments where the beam itself strongly encouraged the re-combination of vacancies from interstitials thus affecting the outcome. Oxygen contamination in crystals plagued attempts at determining formation enthalpies of vacancies and interstitials. Despite all this, some attempts were made to simulate or theoretically calculate the displacement threshold value. These results are summarized in Table 2.1.

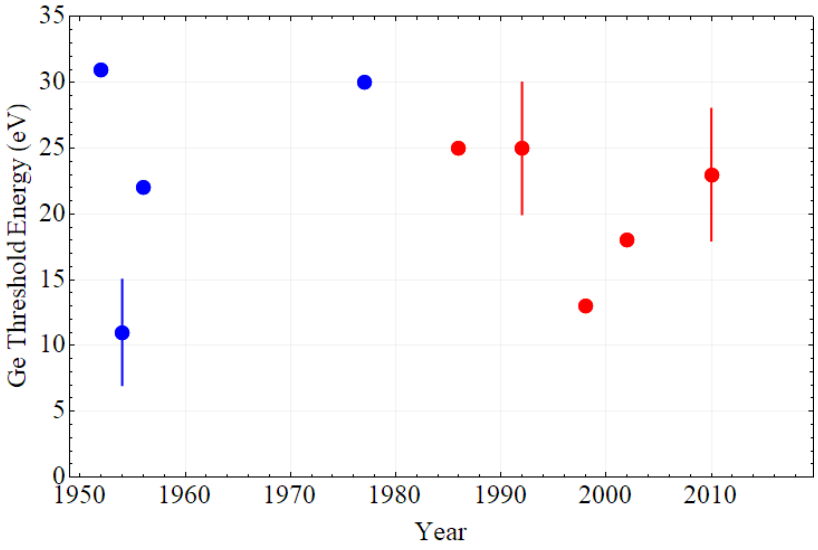

Figure 2.4. Germanium displacement values calculated throughout the years. Blue and red points indicate theory and molecular dynamics calculates, respectively. The exact years, values, and associated references are listed in Table 2.1.

Table 2.1. Values from various studies since 1952 which have calculated the displacement threshold value for Ge. Uncertainties (or the lack thereof) are taken directly from the references.

Year	Value (eV)	Type	Ref.
1952	31	Exp.	[131]
1954	$7-15$	Theory	[132]
1956	22	Theory	[133]
1977	30	Theory	[134]
1986	25	MD	[135]
1992	$20-30$	MD	[136]
1998	13	MD	[137]
2002	18	MD	[138]
2010	23 ± 5	MD	[139]

Chapter 3

SuperCDMS Soudan

The SuperCDMS Soudan experiment was a dark matter direct detection experiment located in the Soudan Underground Laboratory in Soudan, MN [140]. The lab continues to be operated by the University of Minnesota and the SuperCDMS experiment was located in one of two excavated caverns. At 780 m underground, the experiment benefited from 2090 meters water equivalent (MWE) of rock overburden. This reduced the cosmic muon flux by a factor of $\sim 5 \times 10^4$ relative to the surface.

Fifteen Ge detectors were employed to search for WIMP-nucleon scattering events with energies from a few keV to tens of keV. The detectors gathered both phonon and ionization signals making it possible to distinguish electron from nuclear recoils giving the experiment significant background rejection capabilities [141]. Operations began in March 2012 and the experiment was decommissioned in December 2015.

3.1. Experimental Hardware

3.1.1. Shielding & Veto

To decrease the overall background rate, the SuperCDMS Soudan experiment used multiple layers of passive shielding plus an active muon veto. Background sources included neutrons caused by cosmic muon interactions with the shield and cavern materials, gamma rays and neutrons from U- and Th-chain products (also found in the cavern and experimental equipment), and alpha, beta and photon sources on the detector-facing equipment (see Chapter 5 for a detailed explanation of all background sources, their rates, and associated features).

Multiple shield layers were used: a 40-cm-thick cylindrical outer layer of polyethylene, a 22.5-cm-thick layer of lead, the innermost 4.5 cm being of ancient lead for its low ^{210}Pb activity[1], and a further inner 10-cm-thick layer of polyethylene. The shield design is depicted in Fig. 3.1. The combined layers worked to shield against gammas and slow neutrons below the analysis energy threshold.

Surrounding the outer polyethylene layer was the active muon veto which was comprised of 40 scintillator panels, each a 5 cm thick slab of Bicron BC-408 plastic. They were arranged so that they overlap and disallowed any direct line of sight to the detectors. Each panel was connected to one or two 2-inch Hamamatsu R329-02 photomultiplier tubes. The veto system could distinguish between muons and radiogenic photons as minimally ionizing muons typically deposited 10 MeV while the highest radiogenic source would deposit up to 2.6 MeV. Additionally, an event triggered coincidentally in multiple panels was an efficient way to distinguish muon events. The *in situ* measured efficiency of the veto system was 99.4%±0.2% for stopped muons, and 99.98%±0.02% for through-going muons with precision limited by the low muon event rate. The average event rate in the veto system was 600 events per second, which was dominated by ambient gammas. The muon rate was approximately one per minute.

3.1.2. Infrastructure

The SuperCDMS Soudan experiment utilized the infrastructure from CDMS II [140]: a cryostat surrounded by passive shielding and an active muon veto. The cryostat, or "icebox," comprised six concentric cylindrical cans in the center of the apparatus, the innermost being maintained at ∼50 mK by an Oxford Instruments Kelvinox 400-S dilution refrigerator [142]. The cans were made of oxygen free, high thermal conductivity (OFHC) copper and provided an average of 3 cm of additional shielding. The dilution refrigerator was coupled to each can through five nested copper tubes and a central, solid cold finger. This is referred to

[1]This lead was recovered from a sunken ship ballast near Nantes, France, and purchased from Lemer Pax, Protection Anti-X, 3 Rue de lEurope, Zone Industrielle, F-44470 CARQUEFOU - FRANCE. [140]

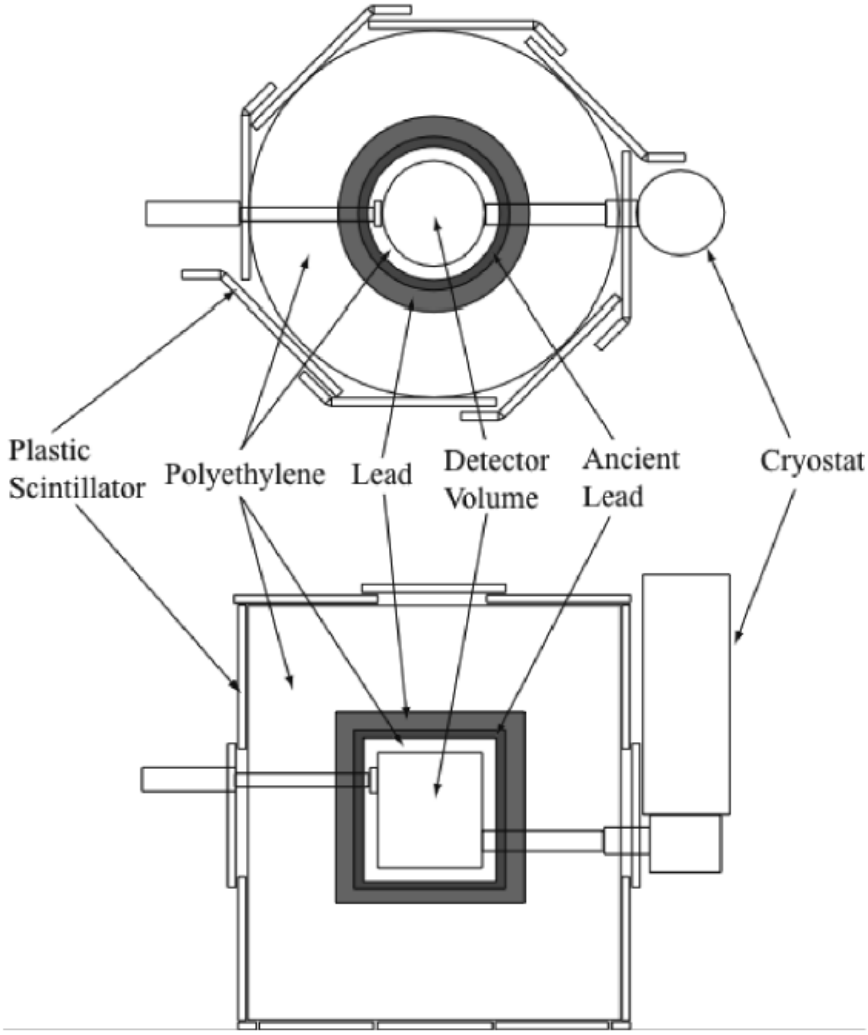

Figure 3.1. Top view and side view of the SuperCDMS shielding and veto. The detector volume is referred to as the icebox. As shown, the stem to the right of the detector volume is the cold stem and connects the detectors and the copper cans to the cryostat. The stem to the left of the detector volume is the electronics stem and contains the wiring that connects the cold electronics to the room-temperature electronics. Adapted from Ref. [140]

as the "cold-stem" or "c-stem" (Fig. 3.2). The solid finger connected to the innermost can which is 30 cm in diameter and 30 cm high. Opposite the c-stem was the electronics stem, or "e-stem," which carried striplines connecting the detector hardware to the room-temperature readout electronics outside the icebox. A 2 mm mu-metal shield surrounded the entire icebox and shielded the cold hardware from outside magnetic fields.

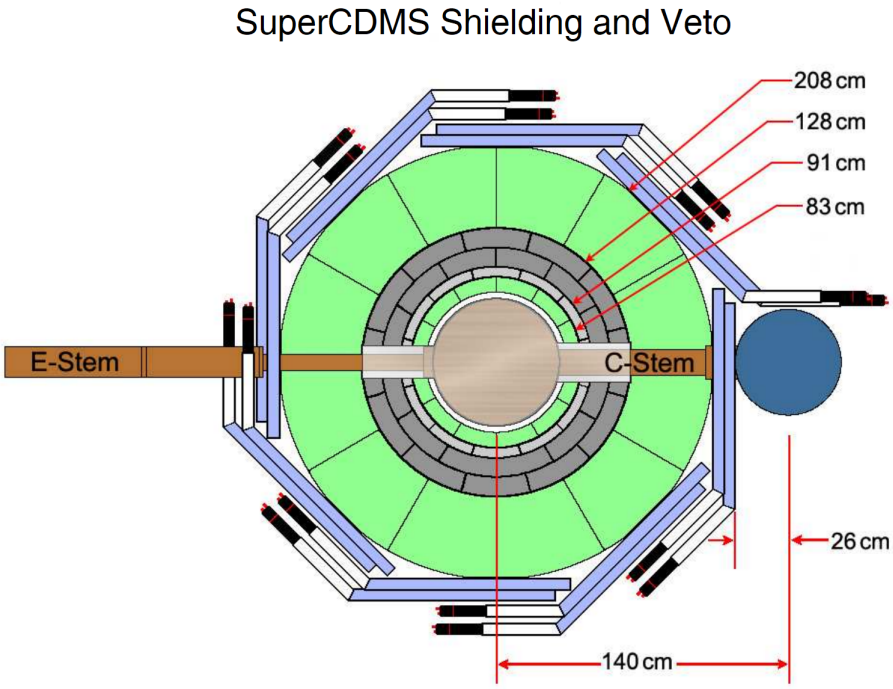

Figure 3.2. Top-side of the SuperCDMS shielding and veto system. Blue and white panels are the scintillator panels and photomultiplier tubes, respectively. The lead and polyethylene shields are drawn as gray and green areas, with the inner ancient lead indicated by a lighter shade of gray. The c-stem and e-stem indicate where the dilution refrigerator and electronics connect to the innermost can.

The entire apparatus (icebox, passive shields, and muon veto) was housed in an RF-shielded enclosure, known as the RF-room. This room was measured as better than a Class 1,000 cleanroom when unoccupied, and a Class 10,000 cleanroom during working hours.

3.1.3. iZIP Detectors

A total of 15 instrumented Z-sensitive Ionization- and Phonon-mediated (iZIP) germanium detectors were used in the operation of the SuperCDMS Soudan experiment. The detectors were arranged in five towers of three detectors as shown in Fig. 3.3. Each detector was 76 mm in diameter and 25 mm high, and was named according to its tower and location: TXDY, where X indicates the tower number (1-5) and Y indicates the detector number within that tower (1-3). The detectors were numbered top-to-bottom, so T3Z1 would indicate the topmost detector in Tower 3.

Ionization and phonons arise from the elastic scattering of particles off the Ge atoms in the cryogenically cooled crystal. On both faces of the crystal were interleaved ionization and grounded phonon electrodes as illustrated in Fig. 3.4. The ionization channels were biased at +2 V and −2 V on the top and bottom faces, respectively, creating a relatively uniform electric field (∼0.5 V/cm) throughout the bulk of the crystal. Ionization measurements were made by drifting electrons and electron-holes through this field to the top and bottom faces of the detector. Phonon measurements were made using the advanced athermal phonon sensor technology developed for CDMS II [143]. When athermal phonons reached the surface of the detector and interacted with superconducting aluminum electrodes, they broke Cooper pairs to form quasiparticles. These quasiparticles diffused into tungsten Transition Edge Sensors (TES) that operated at their transition temperature (Fig. 3.5). This increased the temperature of the tungsten and thus its resistance. The change in current in the TES was detected through the use of SQUID amplifiers.

Events that occurred within ∼1 mm of the surface liberated electrons and electron-holes that drifted only to one detector face. This was due to the asymmetry of the electric field near the surface, illustrated in Fig. 3.4(b). Additionally, the increased strength of the electric field at the surface improved charge collection for such events. The asymmetry in charge collection is a robust method for discriminating surface from bulk events, fiducializing the detector volume.

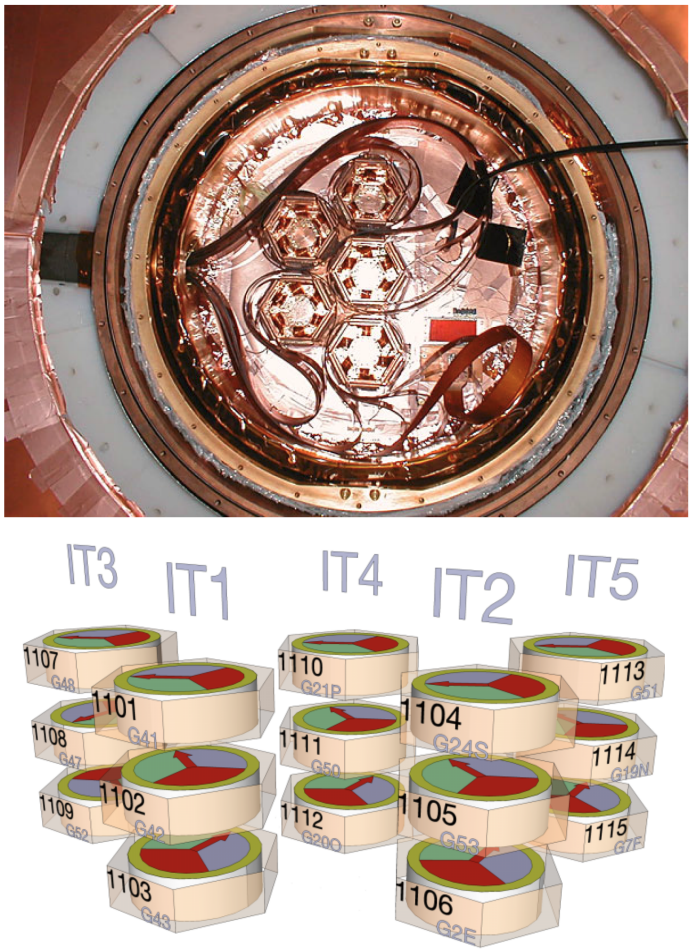

Figure 3.3. Top: Top view of the towers as placed in the icebox. Bottom: An exploded view of the arrangement of the SuperCDMS germanium detectors. The labels above each tower indicate the tower name (i.e. IT3 is iZIP Tower 3). The numbers on each detector indicate the detector number ranging from 1 to 15 (i.e. 1107 is detector seven). The gray labels on each detector were a secondary internal labeling scheme (i.e. G48 indicated germanium detector 48, but is identical to 1107).

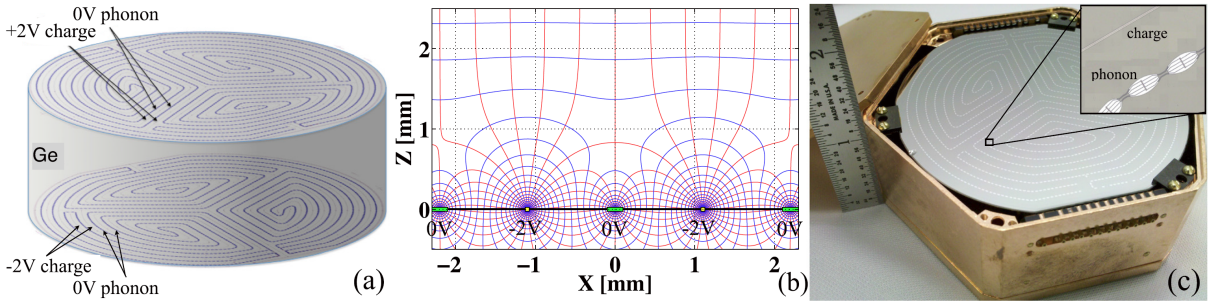

Figure 3.4. (a) Phonon and ionization sensor layout for iZIP detectors deployed at Soudan. The Ge crystal is 76 mm in diameter and 25 mm thick. Both faces are instrumented with ionization lines (one face with +2 V and the other with −2 V) that are interleaved with phonon sensors (0 V) on a ∼1 mm pitch. The phonon sensors are arranged to give four phonon readout channels for each face, an outer sensor surrounding three inner ones. (b) Magnified cross section view of electric field lines (red) and equipotential contours (blue) near the bottom face of a SuperCDMS iZIP detector. The −2 V ionization electrode lines (yellow dots) are narrower than the 0 V athermal phonon collection sensors (green rectangles). (c) Fabricated iZIP detector in its housing. Adapted from Ref. [141].

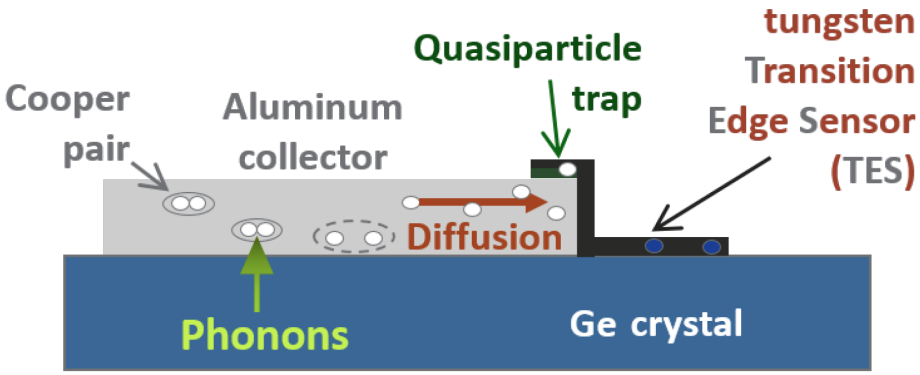

Figure 3.5. Athermal phonons in the detector (blue mass at bottom) propagate to the surface and break cooper pairs in the aluminum electrodes, creating quasiparticles. These quasiparticles diffuse into the TES, raising the temperature and resistance of the tungsten.

The charge electrodes on the detector faces were split into two channels: an inner circular area, and an outer guard ring. There were also four phonon channels: three channels in the inner area of the detector and an outer channel as illustrated in Fig. 3.6. By comparing energy collection in these channels, and the ratios of inner and outer channels, it is possible to reject events that occurred near the sidewalls of the detector, further fiducializing the detector.

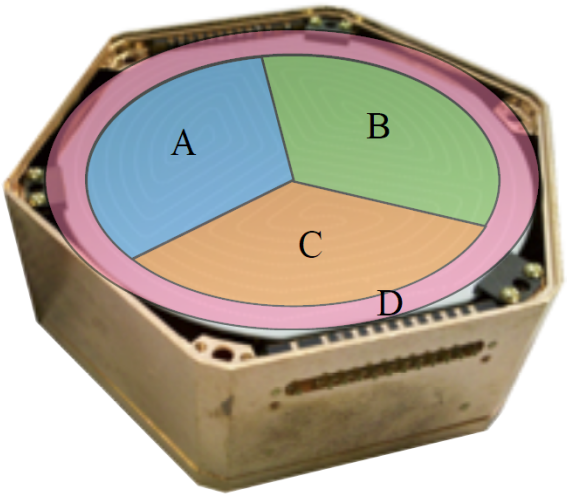

Figure 3.6. The four phonon channels on each detector face labeled A, B, C and D. The outer charge channel covered the same area as the outer phonon channel, with the other charge channel covering all of the inner area.

The detectors provided the ability to discriminate nuclear recoils (NR) from electron recoils (ER) by comparing the ratio of ionization to phonon energy or "ionization yield." Gammas from a ^{133}Ba source were used to define the ER band, and neutrons from a ^{252}Cf source were used to define the nuclear-recoil band. The ionization yield of ER events was normalized to 1 with nuclear recoil events falling around 0.3 as illustrated in Fig. 3.7.

Electrons that interacted at the surface of the detector may have suffered from lower charge collection and thus lower yield, but phonon timing information was used for discriminating criteria as these phonons arrived faster than those in the bulk. By discriminating

events in this way, less than one electron recoil appeared in the nuclear recoil band for every 1×10^6 events in the bulk of the detector [141].

To provide additional surface event rejection statistics, ^{210}Pb sources were installed adjacent to two detectors [141]. The ^{206}Pb recoil band can be clearly seen in the right panel of Fig. 3.7 with a yield around 0.3, while surface betas have a yield around 0.7. The ^{210}Pb decay chain and detector response to these events is covered in much greater detail in Chapter 9.

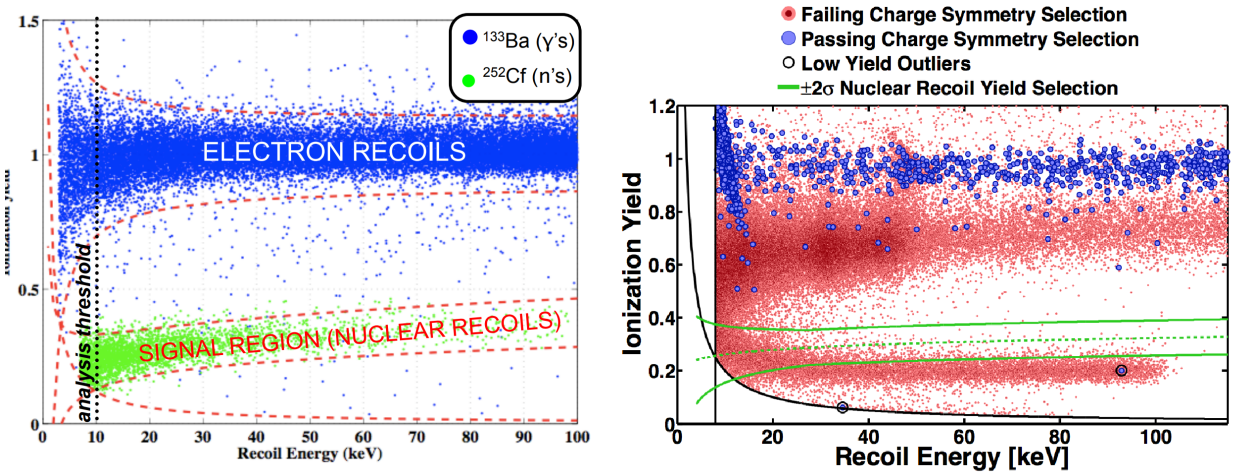

Figure 3.7. Left: The analysis region is the nuclear recoil band defined using neutrons emitted from ^{252}Cf. The electron recoil band is calibrated with gammas from a ^{133}Ba source. Right: Data from one SuperCDMS detector with an adjacent ^{210}Pb source. Red points indicate events that were rejected by a symmetry cut, and blue events pass the symmetry cut. The low-yield, red events are ^{206}Pb recoils impacting the detector face. One can see two "near-misses" where a likely ^{206}Pb atom passed the symmetry discrimination and had yield values that almost put it in the WIMP-search region.

3.2. Data Acquisition & Processing

The charge and phonon information was transmitted via the data acquisition (DAQ) electronics system which consisted of both "cold" and "warm" electronics. The cold electronics, situated within the icebox, included detector interface boards attached to the sides of the detectors and are shown in Fig. 3.8. The charge and phonon information was transferred to

the top of each tower, to the field effect transistors (FETs), and to the SQUID amplifiers, respectively. Striplines then carried the amplified signals to the "warm" electronics system (room-temperature in the RF Room) through the e-stem.

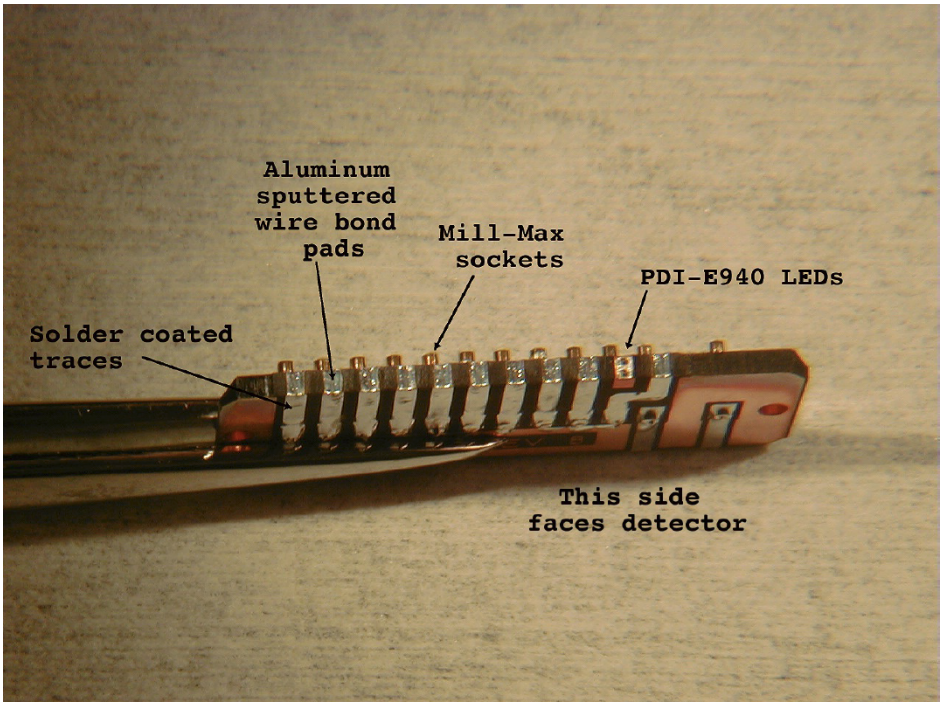

Figure 3.8. The detector interface board (DIB), that was attached to the sides of the Ge detectors. Charge and phonon information collected from the surfaces would pass through these boards and eventually to the top of the tower to the SQUID amplifiers.

The warm electronics performed an initial quality check on the data and decided which events to record. Fast waveform analyzers (ADCs) monitored the analog signals. Whenever an event surpassed the trigger threshold which was set independently for each detector, the DAQ recorded and monitored both detector and veto signals, namely the trace-time information. This information was stored on-site and later transmitted to Fermilab for further processing.

The stored raw data was processed into "reduced quantities" (RQs) and "rational reduced quantities" (RRQs) [140] using a software package called cdmsbats. BatRoot, a part of cdmsbats, created the RQs which included values like unique event numbers, time since the

start of the event, and the trace-time information for charge and phonon pulses for each channel. BatRoot used noise traces that are randomly selected traces (i.e. not associated with an event trigger) and a pulse template to generate the RQs (Fig. 3.9). These RQs were not calibrated quantities, but were used in the production of the RRQs that themselves are calibrated quantities with units. The 356 keV line from a ^{133}Ba source was used to calibrate the ionization energy scale. A software program called BatCalib used this information to generate the RRQs (Fig. 3.10). This information was collectively stored in a ROOT [144] file for later analysis.

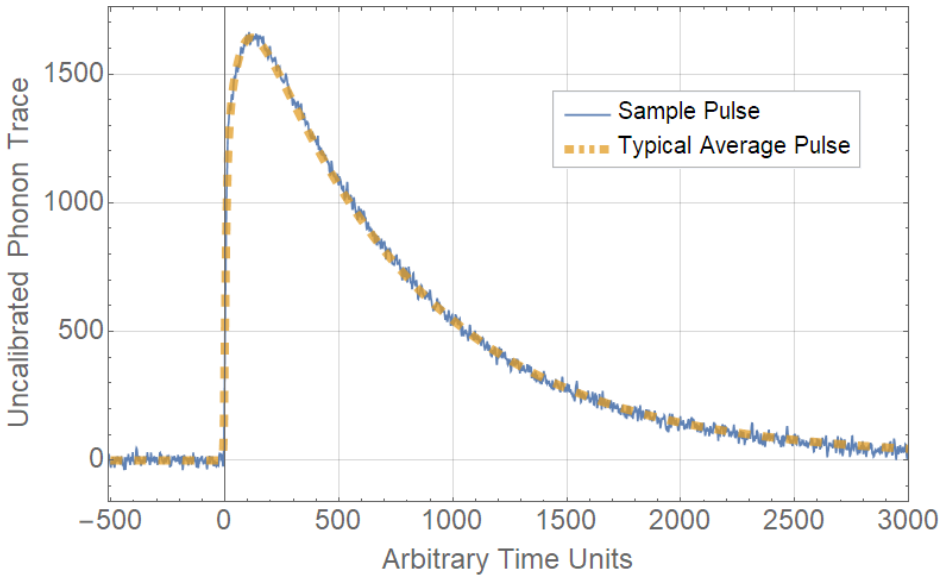

Figure 3.9. Sample total phonon pulse from raw data. The pulse stands out sharply against any noise which is visible in the blue curve. An average pulse shape is shown by the dashed yellow curve.

It is useful to select events with specific criteria for a given analysis, and thus specific RQ and RRQ values. The process of excluding unwanted events will hereafter be referred to as a "cut." These cuts can be made to exclude or select events with a simultaneous veto trigger, events during calibration runs (i.e. with a ^{133}Ba or ^{252}Cf source installed), events with multiple triggers in multiple detectors, and so on. All this information is available in the ROOT files stored as RQs and RRQs. This makes it possible to quickly select events

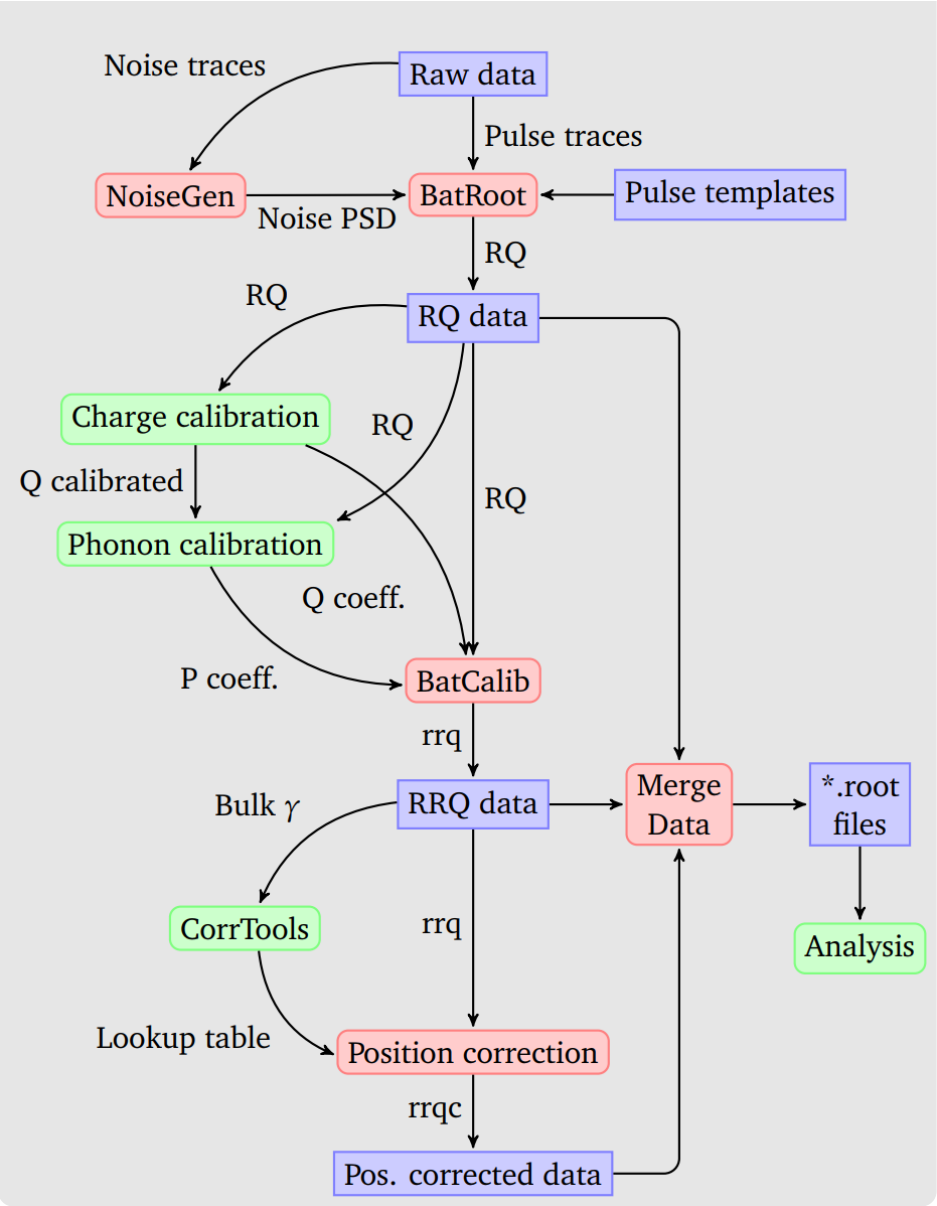

Figure 3.10. The CDMS data processing pipeline.

of interest for analysis such as events in the bulk with good charge and phonon symmetry, charge collection away from the guard channels, not during a calibration run, in the nuclear recoil band, and with a particular recoil energy. Additional details on data, cuts, and their usage is available in Appendix A.

Chapter 4

SuperCDMS SNOLAB

The next generation SuperCDMS experiment has been selected by the Department of Energy and the National Science Foundation to improve current WIMP-search results by at least one order of magnitude for masses $\leq$10 GeV/c^2 [68]. The experiment will utilize cryogenic detectors operating in two different modes and with two target materials. The iZIP mode will benefit from strong electron and nuclear recoil discrimination and of the two modes will have the best sensitivity to masses $\gtrsim$ 5 GeV/c^2. The second mode utilizes a high-voltage (HV) design with greater sensitivity to masses $\lesssim$ 5 GeV/c^2. Germanium and silicon detectors will be deployed in both modes.

The experimental site will be located in the ladder lab drift of SNOLAB [145], a Class 2000 clean room laboratory 6,800 feet below the surface in Lively, Ontario, Canada. The norite overburden provides 6,010 MWE of shielding leading to a cosmic muon flux of 0.27 muons/m^2/day [146], a factor of $\sim$320x less than the Soudan Underground Laboratory. The experiment is scheduled to begin science operations in 2020.

4.1. Infrastructure and Shielding

The SuperCDMS SNOLAB experiment will use a dilution refrigerator that utilizes cryocoolers to maintain detector temperatures of 15–30 mK [68]. The detectors will be housed in the innermost of six concentric copper cans with cold and electronics stems providing thermal and readout electronic connections. The copper cans will be surrounded by a 40 cm layer of polyethylene, which is surrounded by a 20 cm layer of lead. Sixty cm of water shielding will surround the upper and sidewall areas while 60 cm of polyethylene will be located underneath the ensemble as illustrated in Fig. 4.1.

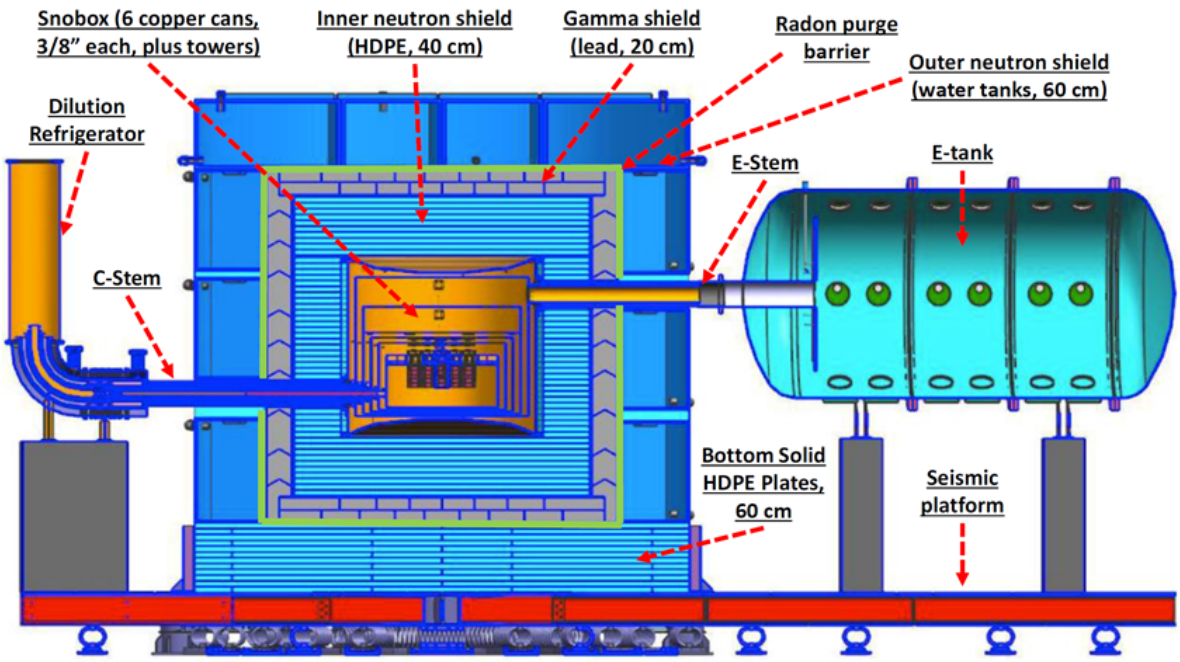

Figure 4.1. A schematic of the experiment shield and cryostat layers. The assembly rests on top of a seismic platform to provide isolation from seismic events. The outer water tanks provide protection from cavern neutrons. A gamma shield protects from external gamma-rays and the inner polyethylene layers serve to absorb radiogenic neutrons emitted from the cryostat and gamma shield.

These layers were specifically chosen for their ability to reduce radiogenic backgrounds in the cavern [147, 148]. The water shielding will reduce the estimated neutron flux by five orders of magnitude, and the lead shielding will reduce the estimated gamma flux by six orders of magnitude. The innermost polyethylene layer will shield against secondary neutrons from spallation as well as gamma rays and neutrons from radio-impurities in the cryostat and lead shield.

4.2. SuperCDMS SNOLAB Detectors

The experiment will exhibit improvements to the detector payload and associated technology. Both Ge and Si detectors will be employed, each with diameter of 100 mm and thickness of 33.3 mm. The mass of each detector will be 1.39 and 0.61 kg, respectively.

The iZIP design is an improvement upon that used by SuperCDMS Soudan with four phonon and two ionization channels on each detector face as illustrated by Fig. 4.2. The ionization channels will be biased at 6 and 8 V for Ge and Si detectors, respectively, while the phonon channels are grounded. The iZIPs ability to discriminate nuclear and electron recoils indicates they can operate in a nearly background-free mode, and will have better sensitivity to WIMP masses $\gtrsim$5 GeV/c^2.

The HV detectors are designed to have better sensitivity to masses $\lesssim$5 GeV/c^2. These detectors have six phonon channels per side with no ionization channels. The phonon channels can be biased up to 100 V creating a much stronger electric field in the crystal than the iZIP detectors. This bias makes it possible to take advantage of the Luke-Neganov effect [149, 150] which amplifies the phonon signal. The amplification can boost the signal of low-energy events above the operating threshold extending the sensitivity of the HV detectors to lower masses.

Unlike the iZIP detectors, the HV detectors cannot distinguish electron recoils (ER) from nuclear recoils (NR) and so these detectors will be dominated by ER backgrounds. The Luke-Neganov effect, however, has greater amplification for ER vs NR events due to the

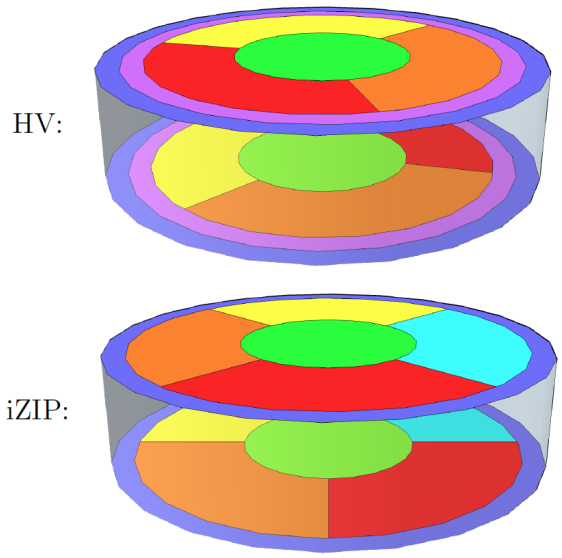

Figure 4.2. Channel layout for the HV (top) and iZIP (bottom) detectors. The HV detector has six phonon channels on each side, arranged as an inner "core," surrounded by three wedge shaped channels and two outer rings designed to reject events near the edge. Each channel contains hundreds of lithographically defined superconducting sensors. The wedge channels on the bottom surface are rotated by 60° with respect to those on the top. The interleaved Z-sensitive Ionization Phonon (iZIP) detector also has six phonon channels on each side, arranged as an inner core, surrounded by four wedge shaped channels and one outer ring. An "outer" ionization channel shares the same area and is interleaved with the outermost phonon ring, and an "inner" ionization channel is interleaved with the remaining phonon channels. The wedge channels on the bottom surface are rotated by 45° with respect to those on the top surface. Adapted from Ref. [68]

higher ionization yield. This pushes low-energy ER backgrounds to higher energies reducing the overall low-energy background rate [151].

4.3. Operation and Projected Sensitivity

There will be 10(2) iZIP and 8(4) HV detectors for Ge(Si) leading to a total exposure of 114.4 kg days for the five years of operation, assuming 80% live-time. These detectors will be deployed in four towers of six detectors each. While the experiment can be upgraded to include 31 towers, the initial four towers will be offset from the line-of-sight of the cold and electronics stems as illustrated in Fig. 4.3. Simulations indicate that this will reduce ER backgrounds by at least a factor of two, and the compact design improves the efficiency of rejecting events with scatters in multiple detectors.

The initial design will have sensitivity to nuclear recoil cross sections $\sim 1 \times 10^{-43}$ cm^2 for a dark matter particle mass of 1 GeV/c^2. Figure 4.4 shows the projected sensitivity for each detector type at the 90% confidence level. The low-mass reach is strongly affected by the detector analysis threshold which, if lowered, will extend the sensitivity towards even lower masses.

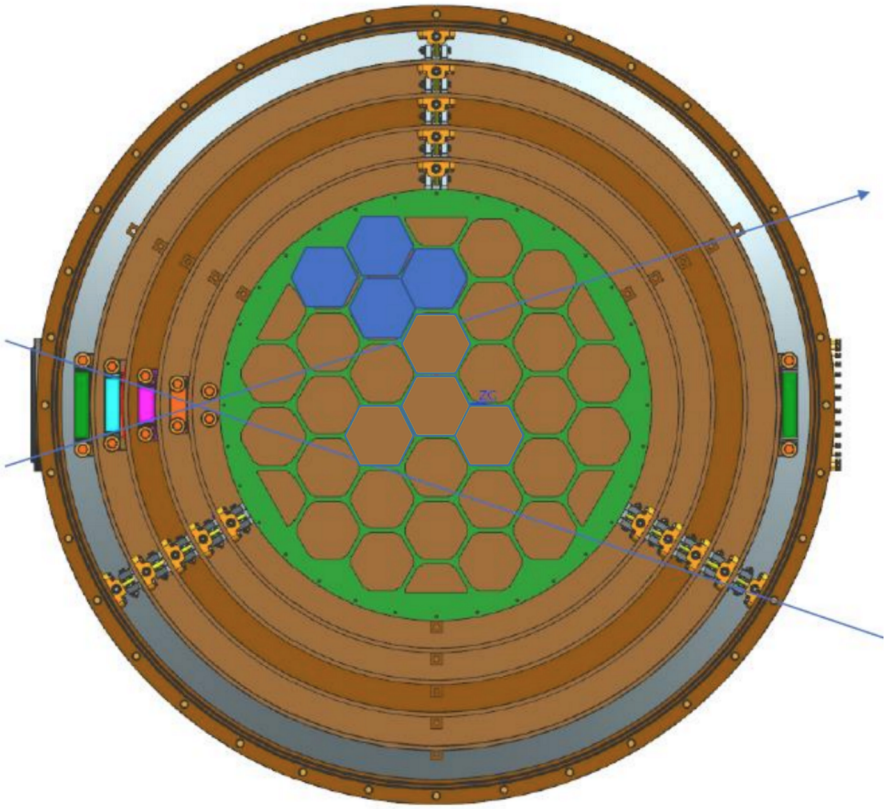

Figure 4.3. Detector tower layout inside the innermost copper can. The initial four-tower payload will be located in the blue positions. The line-of-sight exiting the cold stem is indicated by blue lines.

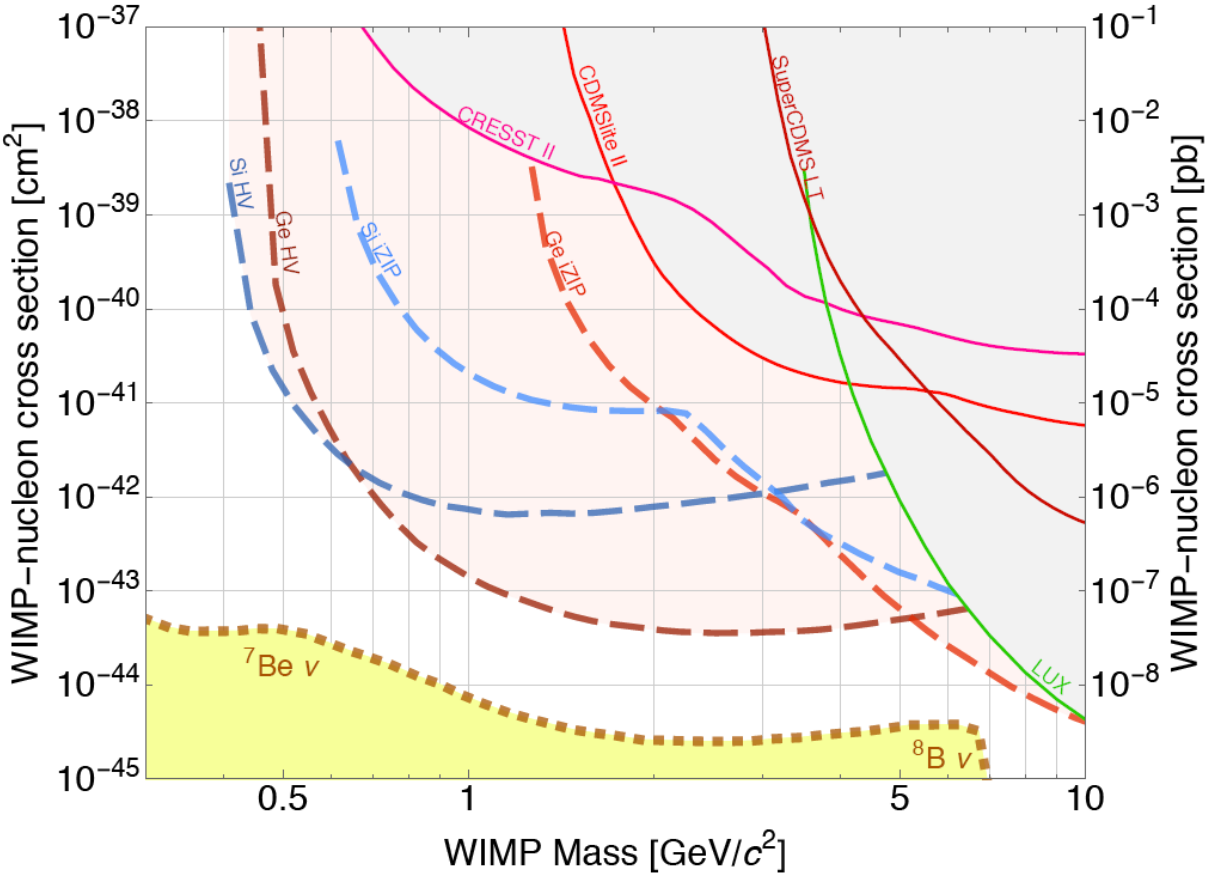

Figure 4.4. Projected exclusion sensitivity for the SuperCDMS SNOLAB direct detection dark matter experiment. The vertical axis is the spin-independent WIMP-nucleon cross section under standard halo assumptions [50], and the horizontal axis is the WIMP mass, where WIMP is used to mean any low-mass particle dark matter candidate. The blue and red dashed curves represent the expected sensitivities for Ge and Si operating in both iZIP and HV modes. The solid lines are the current experimental exclusion limits in the low-mass region, from the CRESST-II [77], SuperCDMS [108, 152] and LUX [75] experiments. The dotted orange line is the dark matter discovery limit from Ref. [153], which represents the cross section at which the interaction rate from dark matter particles becomes comparable to the solar neutrino coherent elastic scattering rate. Adapted from Ref. [68].

Part II

Backgrounds & Simulations

Chapter 5

SuperCDMS Backgrounds

Constant background radiation can come from, among other things, naturally occurring radioactive isotopes in materials, airborne radon, and cosmic rays. With the extremely low event rates predicted for the SuperCDMS experiments described in Section 1.2.4, and with the sensitivity goals of the experiments described in Chapters 3 and 4, understanding and controlling backgrounds is of high importance, particularly for neutrons in iZIP detectors and electron recoil backgrounds in the HV detectors.

5.1. Cosmogenic Background Sources

The Earth is constantly bombarded by cosmic rays which include electrons, protons, alpha particles and heavier nuclei [154]. The energy of a cosmic ray can be very high (up to 10^{20} eV) and the production methods are not yet fully understood [155]. Primary cosmic rays can interact with atmospheric molecules creating particle showers of secondary cosmic rays, most of which are muons. Regardless of whether a particle is a primary or secondary cosmic ray, it has great penetrating power making surface-based rare-event searches impractical, even with substantial shielding.

Common among dark matter direct detection experiments is the fact that they are nearly all placed deep underground in mines or underneath mountains as illustrated in Fig. 5.1. Such locations provide substantial shielding and very few cosmic muons are able to penetrate the rock overburden. Stemming from the fact that water is an efficient cosmic ray shield [156], it is more common to quote the shielding power of the rock overburden in "meters water equivalent" or MWE. This unit also accounts for differences in the composition of the overburden making it a better proxy for shielding efficiency as compared to depth alone.

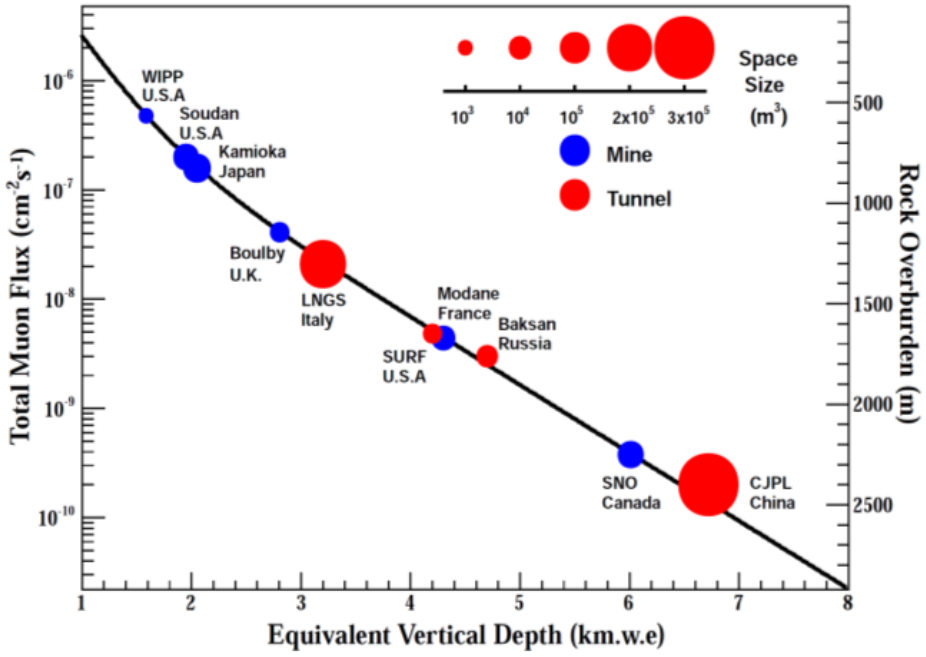

Figure 5.1. A selection of dark matter experiment locations and relative lab sizes. The total muon flux measured for the various underground sites is shown as a function of the equivalent vertical depth relative to a flat overburden. The smooth curve is a global fit function to those data taken from sites with flat overburden. Adapted from Ref. [157]

The dramatic reduction in total muon flux makes deeper experiment locations most favorable. The CDMS collaboration determined that $\gtrsim$5,000 MWE of overburden is required to push WIMP-nuclean interaction sensitivities to $\sigma \sim 10^{-46}\text{cm}^{-2}$ or lower for a WIMP mass of 100 GeV/c^2 [158].

SNOLAB is located 2 km ($\sim 6,800$ ft) underground in the active Vale Creighton nickel mine which is in Sudbury, Ontario, Canada and exhibits an impressive 6,010 MWE of norite rock overburden. The measured cosmic muon flux is $\sim 100\ \mu\text{m}^{-2}\text{y}^{-1}$ [146] which was a world record until the China Jinping Underground Laboratory opened in 2010.

Cosmic rays can create additional backgrounds by activating experiment materials during shipping or storage at the surface. The cosmic ray flux depends on elevation, geographic location, and solar activity. The elevation dependence is illustrated in Fig. 5.2. Activation rates of materials have been widely studied and improvements have been made in the last ten years to more accurately simulate and predict activation. Great care must still be taken, however, to protect materials from high altitude or long-term, unshielded exposure. A recent and very thorough study of cosmogenic activation of rare-event experiment materials was done by Chao Zhang and colleagues. This study compared Geant4 [159–161] and ACTIVIA [162] simulations to a variety of experimental measurements for a wide variety of activated materials [163]. These results guide decisions on procurement, shipping, and logistics in regards to experimental materials, and subsequently inform modeling of predicted activation.

For the SuperCDMS experiments, copper is important for activation modeling, especially in regards to isotopes like ^{60}Co and its five-year half-life. Copper is used in many parts of the apparatus, including the detector housings and so have a substantial line-of-sight exposure area to the detectors themselves. Initial sensitivity estimates for SuperCDMS SNOLAB are based upon a sea-level exposure to cosmic rays for 90 days, followed by a 90 day "cool-down" period to let short-lived isotopes decay away. The predicted contamination rates are summarized in Table 5.1. As discussed in Section 5.3, the various decay products produce a variety of different responses in the detector, so each type of interaction must be studied in detail.

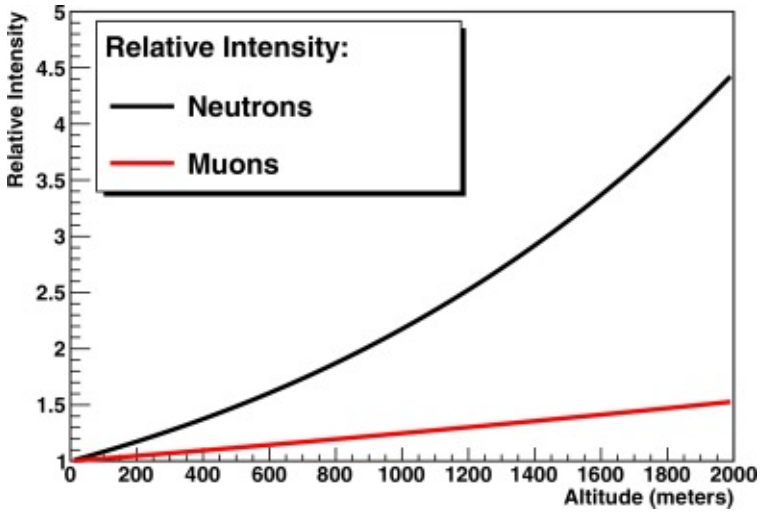

Figure 5.2. The relative intensity of muons and neutrons as a function of altitude. Adapted from Ref. [163].

Table 5.1. Assumptions used to determine the cosmogenic exposure and activation of copper for the SuperCDMS SNOLAB sensitivities. Adapted from Ref. [68].

	Production Rate	Contamination Rate (μBq/kg)	
Isotope	(atoms/kg/day)	Housing/Towers	Cryostat
^{46}Sc	4.6	0.88	0.62
^{48}V	9.5	0.76	0.25
^{54}Mn	19	7.9	12
^{56}Co	20	3.5	2.3
^{57}Co	155	62	89
^{58}Co	143	23	13
^{59}Fe	39	2.9	0.9
^{60}Co	181	47	90

5.2. Radiogenic Background Sources

While placing a rare-event experiment deep underground provides substantial benefits for muon-induced neutrons, it also comes with additional backgrounds challenges from radiogenic sources. The norite rock at SNOLAB contains natural uranium, thorium, and potassium isotopes, as does the concrete and shotcrete that line the floors and walls of every cavern [147]. As these materials and their daughter products decay, they release alpha, beta, and gamma radiation that can interfere with rare-event searches.

Table 5.2. Levels of K, U, and Th found in the norite, concrete and shotcrete used at SNOLAB. Measurements were made using ICP-MS and Ge detectors [147].

Material	^{40}K (%)	^{235}U (ppm)	^{228}Th (ppm)
Norite	1.00 ± 0.13	1.11 ± 0.13	5.56 ± 0.52
Concrete	1.75 ± 0.05	2.41 ± 0.03	15.38 ± 0.40
Shotcrete	1.78 ± 0.05	2.46 ± 0.09	15.24 ± 0.14

Additionally, experiment construction materials must be produced or selected with very low levels of these and other radioactive isotopes. A large assays database is available at Radiopurity.org for the reference of and selection of various vendors and materials [164]. For the SuperCDMS SNOLAB experiment, Table 5.3 lists the assumed material contamination levels for various isotopes and hardware components.

As described in Chapters 3 and 4, substantial shielding is put in place to limit the penetration of cavern activity, and great care is taken to create and use high purity materials in construction. However, additional complications arise from the presence of airborne ^{222}Rn, a daughter product in the uranium chain. Radon is usually present in elevated levels in underground facilities due to its density ($\sim$8$\times$ greater than air at standard temperature and pressure). Seasonal fluctuations at SNOLAB vary from $\sim$ 125 to 135 Bq/m^3 (3.4–3.6 pCi/L) for airborne radon activity (Fig. 5.3), whereas the surface activity is around 6 Bq/m^3 (0.2 pCi/L) [167].

Table 5.3. Radioactive impurity concentrations assumed for construction materials contained within the SuperCDMS SNOLAB experiment. ^{60}Co in copper (indicated by *) is assumed to be produced cosmogenically rather than introduced during production and so the assumed rate varies for different pieces. Adapted from Ref. [68].

	Impurity Concentrations (mBq/kg)					Ref
Material	^{238}U	^{232}Th	^{40}K	^{60}Co	^{137}Cs	
Copper	0.07	0.02	0.04	*		[165]
Cirlex	6.3	2.2	1.6	0.01	0.01	[164]
Kevlar	430	140	870			[166]
μ-metal	4.2	4.2	1.7	0.51	0.27	[164]
HDPE	0.6	1.5	1.9	0.13	0.19	[164]
LEAD	0.66	0.5	7			[165]
Polypropelyne	0.6	1.5	1.9	0.13	0.19	HDPE
Water	0.6	1.5	1.9	0.13	0.19	HDPE

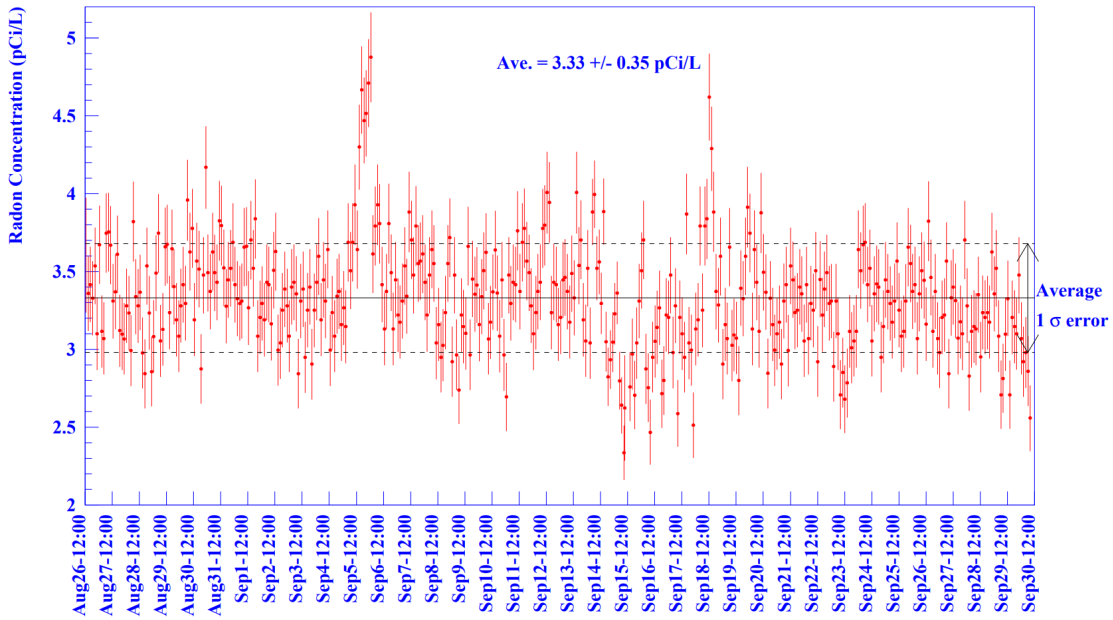

Figure 5.3. The radon concentration levels in the SNO underground control room. Measured in 2006. Adapted from Ref. [167].

The recoiling nuclei of radon daughter products can attach to or "plate-out" onto experiment materials. These daughters can give rise to neutron and gamma-ray backgrounds from (α,n) and Bremsstrahlung interactions, respectively. After a series of short ($<$ 30 min) decays, ^{210}Pb ($t_{1/2}$ = 22.3 y) comprises the majority of remaining contaminants. The full decay chain from ^{222}Rn to stable ^{206}Pb is illustrated in Fig. 5.4. A detailed study on radon-daughter plate-out rates at SNOLAB is found in Chapter 7.

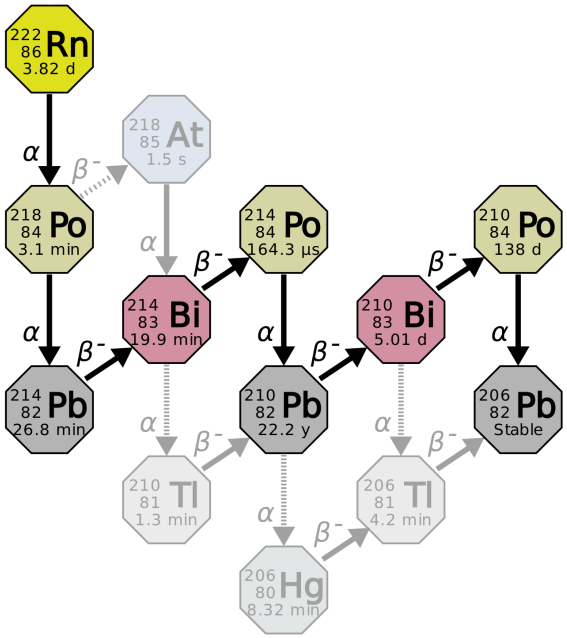

Figure 5.4. The ^{222}Rn decay chain. Very rare ($<$ 0.1%) processes are shaded.

5.3. Detector Response

The SuperCDMS iZIP and HV detectors (see Chapters 3 and 4) are sensitive to any recoiling particle. Analyses are specific to a particular energy region-of-interest (ROI) which excludes many background events. For background events within the ROI, further categorization and understanding of the detector response is required. Broadly, particle interactions in the detectors are divided into two categories: surface events which occur at or very near the surface, and bulk events which occur within the fiducial volume of the crystal. These

events are further divided, based upon their interactions, into electron recoils and nuclear recoil events (ER and NR respectively).

Events can be discriminated by their ionization yield, defined as the charge ionization energy divided by the phonon energy from any recoil event. Specific details on detector response to each type of interaction are available in Chapters 3 and 4. The specific signal response to background events are detailed below.

5.3.1. Surface Events

Beta particles from radiogenic sources outside the detector crystal are likely to interact as surface events. Ions like the ^{206}Pb nucleus or alpha particles from ^{210}Po decay have limited penetration in germanium (27 nm and 19 μm with initial energy of 103 keV and 5.3 MeV, respectively [168]). The detectors provide very good surface event discrimination from charge collection information from each face. A lack of charge collection symmetry identifies these as surface events as illustrated in Fig. 5.5. The rejection power of the SuperCDMS iZIP detectors has been shown to the order of 10^{-5} [141].

As the iZIP WIMP search analysis is performed in the region between the green lines of Fig. 5.5 (b), it is clear that the vast majority of events in this region will be rejected by surface event discrimination. However, charged ion and beta events at the surface can have inefficient charge collection, lowering the measured ionization yield. These events could potentially pass both the ionization yield and symmetry cuts, placing them into the WIMP-search region. This is illustrated in panels (b) and (c) of Fig. 5.5.

5.3.2. Bulk Events

Bulk events are those which occur in the fiducial volume of the detectors described in Section 3.1.3. While gamma rays in the bulk can be discriminated by their ionization yield, neutrons in the bulk are indistinguishable from a WIMP. Neutron backgrounds include cosmic rays, spontaneous fission, or (α,n) interactions in nearby materials. Neutrons in the WIMP-search region are irreducible backgrounds so extreme care is taken to use clean

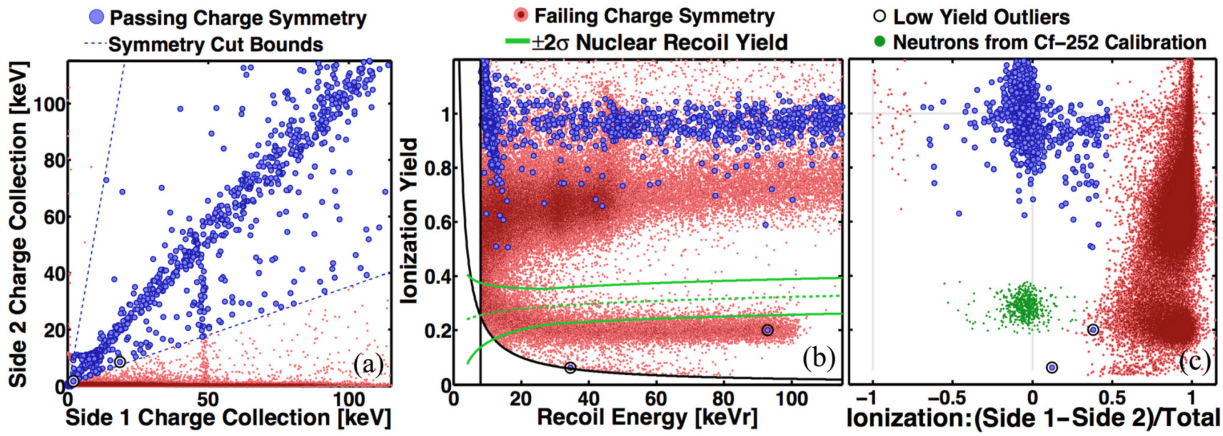

Figure 5.5. All panels show the same data from ∼900 live hours of detector T3Z1 with the ^{210}Pb source facing side 1. Clearly visible are the symmetric charge events (large blue dots) in the interior of the crystal, and the events that fail the symmetric charge cut (small red dots) including surface events from betas, gammas, and lead nuclei incident on side 1 from the source. The two blue dots with circles around them are outliers that show a very low charge yield and just satisfy the symmetry requirement. (a) The symmetry cuts (dotted blue lines) flare out near the origin so that events are accepted down to the noise wall. The band just below 50 keV is from the 46.5 keV gamma rays from the source. (b) Ionization yield versus phonon recoil energy with $\pm 2\sigma$ ionization yield range of neutrons indicated (area within green lines). The hyperbolic black line is the ionization threshold (2 keVee–"ee" for electron equivalent); the vertical black line is the recoil energy analysis threshold (8 keVr). Electrons from ^{210}Pb (below ∼60 keVr) and ^{210}Bi (mostly above 60 keVr) are distinctly separated from ^{206}Pb recoils (low yield, below ∼110 keVr). (c) In addition to the data in (a) and (b) this panel also shows nuclear recoils from neutrons from a ^{252}Cf source (green, low yield). As bulk events these show a symmetric ionization response between sides 1 and 2 like the bulk electron recoils at higher yield, and are thus nicely separated from charge-asymmetric surface events. Reproduced from Ref. [141].

materials and to limit further contamination underground. Furthermore, any event whose reconstructed recoil energy places it within WIMP-search parameters is checked for scattering in multiple detectors. Neutrons can easily pass from one detector to another within a short time-frame and events with scattering in multiple detectors can be excluded from analysis. Neutron single-scatter events are the most difficult events to rule out.

In addition to background sources outside the detector, there are sources from within the crystal itself. The detector is grown as pure as possible, but there is still the possibility of cosmogenic activation of the germanium or silicon atoms. In silicon detectors, there is further contamination from naturally occurring ^{32}Si.

Tritium ($t_{1/2}$ = 12.3 years) is a spallation product from cosmic ray secondaries with germanium or silicon. Tritium will produce betas throughout the detector bulk. These beta events, which have an 18.6 keV endpoint, can have inefficient charge collection and pass into the WIMP-search region due to lower ionization yield. Another spallation product, ^{32}Si ($t_{1/2}$ = 153 years) is produced from interactions of cosmic ray secondaries with ^{40}Ar in the atmosphere [169]. ^{32}Si is carried via rain and water transport to deposits within the crust which are later mined. There are recent studies showing that older and sometimes deeper silicon deposits may contain a lower proportion of ^{32}Si [170], but surface mining techniques are usually employed with water (itself containing some ^{32}Si) being used to lower airborne dust [171]. For a comparison of what is commercially and practically available today, the DAMIC collaboration measured 80^{+110}_{-65} decays/kg/day at the 95% confidence level in their silicon CCDs [172]. Similar levels of purity should be possible for SuperCDMS SNOLAB Si detectors.

Likewise for germanium, cosmic interactions can activate isotopes. Those whose half-lives are long enough to remain during a WIMP search are ^{68}Ge, ^{65}Zn, ^{73}As, ^{57}Co, ^{55}Fe, ^{54}Mn and ^{49}V. Production and activity estimates for germanium and silicon activation are listed in Table 5.4. A detailed plot of various background components is shown in Fig. 5.6.

Table 5.4. The assumed sea-level cosmic ray exposure for the HV(iZIP) detectors is 60(125) days, followed by a 365 day underground "cooldown" period before acquisition of science data. ^{32}Si is intrinsic to the production process and is expected to be the same for iZIP and HV detectors.

		Production Rate	Concentration	
		(atoms/kg/day)	(decays/kg/day)	
Material	Isotopes		HV	iZIP
Ge	^{3}H	80	0.7	1.5
Si	^{3}H	125	1	2
Si	^{32}Si	–	80	80

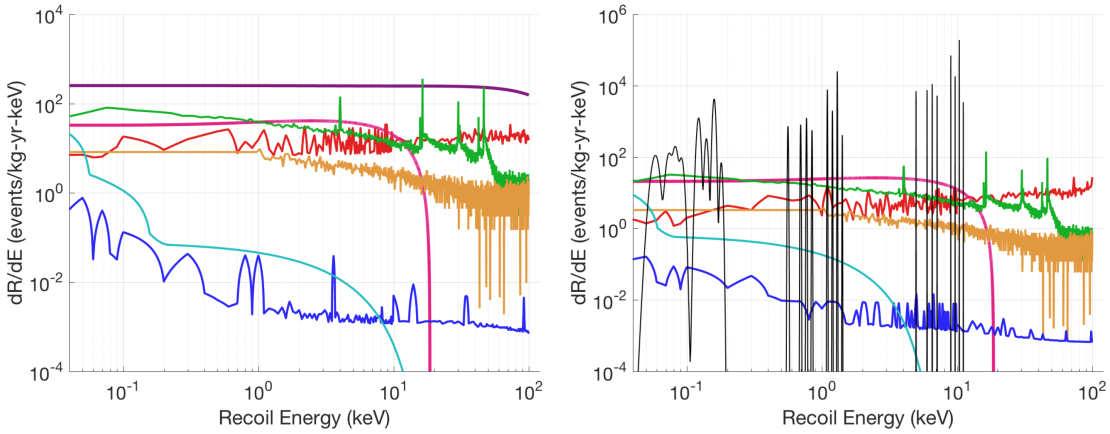

Figure 5.6. Raw background spectra of single scatter interactions in a Si (left) and Ge (right) detector obtained from the Monte Carlo simulation. The spectra are broken out by components and shown as a function of recoil energy (ER or NR depending on the interaction). ^{3}H (pink) and ^{32}Si (purple) are the largest individual contributors to the backgrounds in the Ge and Si detectors, respectively. The Ge activation lines (black) are shown convolved with a 10 eV r.m.s. resolution (σ_{Phonon} for the Ge HV detectors) to allow them to be clearly displayed in this figure. The remaining components are Compton scatters from gamma rays (red), surface betas (green), surface ^{206}Pb recoils (orange), neutrons (blue) and coherent elastic neutrino-nucleus scattering (cyan). Note that the neutron spectrum (blue) has some spurious structure from the limited simulation statistics in the cavern component of the neutron background. Adapted from Ref. [68].

5.4. Background Summary

The SuperCDMS Soudan and SNOLAB experiments used (or will use) significant rock overburden to mitigate the cosmic ray background. Substantial effort is later put into place to select and use the most radiopure materials. Despite these efforts, some background contamination will still remain. The SuperCDMS Soudan iZIP detectors have been demonstrated to have very low probability for misidentifying surface ER events as bulk NR events: $< 1.7\times10^{5}$ in the 8-115 keV recoil energy analysis region. Monte Carlo simulations predicted 0.13 neutron background events in the analysis region for SuperCDMS Soudan after all cuts were applied [103].

For the SuperCDMS SNOLAB experiment, Monte Carlo simulations predict 3.3×10^{-3} (2.9×10^{-3}) NRs/kg/keV/year for Ge(Si) iZIPs. For the HV detectors without ER/NR discrimination, ERs are the dominant background with a predicted rate of 27(300) ERs/kg/keV/year for Ge(Si). These rates are for events in the analysis region of each detector after analysis cuts have been applied. The background spectra for each detector type and mode is illustrated in Fig. 5.7.

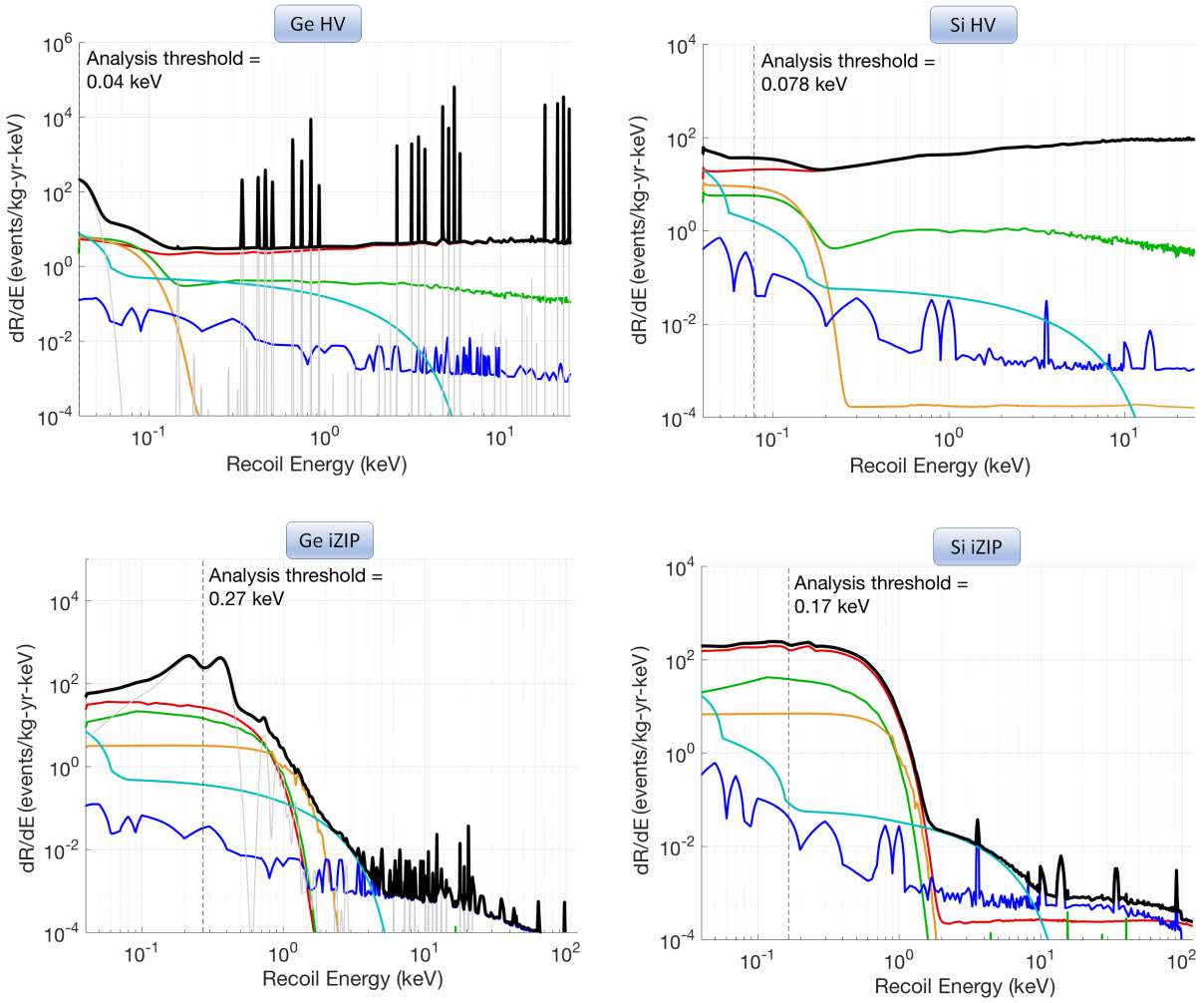

Figure 5.7. Background spectra after analysis cuts in Ge (left) and Si (right) HV (top) and iZIP (bottom) detectors, shown as a function of nuclear recoil energy (keV). Thick black lines represent the total background rates. Electron recoils from Compton gamma rays, ^{3}H, and ^{32}Si are grouped together (red). The Ge activation lines (grey) are shown convolved with a 10 eV r.m.s. resolution. The remaining components are surface betas (green), surface ^{206}Pb recoils (orange), neutrons (blue), and coherent elastic neutrino-nucleus scattering (cyan). Adapted from Ref. [68].

Chapter 6

Shielding Simulations and Design Optimization

As detailed in Chapter 5, substantial shielding against cosmogenic and radiogenic backgrounds is required for SuperCDMS to meet its primary physics goals. The SuperCDMS SNOLAB passive shield will be permanent for the duration of the experiment so extensive simulations were undertaken to optimize the shield design. Shielding design is based on the well-established techniques for using hydrogenous materials for neutron moderation and high-Z materials to reduce the gamma flux.

Neutrons and gammas in the cavern are emitted by radioactive isotopes in the norite rock [147,148,173]. Monte Carlo simulations of these isotopes in the cavern yield a spectrum which is normalized to the measured rates of 4000 neutrons/m^2/day and 4×10^4 gammas/m^2/day [167].

The shield is designed to lower the external environmental flux to below that required for the experiment to reach the neutrino background. Related to the environmental flux is the number of events that deposit energy in a detector in the WIMP-search region of interest (ROI). For HV detectors, the ROI is 3 eV to 2 keV whereas for iZIP detectors, the ROI is 1–50 keV. For iZIP detectors, electron recoils (ERs) are distinguishable from nuclear recoils (NRs) so NRs are the most relevant background. The dominant background in HV detectors, which do not have ER rejection, will come from beta decays from ^{3}H and ^{32}Si impurities. Thus, ERs are the most relevant background from HV detectors.

To achieve the science goals of the SuperCDMS SNOLAB experiment, the background rate is required to be below 10^{-5} NR/keV/kg/year in the iZIP detectors, and 5×10^{-2} ER/keV/kg/year in the HV detectors. The shield design optimization study determined which configuration of water, lead and polyethylene shield layers met these background goals.

6.1. Computational Challenges

An ideal solution would be to use Geant4 to simulate a large number of shield configurations by varying the thickness of each layer. Geant4 simulations, however, are very time consuming. As an example, ManeFrame is a high-performance compute cluster at SMU with 8,800 available threads on Intel® Xeon® X5560 CPUs operating at 2.80GHz. Resources are divided into queues for parallel and single-threaded applications. Queue restrictions are set at 24 hours per thread for single-threaded applications, thus we could simulate a maximum of 3.8×10^8 gammas or 1.6×10^7 neutrons per execution. Taking into account a small time buffer for slow nodes or execution-time variance would lead to a smaller number of simulated particles.

While 10^7 or 10^8 particles per thread per day may seem substantial, the overall attenuation factor of the shield can be on the order of 10^{-12} or higher, as will be seen later in this chapter. It would require full-time access to many threads (and for many days) to yield results for a single configuration. However, compute time and disc space allocations would start to become a concern as well. For example, simulating a single gamma event which deposits energy in the HV ROI may take up to two days and ∼10 GB of disk space, utilizing the maximum number of threads available for single-threaded jobs on ManeFrame. This would yield (on average) only one event in the ROI for one possible configuration of the shield, and more events would need to be simulated to create a realistic estimate of the event rate. There is also the continuous need to simulate more shield variations to find the optimal configuration.

6.2. Stitching the Pieces

In light of the possibility of taking years of compute time and petabytes of data, a different approach was ultimately decided upon. A flat spectrum of neutrons and gammas were simulated independently through all three shield materials with a variety of different shield thicknesses: eleven for water, seven for lead, and eight for polyethylene. For the detector response, two tower configurations were simulated: a full 31-tower configuration,

and a smaller 5-tower configuration. A total of 1,232 possible configurations were then available to examine. The details are summarized in Table 6.1. The resulting dataset from each simulation was collected on SMU's ManeFrame taking little over one terabyte of data.

Table 6.1. A summary of the simulated shield materials and configurations. Both neutrons and gammas were simulated with a flat spectrum through each material and configuration, leading to a total of 2,464 possible outcomes. *For the towers, the numbers indicate the configuration type instead of a thickness.

Layer	**Thicknesses (cm)**	**Total**
Water	0, 6, 12, 18, 24, 30, 36, 42, 48, 54, 60	11
Lead	4, 8, 12, 16, 20, 24, 28	7
Polyethylene	5, 10, 15, 20, 25, 30, 35, 40	8
Towers*	5, 31	2
Total Configurations Possible:		1,232

6.3. Simulation Details

In simulations for each material and thickness found in Table 6.1, a flat spectrum of particles (neutrons and gammas) were thrown from the outside of the shield layer. Any particles emerging from the inner surface of a shield layer had their kinetic energy and momentum recorded. To boost statistics in specific energy regions, simulations were carried out with a non-linear distribution across the input spectrum. The details of this breakdown are available in Table 6.2.

For each shield simulation, the primary particles (those initially entering the shield layer) were thrown from the outer surface. The angular distribution for particles entering the water tanks was uniform, simulating random particles thrown from the cavern walls around the experiment. For particles entering subsequent shield layers, a Lambertian angular distribution was used. Upon further inspection of the outgoing tagged particles, however, the Lambertian

Table 6.2. The energy ranges simulated for each material and thickness found in Table 6.1. The ranges were selected to offer increased statistics in particular areas of interest.

Energy Ranges (keV)	
Gammas	**Neutrons**
1–100	1–10
100–300	10–30
300–600	30–100
600–1,000	100–300
1,000–1,400	300–1,000
1,400–2,000	1,000–3,000
2,000–3,000	3,000–10,000

assumption proved erroneous[1]. A weighted matrix was then applied to correct the Lambertian angular distribution for all incoming and outgoing particles in subsequent layers. This enabled the correction to be applied without re-running all the previous simulations.

6.4. Analysis & Data Processing

All simulation files, held in a ROOT format, were collected from other clusters and consolidated on ManeFrame. The analysis method for each set of data followed the same format:

- For each incident particle, we ensured that the energy used (energy recorded in the detector) was the sum from each event (sum over Geant4 steps).
- We determined the probability of an incoming particle to cross the given shield layer as a function of output energy.

  An incoming mono-energetic beam of particles will create a unique, attenuated spectra. Since the data was produced with a flat spectrum, the incoming

[1]This would have been true for flat, infinitely large, parallel layers but the actual shield layers are cylindrical

spectra was lumped into 5 keV bins. For each bin, a unique output spectra was created from 1–10,000 keV. By dividing the output spectra by the total number of primaries (in this bin), a probability spectrum is created for that particular primary energy bin. This is repeated for every bin in the input spectrum. Along with this, a total probability to cross the layer per input energy bin can be created.

- From a given input spectrum (whether cavern, or from a previous shield layer), we found the total number of primaries that successfully pass per input bin.

  This was done by multiplying the input primary numbers (per bin) by the unique spectrum for that energy bin found in the previous step. Additionally, there was a weight applied to the input bin's total counts to correct for the Lambertian distribution assumption.

- The individual output spectra (for each input bin) was summed to find the total passing spectrum.

- This process was repeated for each shield thickness and input spectrum being analyzed.

  For example, for the water shield, two input spectra (the cavern neutron and gamma spectra) were used. For each case, the input spectrum was passed through each thickness of the water shield yielding 22 total output spectra (11 gamma spectra and 11 neutron spectra). This spectra was passed as input to the subsequent layers, which generated further output spectra, and so on until all 2,464 spectra were created.

To facilitate the selection of an optimized shield, a graphical program named Shield Explorer was created to explore the various shield configurations. A screenshot of the interface can be seen in Fig. 6.1. In addition to the results of this analysis, some "end-to-end" simulations were performed using the full detector geometry for particular shield configurations. The initial purpose was to validate the results of the shield stitching project, and it was found that after correcting for the Lambertian distribution assumption, the results of the

"stitched shield" agreed with the end-to-end simulations within a factor of approximately two.

Taking this into account, a few particular shield parameters were selected for further end-to-end simulation. The results of the stitched shield analysis made it possible to select only a handful of shield configurations (as opposed to thousands) for detailed study. These simulations along with the stitched values are shown in Figs. 6.2 and 6.3.

The final configuration selected was 60 cm of water, 20 cm of lead, and 30 cm of polyethylene. The total counts in each region of interest for each detector type for gammas and neutrons is summarized in Tables 6.3 and 6.4.

Table 6.3. Overall differential count rate for gammas and neutrons in each detector material in each region of interest (counts per kg of detector per year of exposure per keV). The asterisk for gammas in Si in the 3 eV–2 keV range indicates that this value is an upper limit as no counts were seen in $> 10^{13}$ simulated primaries.

Counts/(kg·keV·year)				
ROI	**1–50 keV**		**3 eV–2 keV**	
Type	Ge	Si	Ge	Si
Gammas	3.89×10^{-2}	1.33×10^{-1}	3.18×10^{-1}	$3.27 \times 10^{0*}$
Neutrons	1.26×10^{-5}	6.66×10^{-5}	1.06×10^{-5}	1.09×10^{-4}

Table 6.4. Overall normalized rate for gammas and neutrons in each detector material in each region of interest (counts per primary thrown at the shield). The asterisk for gammas in Si in the 3 eV–2 keV range indicates that this value is an upper limit as no counts were seen in $> 10^{13}$ simulated primaries.

Normalized Counts				
ROI	**1–50 keV**		**3 eV–2 keV**	
Type	Ge	Si	Ge	Si
Gammas	8.17×10^{-13}	2.72×10^{-13}	2.72×10^{-13}	$2.72 \times 10^{-13*}$
Neutrons	1.21×10^{-10}	6.25×10^{-11}	4.17×10^{-12}	4.17×10^{-12}

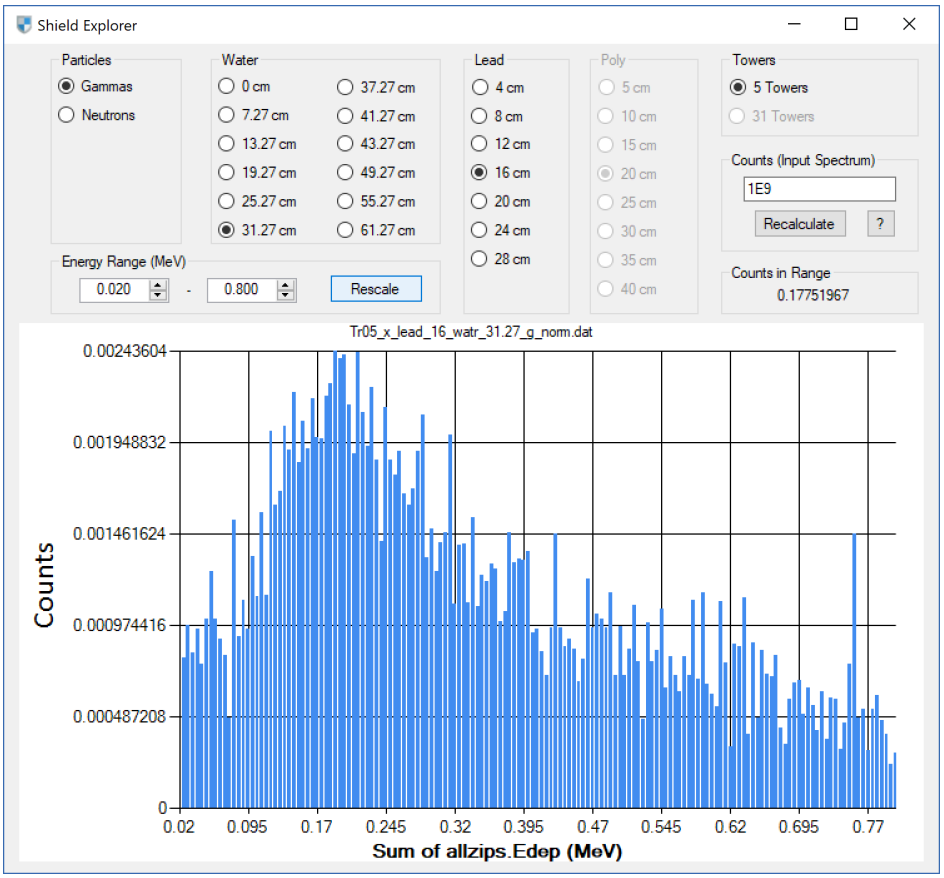

Figure 6.1. The Shield Explorer graphical program. The number of primaries thrown is set by the user, as well as the shield layer thicknesses and viewed output energy spectra. Total counts in the range shown are also displayed for rapid analysis.

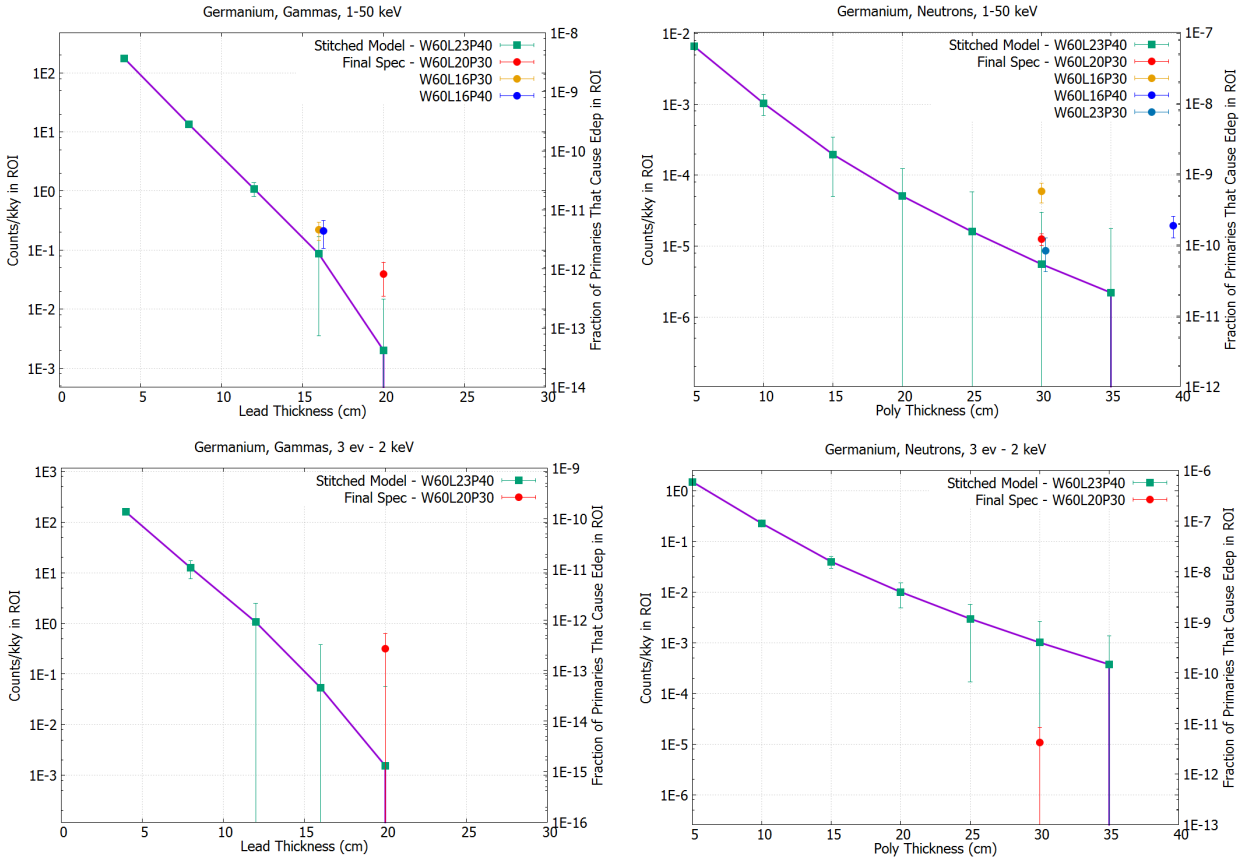

Figure 6.2. The overall count rate in Ge for various shield configurations. Green squares indicate the value determined from the stitched shield model, with error bars signaling 1-sigma confidence interval. The purple line visually indicates the trend with changing configurations. The round dots (and error bars) indicate full end-to-end simulations conducted to validate and confirm final shield specification selection. The legend corresponds to the thickness (cm) in W (water), L (lead), and P (polyethylene). Top left: Gamma rates for varying lead in the 1–50 keV range. Top right: Neutrons rates for varying HDPE in the 3 eV–2 keV range. Bottom left: Gamma rates for varying lead in the 1–50 keV range. Bottom right: Neutrons rates for varying HDPE in the 3 eV–2 keV range.

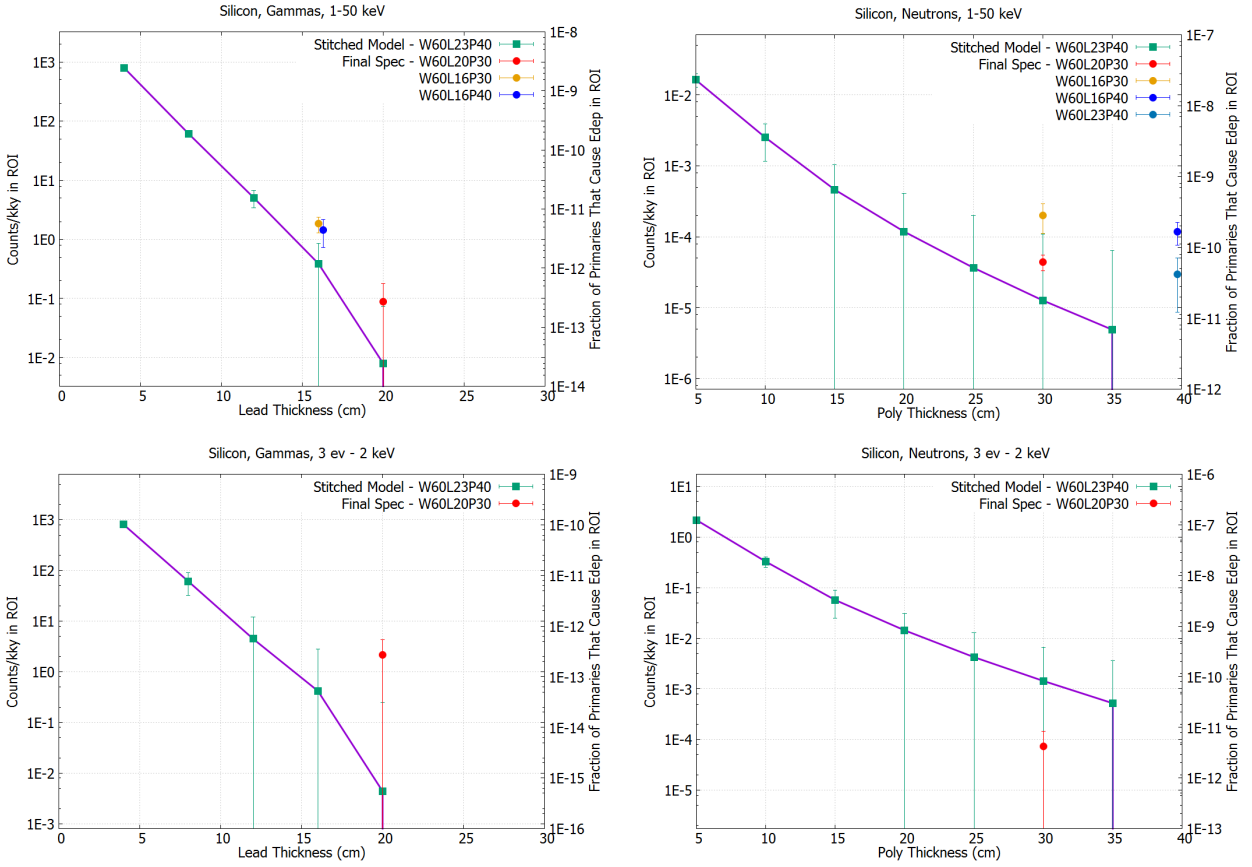

Figure 6.3. The overall count rate in Si for various shield configurations. Green squares indicate the value determined from the stitched shield model, with error bars signaling 1-sigma confidence interval. The purple line visually indicates the trend with changing configurations. The round dots (and error bars) indicate full end-to-end simulations conducted to validate and confirm final shield specification selection. The legend corresponds to the thickness (cm) in W (water), L (lead), and P (polyethylene). Top left: Gamma rates for varying lead in the 1–50 keV range. Top right: Neutrons rates for varying HDPE in the 3 eV–2 keV range. Bottom left: Gamma rates for varying lead in the 1–50 keV range. Bottom right: Neutrons rates for varying HDPE in the 3 eV–2 keV range.

Chapter 7

^{210}Pb Plate-out at SNOLAB

To achieve the projected SuperCDMS SNOLAB sensitivity shown in Fig. 4.4, constraints are placed on the allowable radioactive contamination of detector materials. Contamination can include impurities within materials as well as "plate-out" of surface contaminants such as daughter products of ^{222}Rn. These can attach to nearby surfaces leaving long-lived ^{210}Pb in place for the duration of the experiment. ^{210}Pb is problematic as it will eventually decay to ^{210}Po whose 5.3 MeV alpha decay can generate neutrons through (α,n) reactions. Neutrons are a non-reducible background. Therefore, it is important to limit ^{210}Pb contamination. For the non-line-of-sight surfaces of the polyethylene shield, the maximum allowable ^{210}Pb activity is 10,000 nBq/cm^2.

The radon levels expected at SNOLAB indicate that a time-constraint on exposure to lab air may be necessary during the construction phase of the experiment. This chapter describes a study into the plate-out rate of radon daughters onto polyethylene and copper. From the results of this study, an estimate for the maximum possible exposure time for the shield materials is calculated.

7.1. Estimating Backgrounds in Polyethylene

There are several commercially available forms of polyethylene $(C_2H_4)_n$. This study focused on high density polyethylene (HDPE) which has density of 0.941–0.965 g/cm^3. With a natural abundance of ~1.07% [174], ^{13}C accounts for 0.36% of all atoms in HDPE. The SuperCDMS SNOLAB experiment will use the same type of polyethylene in the passive shield.

A modified version of SOURCES 4C [175, 176] was used to model the (α,n) reactions in HDPE resulting in an expectation of 7.7×10^{-8} n/s/cm^3 per 1 Bq of ^{210}Pb activity at secular

equilibrium[1] in the bulk of the polyethylene. The expected neutron spectrum is illustrated in Fig. 7.1. Polyethylene shielding exposed to a high radon environment such as that at SNOLAB would quickly become contaminated with residual ^{210}Pb. Though the ^{210}Pb would be implanted near the surface, and some alphas from the ^{210}Po decays would be emitted away from the bulk, there is still the possibility these alphas could interact with ^{13}C on an exiting trajectory. To make the estimate conservative, any alpha from ^{210}Po was considered as having the potential to create neutron backgrounds.

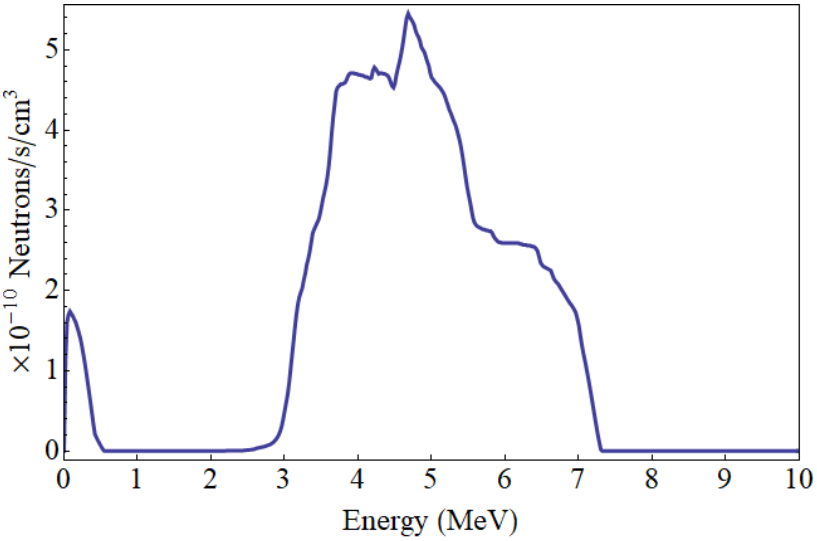

Figure 7.1. SOURCES 4C neutron spectrum from 1 Bq of ^{210}Pb contamination in polyethylene. See also Fig. 6.38 in Ref. [177] for a similar spectrum derived from GEANT4 simulation.

7.2. Experimental Setup & Environment

The experimental site was located in SNOLAB, a laboratory that is a Class 2000 cleanroom. The setup was located within Room 127 in the laboratory, in an area referred to as the Ladder Labs, illustrated in Fig. 7.2. During the exposure at SNOLAB, environmental factors were continuously monitored including radon activity, temperature, relative humidity, and counts of dust particles $\geq 0.3\mu$m. The instruments used to record these data were located

[1]Secular equilibrium, sometimes described as radioactive equilibrium, describes when a short-lived daughter isotope of a long-lived parent has relatively constant activity, being constantly replenished by the parent.

on a table immediately adjacent to the samples at Site 1 and the data is given in Table 7.1. We monitored these values such that we could either rule out or include possible effects from fluctuating environmental factors. Average radon levels in the laboratory area are known to seasonally vary from ∼125 to 135 Bq/m^3 whereas the outside air activity at ground level is around 6 Bq/m^3 [167]. The average radon activity during the 83 day exposure was measured at 135 Bq/m^3 as illustrated in Fig. 7.3.

Table 7.1. Average environmental values of the experiment location over 83 days, with one standard deviation calculated from the population of data points. Dust particles were monitored with a ParticleScan CR, radon activity with a RadStar RS300, and temperature and humidity with a Lascar EL-USB-2-LCD+. The particle counts we measured were consistent with a Class 1000 cleanroom rating.

Data	Average	σ
Particles $\geq 0.3\mu$m (pp. ft^3)	238	679
Radon (Bq/m^3)	135	23
Temperature (°C)	22.5	0.4
Humidity (%)	57.9	1.6

A total of ten 12"×12"×3/16" HDPE panels were used, all cut from the same 4'×8' sheet purchased from Johnston Industrial Plastics, Ontario, Canada. We chose this sample size to optimize the assay of measurements made in the UltraLo-1800 alpha counter. The panels were set in pairs at four different locations in SNOLAB with varying height and room position to test for variations in plate-out from position and proximity to nearby walls. Details on the position of each measurement location is available in Table 7.2. Each pair of samples was set immediately adjacent to one another with each panel laid flat.

Four copper panels were also placed at Site 1, each of dimension 6"×12"×1/4". Every panel was placed on a non-conducting surface for the duration of the exposure. During shipment to and from SNOLAB, all panels were sealed inside two nitrogen flushed nylon bags with an outer polyethylene bag. The outer polyethylene bag was used as a general

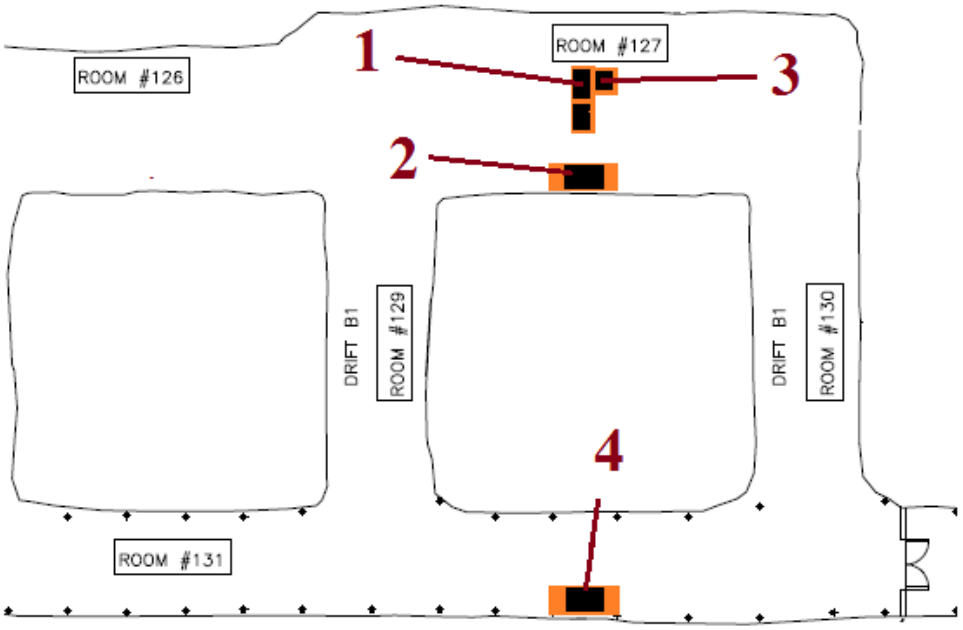

Figure 7.2. Map of the four exposure sites in the Ladder Labs at SNOLAB. Distances from the floor and walls are given in Table 7.2.

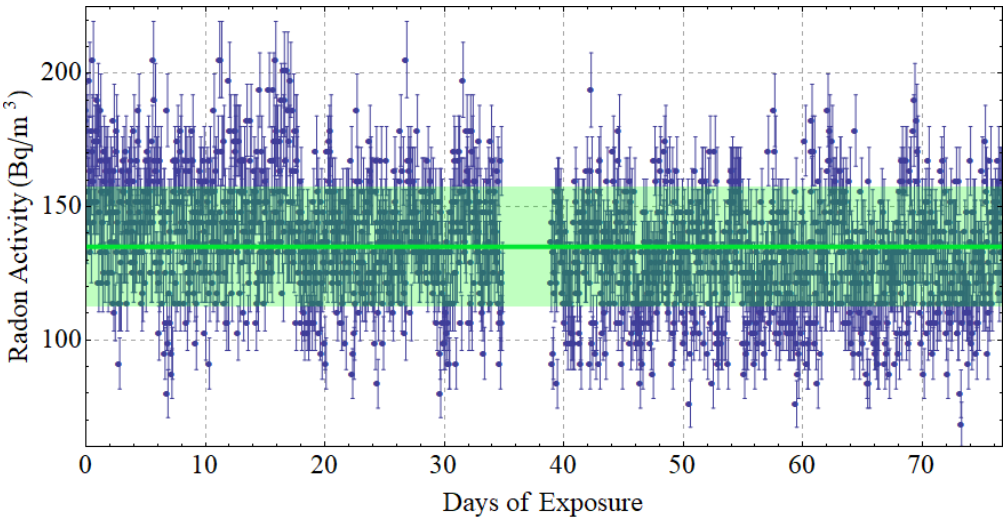

Figure 7.3. Radon activity at SNOLAB over the exposure period as measured by a RadStar RS300. Green line indicates average measured value (135 $\mathrm{Bq/m^3}$) with 1-σ interval in shaded region.

protection around the inner bags while the nylon bags were chosen for their low radon permeability [178].

For the trip to SNOLAB, the panels were laid face-to-face with no air gaps. For the return trip, the panels were packed in pairs (one pair from each site) with a small air gap between panels to best maintain the integrity of the surfaces. FOr the return shipment, the bags were once again nitrogen back-filled to limit any plate-out that might occur during shipment.

Table 7.2. Position information for each exposure location used. Height is measured as the distance from the floor to the surface of the panels. Two polyethylene samples were placed at each location. Additionally, four copper samples were placed at Site 1. The variety of locations was motivated to test for variations in plate-out height due to position and proximity to nearby walls.

Site Number	Room Number	Nearest Wall (m)	Height (m)
1	127	3.63	0.94
2	127	0.38	0.94
3	127	3.63	2.01
4	131	0.38	0.94

7.3. Analysis & Results

To estimate total contamination, a model was developed that predicts the activity of ^{210}Po over time. For more accurate projections, this model also accounts for other alpha-emitting contaminants in dust such as those in the U and Th chains. This section describes the development of the model, first as a pure ^{210}Po model, and then with the added consideration of long-lived contaminants in dust.

7.3.1. Pure ^{210}Po Model

Because the expected alphas come from the short-lived daughter (^{210}Po) of a long-lived parent (^{210}Pb), a model for the number of ^{210}Po atoms over time was built from the Bateman equation [179]

$$N_{Po}(t) = N_{Pb}(0)\frac{\lambda_{Pb}}{\lambda_{Po} - \lambda_{Pb}}\left(e^{-\lambda_{Pb}t} - e^{-\lambda_{Po}t}\right) \tag{7.1}$$

where λ_{Pb} and λ_{Po} are the decay constants for Pb and Po respectively. Equation 7.1 can be altered to account for a particular number of ^{210}Pb atoms (N_i) added at a specific non-zero time t_i

$$\begin{aligned} N_{Po,i}(t, t_i, N_i) = N_i\frac{\lambda_{Pb}}{\lambda_{Po} - \lambda_{Pb}}\left(e^{-\lambda_{Pb}(t-t_i)} - e^{-\lambda_{Po}(t-t_i)}\right) \\ \times \Theta\left(t - t_i\right) \end{aligned} \tag{7.2}$$

where Θ is the Heaviside step function. Note that because of the relatively stable radon activity at SNOLAB during this exposure, illustrated in Fig. 7.3, the radon-daughter plate-out rate onto the sample surfaces was approximately constant with time. Thus, we assume that ^{210}Pb atoms were being added at a constant rate R_{Pb}. The total number of ^{210}Po atoms is then a sum of Equation 7.2 over an exposure period, t_{exp} in discrete step sizes.

As an example, consider a 150 day exposure in an environment where $R_{Pb} = 100$ atoms/cm^2/day. Rather than assuming all the atoms plate-out at once, the exposure can be broken down into four depositions separated by 50 days as illustrated in Fig. 7.4. Each deposition takes the form of Equation 7.2. Smaller gaps between depositions will result in a more accurate total value, both during and after exposure. The total activity of ^{210}Po is then

$$A_{Po}(t, t_{exp}) = \lambda_{Po}\left[\sum_{i=1}^{t_{exp}/b} N_{Po,i}(t, i \times b, R_{Pb} \times b)\right] \tag{7.3}$$

where b is the time-step size. Making the substitution of $n \equiv \frac{t_{exp}}{b}$ and taking the limit of Equation 7.3 as $n \to \infty$, the following closed-form expression describes the activity over time

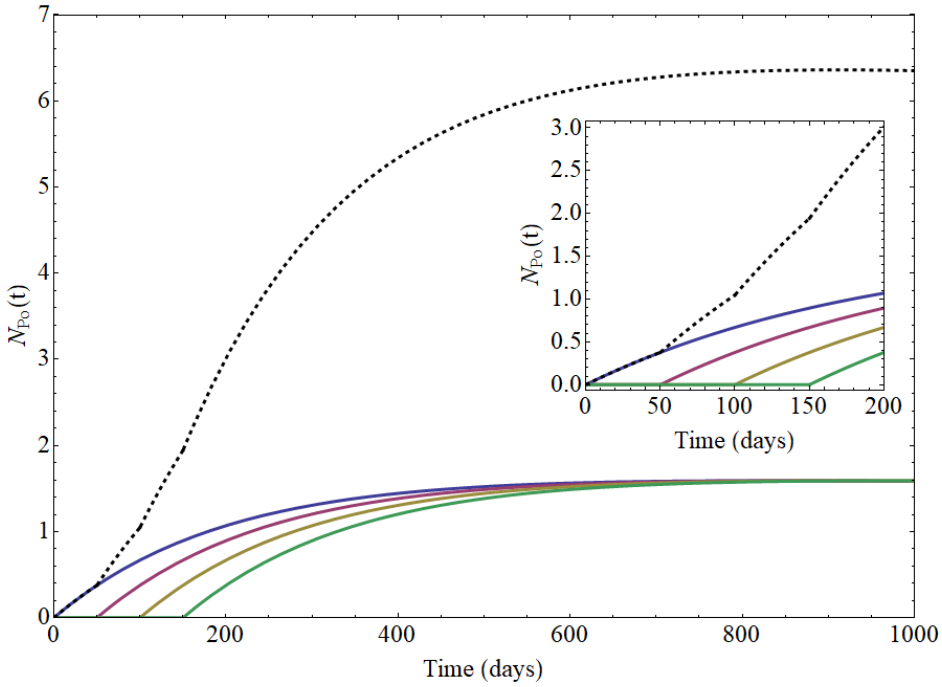

Figure 7.4. Four individual forms of Equation 7.2 (blue, red, yellow, and green curves) summed up (black dashed curve), showing exponential growth during exposure, and then later coming into secular equilibrium. Inset more clearly shows exponential growth during exposure period which in this example ends at a time of 150 days, and the step size is 50 days.

$$A_{Po}(t, t_{exp}) = \frac{R_{Pb}}{\lambda_{Pb} - \lambda_{Po}} \cdot \Big[\lambda_{Pb}\left(1 - e^{-\lambda_{Po}t}\right) + \lambda_{Po}\left(e^{-\lambda_{Pb}t} - 1\right) + \Theta\left(t - t_{exp}\right) \cdot \left(\lambda_{Pb}\left\{e^{-\lambda_{Po}(t-t_{exp})} - 1\right\} + \lambda_{Po}\left\{1 - e^{-\lambda_{Pb}(t-t_{exp})}\right\}\right)\Big] \tag{7.4}$$

Knowing the exposure time t_{exp}, measurement time t_m, and measured activity $A_{Po}(t_m, t_{exp})$, Equation 7.4 can be solved for R_{Pb}.

7.3.2. Including Long-Lived Activity

A model of total activity should include the possibility that long-lived activity from U and Th in dust may be present on the sample surfaces. Because U and Th are so long-lived, their decay chains—assuming secular equilibrium—would contribute an approximately constant rate of radioactivity for a given amount of dust. Consequently, if dust settled at a constant rate per unit time S_{dust}, then the total activity from dust (A_{dust}) accumulated linearly during exposure to the SNOLAB environment and would remain constant once the exposure concluded

$$A_{dust}(t, t_{exp}) = \begin{cases} S_{dust}t & t < t_{exp} \\ S_{dust}t_{exp} & t \geq t_{exp} \end{cases} \tag{7.5}$$

The total activity from all sources — ^{210}Po and dust (Fig. 7.5) — is then

$$A_T(t, t_{exp}) = A_{Po}(t, t_{exp}) + A_{dust}(t, t_{exp}) \tag{7.6}$$

The values R_{Pb} and S_{dust} can be separated from the other parts of $A_{Po}(t, t_{exp})$ and $A_{dust}(t, t_{exp})$ respectively, yielding time-dependent functions that also depend on the exposure time

$$A_T(t, t_{exp}) = R_{Pb}f(t, t_{exp}) + S_{dust}g(t, t_{exp})$$

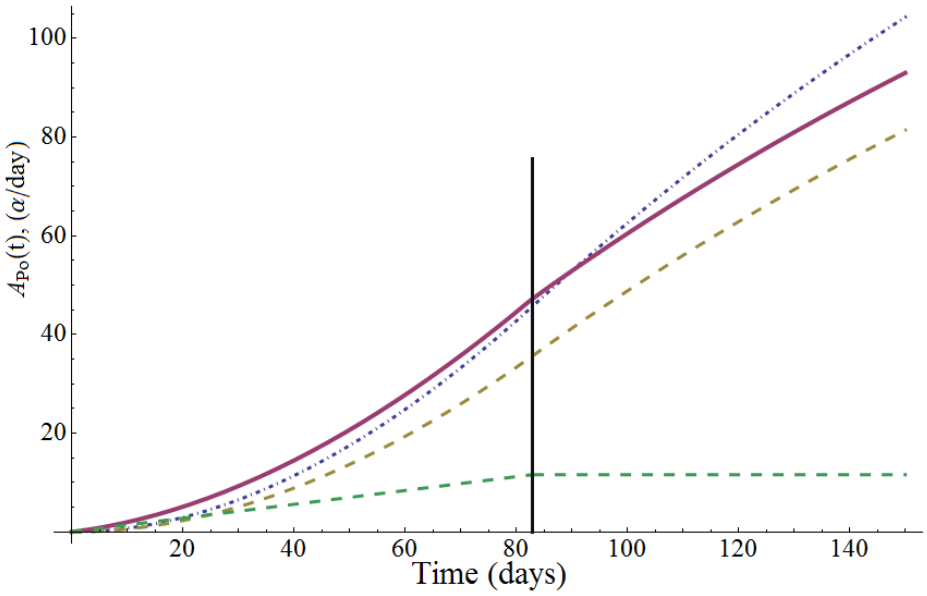

Figure 7.5. The model of total activity (solid red curve, Equation 7.6) from ^{210}Po (dashed yellow curve) and dust (dashed green curve). The vertical line indicates the end of the 83 day exposure of our HDPE and copper samples to the SNOLAB environment. The case of no contribution from dust is also shown (dot-dashed blue curve, Equation 7.3). Both models (with and without dust) are fit to a measurement at approximately 90 days, which is why they agree at that time. The impact of ignoring dust is seen as a potential future overestimate of activity.

With two measurements of activity spaced adequately apart ($t = t_1$,$t = t_2$), and with a known exposure time, R_{Pb} and S_{dust} can be found from a linear system of equations

$$\begin{pmatrix} A_T(t_1, t_{exp}) \\ \\ A_T(t_2, t_{exp}) \end{pmatrix} = \begin{pmatrix} f(t_1, t_{exp}) & g(t_1, t_{exp}) \\ \\ f(t_2, t_{exp}) & g(t_2, t_{exp}) \end{pmatrix} \begin{pmatrix} R_{Pb} \\ \\ S_{dust} \end{pmatrix} \tag{7.7}$$

7.4. Measurements

Assays were performed using the XIA UltraLo-1800 alpha particle counter. The UltraLo-1800 is the most sensitive instrument available for the detection of alpha particles from the decay of ^{210}Po. The detector is an ionization counter which uses an argon-filled volume with a lower grounded electrode and an upper set of positively charged electrodes, illustrated in Fig. 7.6. The lower electrode also acts as a tray which holds the sample to be assayed. The anode sits directly above the sample and can operate in one of two modes which cover an area of 707 or 1800 cm^2 respectively. A guard electrode surrounds the anode. Signals from the electrodes are amplified, digitized, and processed by a pulse-shape analyzer. Pulse-shape discrimination gives the UltraLo-1800 the ability to identify the vertical location of alpha particle emission. This makes it possible to identify alphas from the sample, or those emitted in the elsewhere in the volume. The guard electrode allows for the identification of alphas emitted from the sides of the volume.

The simulation program TRIM [168] was used to simulate the implantation of radon daughters into polyethylene and copper. Also examined were the exiting energy of alphas from ^{210}Po decays. From this simulation, $\sim 98\%$ of all exiting alphas are expected to have energy within the 2.0–5.8 MeV range after taking the UltraLo-1800 resolution into account. In this study, calculations of total alpha activity from each panel are made by integrating over this energy range. The measured surface activity of each panel is illustrated in Fig. 7.7.

7.4.1. Pre-exposure Assays

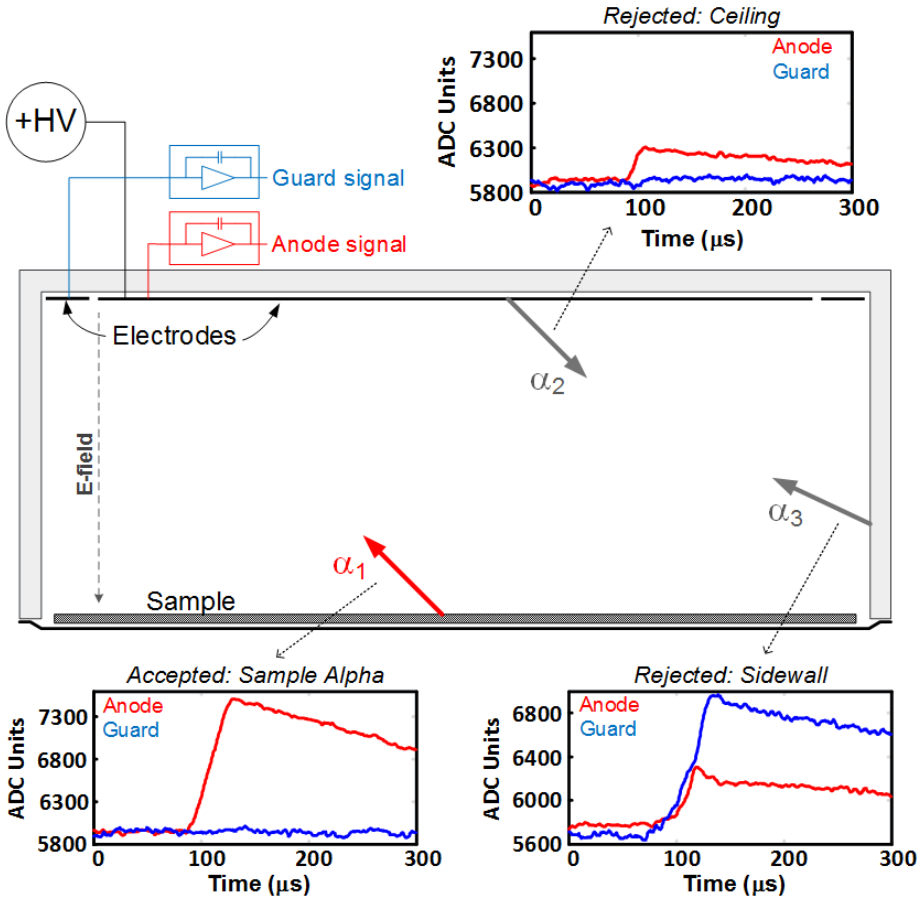

Figure 7.6. The XIA UltraLo-1800 alpha particle counter. The sample sits at the bottom of the argon-filled counting chamber. The pulse-shapes from the anode and guard make it possible to distinguish alphas emitted near the anode (top inset), the guard (bottom right inset) or the sample (bottom left inset). Adapted from Ref. [180].

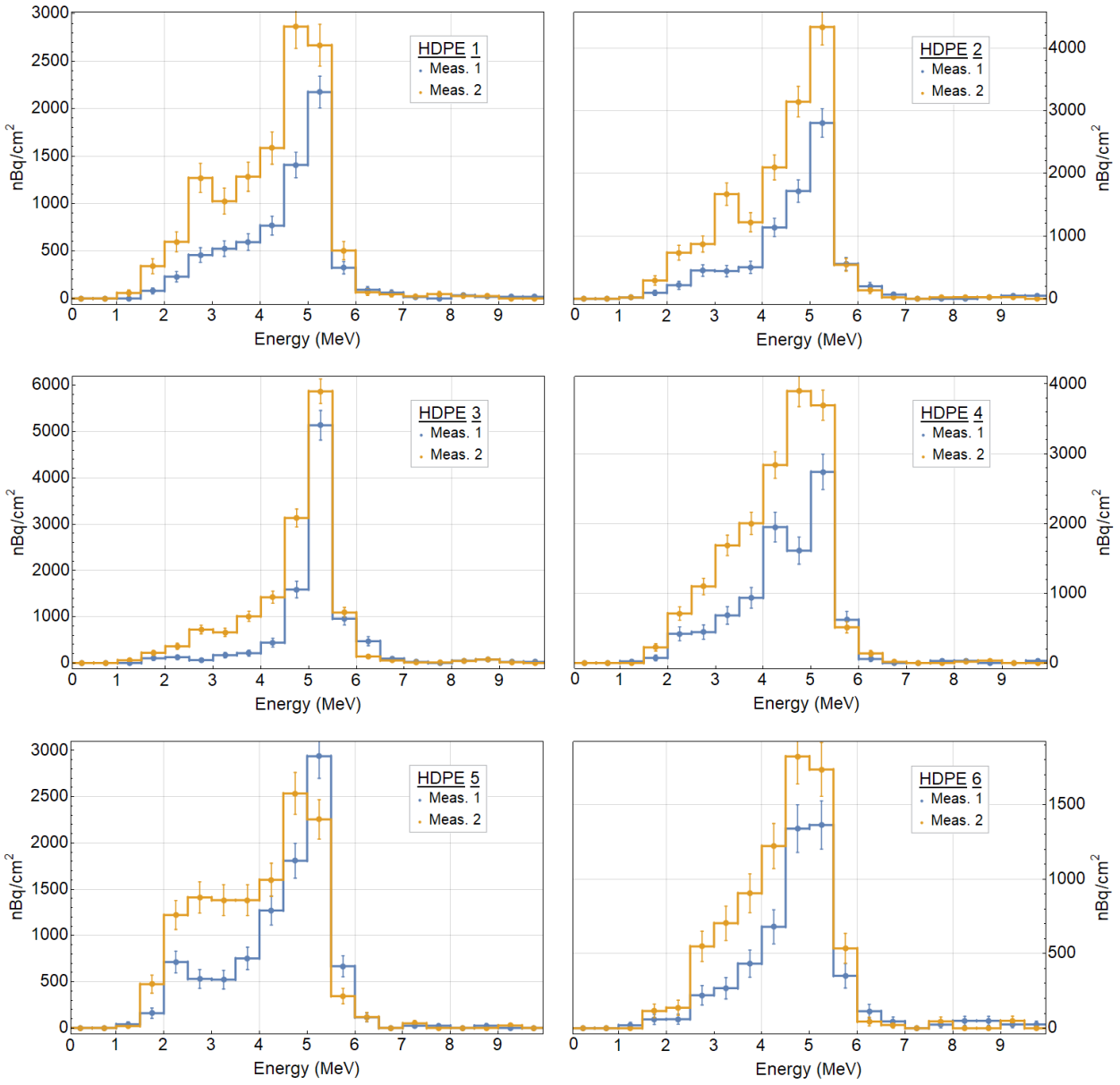

Figure 7.7. Efficiency-corrected surface alpha activity of each HDPE sample used in the analysis (see also Table 7.4). The HDPE samples were exposed underground at SNOLAB for 83 days, then measured 10 and 90 days after the end of the exposure ("Meas. 1" and "Meas. 2" respectively). There is a clear ^{210}Po peak centered at 5.3 MeV. The low-energy tails are more extensive than that expected from TRIM simulations, so this may correspond to energy losses from surface roughness.

After cleaning all copper and polyethylene samples with Radiacwash^{TM}, deionized water, and isopropyl alcohol, three polyethylene panels (all from the same stock) and all four copper panels were assayed with the UltraLo-1800 to measure baseline activity. Emissivity in the 2–10 MeV and 2.0–5.8 MeV ranges were examined to determine the samples' surface activities prior to exposure underground at SNOLAB. The results are summarized in Table 7.3. The activities were found to be sufficiently low to ensure that any surface contamination accumulated at SNOLAB would be clearly identifiable.

7.4.2. Control Samples

Two polyethylene samples were used as control samples and not initially brought underground. They were instead left in a surface building at SNOLAB in the nylon bags they were shipped in. At the very end of the exposure period, these control samples were brought underground, briefly removed from their nylon shipping bags, and packed with the other samples for the return trip to SMU where the alpha activity was measured. All nylon bags were backfilled with N_2 before shipment.

After returning to SMU, the average alpha activity in the 2–10(2.0–5.8) MeV range was determined to be $196.9 \pm 32.0(90.4 \pm 21.7)$ nBq/cm^2. These levels were consistent with the average pre-exposure activities measured for the HDPE samples in Table 7.3. It was therefore concluded that no significant increase in activity was acquired from the shipping and transport of the samples.

Table 7.3. Initial alpha activity of polyethylene and copper samples after initial cleaning and prior to exposure at SNOLAB.

Material	Pre-exposure Activity (nBq/cm^2)	
	2–10 MeV	2.0–5.8 MeV
HDPE	187.5 ± 25.6	97.2 ± 18.4
Copper	524.9 ± 71.1	393.7 ± 61.6

7.4.3. Exposed Samples

Samples were rebagged as described in Section 7.2 and shipped back to SMU after the 83 day exposure. Each sample was then measured in the UltraLo-1800 approximately 10 days after the end of the exposure period, providing a first measure of the total surface alpha activity due to ^{210}Po and dust. The samples were then rebagged and stored for ∼80 days in an acrylic cabinet purged with low-radon liquid-nitrogen boil-off gas. A follow-up measurement was performed to obtain the time dependence of the surface activity, thus allowing Equation 7.4 to be solved for R_{Pb} and S_{dust}. The estimated ^{210}Pb and dust contamination rates are summarized in Table 7.4. The measured spectra for one of the HDPE samples are shown in Fig. 7.7, and all measured HDPE alpha rates are shown in Fig. 7.8.

Table 7.4. Determined values of R_{Pb} and S_{dust} from Equation 7.7 for each sample and weighted averages. HDPE samples 7 and 8 were measured during a period of high noise in the UltraLo-1800 and have been excluded from the analysis.

Sample #	Site	R_{Pb} $\left(\frac{\text{atoms}}{\text{day}\cdot\text{cm}^2}\right)$	S_{dust} $\left(\frac{\text{nBq}}{\text{day}\cdot\text{cm}^2}\right)$
HDPE 1	1	257.0 ± 26.2	19.6 ± 8.1
HDPE 2	1	334.0 ± 31.7	15.8 ± 10.6
HDPE 3	2	278.1 ± 28.5	34.7 ± 10.8
HDPE 4	2	385.9 ± 36.1	4.0 ± 14.7
HDPE 5	3	155.6 ± 33.6	69.4 ± 12.5
HDPE 6	4	150.8 ± 25.0	15.5 ± 9.2
Copper 1	1	413.8 ± 11.8	4.5 ± 9.8
Copper 2	1	443.6 ± 17.8	4.9 ± 8.4
Average HDPE		248.6 ± 12.0	24.9 ± 4.3
Average Copper		422.9 ± 9.9	4.7 ± 6.4

7.5. Discussion

The model developed in this study is useful for predicting activity over time, and also the peak activity for a given exposure time. Contributions to total activity from radon diffusion or dust are also further detailed in this section.

7.5.1. Peak Activity

With R_{Pb} and S_{dust} determined, it is possible to calculate the time at which maximum alpha activity occurs as a function of the exposure time

$$t_{max}(t_{exp}) = \frac{1}{\lambda_{Po} - \lambda_{Pb}} \ln \left[\frac{e^{(\lambda_{Po} t_{exp})} - 1}{e^{(\lambda_{Pb} t_{exp})} - 1} \right] \tag{7.8}$$

Using Equation 7.8 for t in Equation 7.6 yields the maximum activity for any exposure time. If a predetermined maximum activity is desired, this configuration of Equation 7.6 can be solved for t_{exp} to determine the maximum allowable exposure time.

7.5.2. Contributions From Diffusion

Radon can diffuse several millimeters into HDPE. For exposure times that are long relative to the half-life of ^{222}Rn ($t_{1/2}$ = 3.8 d), ^{210}Po activity will increase as 4.5 ± 1.0 pBq/cm^2/day/(Bq/m^3) [181]. From SRIM calculations, a 5.3 MeV alpha has a projected range in HDPE of 37 μm, leaving 4.5% of the total diffusion-related activity within range to exit the bulk. Of the alphas that manage to exit, 19% will have an energy greater than the 2.0 MeV threshold used in this analysis. Finally, the UltraLo-1800 will only count ~50% of all alphas (those emitted upwards). For an 83 day exposure in the 135 Bq/m^3 SNOLAB environment, the total expected diffusion-related activity measured in the UltraLo-1800 is 0.2 nBq/cm^2. All of the samples measured greater than 2300 nBq/cm^2, so diffusion-related activity was not expected to contribute to the overall determination of the R_{Pb} and S_{dust} parameters.

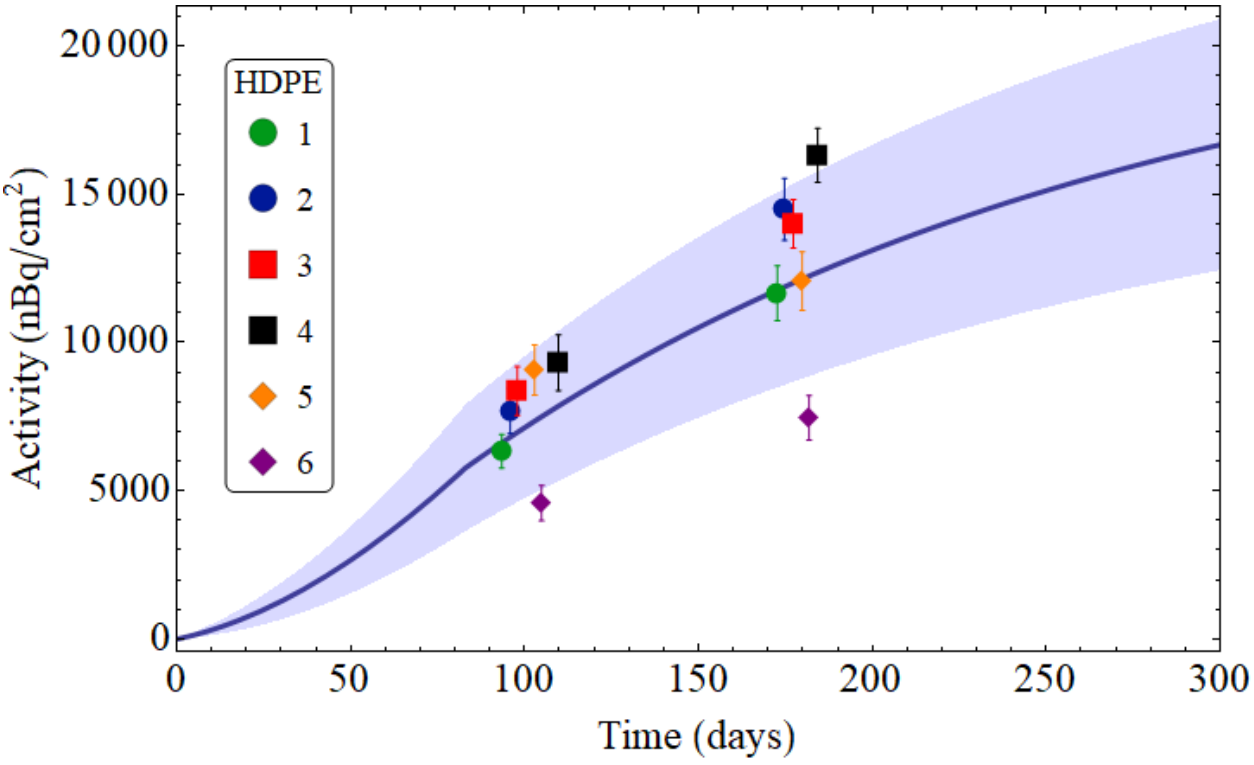

Figure 7.8. Measurements of the HDPE samples plotted over the 95% confidence interval of Equation 7.4 with R_{Pb} and S_{dust} taken from the weighted averages in Table 7.4. Time is measured from the beginning of the exposure at SNOLAB.

7.5.3. Activity From Dust

Previous studies in SNOLAB technical reports have assessed dust fallout and activity in the norite, shotcrete and concrete materials in the mine and lab. While SNOLAB advertises itself as a Class 2000 clean room, the measured particle-count levels from this study were consistent with Class 1000. If an assumed typical Class 1000 dust fallout rate of 10 ng/hr/cm^2 is used with an average dust density of 2.5 g/cm^3, dust would deposit at a rate of ∼96 nm/day yielding an 8 μm layer at the end of exposure in this study.

In determining the total expected dust activity per kg, emanation efficiency losses were considered. Radon is likely to have been flushed out by the argon gas flow in the UltraLo-1800, so the expected alpha rate from ^{222}Rn and its progeny were reduced by 20% [182]. In the thorium series, ^{220}Rn may have decayed while still in the UltraLo-1800 ($t_{1/2} = 56$ s). An assumed 75% of these decays plated onto a nearby surface. Taking the ratio of the sample size to UltraLo-1800 tray size, it was expected that the total alpha rate from ^{220}Rn and its progeny was reduced by 14%. Based on the measured activity of norite, shotcrete and concrete at SNOLAB [147], the total U and Th chain alpha activity was ∼150 Bq/kg, or ∼36 nBq/day/cm^2 from dust activity accumulation.

A different activity measurement was made for dirt from the vacuum cleaners in the clean room area of SNOLAB (64.2 Bq/kg, [148]). If this value is used for activity in dust, that would translate to an expected growth rate of ∼15 nBq/day/cm^2. Without knowing the filtration level of the vacuum filter or bag, this was taken as a reasonable lower limit. For polyethylene, the determined value of 24.9±4.3 nBq/day/cm^2 falls closer to the estimate based on rock activity and typical Class 1000 fallout rates. The lower rate determined from the copper samples may be further evidence of surface roughness on the polyethylene samples, which could trap and hold dust particles better during shipping and handling as compared to the smoother surfaces of copper.

7.5.4. Differences in HDPE and Copper

The HDPE samples showed a markedly lower plate-out rate for ^{210}Pb and higher dust accumulation as compared to copper. Surface roughness effects may explain both the higher dust-capture rate and the longer low-energy tails. The higher plate-out rate for copper may indicate a higher bonding strength with radon progeny. One copper sample was cleaned with isopropyl alcohol and given a third measurement, showing a modest 16% reduction from the expected activity for that measurement time assuming no cleaning was performed. Comparitively, an HDPE sample cleaned the same way showed a 90% reduction from expected activity for that measurement time. The same copper sample was further cleaned with Radiacwash^{TM} and deionized water, showing a $\sim$60% reduction from expected activity for that measurement time.

7.5.5. Location Dependence

There was not a strong case for suggesting a difference in plate-out rate for different locations, except possibly for the panels placed in Room 131. While there are no doors or barriers between any of the sites, there are two large air handlers above Room 127 and Room 131. The lower plate-out rates for samples 6 and 7 may be explained by a difference in the airflow rate immediately nearby the individual air handlers. There did not seem to be a strong case for a difference in plate-out rate for samples placed at different heights or proximity to walls.

7.6. Exposure Timing for SuperCDMS SNOLAB

The projected sensitivity of the SuperCDMS SNOLAB experiment currently assumes a peak ^{210}Pb contamination of 10,000 nBq/cm^2 for the surfaces of the polyethylene shield [68]. The original exposure limit was 100 days assuming an environment with 130 Bq/m^3 of radon activity. Dust was not included in this estimate, and was assumed to contribute $\leq$ 850 nBq/cm^2 of further contamination.

Results from this study indicate that this limit would be reached after ∼39 days in the measured SNOLAB environment (135 Bq/m^3), less than half the previously anticipated time. In this time, dust will add 972 nBq/cm^2 of activity, about 15% higher than previously predicted. The results of this study have informed the construction process and exposure will be limited accordingly.

Part III

Condensed Matter Physics & CDMS Analysis

Chapter 8

A Fast Parallel Algorithm for Condensed Matter Physics

Calculations of crystal potentials or force interactions, whether through molecular dynamics or classical potentials, rely on functions of distances $f(r)$ between many atoms. In either case, computational complexity and time limit the precision with which values are calculated. Even in the case of classical potentials, which are less computationally intense, crystal simulations and calculations are usually limited to the millions of atoms, with determined values often having fewer significant figures than a single-precision float[1].

Classical potential fitting has also become more complex in attempts to adapt a single model to a greater number of situations. The Lennard-Jones potential [183] is simple and widely used for its computational speed. However, much more accurate models exist. The Buckingham potential [184] expanded on the Lennard-Jones potential, replacing the Pauli repulsive term with an exponential function but at computational cost. The Stillinger-Weber potential [127] (hereafter SW potential) was proposed as a further improvement. It takes into account not just the distance between atoms but also the angles of their bonds in a new 3-body term.

Improvements on the classical potentials have thus progressed for decades [128, 185–187], with attempts to find a potential model that works not only with perfects crystals, but those with point defects, plane defects, and more. A fitted formula in one situation (temperature, lattice, atomic composition) often does not suitably agree with experimental values from another. As such, the potentials grow ever more complex, and determining parameters comes at greater computational cost, but the objective of a more universal model remains a priority.

[1] Depending on the implementation, single-precision floats have 6–9 significant decimal digits of precision. The IEEE 754 float has seven decimal digits of precision and is one of the most common implementations.

Rather than limiting calculations to a small number of atoms and thus limited precision, or expanding computational time which schedules and resources may not permit, a faster optimized algorithm could be used to achieve better and/or less computationally costly results. Additionally, potentials with arbitrary cut-off values that are often used to shorten compute time can be relaxed for better fitting of other parameters and more realistic simulation. An adaptive algorithm is also ideally suited for studies of non-ideal lattices with defects, vacancies or other imperfections.

The inclusion of contributions from more distant atoms or those with defect locations should also come with questions about the precision of the implemented variables. For example, a single interstitial defect sufficiently far away from a reference atom may not affect the total potential energy, but a plane defect at the same distance may have significant contributions when all atoms across the plane are considered. Thus, it may be beneficial to use very high-precision variables in computation, further advancing the need for a faster algorithm.

8.1. Computational Approach

Potential and force calculations in a crystal depend on distances between pairs of atoms. Any summation over lattice points will first require the calculation of the distance between these atoms r_{ij}, and then application of some function $f(r_{ij})$ to that distance. The value of f is included in the total sum. The algorithms presented here can be used for any such distance-dependent function.

For illustrative purposes, the Lennard-Jones potential is used as an example of the computational power of this new algorithm. Further extensions and adaptations of the same algorithm to other functions and potentials are discussed in Section 8.2.

There are many common techniques to optimize algorithms such as avoiding the repetitive calculation of the same value in nested loops. Likewise there are algorithms to avoid round-off error such as the Kahan summation algorithm [188]. These common tools are omitted

from the algorithms presented here to more clearly show the logic structure, and to more clearly demonstrate the methods applied.

8.1.1. An Illustrative Example

The Lennard-Jones potential [183] is a simple but widely-used potential energy formula. The total potential energy of a crystal with N atoms is described by the sum of Equation 8.1 between all pairs of atoms. The constant parameter σ is the distance at which the potential is zero due to the attractive and repulsive terms canceling. The parameter ϵ is the maximum depth of the potential well. Both parameters are determined from experimental measurements, and d_j is the distance from a fixed reference atom to any other atom j as a multiple of the nearest-neighbor distance.

$$U_{tot} = 2N\epsilon \left[\sum_{j=1}^{\infty} \left(\frac{\sigma}{d_j} \right)^{12} - \sum_{j=1}^{\infty} \left(\frac{\sigma}{d_j} \right)^{6} \right] \tag{8.1}$$

To simplify calculations, it is useful to separate the d_j terms and examine them independently

$$L_p \equiv \sum_{j=1}^{\infty} \left(\frac{1}{d_j} \right)^{p} \tag{8.2}$$

It is seen that Equation 8.1 can be determined by first calculating these lattice constants L_p for $p = 6$ and $p = 12$. The $p = 6$ term represents the attractive van der Waals force, whereas the Pauli exclusion principle is responsible for the repulsive $p = 12$ term. The choice of $p = 12$ is not fully motivated from first principles, so it is useful to compute a range of p values. For $p < 4$, the series does not converge [189], and for $p > 30$, the series is seen to converge to the coordination number of the lattice. While any real value of p could be computed, this example uses integer values for comparison to other published results which also examine integer values of p [189, 190].

To achieve a useful value of the lattice constants L_p in Equation 8.2, the series need only converge to the precision required. The double-precision float has ∼15 decimal digits, and is a very fast variable to use with most modern compilers. Results have been published for the

simple cubic (SC), face-centered cubic (FCC), body-centered cubic (BCC), hexagonal-close-pack (HCP) lattices with up to 15 decimal digits [189], but not every term published has actually converged to the precision given, especially for $p < 12$. The diamond (DIA) lattice has been published up to 9 decimal digits [190], roughly the precision of a 32-bit single-precision float. To fully demonstrate the power of the algorithms in this work, the Portable, Extensible Toolkit for Scientific Computation (PETSc) [191] was used to implement 128-bit floats to achieve 32 decimal digit precision.

8.1.2. Brute Force Method

Consider a SC lattice whose side length is D, and whose unit cell has a side length of 1 in arbitrary units. To calculate a distance-dependent function $f(r_{ij})$ over all lattice sites such as Equation 8.2, three nested **for**–loops can be invoked to cover a 3-dimensional grid. Each integer value of the respective loop variables (X, Y, Z) represent the coordinates of a particular atom. Sweeping from $-(D/2)$ to $(D/2)$ in all three loops covers all $(D+1)^3$ atoms in the cube.

The distance d_j from the origin to any other atom j is $\sqrt{X^2 + Y^2 + Z^2}$ so the program structure then is described by Algorithm 1.

Algorithm 1 Brute Force Method

```
L_p = 0
for X ← −(D/2) to (D/2) do
    for Y ← −(D/2) to (D/2) do
        for Z ← −(D/2) to (D/2) do
            if X = 0 and Y = 0 and Z = 0 then
                Next
            else
                L_p += 1 / (X^2+Y^2+Z^2)^{p/2}
return L_p
```

The **if**–statement is present to avoid the $\frac{1}{0}$ term (at the origin) which would otherwise set L_p equal to infinity or NaN. At this point, knowing that there will be $(D+1)^3$ **if**–statements checked in every run of Algorithm 1, it is worth finding how many terms will be necessary for this sum to converge.

8.1.3. The Convergent Series

Depending on the implementation of the 128-bit floats[2], these variables yield ∼32 decimal digits for each term. Finding where Equation 8.2 converges then requires additional terms to be equal to or less than 10^{-33} (in arbitrary units). Finding the coordinates of where $L_{p_j} = 10^{-33}$ yields little benefit, however, as that is only the value of one such term, and there may be many such terms at that distance.

For example, let $L_{p_j} = \frac{1}{(X_j^2+Y_j^2+Z_j^2)^{p/2}} = 10^{-33}$ for atom j at (X_j, Y_j, Z_j), and let $Y_j = Z_j = 0$ for simplicity. In the brute force method described above, the algorithm will still be computing approximately R^2 more terms for the face at $X_j = R$. Moreover, there will be six such faces to add to the total sum. Higher distances decrease the value of each L_{p_j} term, but there are more terms to the total sum at some fixed R, slowing down the convergence of the series with increasing distance as illustrated in Fig. 8.1. The slow convergence of L_p can be shown by calculating the total amount added to L_p from adding one layer at a fixed R distance. For L_6, the total value added from one layer at distance R goes as $1/R^4$ as shown in Equation 8.3. This is determined by integrating Equation 8.2 with respect to Y and Z for $p = 6$ and $X = R$. That result is multiplied by 6 for symmetry. While an exact result requires the actual summation in Equation 8.2, this result is useful for determining how many terms are required for convergence to a particular precision.

$$\mathrm{Sum}_{p,\mathrm{face@}R} \propto \frac{1}{R^{(p-2)}}$$

$$\mathrm{Sum}_{6,\mathrm{face@}R} = 6 \times \frac{2 + 15\sqrt{2}\mathrm{ArcCot}\sqrt{2}}{12R^4} \approx \frac{7.52815}{R^4} \tag{8.3}$$

[2]The IEEE-754 floating point standard defines quadruple-precision, 128-bit floats. These are implemented differently by various compilers as long-double, __float128, PetscReal, and others.

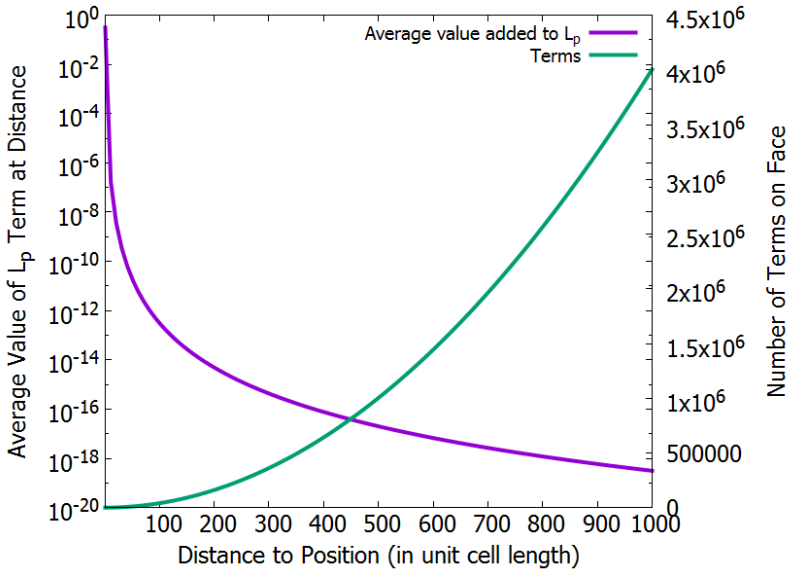

Figure 8.1. Average value of terms added to L_6 from the face at some fixed R versus the distance and number of terms added to L_6 at that face.

The convergence of Equation 8.2 is much faster for higher values of p but presents a significant computational challenge for low p as illustrated in Fig. 8.2. Converging to any desired precision at low p will then require finding fast algorithms that will capitalize on efficiency, parallelism, and any inherent symmetries in the crystal lattice.

8.1.4. Computational Analysis to Improve Performance

In nested loops and three-dimensional problems, performance gains can be found by avoiding repeated calculations, exploiting symmetries of the problem, and leveraging the advantages of high-performance computing clusters.

8.1.4.1. Avoiding Unnecessary Operations

In the simple case of Algorithm 1, the $(D+1)^3$ **if** statements can be avoided by structuring the program to calculate different regions of the same cube, none of which contain the (0,0,0) position as illustrated by Fig. 8.3. There are now six regions to consider: two rectangular

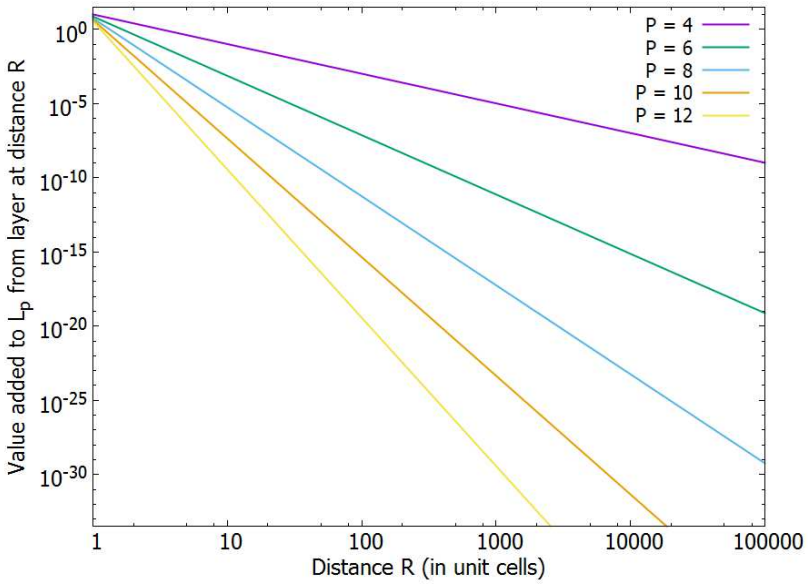

Figure 8.2. Average value of terms added to L_p across the face at some fixed R versus the distance R. One can draw a horizontal line across the graph at the desired precision on the vertical axis. Where that line intersects each p function will be approximately the distance required to converge the sum at that precision.

parallelepipeds, two planes, and two lines. The loops for these regions are executed in serial as described in Algorithm 2.

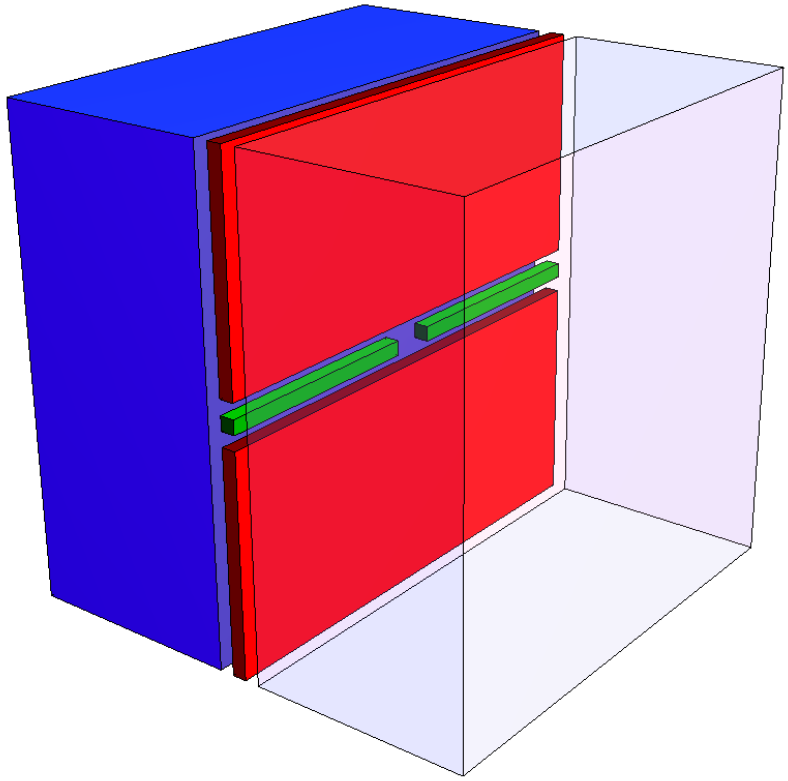

Figure 8.3. The six volumes to loop over, automatically avoiding the unit cell at the origin. The red regions indicate the 2-dimensional face planes, and the green regions are the 1-dimensional axes.

8.1.4.2. Parallelization

Since each individual L_{p_i} value is independent of every other L_{p_j}, Algorithm 2 is an excellent candidate for parallelization via MPI [192]. The parallelization of these nested **for**–loops, however, requires the following careful prescription such that each thread does approximately the same amount of work, and the entire 3-dimensional grid of lattice points is covered. For $NumProcs$ threads, one cannot simply set thread number $MyID$ to cover a range of $(D/NumProcs)$ in $(X/Y/Z)$ as can be trivially done in the case of a 1-dimensional

Algorithm 2 Broken Down into Six Separate Regions

$L_p = 0$

// Cube Volumes

for $X \leftarrow -(D/2)$ to $(D/2)$ **do**
  for $Y \leftarrow -(D/2)$ to $(D/2)$ **do**
    for $Z \leftarrow -(D/2)$ to -1 **do**
      $L_p \mathrel{+}= \frac{1}{(X^2+Y^2+Z^2)^{p/2}}$

for $X \leftarrow -(D/2)$ to $(D/2)$ **do**
  for $Y \leftarrow -(D/2)$ to $(D/2)$ **do**
    for $Z \leftarrow 1$ to $(D/2)$ **do**
      $L_p \mathrel{+}= \frac{1}{(X^2+Y^2+Z^2)^{p/2}}$

// Faces @ $Z = 0$

for $X \leftarrow -(D/2)$ to $(D/2)$ **do**
  for $Y \leftarrow -(D/2)$ to -1 **do**
    $L_p \mathrel{+}= \frac{1}{(X^2+Y^2)^{p/2}}$

for $X \leftarrow -(D/2)$ to $(D/2)$ **do**
  for $Y \leftarrow 1$ to $(D/2)$ **do**
    $L_p \mathrel{+}= \frac{1}{(X^2+Y^2)^{p/2}}$

// Axes @ $Y = 0$ and $Z = 0$

for $X \leftarrow -(D/2)$ to -1 **do**
  $L_p \mathrel{+}= \frac{1}{X^p}$

for $X \leftarrow 1$ to $(D/2)$ **do**
  $L_p \mathrel{+}= \frac{1}{X^p}$

return L_p

array. Instead, the original cube from Algorithm 1 is broken down into $NumProcs$ interpenetrating cubes with a different basis. This allows every thread to compute $\frac{(D+1)^3}{NumProcs}$ elements of L_p, the results of which can be combined at the end of the algorithm. The integer basis of each new lattice is computed as follows

$$Basis = Floor(\sqrt[3]{NumProcs}) \tag{8.4}$$

The initial (X, Y, Z) position of each thread is

$$\begin{aligned} X_i &= (MyID\%Basis) + (D/2) \\ Y_i &= (\text{Floor}\left[\frac{MyID}{Basis}\right]\%Basis) + (D/2) \\ Z_i &= (\text{Floor}\left[\frac{MyID}{Basis^2}\right]\%Basis) + (D/2) \end{aligned} \tag{8.5}$$

Fortunately, only one thread (hereafter the *origin thread*) will pass through the $(0, 0, 0)$ position. All other threads can execute a fast triple-nested **for**–loop described by Algorithm 3. Figure 8.4 highlights an example of sites covered by Algorithm 3 for an eight-thread parallel execution. The origin thread will execute a slightly modified version of Algorithm 2. The origin thread is identified as

$$k = (D/2)\%Basis$$

$$OriginThreadNum = k * Basis^2 + k * Basis + k$$

A simple MPI summation is performed at the end of the program, and the result is returned.

One caveat with this prescription is that it requires $NumProcs$ to have an integer cube root. On small clusters with a limited number of threads, this can prevent the full utilization of this method. However, even consumer processors are widely available in 8-core (or more)

Algorithm 3 Invoked in Parallel (Threads other than origin thread)

$L_p = 0$

... set X_i, Y_i, Z_i...

for $X \leftarrow X_i$ to $-(D/2)$ in steps of $-Basis$ **do**

  for $Y \leftarrow Y_i$ to $-(D/2)$ in steps of $-Basis$ **do**

    for $Z \leftarrow Z_i$ to $-(D/2)$ in steps of $-Basis$ **do**

      $L_p \mathrel{+}= \frac{1}{(X^2+Y^2+Z^2)^{p/2}}$

... MPI summation ...

return $L_{p,total}$

configurations which is the minimum number required. More flexible methods not requiring a cubic number of threads are possible, but result in reduced performance. The cluster used for this example (Southern Methodist University's ManeFrame) has over 1,100 CPU nodes available, each with eight cores, making over 8,800 simultaneous threads possible, eliminating the need for programming more flexible methods.

8.1.4.3. Exploiting Symmetry

In the case of the SC lattice, the calculation of L_p can be shortened by considering that the cube is made of eight identical, smaller pieces corresponding to each octant. Therefore, a speedup of almost eightfold can be found by calculating only one of these octants and multiplying the end result. However, the algorithmic range of each octant is not as obvious as it seems. There are unit cells along the planes between octants whose atoms need to have their contributions handled carefully as some of the atoms sit astride different octants as illustrated in Fig. 8.5, and likewise for cells along the axes. For unit cells immediately adjacent other octants, consider these as being in separate volumes called the axis or face volumes as illustrated in Fig. 8.6. The remaining cells are considered to be in one of eight cubic volumes spanning the rest of each octant. Therefore, in the entire lattice, there are

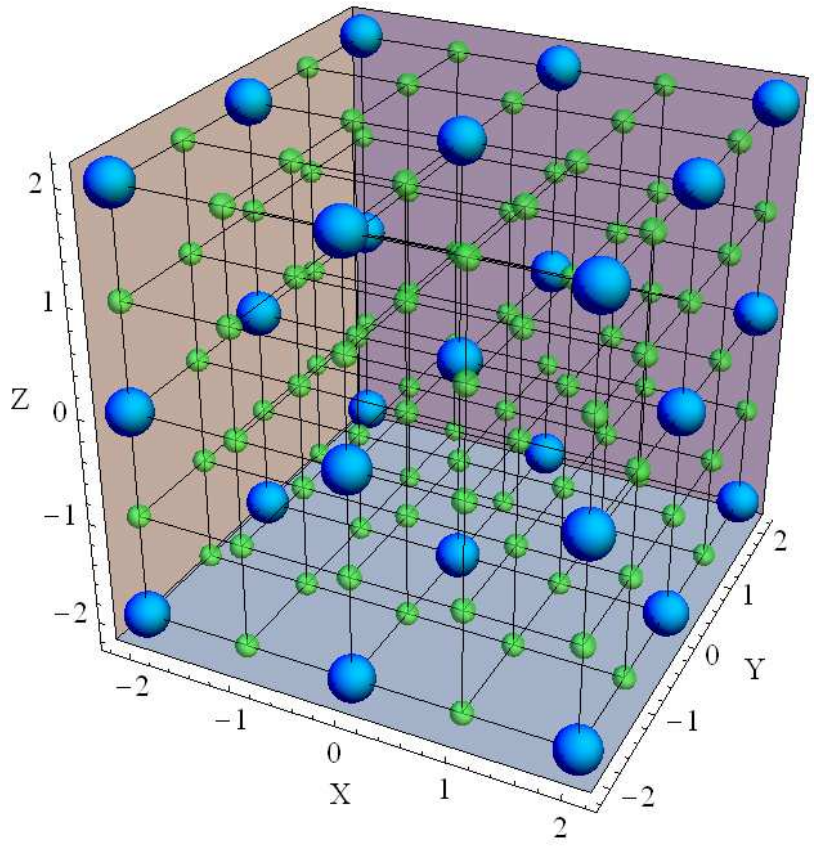

Figure 8.4. Example of atom sites in the SC lattice that are looped over by a single thread (blue) for an 8-thread invocation of Algorithm 3. The remaining green sites are divided among the other seven threads. In a real lattice, the spheres should be uniform and expanded to fill the maximum volume possible, but are shown with different sizes here for clarity.

eight cubic volumes, 12 face volumes, and six half-axis volumes. In the case of the SC lattice, one need only calculate the sum of a single cubic volume L_{cube}, a single face L_{face}, and a single half-axis L_{axis} to determine L_p as shown in Equation 8.6.

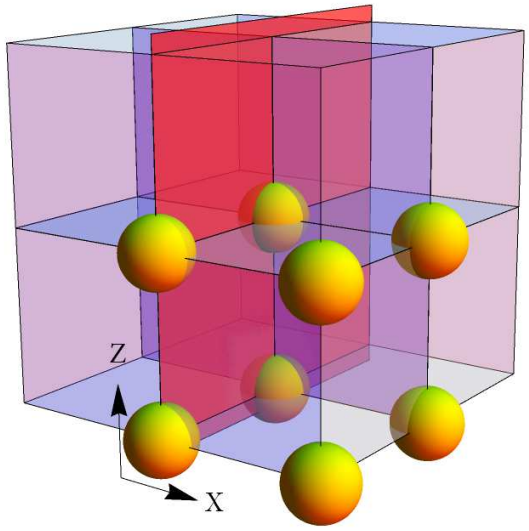

Figure 8.5. SC unit cells are shown along the plane at $X = 0$. The atoms (shown in yellow; not to scale) can be shared between different octants at such a plane.

$$L_p = [L_{cube} + (1.5 * L_{face}) + (0.75 * L_{axis})] * 8 \tag{8.6}$$

The values 1.5 and 0.75 arise in Equation 8.6 from the fact that there are 12 faces and six half-axes that should contribute equally to each of the eight octants, so $\frac{12}{8}$ for the faces, and $\frac{6}{8}$ for the axes. The new serial algorithm, which automatically avoids the origin, can be written compactly as in Algorithm 4.

To parallelize this, the basis is calculated as before, but the same basis does not hold for calculation of the face or axis (2- and 1-dimensional arrays, respectively). The calculation of those bases is described in Algorithm 5. When looping through the cube, face, or axis volume as described in Algorithm 6), the values of (X_i, Y_i, Z_i) must be calculated relative to the appropriate basis for that volume. This is done with Equation 8.5 with $Basis$, $Basis_f$

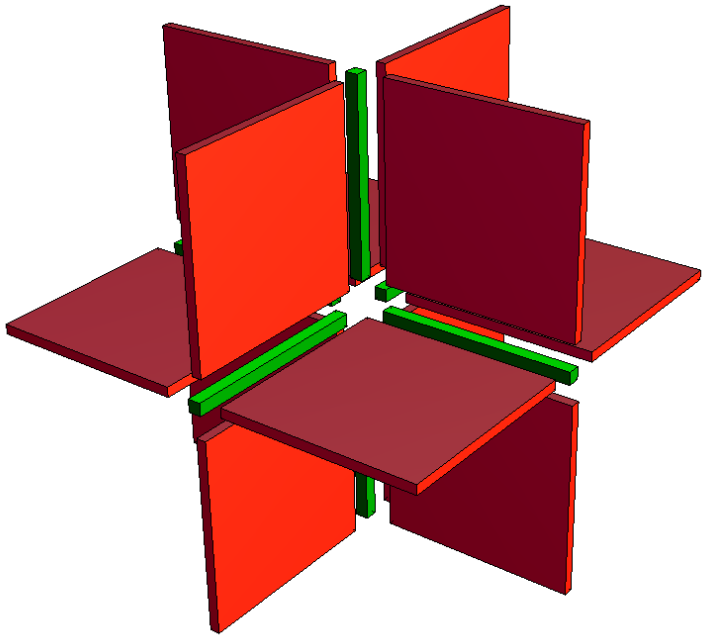

Figure 8.6. The shared volumes of the planes and axes between the octants.

Algorithm 4 Symmatrized

$L_{cube} = L_{face} = L_{axis} = 0$

for $X \leftarrow (D/2)$ to 1 **do**

  for $Y \leftarrow (D/2)$ to 1 **do**

    for $Z \leftarrow (D/2)$ to 1 **do**

      L_{cube} += $\frac{1}{(X^2+Y^2+Z^2)^{p/2}}$

    L_{face} += $\frac{1}{(X^2+Y^2)^{p/2}}$

  L_{axis} += $\frac{1}{X^p}$

return $[L_{cube} + (1.5 \times L_{face}) + (0.75 \times L_{axis})] * 8$

or $Basis_a$, as needed. Note that the step sizes must be negative since the initial positions are set at points away from the origin. The new algorithm is computed by all threads as there is no need to find an origin thread.

8.1.4.4. Extending the Exploitation of Symmetry: BCC and FCC

For the BCC and FCC lattices, the same exploitation of octants can be used, but with special handling. In this case, the lattices must be thought of as an SC lattice with two and four basis atoms, respectively. The **for**–loop variables now indicate the coordinates of the new conventional unit cells, instead of just the atoms. The nearest-neighbor distance must be normalized properly to this new conventional unit cell (Table 8.1), and the first triple-nested **for**–loop in Algorithm 7 can be computed similarly to the SC case, with the additional basis atom(s) added at each unit cell location. However, the face- and axis-cells are handled uniquely.

The multiple counts of basis atoms in Algorithm 7 are due to the way they are "shared" between the octants of the divided cube. Along the face or axis, there are cells where an atom sits astride the plane separating the octants. These atoms should only be counted once. However, there are other basis atoms in the volume of the unit cells immediate next to these planes (or around the axes) which need to be effectively counted once but since the number of faces and axes that are shared is different from the number of octants, they need to be counted with special weights.

Algorithm 5 Calculation of Basis

$T = NumProcs$

while $(\sqrt{T} - \text{Floor}(\sqrt{T})) > 0$ **do**

  $T - -$

$Basis_f = \text{Floor}(\sqrt{T})$

$Basis_a = NumProcs - T$

Algorithm 6 Parallelized & Symmatrized

$L_{cube} = L_{face} = L_{axis} = 0$

// Cube Volume

... calculate X_i, Y_i, Z_i relative to $Basis$ ...

for $X = X_i$ to $X > 0$ in steps of $-Basis$ **do**
  for $Y = Y_i$ to $Y > 0$ in steps of $-Basis$ **do**
    for $Z = Z_i$ to $Z > 0$ in steps of $-Basis$ **do**
      L_{cube} += $\frac{1}{(X^2+Y^2+Z^2)^{p/2}}$

// Face & Axis

if $Basis_a > 0$ **then**
  if $MyID < T$ **then**
    ... calculate X_i, Y_i relative to $Basis_f$ ...
    for $X = X_i$ to $X > 0$ in steps of $-Basis_f$ **do**
      for $Y = Y_i$ to $Y > 0$ in steps of $-Basis_f$ **do**
        L_{face} += $\frac{1}{(X^2+Y^2)^{p/2}}$
  else
    ... calculate X_i relative to $Basis_a$ ...
    for $X = X_i$ to $X > 0$ in steps of $-Basis_a$ **do**
      L_{axis} += $\frac{1}{X^p}$

else
  ... calculate X_i, Y_i relative to $Basis_f$ ...
  for $X = X_i$ to $X > 0$ in steps of $-Basis_f$ **do**
    for $Y = Y_i$ to $Y > 0$ in steps of $-Basis_f$ **do**
      L_{face} += $\frac{1}{(X^2+Y^2)^{p/2}}$
  ... set X_i as $ProcID + D$ ...
  for $X = X_i$ to $X > 0$ in steps of $-NumProcs$ **do**
    L_{axis} += $\frac{1}{X^p}$

... MPI summation ...

return $[L_{cube} + (1.5 \times L_{face}) + (0.75 \times L_{axis})] * 8$

Algorithm 7 FCC - Symmatrized

$L_{cube} = L_{face} = L_{axis} = 0$

$n = 2.0$ // n = Normalization factor

// Basis atom offsets

$b2x = 0.5; b2y = 0.5; b2z = 0.0$

$b3x = 0.0; b3x = 0.5; b3z = 0.5$

$b4x = 0.5; b4y = 0.0; b4z = 0.5$

for $X \leftarrow (D/2)$ to 1 **do**

  for $Y \leftarrow (D/2)$ to 1 **do**

    for $Z \leftarrow (D/2)$ to 1 **do**

      // First basis atom

      $R = (X^2 + Y^2 + Z^2) * n$

      L_{cube} += $\frac{1}{R^{p/2}}$

      // Second basis atom

      $R = ((X + b2x)^2 + (Y + b2y)^2 + (Z + b2z)^2) * n$

      L_{cube} += $\frac{1}{R^{p/2}}$

      ... similarly for the other basis atoms ...

    $R = (X^2 + Y^2) * n$

    L_{face} += $\frac{1}{R^{p/2}}$

    ... then count basis atom 2 once ...

    ... then count basis atoms 3 & 4 twice ...

  $R = (X^2) * n$

  L_{axis} += $\frac{1}{R^{p/2}}$

  ... then count basis atom 2 twice ...

  ... then count basis atom 3 four times ...

  ... then count basis atom 4 once ...

return $[L_{cube} + (1.5 \times L_{face}) + (0.75 \times L_{axis})] * 8$

Consider the unit cells spanning the X-Y plane of a single octant. To minimize calculations, it is possible to compute only terms from these cells and use symmetry to apply the results to the Y-Z and X-Z planes. In the case of the SC lattice, all atoms sit astride the axes and faces evenly, so no special counting or weighing is needed. In the FCC case, two of the atoms sit evenly across the X-Y plane, and two are mirrored as illustrated by Fig. 8.7. These mirrored atoms must be counted twice as in Algorithm 7, and then the total contribution from the face can be added to the sum.

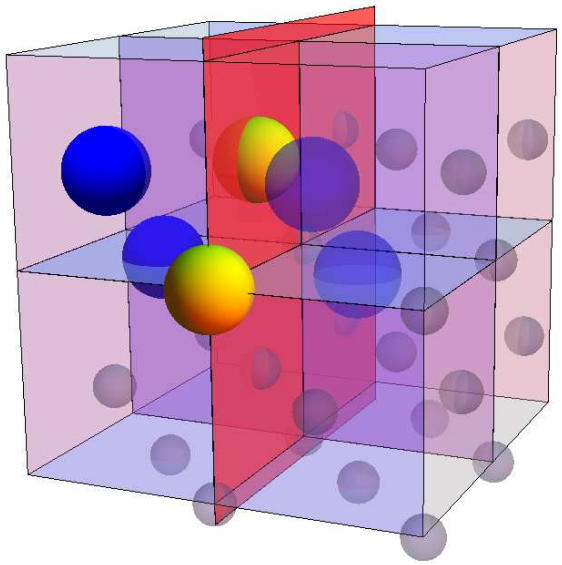

Figure 8.7. Conventional FCC unit cells along the X-Y plane (red). For face terms, the shared atoms (yellow spheres) are counted once in Algorithm 7, whereas the mirrored atoms (solid blue spheres) must be counted twice to make full use of symmetry. The faded blue spheres indicate which atoms are mirroring those indicated by the solid blue atoms. Gray spheres indicate other FCC atoms in other unit cells along the red plane.

Similar to the faces, the algorithm need only compute the unit cells along a single half-axis. In the case of cells along the X-axis, the first basis atom is counted once as it is shared evenly between all four unit cells located around around the axis. The second and fourth basis atoms described in Algorithm 7 are shared evenly between two cells and mirrored across

one plane, so they are each counted twice. The third basis atom is mirrored in all four unit cells along the axis, so it is counted four times.

In the BCC structure, the same mirroring principle applies: the second basis atom is counted once for cells in the 3-dimensional volume spanned, twice for cells along the face, and four times for cells along the axis.

Table 8.1. Number of basis atoms and normalization factors in the conventional unit cells for each lattice.

Lattice	Basis Atoms	Normalization Factor
SC	1	1
BCC	2	$\frac{4}{3}$
FCC	4	2
DIA	12	$\frac{16}{3}$

8.1.4.5. Extending the Exploitation of Symmetry: DIA

For the diamond lattice, the conventional unit cell is essentially an FCC conventional cell with the addition of four more basis atoms within the volume of the cell at the tetrahedral positions. The algorithm requires further special handling due to the asymmetry of the tetrahedral positions across one axis. In the BCC and FCC cases, the symmetry between octants obeys rotational symmetry. This can be seen by rotating the view 90 degrees about any axis resulting in viewing the exact same configuration of atoms. However, the diamond lattice does not have this symmetry. If the diamond lattice is rotated 90 degrees, the tetrahedral atoms appear at different distances. This lack of symmetry is depicted in Fig. 8.8.

Rather than settling for only a four-fold speedup from symmetrization, a new conventional unit cell can be fashioned that, while physically unrealistic, presents the same mathematical results as a real DIA lattice for this calculation. The new conventional unit cell has 12 basis atoms where four are the usual FCC-like atoms, four are the original tetrahedral atoms, and

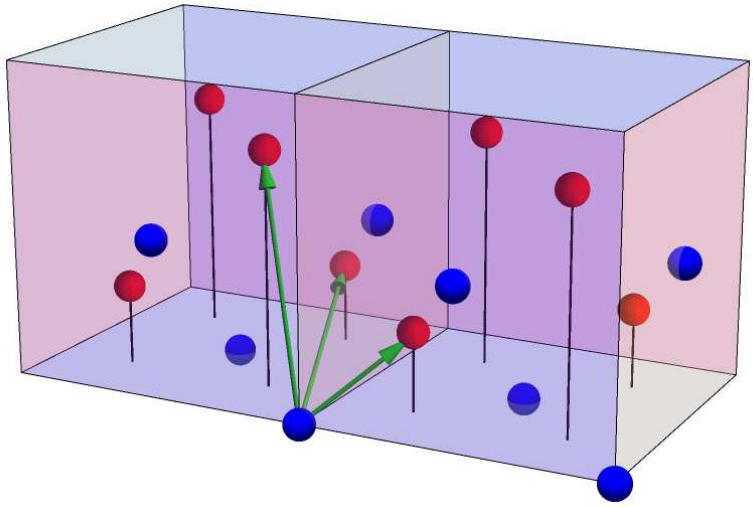

Figure 8.8. Two conventional cells of the DIA lattice are shown. Distances to the tetrahedral atoms are not the same when rotating 90 degrees about any point. The blue spheres are the FCC-like basis atoms, and the red spheres indicate the tetrahedral atoms. The sizes of the spheres are not indicative of the sizes of the atoms at these sites.

an additional four atoms occupy the location of where the tetrahedral atoms would appear to be if the viewer rotates 90 degrees as illustrated in Fig. 8.9.

In this case, the tetrahedral atom contributions to L_p need to be counted for half of what they would in the previous case since there are now twice as many. Counting in this manner yields an identical mathematical result from any other approach, but allows for an eight-fold speedup by only calculating one octant. The exact weights for each basis atom in each volume of the algorithm are described in Table 8.2.

8.1.4.6. Extending the Exploitation of Symmetry: HCP

Due to the hexagonal nature of the HCP lattice, a completely different approach is used. Using the fact that the HCP lattice has alternating layers (ABABAB) and that those layers have alternating and repeating rows, the structure can be logically constructed as four interpenetrating orthorhombic sublattices. One sublattice must be chosen to contain the $(0, 0, 0)$ position whereas the others are identical in shape but offset from this first sublattice

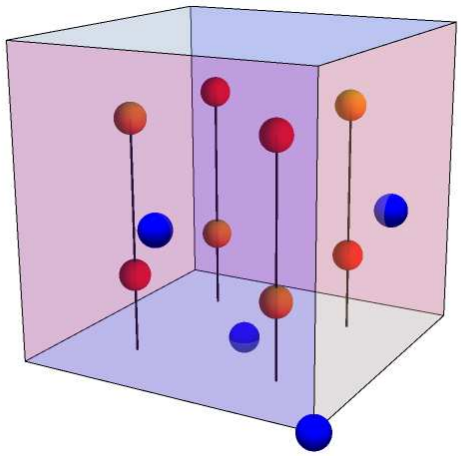

Figure 8.9. The 12-basis-atom conventional unit cell for calculations involving the diamond lattice. The orange spheres indicate the additional tetrahedral atoms.

Table 8.2. Convential DIA lattice basis atoms (2-8) and additional tetrahedral basis atoms (9-12) for use in Algorithms 4 and 6. The Cube Multiple represents the numerator used for the ($L_{cube/face/axis}$ +=) lines in psuedocode.

Basis Atom	Offset (X,Y,Z)	Cube Multiple	Face Multiple	Axis Multiple
1	$(0,0,0)$	1	1	1
2	$(\frac{1}{2},\frac{1}{2},0)$	1	1	2
3	$(0,\frac{1}{2},\frac{1}{2})$	1	2	4
4	$(\frac{1}{2},0,\frac{1}{2})$	1	2	2
5	$(\frac{1}{4},\frac{1}{4},\frac{1}{4})$	0.5	1	2
6	$(\frac{3}{4},\frac{3}{4},\frac{1}{4})$	0.5	1	2
7	$(\frac{3}{4},\frac{1}{4},\frac{3}{4})$	0.5	1	2
8	$(\frac{1}{4},\frac{3}{4},\frac{1}{4})$	0.5	1	2
9	$(\frac{1}{4},\frac{1}{4},\frac{3}{4})$	0.5	1	2
10	$(\frac{3}{4},\frac{3}{4},\frac{3}{4})$	0.5	1	2
11	$(\frac{3}{4},\frac{1}{4},\frac{1}{4})$	0.5	1	2
12	$(\frac{1}{4},\frac{3}{4},\frac{1}{4})$	0.5	1	2

as illustrated in Fig. 8.10. An algorithm can be constructed to calculate these four sublattices separately, and each can be parallelized as before.

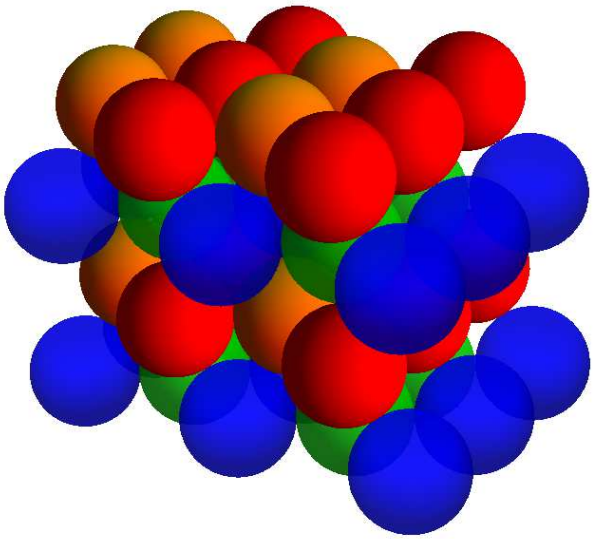

Figure 8.10. The HCP lattice as composed of four (red, blue, green, and orange) interpenetrating orthorhombic lattices.

The symmetry of this lattice can be easily broken down into quartets, but using octants will present a similar challenge as the DIA lattice. One of the four sublattices will extend slightly beyond what would be one of the faces between octants as illustrated in Fig. 8.11. Distances to each atom from the origin are not the same across this axis. The other three sublattices have atoms that either lie exactly on the faces, or completely within an octant. The solution, similar to DIA, is to double the number of atoms in the only sublattice with unevenly shared atoms. The positions of the extra atoms will be those that respect the rotational symmetry required for splitting the entire HCP lattice into equal octants. As with DIA, the algorithm halves the value added to L_p from each atom in this sublattice.

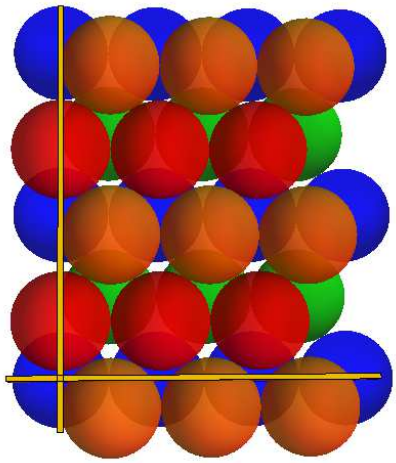

Figure 8.11. Top-down view of the HCP lattice. The orange sublattice shown cuts unevenly across one of the yellow axes, whereas the others either cut evenly or not at all.

8.1.4.7. Onionization

Running large, parallelized jobs on a cluster is convenient for solving large problems such as the algorithms described above. However, software and hardware errors do occasionally occur which can result in many lost CPU hours. As such, it is beneficial to break one large computation into many small ones. The result is a series of jobs that stack like layers of a (cubic) onion that are gradually added to the problem set as illustrated in the left panel of Fig. 8.12. This method has the added benefit of reducing roundoff error for extremely small terms (i.e. those layers at greatest distance) if one performs the sum of each job's return value from smallest to greatest.

In the symmatrized version of the program, the optimized use of this method would involve breaking the onion layer down into six new volumes: three volumes that span the main cube volume from the inner layer to the new outer layer, two regions to cover the face, and one region to cover the axis as illustrated in the right panel of Fig. 8.12. This avoids having to check that the coordinates covered are outside of the previous layer, and the computational cost of entering and leaving the **for**–loops is negligible compared to the

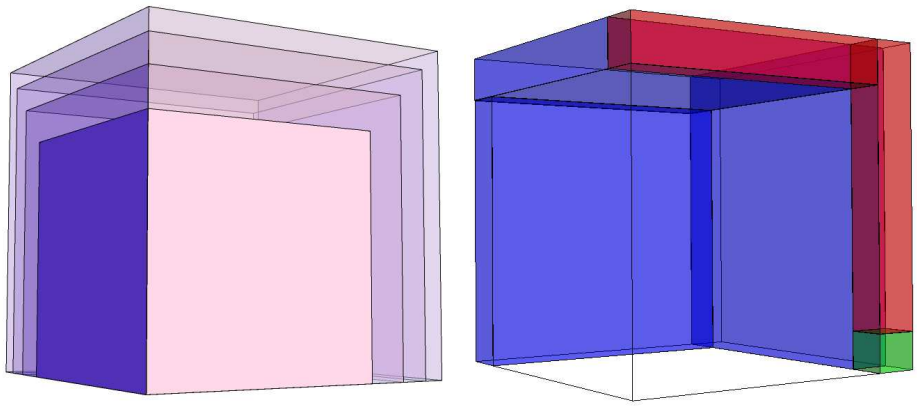

Figure 8.12. Left: Layers of computational ranges for different jobs shown stacked. The results are summed using the farthest first method. Right: Each layer can be split into six volumes: three volumes for the cubic space (blue), two volumes for the face (red), and one volume for the axis (green).

number of **if**–statements avoided. Fortunately, the calculation of bases for each volume are identical to the non-onionized version.

8.2. Results & Applications

A new method of computing any value that depends on distance between atoms in a crystal lattice has been created and optimized. This same algorithm can be tailored to look at other crystal energy functions, such as the Buckingham potential, SW potential, and others.

8.2.1. Lennard-Jones Lattice Constants

Using the symmetrized and parallelized algorithms described above, the Lennard-Jones lattice constants L_p have been calculated in the SC, BCC, FCC, HCP, and DIA lattices. Terms with $p > 9$ are computed to 32 decimal digits, convenient for quadruple precision calculations. Those with $p \leq 9$ are computed to lower precision due to computational limits (Fig. 8.2). In addition to extending the precision of these constants, there are corrections to terms with $p < 12$ previously published [189,190]. The total speedup achieved going from the

brute force method to the symmetric, parallel program was ∼29 fold. Speedup results from each method are summarized in Table 8.3. The computed Lennard-Jones lattice constants are given in Table 8.4.

To validate these results, a Mathematica program similar to Algorithm 2 was used for several terms with $p \geq 12$ using infinite precision in all five lattices. Higher order terms were chosen because of the faster convergence of higher p values, and the comparative slowness of Algorithm 2 with the use of infinite precision. The results all agreed to the given precision in Table 8.4.

Table 8.3. Speedup achieved for each algorithm in the SC lattice, as normalized to the calculation time of Algorithm 1. Results are similar for any distance-dependent calculation. Gains in Algorithm 2 are from avoiding the **if** statements. Likewise for Algorithm (3) but most threads are also able to avoid jumping into and out of **for** loops, which also avoids calculating some of the same components of the distance value. Algorithm 6 combines the advantages of parallelism and 8-fold symmetry for the greatest gains. All values of speedup are given per CPU core.

Algorithm	Fraction of D^3 terms in L_p	Effective Speedup per CPU core
Simple (1)	1	1
Broken Down (2)	1	2.671
Parallel (3)	1	3.476
Symmetric Parallel (6)	0.1249	28.99

8.2.2. Other Classical Potentials

The results in Table 8.3 are normalized to 1. As such, similar speed-up values should be attainable for applications of this approach to other crystal calculations. For example, the SW potential is fit with as many as nine parameters as previously shown in Equation 2.9.

Fitting these parameters over many lattice sites and simulation requires lengthy computation, but it is also the case that the range of the potential is cut off at some arbitrary value (in this case, a). Indeed the cutoff is typically so short that only nearest- or next-to-nearest

neighbors contribute to the total energy. Relaxing this parameter would allow simulation of more effects from vacancy or interstitial events. The algorithms described above can be used to compensate for the additional calculations, resulting in a potentially more transferable fit.

8.2.3. Applications to Crystal Defects

To simulate defects, one cannot use an algorithm for calculating over lattice sites in a perfect crystal. For example, to test or fit parameters for the creation energy of a Frenkel pair [120], the atom at the origin in the algorithms in this study can instead be integrated over the path of defect creation. Moreover, the application of the algorithms summarized in Table 8.3 could provide substantial speedup and precision improvements to molecular dynamics simulations of defect formation (see Section 2.3 for a review of the varying molecular dynamics calculations of the Ge displacement threshold energy).

In addition to point defects, plane defects can be simulated by displacing an entire algorithmic volume (as illustrated in Figs. 8.3 and 8.12) for as many planes as desirable. This allows for a faster way to test the transferability of plane defects to other parameterizations of potentials. Either point or plane defects could be implemented as single occurrences, or uniform occurrences at regular intervals. Uniformly spread defects or point defects at the origin would still allow use of all the algorithms presented.

Table 8.4. The Lennard-Jones lattice coefficients L_p in the SC, BCC, FCC, HCP, and DIA lattices.

L_p	SC	BCC	FCC	HCP	DIA
L_4	16.53228	22.63872	25.33826	25.33908	10.23284
L_5	10.37752483	14.75850937	16.96751846	16.96843635	6.3127603582
L_6	8.40192397482754	12.2536678672923	14.4539210437445	14.4548972778416	5.11677158774719
L_7	7.4670577809188105309	11.054243479244464865	13.359387700742084043	13.360346776195552357	4.5944760255509476375
L_8	6.945807927226369624170778	10.3551979084025147271239 3	12.80193723137813255579318	12.802821852809895887166 11	4.331913743971506684986912
L_9	6.628859198886779099036097 2133	9.894589656321115351649600 3879	12.492546702137558143156650385	12.493321725001781579567943092	4.190372125650368546584522 7190
L_{10}	6.426119102533089006632121 3261759	9.564400615359947873292895838 7003	12.311245665477405791382158094686	12.311896233818981044642686360567	4.111023599490959030320769 7180817
L_{11}	6.292294499234567377969213 0757460	9.313262537399100106223791528 6944	12.200920351277113166130939018073	12.201447099831954637516858217646	4.065467598974608216842067 4657813
L_{12}	6.202149045047518551930416 3922851	9.114183268075358867656457088 5073	12.131880196544579708261946410532	12.132293769098917625885375250999	4.038904712881416028325490 3749042
L_{13}	6.140599580021692135628988 3683193	8.951807318574715161518198669 2628	12.087726321352052662825461301813	12.088042550298439000808701615697	4.023251187001690160637777 7123470
L_{14}	6.098184125712152132752913 1655605	8.816770228485919867640829190 2320	12.058991944350859312923039015626	12.059228255068241446619187406471	4.013956088437780728688980 6009992
L_{15}	6.068764295038892108594367 6325996	8.702984559980925548488900974 3042	12.040024055099088629979906152137	12.040197144347223255169612620282	4.008405236427064607592202 2605494
L_{16}	6.048263469585841667946446 8171129	8.606254047544529409963131098 7788	12.027354844018570329377774991884	12.027479419303856131335523169808	4.005075870783929770297305 5370689
L_{17}	6.033929316367207410486729 1112617	8.523531250439298216078302755 3316	12.018809436710457796909425073283	12.018897719622859506995597162558	4.003072042245727447762525 6930317
L_{18}	6.023881707866714774925809 6087048	8.452503168608381773845719834 0021	12.012998309665959588741240723167	12.013060023177408319000392309630	4.001862653728703683566085 9738894
L_{19}	6.016825456331737707501294 7930151	8.391350791413117799935996848 5349	12.009019604439323572913310649568	12.009062224111209496811523499010	4.001131080110212866508684 1693924
L_{20}	6.011862830889945727100573 5996598	8.338604005679562967751788420 5378	12.006280041326342657408789230664	12.006309158114658698075084825914	4.000687709223456291466253 7575434
L_{21}	6.008368757546683167237434 9304180	8.293050370415294363339674233 4136	12.004384809362303299396537324646	12.004404510084773210744581189288	4.000418581502782884203666 2413099
L_{22}	6.005906526134291116596313 5002055	8.253675218084779608006966508 9658	12.003068569322929886793306584316	12.003081784233296681711658420583	4.000255004260839438292224 5458342
L_{23}	6.004170240070748022213373 5785364	8.219620534883649172353758848 5715	12.002151490974712110042308831699	12.002160286739322615229650383062	4.000155470317937805666683 3678459
L_{24}	6.002945208184129497401907 0764771	8.190155475483163084161586827 6327	12.001510824939707072003031295877	12.001516638577045961535386165550	4.000094848440245708930795 4562207
L_{25}	6.002080520374913336672263 4113763	8.164654351927330695212831426 5671	12.001062278709246141393049474196	12.001066097142027202635675470834	4.000057896645991953917702 8099623
L_{26}	6.001469972496086057616308 0284069	8.142579615920798837270619190 3706	12.000747674897726915713658895972	12.000750168624485190911852889731	4.000035357491892194513677 0397920
L_{27}	6.001038752238304844131731 0970378	8.123468315872789188316176296 3052	12.000526690212160028001079232466	12.000528310428505143624399658244	4.000021601507598372784318 2332604
L_{28}	6.000734121070789493633653 3237460	8.106921071038717340377204764 2013	12.000371277553079701932705119123	12.000372325322411021726121333862	4.000013201871853892795471 6341537
L_{29}	6.000518879212211412386071 0817340	8.092592938376121777591886236 9037	12.000261871447419639515536483048	12.000262546150133902013292069507	4.000008070750176723597440 7653933
L_{30}	6.000366774897184038835458 7433669	8.080185749906173104749490991 7169	12.000184790059821196656550158876	12.000185222851788273771215661366	4.000004935152539297491758 2258906
L_∞	6	8	12	12	4

Chapter 9

Measurement of Energy Loss to Frenkel Defects from ^{206}Pb Recoils in SuperCDMS Germanium Detectors

As described in Chapter 2, crystal defects can occur when incident radiation recoils off an atom with sufficient energy to displace it from its lattice site, thus creating a vacancy. The combination of a vacancy and an interstitial atom are referred to as a Frenkel pair, or a Frenkel defect [120]. The creation of defects permanently stores energy in the crystal. The fraction of incident energy that goes into defect formation depends on the mass of target, and the mass and kinetic energy of the impinging particle [121, 123]. The energy required to displace a germanium atom from its lattice site is the displacement threshold energy. Previously determined displacement threshold energies from theory and various molecular dynamics simulations are inconsistent, ranging from 7–30 eV [133–139].

The value of the displacement threshold energy has implications for low-background physics experiments that employ solid-state detectors to search for rare processes with sub-keV energy depositions. The SuperCDMS program is targeting low-mass dark matter candidates [68] from a few hundred MeV/c^2 to several GeV/c^2 with detection thresholds comparable to the Ge-atom displacement threshold energy. Because the energy that goes into the formation of a Frenkel defect is not directly observable, an accurate determination of the displacement threshold is important for establishing the low-energy detector response and thus for understanding the ultimate low-mass dark matter sensitivity reach.

During the operation of the SuperCDMS Soudan experiment, two ^{210}Pb sources were installed adjacent to two detectors (T3Z1 and T3Z3) to evaluate their *in situ* response to non-penetrating radiation from the decays of ^{210}Pb and its daughters. These data include ^{206}Pb-on-Ge recoils, for which a significant disagreement between the simulated and measured spectra is evident near the expected 103 keV endpoint energy [193]. This discrepancy

is considered to be evidence of the formation of Frenkel defects. From analysis of this disagreement, the Ge displacement threshold value can be determined.

9.1. Simulation of ^{206}Pb Recoils

The Geant4-based simulation package Supersim was used to model the SuperCDMS Soudan experiment. In simulation, the full experiment was created with detectors, shielding, and the silicon source wafers.

The source wafers have a layer of amorphous silicon dioxide from exposure to air. The SiO_2 layer thickness was calculated based on the time of exposure of the source wafers to air after the last etching. The exposure time was estimated to be 60 ± 19.7 hours, yielding 1.6 ± 0.1 nm of SiO_2 growth.

In simulation, the source wafers were implanted with ^{210}Pb using a trapezoidal PDF as illustrated in Fig. 9.1. The reduced counts in the first few bins reflects the lower density of ^{210}Pb in SiO_2 versus the bulk due to the lower density of SiO_2 when compared to pure Si ($2.2\,g/cm^3$ and $2.33\,g/cm^3$ respectively).

One million ^{210}Pb decays were simulated, allowing Geant4 to handle the full decay chain to ^{206}Pb. The available screened nuclear recoil physics list was invoked to more accurately simulate the nuclear recoil events in the detector. Energy loss to defect formation was not, however, part of the simulation.

At the end of simulation, all the data was stored in ROOT [144] output, including the following information on each simulated decay: the particle type, the parent particle type, and the time of the decay. All recorded times are relative to the beginning of the simulation. Because the time units are in nanoseconds, it is imperative that a double (or long double) variable be used to track and handle these times[1].

The decay information enables the selection of particular decay types. For example, it is possible to select excited ^{210}Bi decays (i.e. ^{210}Bi internal conversion, Fig. 9.2) by selecting

[1] All variables in this simulation are G4double types. The standard text output of Supersim was boosted to 17 decimal digits to accommodate this.

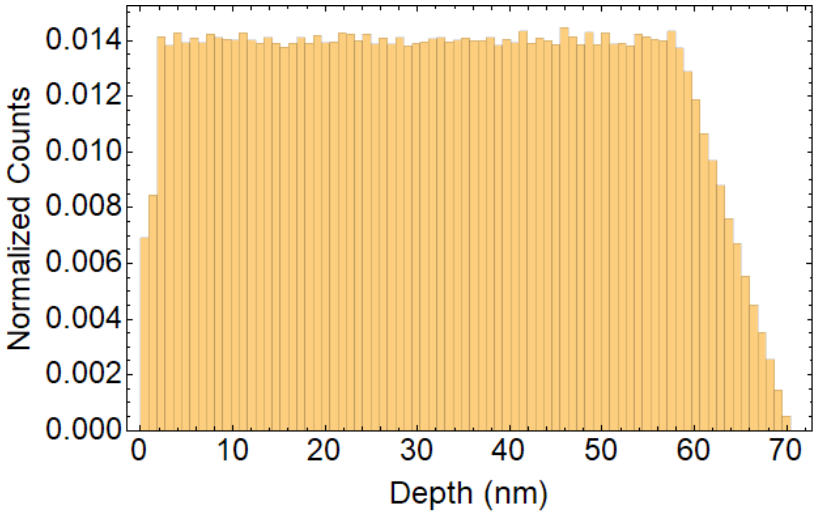

Figure 9.1. The implantation profile for ^{210}Pb atoms in the silicon source wafers.

events where both the parent *and* the particle type are the same. It is then possible to sum by event the energy deposited in the detectors (`Edep`) over all steps that occur within 1 μs of this decay time. As shown in Fig. 9.3, it is possible to select and extract a specific decay type and associated event energy.

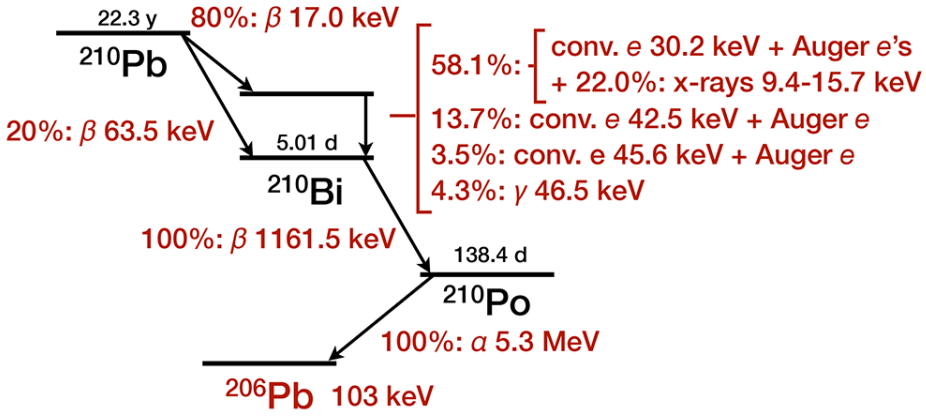

Figure 9.2. Decay chain for ^{210}Pb showing the most significant decays which end in a ^{206}Pb nucleus from the ^{210}Po alpha decay. Adapted from Ref. [141].

Similar to the example of ^{210}Bi internal conversion, ^{206}Pb recoil events were selected by looking at a 1 μs window around ^{210}Po decays. While it is possible to select only the

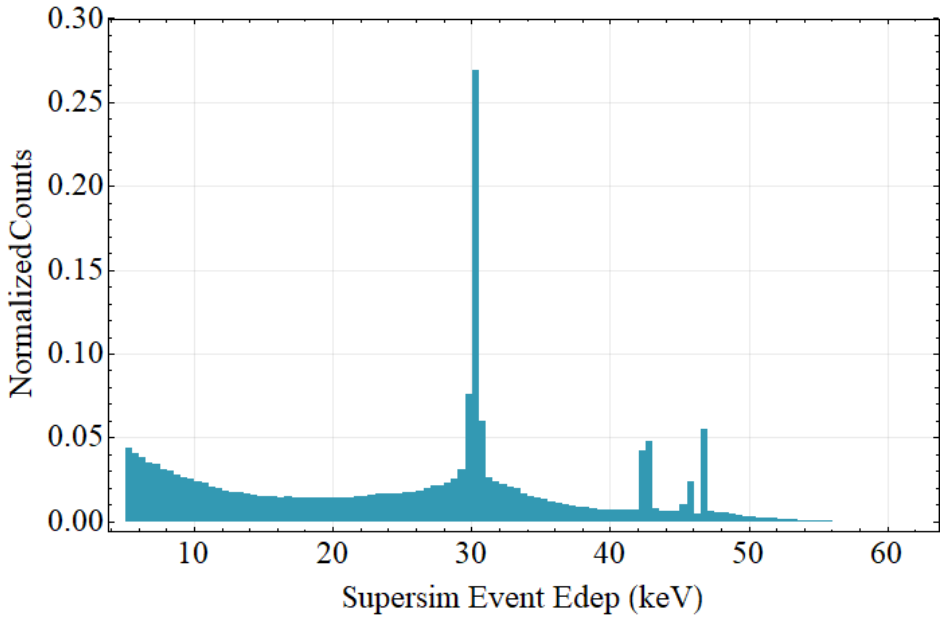

Figure 9.3. The internal conversion of excited ^{210}Bi involves the emission of an Auger electron or a ∼46 keV gamma. Shown here are events from one million ^{210}Pb primaries simulated in the SuperCDMS Soudan experiment which include these betas and gammas. This is the predicted energy deposited without accounting for detector resolution.

energy deposited by particles whose parent is a ^{210}Po atom, this would exclude any further created PKAs and their own deposited energy. These PKAs do not hold any decay ancestry information so the total event energy reconstruction would be incomplete.

In the ^{210}Po decay events, the ^{206}Pb nucleus recoils isotropically. The ^{206}Pb nucleus and alpha particle from the ^{210}Po decay recoil in opposite directions. There is the possibility that any energy deposited in the timing window may or may not involve an actual ^{206}Pb recoil in the detector. For example, the ^{206}Pb nucleus may go further into the silicon source plate, and an alpha particle recoiling in the opposite direction may hit the detector instead as shown in Fig. 9.4. It is also possible that a ^{206}Pb nucleus recoils on a silicon atom, transferring enough energy such that the silicon atom itself hits the detector (i.e. sputtering). The separation of these types of events and the final chosen spectrum for data comparison is shown in Fig. 9.5.

9.2. SuperCDMS Soudan Data Selection

To create the ^{210}Pb sources, two silicon wafers were exposed to a 5 kBq ^{226}Ra source which produces ^{222}Rn gas inside a sealed aluminum box for 12 days (see Section 5.2 for details of the entire decay chain). After the exposure, the wafers were surface etched to remove any dust, and subsequently a 1.6 nm oxide layer grew on the surface due to exposure to atmospheric oxygen. This process resulted in near-uniform implantation of ^{210}Pb, a long-lived daughter of ^{222}Rn, to a depth of approximately 58 nm.

The data used in this analysis is taken from the periods of March 2012–July 2013 and July 2013–July 2014. The ^{210}Pb source wafers were installed above and below the T3Z1 and T3Z3 detectors for the duration of the data-taking periods. This gave a continuous exposure from ^{210}Pb and its progeny on a single side of each of the aforementioned detectors.

9.2.1. Data Types, Cuts, and Variables

The charge and phonon output was converted from an analog to a digital signal, and eventually stored as RQs and RRQs as described in Section 3.2. To aid in analysis, there are a variety of cuts made available to analyzers that select certain events based on predefined

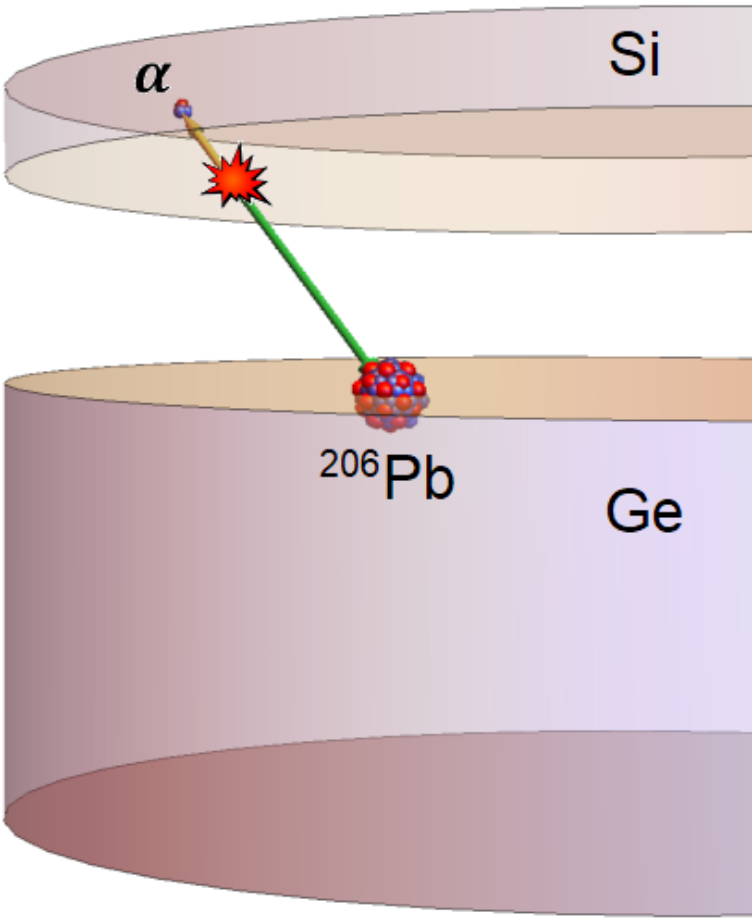

Figure 9.4. This figure shows a representation the experimental setup which is not to scale. The silicon wafer is mounted above a germanium iZIP detector in this case. The alpha decay of the ^{210}Po nucleus produces a 103 keV ^{206}Pb ion that has a chance of being observed by the iZIP detector.

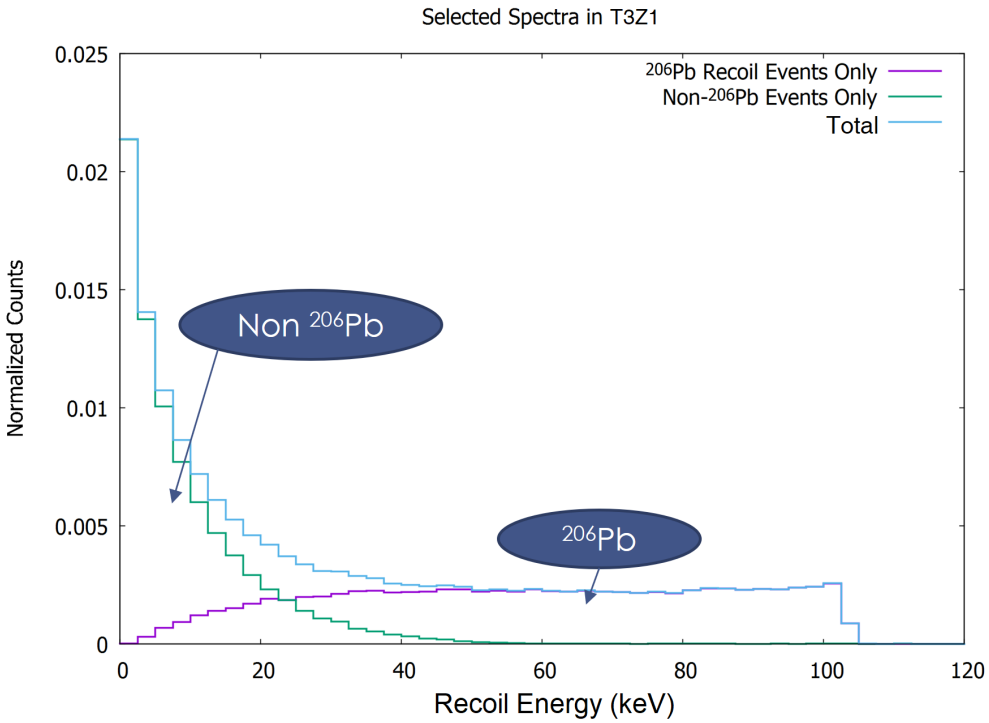

Figure 9.5. Supersim event `Edep` for events selected from a 1 μs window around ^{210}Po decays. The light blue line indicates the overall spectrum while the purple and green lines indicate events where ^{206}Pb did or did not interact with the detector directly. The 103 keV end-point of the ^{206}Pb recoil energy is clearly visible. Detector resolution effects have not been applied to this spectrum.

criteria. The cuts and RRQs used in this analysis are described in Table 9.1 and their usage is described below in detail. Further details on data, cuts, and their usage is available in Appendix A.

Table 9.1. Description of all RRQs and cuts related to this analysis.

RRQ	**Description**
`plukeqOF`	Estimate of Luke-Neganov phonons, using only the charge signal
`ptNF`	Phonon total pulse energy from non-stationary optimal filter
`precoiltNF`	The non-Luke-Neganov phonon energy (ptNF - plukeqOF)
`qsum#OF`	Charge energy sum of side # (1 or 2)
`qsummaxOF`	Sum for the side with the maximum qsum
`pgqOF`	The total phonon energy, using only charge information
`ygtNF`	Ionization yield (charge energy over phonon energy, i.e. pgqOF/ptNF)
Cuts	**Description**
`cGoodEv_v53`	Primary good-event selection
`cPostCf_133_HT`	Selects series up to 48 hours after a Cf neutron calibration (up to 72 hours for extended Cf calibrations in Feb and May of 2014)
`cRandom_133`	Selects randomly triggered events
`cQsym_v53`	Ionization-derived z-symmetry cut for selecting bulk events
`cLead_ptNF_qsummaxOF_v53_HT`	2-σ ^{206}Pb recoil band in the qsummaxOF vs. ptNF plane

9.2.2. Data Selection: ^{206}Pb Recoils

Along with a 5.3 MeV alpha particle, a 103 keV ^{206}Pb nuclei is formed from a ^{210}Po decay. Events were selected with 2 keV $\leq$ `precoiltNF` $\leq$ 120 keV to fully capture this range. From SRIM calculations, a 103 keV ^{206}Pb nucleus has a projected range in Ge of

26.7 nm (99.7% confidence limit) [168]. These recoils are therefore considered surface events, taking place well outside the fiducial volume that WIMP searches are otherwise performed. A comparison of the yield planes for detectors T2Z2 and T3Z1 is shown in Fig. 9.6.

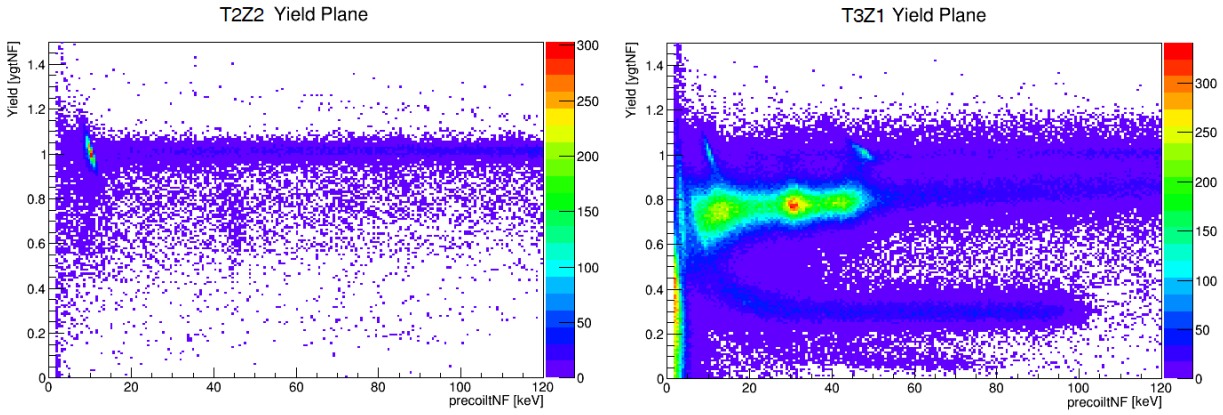

Figure 9.6. Yield planes for detectors T2Z2 and T3Z1 shown in the left and right panels respectively). Surface betas and Auger electrons from ^{210}Pb and excited ^{210}Bi are visible in the right panel in the 0.6–0.9 yield range. The ^{206}Pb recoils are visible as the band near 0.4 on the vertical axis. The 46 keV gamma line is also visible with a yield around 1. From comparison to T2Z2, we assume the ^{206}Pb events selected from T3Z1 and T3Z3 will be pure samples of ^{206}Pb recoils.

For T3Z1 and T3Z3, the surface events consisted primarily of ^{206}Pb recoils with a yield roughly in the 0.2 to 0.4 range. Betas from ^{210}Pb and Auger electrons from excited ^{210}Bi appear with yield in the 0.6 to 0.9 range. The ^{206}Pb events are selectable with the `cLead_ptNF_qsummaxOF_v53_HT` cut. However, the cut appears asymmetrical around the ^{206}Pb events, so an additional cut is used to tighten the selection closer to the recoil band (Equation 9.1).

$$\texttt{ygtNF} \leq a \cdot e^{-b \cdot \texttt{ptNF}} \tag{9.1}$$

$$a = 2.14757$$

$$b = 0.121937$$

This additional cut is illustrated in Fig. 9.7.

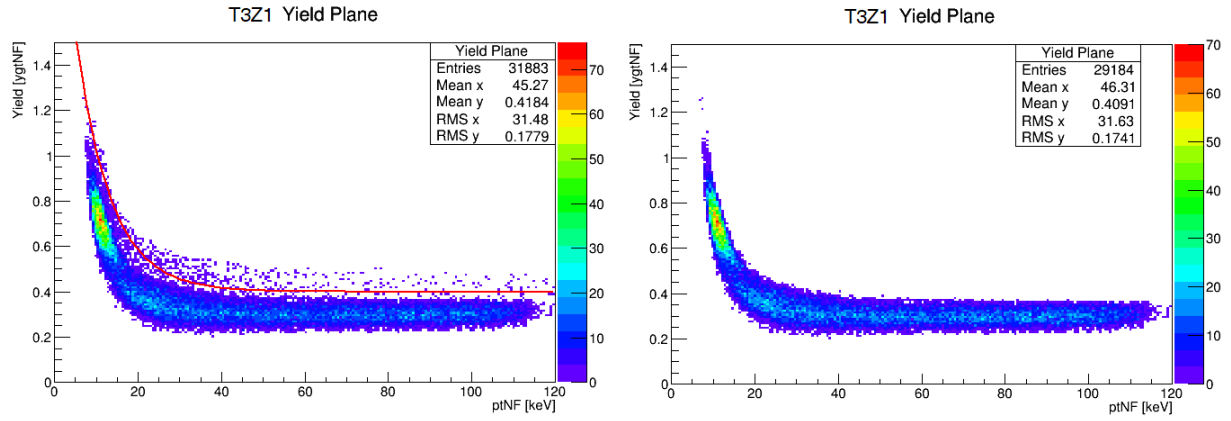

Figure 9.7. Left: The yield plane of T3Z1 after applying the `cLead_ptNF_qsummaxOF_v53_HT` cut. Red line indicates the functional values of Equation 9.1. Right: Same as left but after applying the cut in Equation 9.1.

Once these cuts were applied, further refinement for selection of surface events was required. While a symmetry cut was available (`cQsym_v53`), the inverse of this cut was not tight enough for surface event selection. Additionally, it also allowed events from both surfaces, but this study was only interested in the side exposed to the ^{210}Pb source wafers. A cut was applied to select only events with $\texttt{qzpartOF} < 0.65$ for T3Z1 ($\texttt{qzpartOF} < -0.65$ for T3Z3) which removed all events from the opposite face as illustrated in Fig. 9.8. The resultant events which passed the cut were thus dominated by ^{206}Pb events as shown in Figs. 9.7 and 9.9. The final set of data is shown in Fig. 9.10.

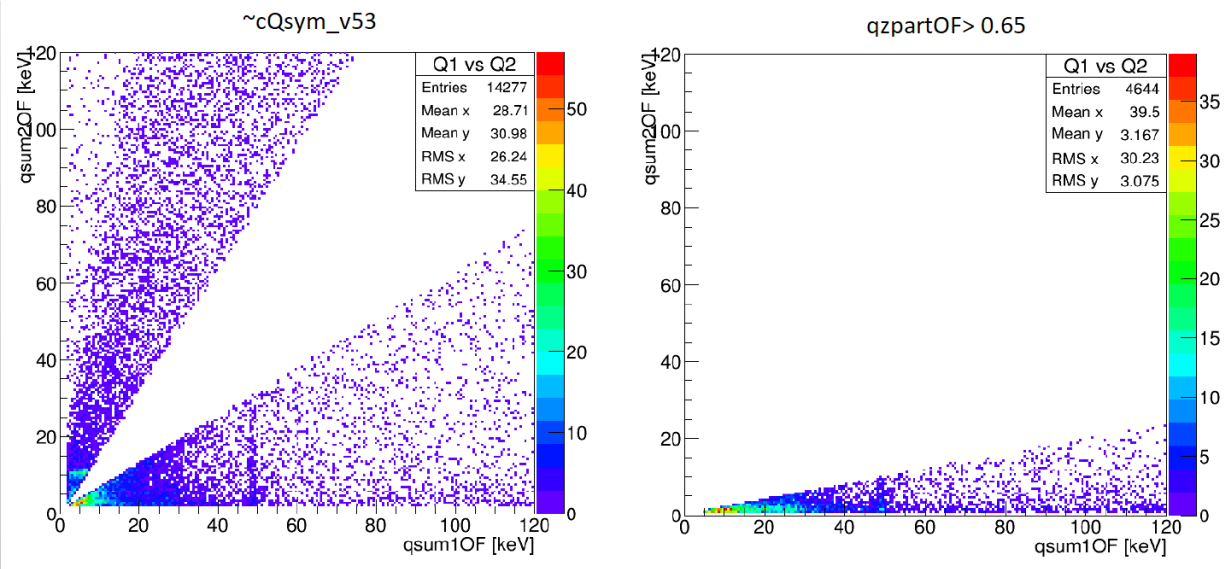

Figure 9.8. Left: The charge symmetry plane of T3Z1, showing the inverse of the `cQsym_v53` cut which leaves events from both sides of the detector. Right: Using events with `qzpartOF` $<$ 0.65 cuts all events from the opposite side of the detector, and yields a tighter cut for surface events.

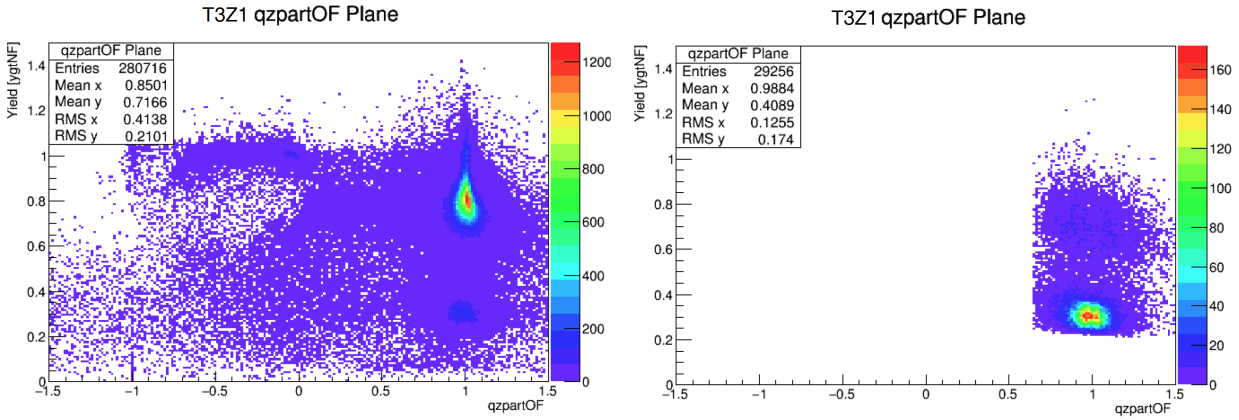

Figure 9.9. The RRQ `qzpartOF` is defined as the difference of charge collected on each face divided by the total charge. This variable allows some form of surface or bulk event discrimination. Left: The `qzpartOF` plane with ∼`cRandom_133`, ∼`cPostCf_133_HT` and `cGoodEv_v53` cuts applied. Energy was selected as 2 keV ≤ `precoiltNF` ≤ 120 keV. The surface betas visible in Fig. 9.7 (right panel) are visible as the high counts near `qzpartOF` ∼ 1. Right: The same cuts as the left panel but also with `cLead_ptNF_qsummaxOF_v53_HT` and `qzpartOF` ≥ 0.65. The dominant events are now the ^{206}Pb recoils.

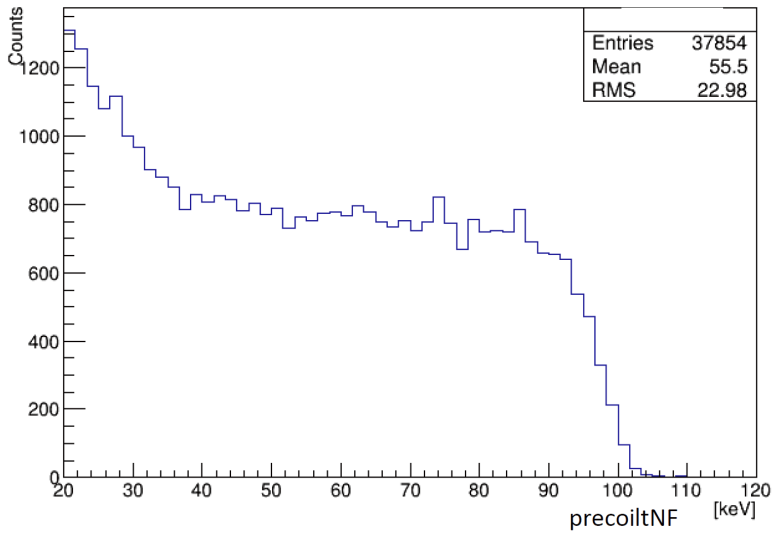

Figure 9.10. The final recoil spectrum of events selected for Frenkel defect analysis after all cuts have been applied.

9.2.3. Detector Resolution

The Geant4 simulations of the ^{206}Pb recoils record the exact energy deposition with perfect resolution. It was, therefore, necessary to smear the simulation to account for the detector resolution.

Two resolution studies have been previously performed [193]. Equations 9.2 and 9.3 describe the mathematical form of each resolution function, and give the associated parameters. In Equation 9.2, the parameters are specific to each detector and to specific RRQs with i indicating where this resolution function applies to phonon (`ptNF`) or charge (`qsummaxOF`) resolution. The parameters in Equation 9.2 are given in Table 9.3. In Equation 9.3, the same parameters are used for both detectors and can be applied to the event recoil energy.

$$\Delta E_{Jardin,i}(E) = \sqrt{a_i + b_i E + c_i E^2} \tag{9.2}$$

$$\Delta E_{Redl}(E) = \sqrt{a^2 + (bE)^2} \qquad a = 0.303881, b = 0.017114 \tag{9.3}$$

Table 9.3. Parameters for Equation 9.2. The parameters are specific to each detector and RRQ.

	RRQ	a	b	c
T3Z1	`ptNF`	0.327138	-0.0137804	0.000520678
	`qsummaxOF`	0.0922709	0.000696472	0.00014649
T3Z3	`ptNF`	0.132230	5.55112×10^{-12}	0.000572963
	`qsummaxOF`	0.0863211	0.0137235	0.00011678

The parameters in Equations 9.2 and 9.3 were derived from bulk events. For this analysis, another resolution study was conducted in the manner of these previous studies but focusing specifically on surface events. This created a third resolution function, derived from *surface* events, with which to smear the simulated data.

As T3Z1 and T3Z3 were immediately adjacent the ^{210}Pb source wafers, the 46 keV gamma line had sufficient statistics for performing a resolution check. Similarly, a gamma line at 66.7 keV from Cf calibration runs with lower statistics could also be used. Events were selected with `qzpartOF` ≥ 0.65 for T3Z1 (`qzpartOF` ≤ -0.65 for T3Z3), similar to the ^{206}Pb data. A cut was made on the ionization yield to select only gamma events (yield ≥ 0.9), and Gaussian functions were fitted to the resultant spectra. A 1σ standard deviation was extracted from the fit. In the energy region of interest for this study, both previous resolution functions exhibited nearly linear behavior, motivating the choice of a linear fit to the data given by Equation 9.4 and illustrated in Fig. 9.11.

$$\boxed{\begin{array}{l}\Delta E_{Stein}(E) = a + bE \\ a = 0.631269, b = 0.024073\end{array}} \tag{9.4}$$

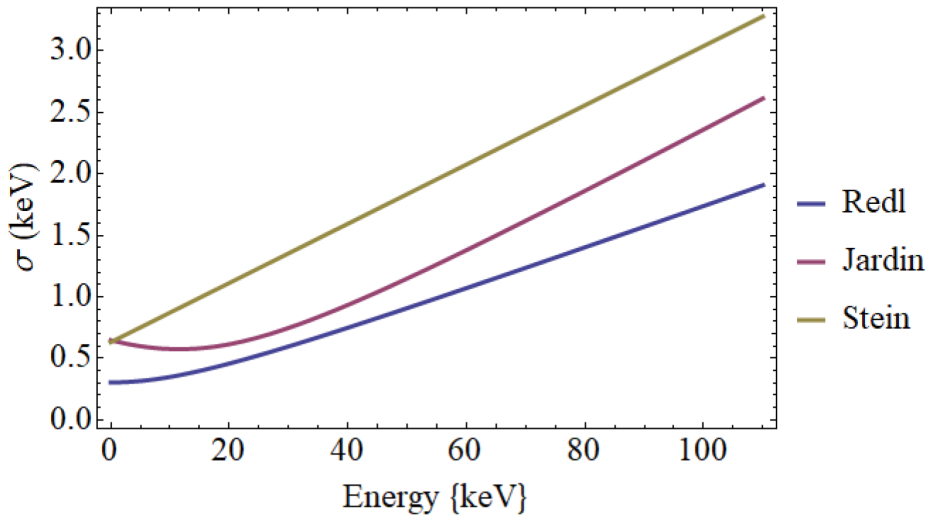

Figure 9.11. A comparison of each energy resolution function (Equations 9.2, 9.3 and 9.4) over the energy region of interest. Each function yields a 1σ value at the indicated energy on the horizontal axis.

9.2.3.1. Resolution Function Application

With Equation 9.4 defined, all ^{206}Pb recoil events were smeared via a Gaussian distribution with the mean at `precoiltNF` and a standard deviation of ΔE_{Stein}(`precoiltNF`). This was intended to give an initial estimate of the expected detector resolution. To account for any possible difference in resolution between gamma and ^{206}Pb events, the smearing strength was allowed to float as described in Section 9.3. The total smearing strength was defined as

$$\Delta E_{total}(E) = P_s \Delta E_{Stein}(E)$$

where P_s was the smearing strength parameter. As demonstrated in Section 9.4.1, a fit to a full Monte Carlo simulation of the 46 keV gamma line to data yielded a factor very close to 1, indicating that Equation 9.4 was indeed a good estimate for overall detector resolution.

9.3. Analysis

9.3.1. Fitting Parameters

There were two parameters taken into account for the analysis: an energy scale parameter f, and a smearing strength parameter P_s. The energy scale parameter was the fraction of energy taken away from each simulation event energy (E_{sim}), leaving a scaled energy value

$$E_{scaled} = E_{sim}\,(1 - f) \tag{9.5}$$

After this was applied, all energies were smeared by a Gaussian distribution whose standard deviation was given by Equation 9.4 times the smearing strength parameter P_s. What remained was a population of smeared and scaled events that was used to compare to the data.

9.3.2. Energy Range and Setup

All analysis of the ^{206}Pb recoil events took place between 80 and 110 keV. This energy region highlights where the mismatch between the data and the simulation was most promi-

nent, especially as the ^{206}Pb recoil event spectrum was flat from ∼40–80 keV. Below 40 keV, ^{206}Pb recoil events became less dominant as illustrated in Fig. 9.5, and separation of event types by yield became increasingly difficult.

Before a fit was performed, the number of bins was chosen according to the Freedman-Diaconis rule [194]

$$Bin_{width} = \frac{2IQR(data)}{N^{1/3}}$$
$$Num_{bins} = \frac{Max(data) - Min(data)}{Bin_{width}}$$

where *data* is a list of event energies, *IQR* is the interquartile range, and N is the number of events in *data*. The number of bins was found for both the data and simulated events, and a mean (40) between the two was used for the analysis. Analyses were also performed with the number of bins varying from 20 to 60, exhibiting a maximum change of fitted parameters on the order of 1%, showing that the fit did not depend strongly on the number of bins.

9.4. The Fit

The energy scale and smearing strength parameters were allowed to float, and a least-squares fit was performed to find the best values. The fit took two unique data sets of recoil energies

$$A = \{E_1, E_2, \ldots E_N\}$$
$$B = \{\tilde{E}_1, \tilde{E}_2, \ldots \tilde{E}_M\}$$

where each data set was size N and M, respectively. Each set was binned by energy into q bins ($q = 40$ in this analysis, as described in Section 9.3.2)

$$Bins_A = \{a_1, a_2, \ldots a_q\}$$
$$Bins_B = \{b_1, b_2, \ldots b_q\}$$

where a_i and b_i was the number of events in that bin. The χ^2 value was determined by summing the residuals across all bins

$$\chi^2 = \sum_{i=1}^{q} \frac{\left(\frac{a_i}{N} - \frac{b_i}{M}\right)^2}{\frac{a_i}{N^2} + \frac{b_i}{M^2}}$$

Approximately one million sets B for each detector were generated, corresponding to different smearing strength (P_s) and energy scaling (f) parameters. Each set had its own χ^2 value, creating a well-defined parameter space from which a minimum χ^2 was found, yielding the best-fit parameters.

The parameter space for both detectors is illustrated in Fig. 9.12. The determined value for energy loss was 5.52 ± 0.10 % for T3Z1, and 6.67 ± 0.11 % for T3Z3. The uncertainty is calculated by projecting a $\Delta\chi^2 = 1$ contour to the axes. The best fit values as applied to simulation are depicted in Figs. 9.13 and 9.14. The determined values from this fit include not only effects from Frenkel defects, but also that of any intrinsic systematic error from the detectors. This intrinsic scaling, and ways to account for it, is discussed in Section 9.4.1.

9.4.1. Intrinsic Scaling

The probability of creating a Frenkel defect depends in part on the mass of the incident particle, with heavier particles having higher probability. Interactions of gammas and betas should create so few defects that any scaling effect would be immeasurable at the precision of this study. As such, performing the same 2-parameter fit should reveal a preferred scale factor of zero if the detector were performing perfectly. However, some systematic error is expected from the fact that surface events are being fit, whereas the pulse template used to determine the recoil energy was based on events occurring in the bulk of the detector (see Appendix A for details on pulse templates and their usage).

A small but noticeable difference was visible when comparing the average pulse shape for surface events to bulk events. The pulse template is illustrated in Fig. 9.15. There was also a slight difference between bulk gammas and the fit template. This is due in part to the event

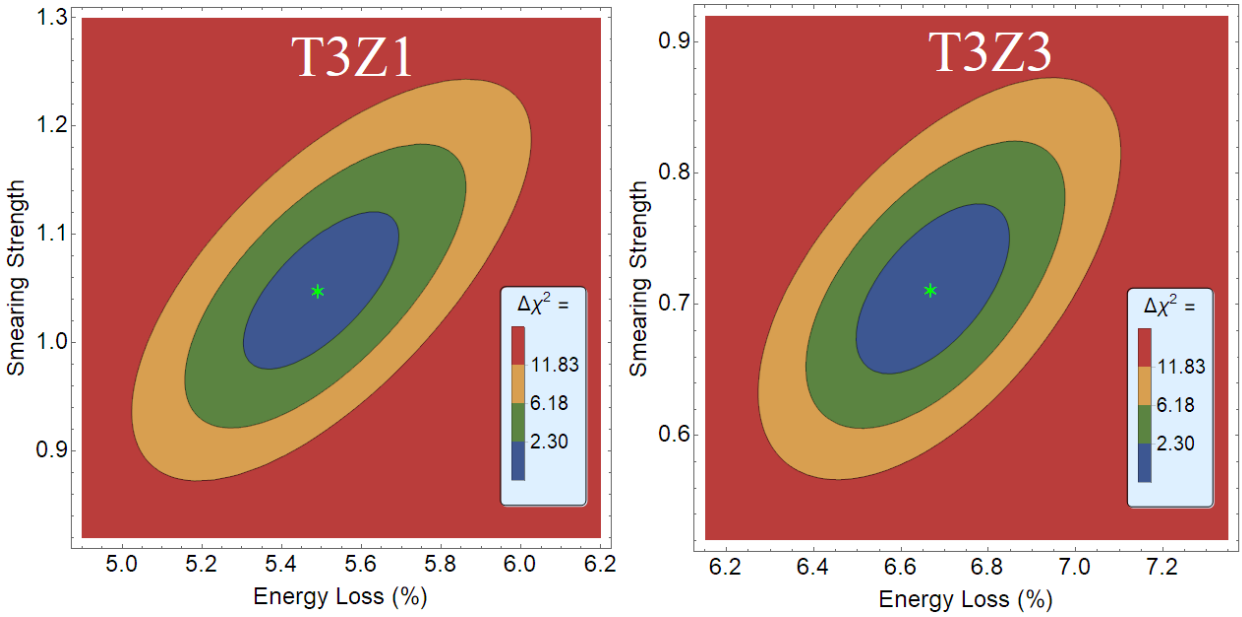

Figure 9.12. Parameter space of energy scale (f) and smearing strength parameters (P_s) for T3Z1 (left) and T3Z3 (right). The best fit values are indicated by a green star. The bands highlighted correspond to the 1-, 2-, and 3-σ confidence intervals.

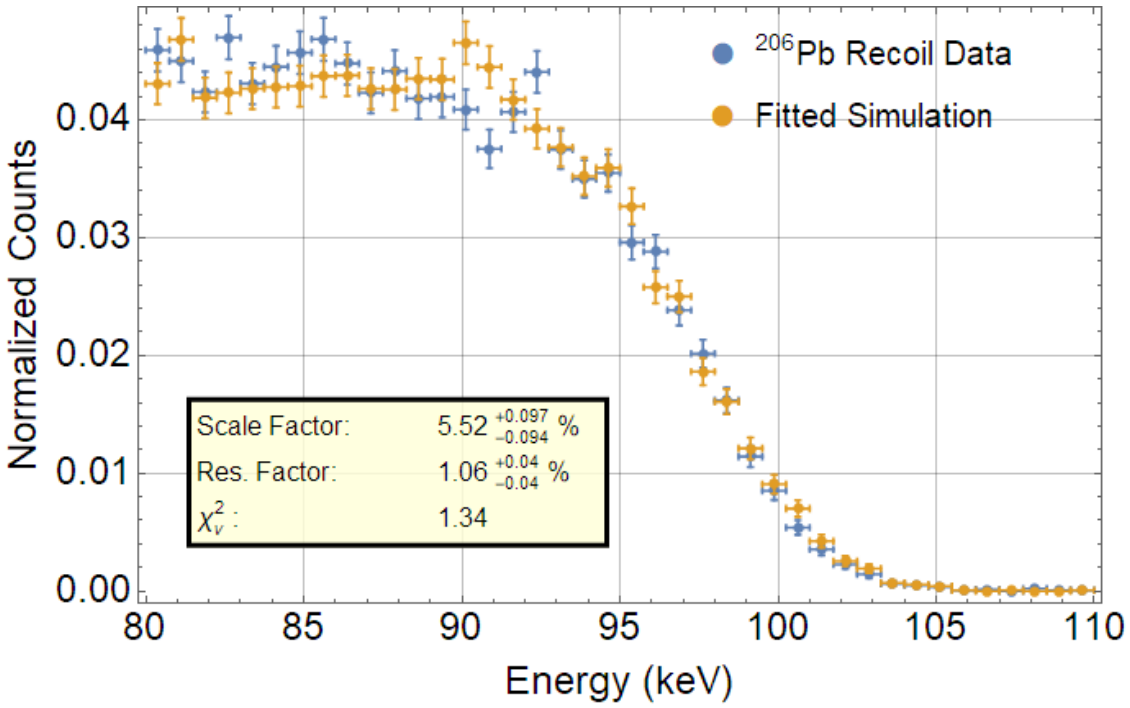

Figure 9.13. The best fit values applied to simulation for T3Z1, and compared to data. The uncertainty on the parameters comes from projecting a $\Delta\chi^2 = 1$ contour to the axes.

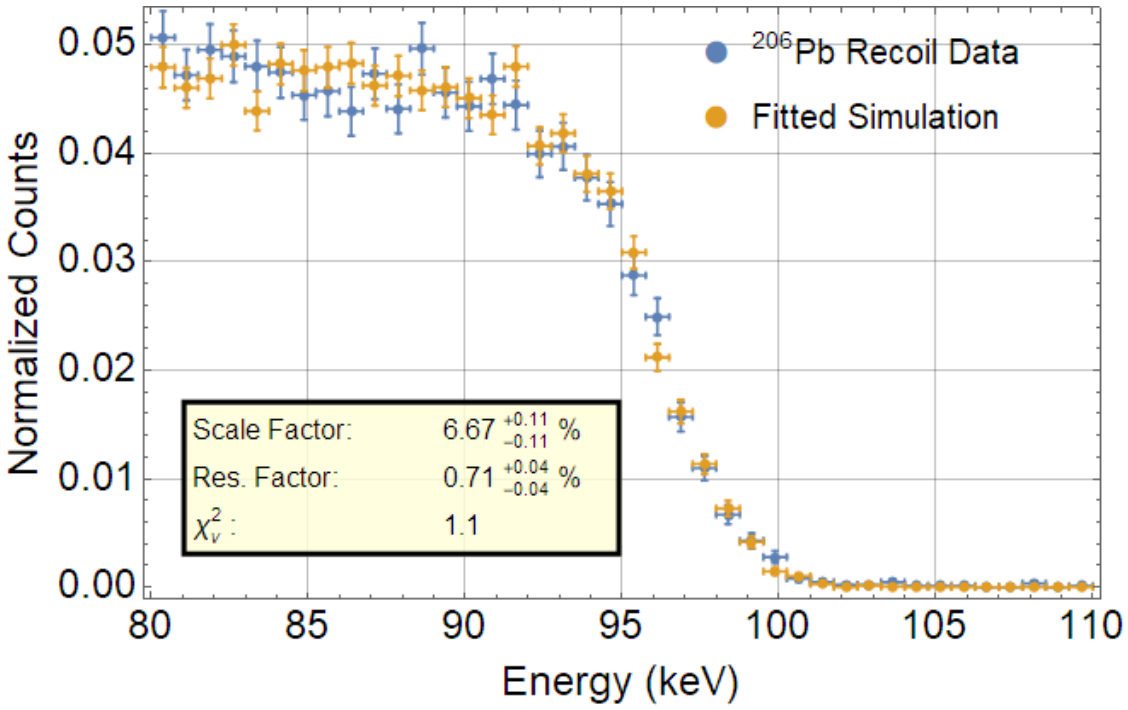

Figure 9.14. The best fit values applied to simulation for T3Z3, and compared to data. The uncertainty on the parameters comes from projecting a $\Delta\chi^2 = 1$ contour to the axes.

selection which includes factors such as the tightness of the cuts and the selected energy range. To account for this effect, the same parameters are determined for surface gammas and betas as was done with the ^{206}Pb recoils. The results are summarized in Table 9.4, and an example fit can be seen in Fig. 9.16.

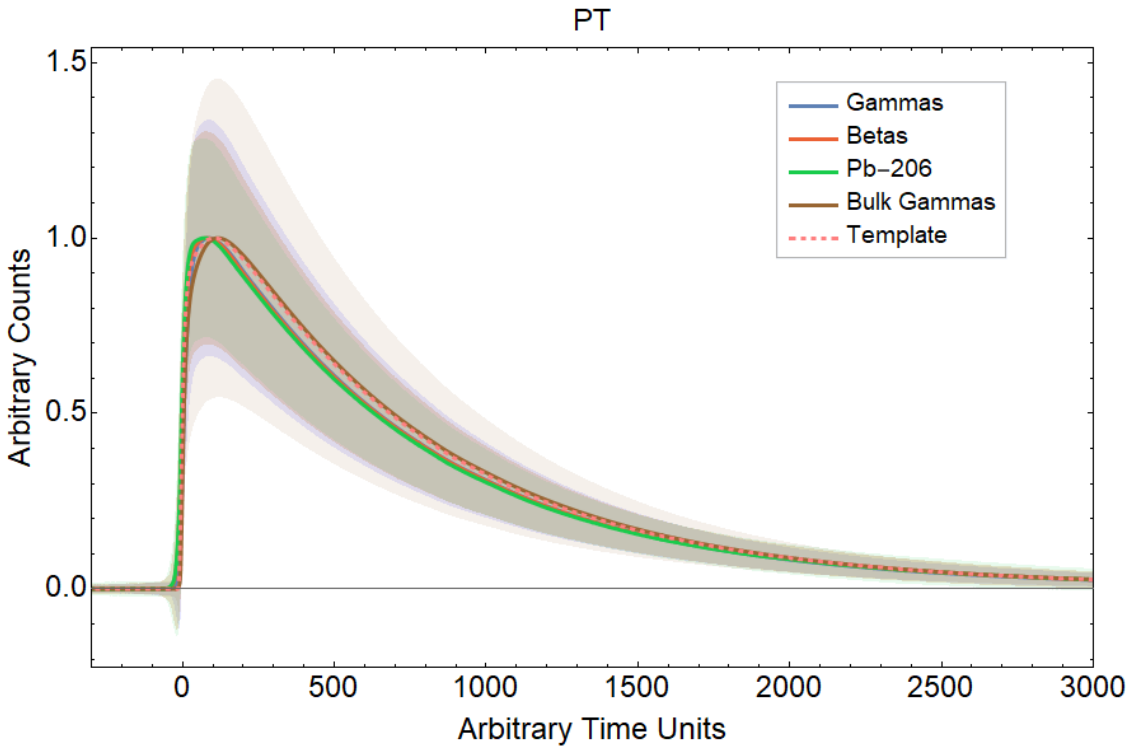

Figure 9.15. The average phonon pulse shape of various types of surface events compared to bulk gammas and the fitting template. Differences between the fitting template and the bulk gamma events arise partially from event selection and can include factors such as the tightness of cuts and the energy range. The shaded bands represent the standard deviation of pulse shape at any given time step.

9.4.2. Determining Energy Loss to Frenkel Defects

The measured event energies are based on the detectors' default energy calibrations, which are developed using gamma rays that interact in the bulk of the crystal. The energy scale for surface events may be slightly different. Consequently, the measured ^{206}Pb recoil energies may differ from their simulated counterparts by an additional energy scaling factor

Table 9.4. The energy scale factor determined by examining gamma and beta events in T3Z1 and T3Z3. A weighted mean is determined for each detector.

Detector	Fit	f
T3Z1	γ	-0.74 ± 0.07
	β	-0.75 ± 0.11
	Mean_w	-0.75 ± 0.06
T3Z3	γ	0.84 ± 0.09
	β	0.87 ± 0.17
	Mean_w	0.85 ± 0.08

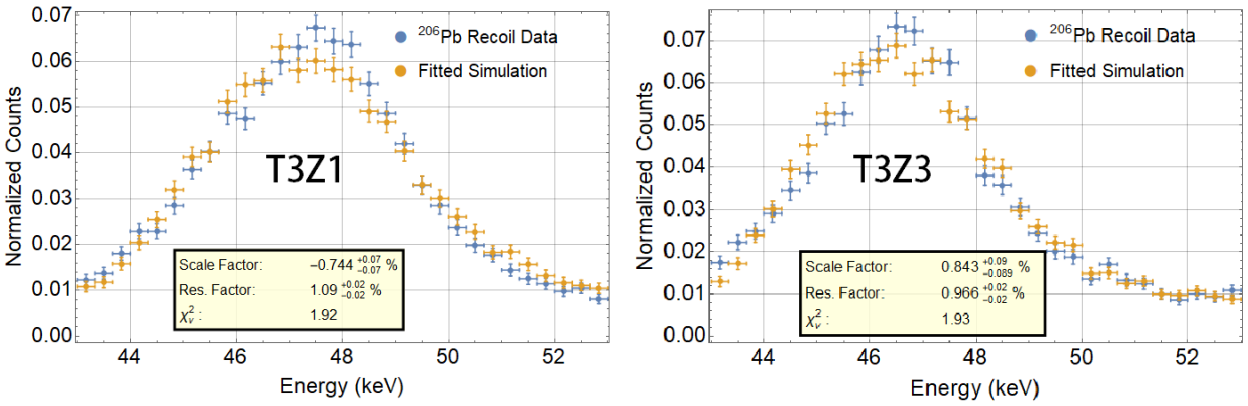

Figure 9.16. Fitted simulation events for T3Z3 for gammas (left) and betas (right). The best fit values from the two-parameter fit are shown as an inset.

that represents an intrinsic miscalibration and, therefore, has nothing to do with defect formation. If present, a best-fit determination of the scaling factor f in Equation 9.5 would account for both this intrinsic miscalibration and energy loss due to defect formation

$$(1 - f) = (1 - f_{FD})\,(1 - f_{int}) \tag{9.6}$$

where f_{FD} is the energy scale factor from Frenkel defects, and f_{int} is the intrinsic energy scale factor. Because Frenkel defect energy losses depend on the mass of the incident particle, gamma and beta events were assumed to have $f_{FD}{\sim}0$ at the precision of this study. This allowed for the determination of any intrinsic energy scale through the separate examination of these events, where f in Equation 9.5 would be equal to f_{int}.

$$\begin{aligned}(1 - f) &= (1 - 0)\,(1 - f_{int}) \\ (1 - f) &= (1 - f_{int}) \\ f &= f_{int}\end{aligned}$$

Having thus determined f from ^{206}Pb events, and f_{int} from surface gamma and beta events, the Frenkel defect energy scale factor was solved for by rearranging Equation 9.6 as

$$f_{FD} = 1 - \frac{(1 - f)}{(1 - f_{int})} \tag{9.7}$$

The best fit parameter for energy loss due to Frenkel defects in Ge was determined to be $6.08^{+0.13}_{-0.13}(\text{stat})^{+0.04}_{-0.03}(\text{syst})\,\%$. This value is a weighted mean from each detector: $5.52 \pm 0.10\,\%$ for T3Z1, and 6.67 ± 0.11 % for T3Z3. The uncertainty is a weighted sample variance.

9.4.3. Uncertainty Propagation

The confidence interval quoted on the energy loss percentage came from errors propagated through several steps. As with the ^{206}Pb fits, the energy scale parameters from fitting gamma and beta events had uncertainty determined by projecting a $\Delta\chi^2 = 1$ contour to the axes.

The intrinsic scale factor f_{int} was a weighted mean between gamma and beta events with results given in Table 9.4. This was used with the scale factor f determined from ^{206}Pb recoil events in Equation 9.7. The uncertainty of f_{FD} was determined by the following error propagation formula

$$\sigma_{f_{FD}} = \sqrt{\left(\frac{\partial f_{FD}}{\partial f}\sigma f\right)^2 + \left(\frac{\partial f_{FD}}{\partial f_{int}}\sigma f_{int}\right)^2}$$

where f_{FD} was replaced by Equation 9.7. With f_{FD} and the uncertainty determined for each detector, a weighted mean was taken as the final value of $6.08 \pm 0.13\,\%$.

This uncertainty is only the *statistical* uncertainty. There is an additional systematic uncertainty of $^{+0.04}_{-0.03}\,\%$ from the native silicon dioxide on the surface of the source plate which we estimate to be 1.6 ± 0.1 nm as described in Section 9.1. The best fit energy loss is then quoted as $6.08^{+0.13}_{-0.13}(\text{stat})^{+0.04}_{-0.03}(\text{syst})\,\%$.

9.5. Applications to Modeling & Simulations

The determined value of energy loss to defects for ^{206}Pb recoil events was incorporated into the Geant4 simulation studies for both the SuperCDMS Soudan and SNOLAB experiments. Coupled with a realistic adjustment for detector resolution, this yielded a spectrum for the ^{206}Pb recoil events that matches the data closer than that previously seen in Ref. [141].

Additionally, the limit setting software used to project the SuperCDMS SNOLAB sensitivities was updated with a new ^{206}Pb recoil spectrum which can be seen in Fig. 9.17. While this change more accurately reflects the ^{206}Pb recoil events, the new ^{206}Pb recoil spectrum had a negligible effect on the HV detectors and a small ($\sim$10%) effect on the iZIP detectors as illustrated in Fig. 9.18.

9.6. Determination of Ge Displacement Threshold Energy

With the determined value for Frenkel defect energy loss, it was possible to extract the germanium displacement threshold energy. This value is the average displacement threshold

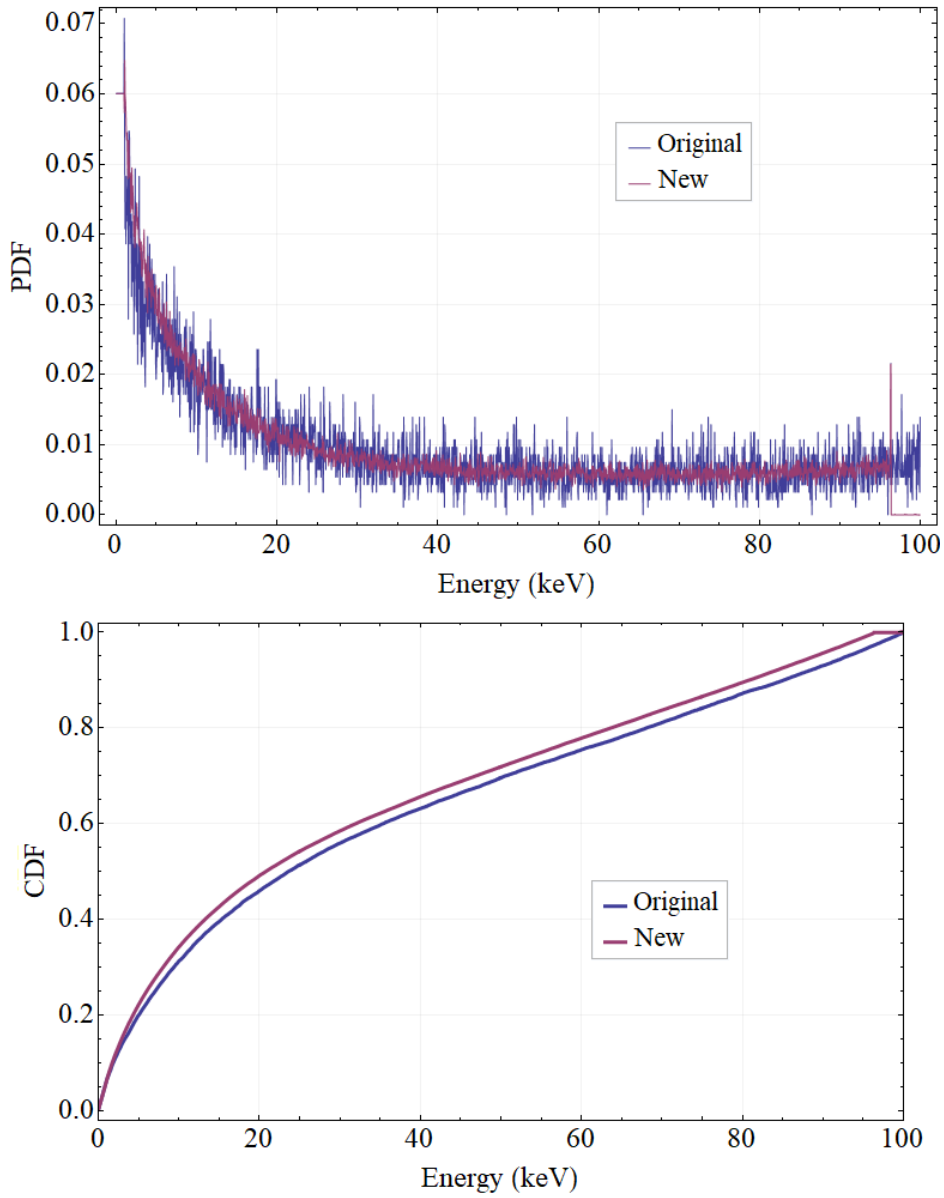

Figure 9.17. The ^{206}Pb recoil probability density function (top) and cumulative density function (bottom) to be used in simulation compared to the current versions used in the limit setting code. No detector resolution effects are taken into account at this level.

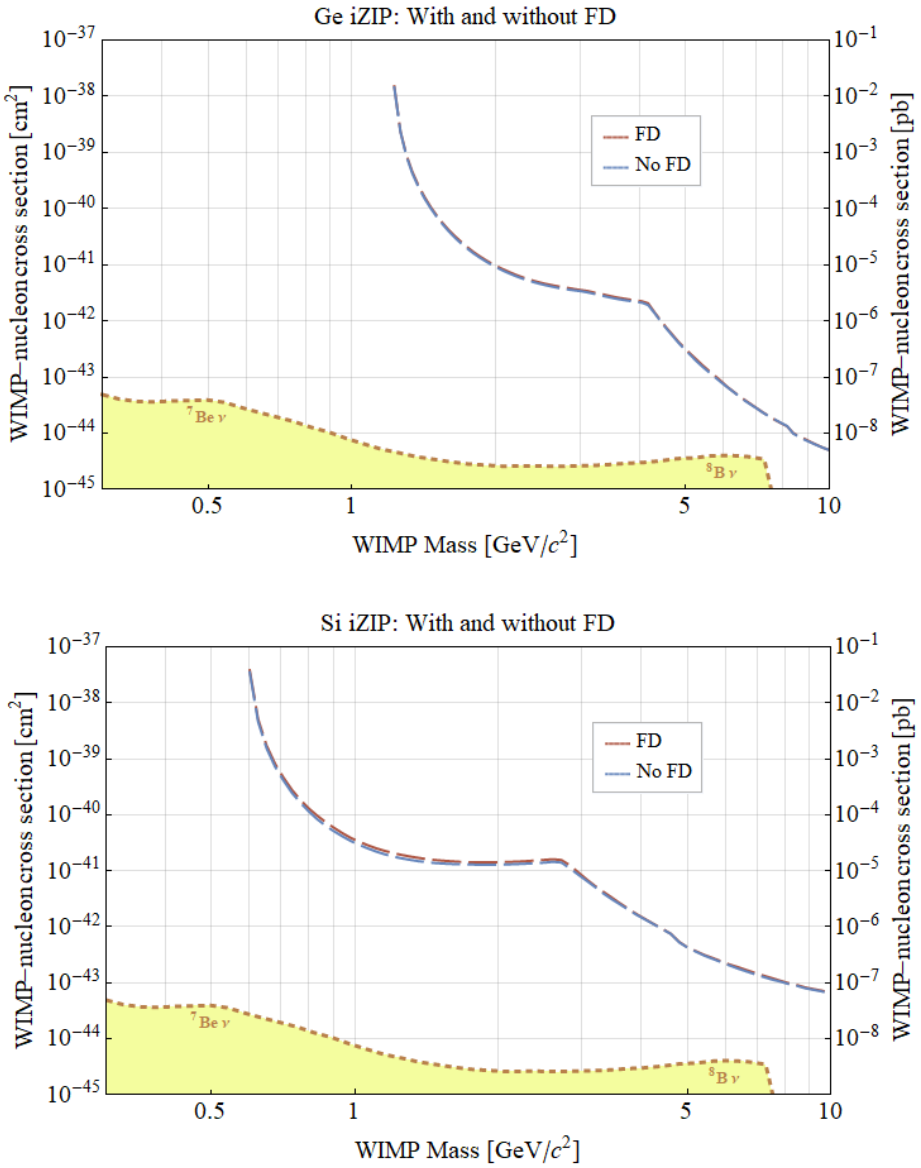

Figure 9.18. Projected sensitivities of iZIP detectors show a maximum change of ∼10% by the inclusion of Frenkel defects in the ^{206}Pb recoil spectrum. Germanium detectors (top) are less affected than silicon detectors (bottom).

energy over all lattice angles [125] and is an important quantity for radiation detectors, dark matter searches, and other applications [130, 139, 195].

For interactions involving the same species of incident and target atoms, the Kinchin-Pease equation estimates the number of defects formed [196] with a later approximation applied by Norgett, Robinson and Torrens [197]. In the case of an incident ^{206}Pb recoil on Ge, displaced Ge atoms may be liberated with enough energy to form additional defects. Thus, there are two types of interactions involved in this analysis: Pb recoiling on Ge and liberated Ge recoiling on Ge. TRIM [168] simulations were used to accurately model the entire defect formation process for varying user-defined Ge displacement threshold energy values.

The TRIM simulations were performed by specifying the incident ion, energy, and angle which interacts with a specified material. In this analysis, the kinetic energies of ions striking the detectors were used as input. This was extracted from the GEANT4 simulation described in Section 9.1. The only events used were those with kinetic energies in which `Edep` fell into the energy region of interest (i.e. 80–110 keV). The incident ions were primarily ^{210}Pb but sputtered Si and O also interacted with the detectors. The TRIM simulations handled every species and incident energy accordingly. Finally, the incident angles were randomly and uniformly selected from a hemisphere in which all angles pointed *into* the detector.

The target material which simulated the detector was a solid mass of pure Ge with a thin layer of GeO_2 on top. As with Si, pure Ge reacts with oxygen in the atmosphere to create GeO_2 with a thickness that logarithmically depends on exposure time [198, 199]. The estimated GeO_2 layer thickness was 0.98 ± 0.02 nm. The Ge displacement threshold value was varied for each simulation from 15 to 23 eV.

TRIM predicts a monotonic, decreasing relationship between the percent energy lost to defects and the Ge displacement threshold value. The determined energy loss value of $6.08^{+0.13}_{-0.13}(\text{stat})^{+0.04}_{-0.03}(\text{syst})\,\%$ corresponds to a displacement threshold energy of $19.7 \pm 0.5(\text{stat}) \pm 0.1(\text{syst})$ eV. The uncertainty in the GeO_2 layer thickness was negligible at this precision.

This showed a noticeable difference with some molecular dynamics simulations. The simulations result in values that range from 7 to 30 eV as summarized in Table 2.1 and illustrated in Fig. 2.4. The simulations often rely on the Stillinger-Weber (SW) potential [127], fitting as many as nine parameters to the energy function. Small changes in the parameters to fit one feature (such as melting point or defect formation enthalpy) yield large fluctuations in predictions of another feature [128] thus the disagreement over time.

9.7. Sensitivity of the SuperCDMS SNOLAB Experiment

For the SuperCDMS SNOLAB experiment, the Ge HV detectors have their projected analysis threshold set at roughly a factor of 2–3x higher than the minimum energy required for dislocating a Ge atom from its lattice site [68]. Given the historical uncertainty in this value, illustrated in Fig. 2.4 and Table 2.1, the current 40 eV threshold value seems prudent. However, with a more robust determination of the threshold from this work, it is possible to lower the threshold, especially as detector readout hardware continues to improve [200].

To capture all displacement events, the analysis threshold should be set no lower than the upper end of the minimum energy required to displace an atom. Molecular dynamics simulations show that the upper end of displacement threshold energies in the most difficult direction is approximately 60% higher than the average value over all directions [126]. As such, a conservative choice for the analysis threshold E_{th} in Ge is

$$\begin{aligned} E_{\text{th}} &= (E_{\text{avg}} + \sigma) \times 1.6 \\ &\approx 32 \text{ eV} \end{aligned}$$

where E_{avg} is the determined average displacement value of $19.7 \pm 0.5(\text{stat}) \pm 0.1(\text{syst})$ eV, and an error of one standard deviation is included. By lowering the Ge HV threshold to 32 eV, these detectors become competitive with Si HV detectors in terms of low-mass dark matter sensitivity. Ge will also have sensitivity to lower interaction cross-sections. This is visualized in Fig. 9.19 for various values of the Ge HV threshold.

The displacement threshold value is as high as 60 % more than the average displacement threshold in the most difficult direction. However, the *average* displacement threshold in the most difficult direction is ∼36 % higher than the average in every direction. Taking into account some additional uncertainty, a motivated choice for the threshold value is

$$E_{\mathrm{th}} = (E_{\mathrm{avg}} + 5\sigma) \times 1.32$$
$$\approx 30 \text{ eV}$$

where five standard deviations are included in the final value.

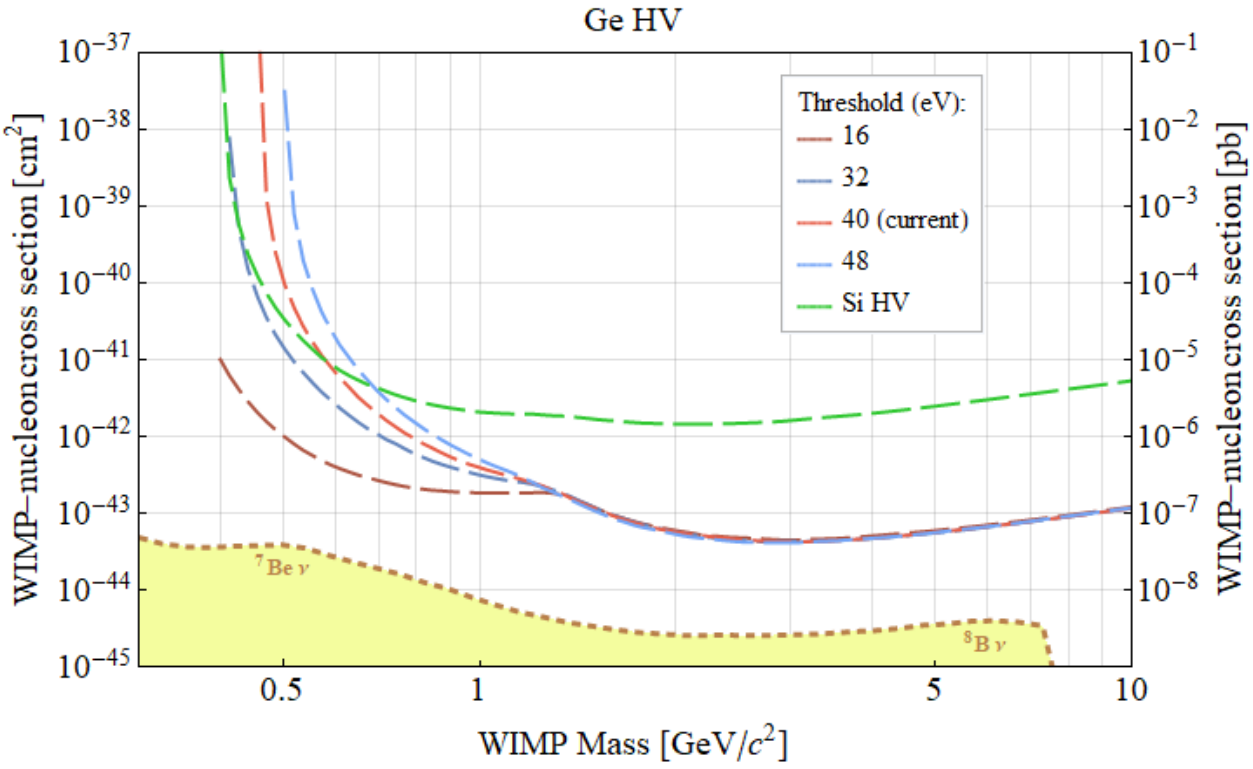

Figure 9.19. Projected sensitivity of SuperCDMS SNOLAB for various values used as the Ge HV threshold. The Si HV sensitivity is shown for comparison.

To better illustrate the potential gains from lowering the threshold, Fig. 9.20 shows recent and projected sensitivities from SuperCDMS and a variety of other experiments. Lowering

the threshold of the Ge HV detectors not only provides gains into low-mass sensitivity, but also makes the Ge HV detector the most effective detector type for searches for dark matter with masses $\lesssim 5$ GeV/c^2.

9.8. Other Applications

A full re-parameterization of the Stillinger-Weber potential could also be performed utilizing the determined displacement threshold value. This could be achieved by simulating defect formation over all lattice angles and fitting parameters such that the average defect formation energy matched this data. This parameterization would be very useful for a proposed directionally sensitive dark matter search [130]. This directional search predicts higher event rates for times when the WIMP wind flows in directions with lower defect formation energies as illustrated in Fig. 9.21. The event rate for such a search is given by

$$R(t) = \oint_{4\pi} \int_{E_{th}(\theta,\phi)}^{E_r^{max}} \frac{\partial^2 R}{\partial E_r \partial \Omega_r} \mathrm{d}E_r \mathrm{d}\Omega_r. \tag{9.8}$$

where $R(t)$ is the WIMP interaction rate over time per day, integrated over the angle-dependent threshold energy for a crystal rotating with the Earth.

Such a search relies on both a very low analysis threshold for event detection and a well parameterized Stillinger-Weber potential. This is necessary to understand where the peak event rates are expected over various angles, which comes from knowing the local maxima and minima of $E_{th}(\theta, \phi)$ in Equation 9.8.

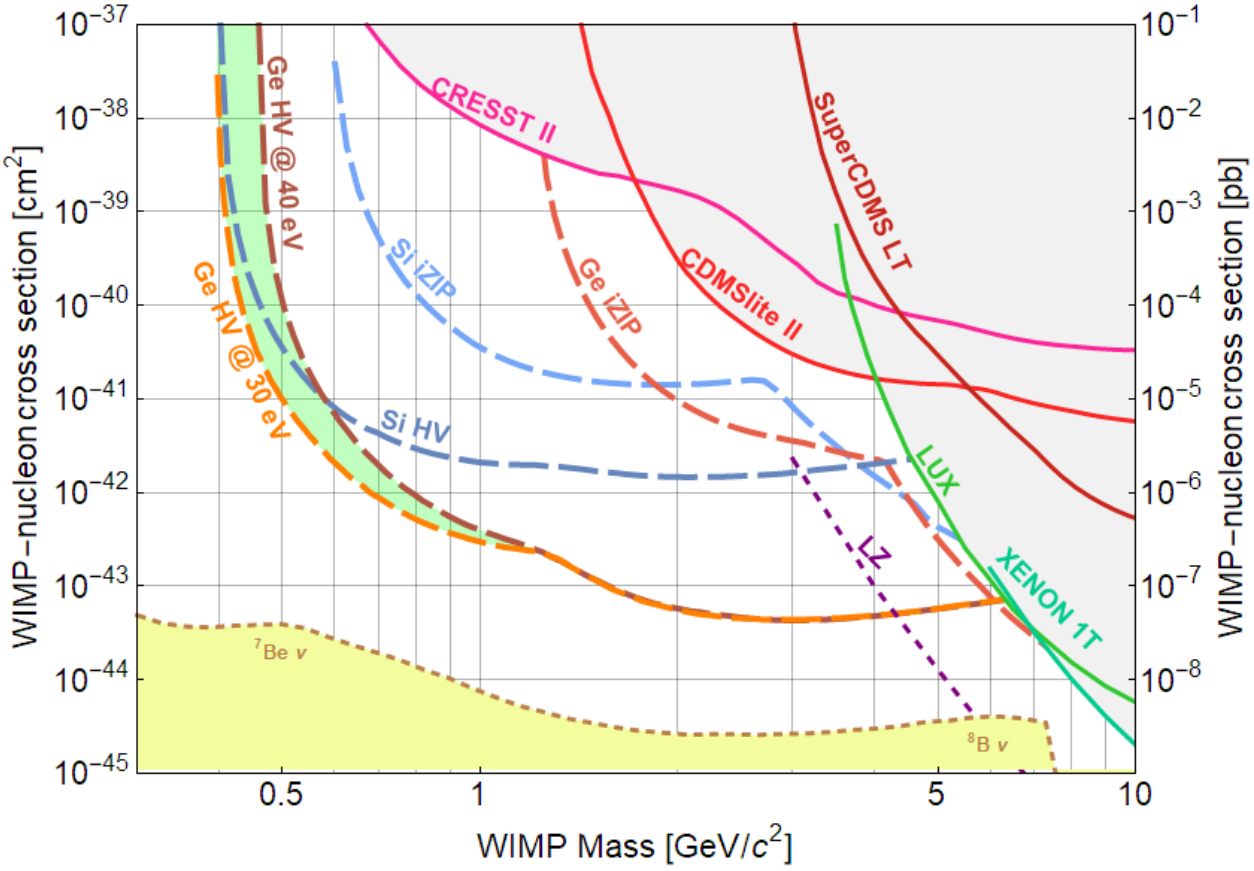

Figure 9.20. The projected exclusion limits of the SuperCDMS SNOLAB experiment. The blue dashed curves represent the expected sensitivities for the Si HV and iZIP detectors and the red dashed curves are the expected sensitivities of the Ge HV and iZIP detectors. The orange dashed curve represents the shift from a 40 eV to a 30 eV analysis threshold for the Ge HV detectors. The solid lines are the current experimental exclusion limits in the low-mass region, from the CRESST-II [77], SuperCDMS [108, 152] and LUX [113] experiments. Also shown in the projected sensitivity of the LZ experiment [76]. The dotted brown line is the dark matter discovery limit from Ref. [153], which represents the cross-section at which the interaction rate from dark matter particles becomes comparable to the solar neutrino coherent elastic scattering rate.

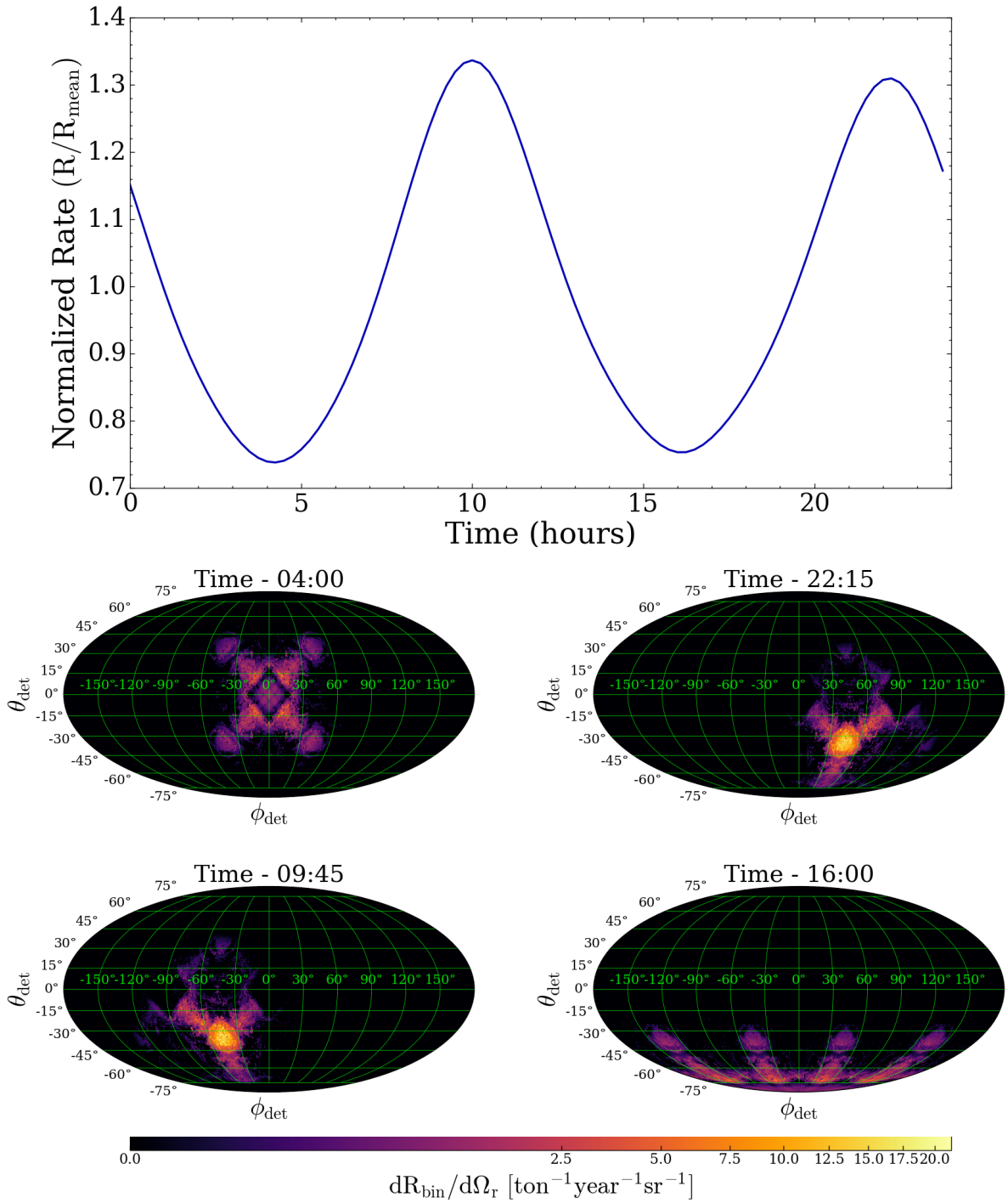

Figure 9.21. (Top) Normalized expected dark matter signal with respect to mean over one day for a 300 MeV/c^2 WIMP at the SNOLAB site. (Bottom) Angular distribution of $\partial R/\partial\Omega_r$for a WIMP-nucleon cross section of 10^{-39}cm^2 over one day for a 300 MeV WIMP at the SNOLAB site. Each of the four times corresponds to a local extremum of the integrated rate. Adapted from Ref. [130]

Part IV

Conclusions

Chapter 10

Conclusions & Future Outlook

The search for dark matter continues and there is much parameter space left to explore. In searching for dark matter-nucleon interactions with solid state detectors, SuperCDMS explores new parameter space for sub-GeV dark matter particles. The field is competitive with many experiments pursuing upgrades to increase low-mass sensitivity. SuperCDMS SNOLAB, however, has world-leading projected sensitivity and the work presented here furthers increases that lead.

10.1. Results

The shielding studies presented in Chapter 6 have determined the optimal thicknesses for shield materials to achieve the scientific goals of the SuperCDMS SNOLAB experiment and is summarized in Tables 6.3 and 6.4. These parameters have been included in Geant4-based simulations that will continue to be used in future analyses.

The radon plate-out model developed in Equation 7.4 represents a new extension of the Bateman equation for realistic exposure times. The plate-out rate R_{Pb} was experimentally determined for both HDPE and Cu surfaces, as well as dust fall-out rates. A time constraint on exposure of these materials for non-line-of-sight surfaces was calculated from these results and will guide the construction process of the SuperCDMS SNOLAB experiment. When construction is complete, the known value of exposure times will further inform backgrounds estimates from surface activity using Equations 7.6 and 7.8. This project resulted in a publication in Nuclear Instruments & Methods in Physics Research Section A [201].

The algorithms detailed in Chapter 8 yield up to 29-fold speedup for calculations of distant-dependent values in the SC, BCC, FCC, DIA and HCP crystal lattices. Additionally, the Lennard-Jones lattice constants have been computed with up to 32 decimal digit

precision, an improvement on existing results by up to 17 decimal digits. This project resulted in a publication in Computer Physics Communications [129].

The Frenkel defects analysis presented in Chapter 9 determined a preferred energy loss to defect formation of $6.08^{+0.13}_{-0.13}(\text{stat})^{+0.04}_{-0.03}(\text{syst})\,\%$ for ^{206}Pb recoils on Ge. From this result, the first experimentally determined germanium displacement threshold energy was found to be $19.7 \pm 0.5(\text{stat}) \pm 0.1(\text{syst})\,\text{eV}$. This result motivates a lower analysis threshold for Ge HV detectors at SNOLAB, further pushing the sensitivity of the experiment to lower masses as illustrated in Fig. 9.20.

10.2. Future Work

The empirically determined values for R_{Pb} could be further developed, possibly with the inclusion of the Jacobi model [202] which accounts for air flow, room volume, attachment and detatchment rates, and the materials involved. The two empirically determined values for ^{210}Pb plate-out rate to polyethylene and copper serves as a starting point for further development of R_{Pb} as a function on its own. This would be useful for predicting plate-out rates on other materials, or in locations with different radon activity or air flow.

The algorithms developed in Chapter 8 can be applied to molecular dynamics simulations of crystals. The speedup achieved would enable simulations of crystals with much larger volumes and, therefore, more realistic interactions as most simulations are limited to only a few hundred or thousand atoms. The Sillinger-Weber potential could be parameterized using these larger crystals with a relaxed cutoff value to allow contributions from more distant neighbors in the crystal.

Based upon the determined Ge displacement threshold value, a parameterized Sillinger-Weber potential can lead to better predictions of the angular dependence of defect formation, and thus, better rate predictions for a directionally dependent WIMP search [130].

Appendix A

SuperCDMS Data Processing and Cuts

A.1. Time-Traces of Phonon and Charge Channels

The SuperCDMS Soudan detectors have four phonon and two charge channels per side. These are named by type (P for phonon, Q for charge), channel (A/B/C/D for phonon, I/O for charge), and side (1 or 2). An example of a phonon channel would be PAS1 for phonon channel A on side 1. An example charge channel would be QOS2 for **o**uter charge channel on side 2. Data from each channel is monitored on a continuous basis, and when the trigger threshold is met, the data is stored as raw time-trace information from each channel. These are uncalibrated analog-to-digital (ADC) counts.

In order to reconstruct a total phonon or charge pulse, the individual channels must be calibrated (Figure A.1). The calibration is specific to each channel within each detector and effectively normalizes the pulses to equal area under the "tail" of the pulse, which is the area from $t = 800$ to the end of the recorded data ($t \sim 5700$).

The time-trace information is also analyzed to get estimates on noise both during and after the event. This information is stored in a quantity referred as a "Reduced Quantity" or RQ. Other RQs include status indicators for periods of unusually high noise and periods during an electric short. An example of some RQs and their definition is available in Table A.1.

The sum of all calibrated channels yields the total phonon or charge pulse. Pulse templates are created for each detector and each data-taking period. These templates are compared to the calibrated total phonon pulse (*c.f.* Figure 3.9) and the total phonon energy is estimated based on optimal filter theory (*c.f.* Appendix B in Ref [203]). The overall energy scale is set by events from a ^{133}Ba calibration source.

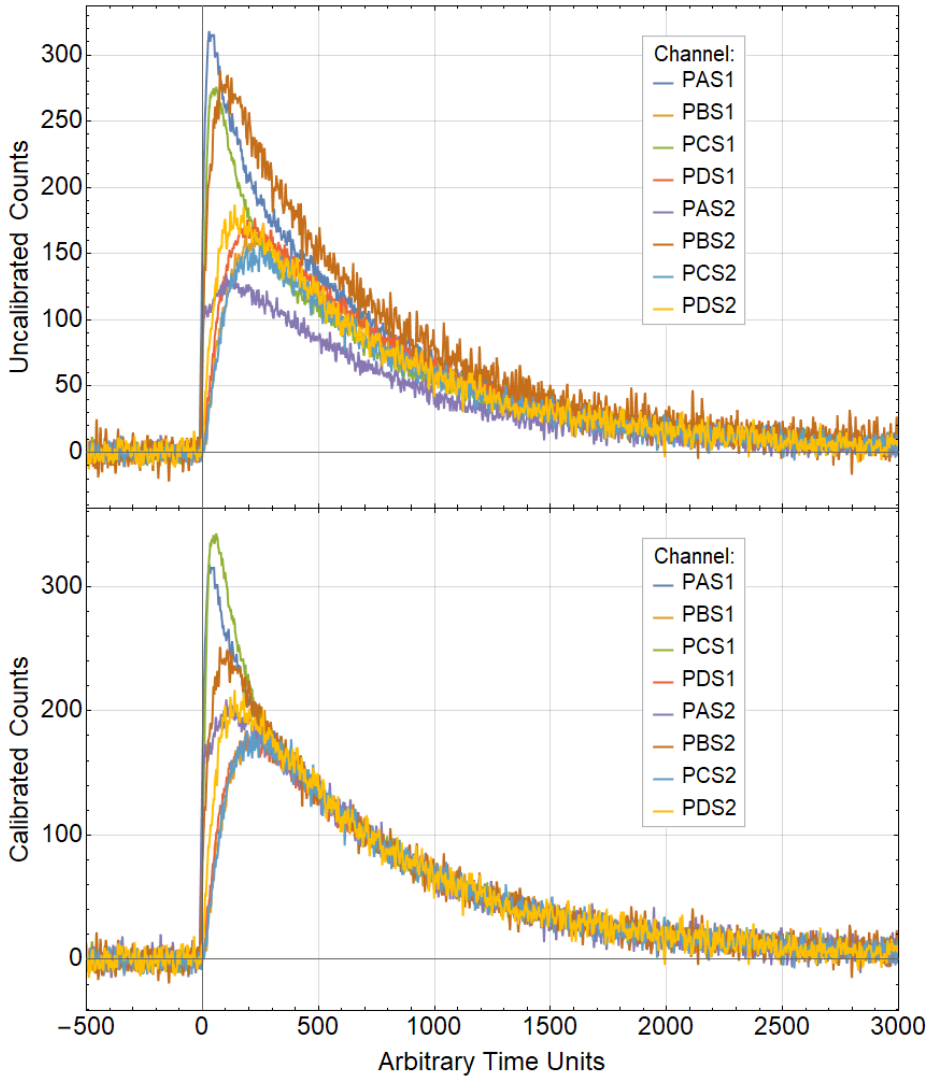

Figure A.1. Top: Uncalibrated phonon channels for one gamma event in the bulk of T3Z1. Bottom: Phonon pulses from the same event after calibration, showing strong similarity in the tails of each pulse.

Table A.1. A selection of example SuperCDMS data RQs. The asterisk * is a placeholder for the channel type, channel name, and side information (i.e. * = PCS2 for phonon channel C on side 2, or * = QIS1 for inner charge channel on side 1).

RQ	Description
*status	Indicates periods of normal operation or high/low resistance shorts in the channel
*bs	Pre-trigger baseline mean (in adc digitizer bins)
*std	Standard deviation
*bias	Phonon QET bias
*gain	Phonon total gain
PTNFamps	Amplitude of the phonon pulse using a non-stationary optimal filter

Calibrated quantities called Refined Reduced Quantities (RRQs) can be used for further analysis. An example of some RRQs is available in Table A.2.

A.2. Data Cuts

The RQs and RRQs can be used to select events based on certain criteria. For example, surface events can be selected by finding events where the charge collection is asymmetric (see Section 3.1.3 for a detailed explanation of charge collection in the SuperCDMS iZIP detectors). To do this, the `qzpartOF` RRQ can be used, which is a measure of charge symmetry based on the charge collected from each side. An event with perfect charge symmetry would have `qzpartOF`=0 and a surface event would have `qzpartOF`$\sim$1. By analyzing the `qzpartOF` value and selecting only events within a certain numeric range, unwanted events can be **cut** from further analysis.

To simplify the processing of selecting events of interest, multiple criteria can be combined into a single "cut." These cuts are stored in ROOT files similar to the event data and make it easier to extract the desired data. A selection of SuperCDMS data cuts is available in Table A.3.

Table A.2. A selection of example SuperCDMS data RRQs. The pound sign # is a placeholder for the side number. The dagger † is a placeholder for channel label (I/O for charge channels.)

RQ	Description
q†#OF	Charge calibrated optimal filter quantity (keV)
qsum#OF	Charge sum of sides 1 and 2 (keV)
qzpartOF	Charge symmetry quantity: (qsum1OF-qsum2OF)/(qsum1OF+qsum2OF)
ptNF	Phonon total pulse energy (calibrated PTNFamps, keV)
plukeqOF	Estimate of Luke-Neganov phonons, using only the charge signal: (abs(qsum1OF-qsum2OF) + min(qsum1OF,qsum2OF)*2)*abs(QIS1bias)/3eV
precoiltNF	The non-luke phonon energy (ptNF - plukeqOF)
pgqOF	The total phonon energy using only charge information (qsummaxOF + plukeqOF)
ygtNF	Ionization yield: pgqOF/ptNF

Table A.3. A selection of example SuperCDMS data cuts. The pound sign # is a placeholder for the side number. The dagger † is a placeholder for channel label (I/O for charge channels.)

RQ	Description
cQin#_v53	Ionization-derived radial cut for side # = 1 or 2 for selecting bulk events
cQsym_v53	Ionization-derived charge symmetry cut (comparing side 1 and 2) for selecting bulk events
cRandom_133	Selects randomly triggered events
cPostCf_133_HT	Selects events up to 48 hours after a ^{252}Cf neutron calibration (up to 72 hours for extended ^{252}Cf calibrations in Feb and May of 2014).
cGoodEv_v53	Selects events with good pulse shape reconstruction, during "good" data taking periods (proper bias voltage, no unusual trigger behavior, and more)
cLead_ptNF_qsummaxOF_v53_HT	Selects events in the ^{206}Pb recoil band

BIBLIOGRAPHY

[1] B. Kelvin. Baltimore lectures on molecular dynamics and the wave theory of light. In *Baltimore lectures on molecular dynamics and the wave theory of light*. Cambridge University Press, 1904. 3, 13

[2] H. Poincare. The Milky Way and the Theory of Gases. *Popular Astronomy*, 14:475–488, October 1906. 3

[3] J. H. Oort. The force exerted by the stellar system in the direction perpendicular to the galactic plane and some related problems. Bull. Astron. Inst. Netherlands, 6:249, August 1932. 3

[4] J. C. Kapteyn. First Attempt at a Theory of the Arrangement and Motion of the Sidereal System. ApJ, 55:302, May 1922. 3

[5] J. H. Jeans. The motions of stars in a Kapteyn universe. MNRAS, 82:122–132, January 1922. 3

[6] B. Lindblad. On the cause of the ellipsoidal distribution of stellar velocities. *Arkiv for Matematik, Astronomi och Fysik*, 20, 1927. 3

[7] Chris Flynn, Johan Holmberg, Laura Portinari, Burkhard Fuchs, and Hartmut Jahrei. On the mass-to-light ratio of the local galactic disc and the optical luminosity of the galaxy. *Monthly Notices of the Royal Astronomical Society*, 372(3):1149–1160, 2006. xiii, 4

[8] J. I. Read. The local dark matter density. *Journal of Physics G Nuclear Physics*, 41(6):063101, June 2014. xiii, 4

[9] F. Zwicky. Die Rotverschiebung von extragalaktischen Nebeln. *Helvetica Physica Acta*, 6:110–127, 1933. 5

[10] E. P. Hubble. *Realm of the Nebulae*. 1936. 5

[11] S. Smith. The Mass of the Virgo Cluster. ApJ, 83:23, January 1936. 5

[12] H. W. Babcock. The rotation of the Andromeda Nebula. *Lick Observatory Bulletin*, 19:41–51, 1939. xiii, 6

[13] Arnaud Dupays, Alberto Beswick, Bruno Lepetit, Carlo Rizzo, and Dimitar Bakalov. Proton zemach radius from measurements of the hyperfine splitting of hydrogen and muonic hydrogen. *Phys. Rev. A*, 68:052503, Nov 2003. 6

[14] H. I. Ewen and E. M. Purcell. Observation of a Line in the Galactic Radio Spectrum: Radiation from Galactic Hydrogen at 1,420 Mc./sec. Nature, 168:356, September 1951. 6

[15] F. D. Kahn and L. Woltjer. Intergalactic Matter and the Galaxy. ApJ, 130:705, November 1959. 6

[16] V. C. Rubin and W. K. Ford, Jr. Rotation of the Andromeda Nebula from a Spectroscopic Survey of Emission Regions. ApJ, 159:379, February 1970. xiii, 7

[17] K. C. Freeman. On the Disks of Spiral and S0 Galaxies. ApJ, 160:811, June 1970. 7

[18] A. Bosma. The Kinematics of a Sample of about Twenty Spiral Galaxies. In E. M. Berkhuijsen and R. Wielebinski, editors, *Structure and Properties of Nearby Galaxies*, volume 77 of *IAU Symposium*, page 28, 1978. 8

[19] E. P. Hubble. The classification of spiral nebulae. *The Observatory*, 50:276–281, September 1927. 8

[20] E.P. Hubble. *The Realm of the Nebulae*. Mrs. Hepsa Ely Silliman memorial lectures. Yale University Press, 1936. 8

[21] A. A. Penzias and R. W. Wilson. A Measurement of Excess Antenna Temperature at 4080 Mc/s. ApJ, 142:419–421, July 1965. 8

[22] G. Hinshaw, M. R. Nolta, C. L. Bennett, R. Bean, O. Dor, M. R. Greason, M. Halpern, R. S. Hill, N. Jarosik, A. Kogut, E. Komatsu, M. Limon, N. Odegard, S. S. Meyer, L. Page, H. V. Peiris, D. N. Spergel, G. S. Tucker, L. Verde, J. L. Weiland, E. Wollack, and E. L. Wright. Three-year wilkinson microwave anisotropy probe (wmap) observations: Temperature analysis. *The Astrophysical Journal Supplement Series*, 170(2):288, 2007. 8

[23] Warren A. Holmes, James J. Bock, Brendan P. Crill, Timothy C. Koch, William C. Jones, Andrew E. Lange, and Christopher G. Paine. Initial test results on bolometers for the planck high frequency instrument. *Appl. Opt.*, 47(32):5996–6008, Nov 2008. xiii, 9

[24] The Planck Collaboration. Planck CMB. *THE EUROPEAN SPACE AGENCY*, 2013. xiii, 9

[25] Planck Collaboration, Ade, P. A. R., Aghanim, N., Arnaud, M., Ashdown, M., Aumont, J., Baccigalupi, C., Banday, A. J., Barreiro, R. B., Bartlett, J. G., Bartolo, N., Battaner, E., Battye, R., Benabed, K., Benot, A., Benoit-Lvy, A., Bernard, J.-P., Bersanelli, M., Bielewicz, P., Bock, J. J., Bonaldi, A., Bonavera, L., Bond, J. R., Borrill, J., Bouchet, F. R., Boulanger, F., Bucher, M., Burigana, C., Butler, R. C., Calabrese, E., Cardoso, J.-F., Catalano, A., Challinor, A., Chamballu, A., Chary, R.-R., Chiang, H. C., Chluba, J., Christensen, P. R., Church, S., Clements, D. L., Colombi, S., Colombo, L. P. L., Combet, C., Coulais, A., Crill, B. P., Curto, A.,

Cuttaia, F., Danese, L., Davies, R. D., Davis, R. J., de Bernardis, P., de Rosa, A., de Zotti, G., Delabrouille, J., Dsert, F.-X., Di Valentino, E., Dickinson, C., Diego, J. M., Dolag, K., Dole, H., Donzelli, S., Dor, O., Douspis, M., Ducout, A., Dunkley, J., Dupac, X., Efstathiou, G., Elsner, F., Enlin, T. A., Eriksen, H. K., Farhang, M., Fergusson, J., Finelli, F., Forni, O., Frailis, M., Fraisse, A. A., Franceschi, E., Frejsel, A., Galeotta, S., Galli, S., Ganga, K., Gauthier, C., Gerbino, M., Ghosh, T., Giard, M., Giraud-Hraud, Y., Giusarma, E., Gjerlw, E., Gonzlez-Nuevo, J., Grski, K. M., Gratton, S., Gregorio, A., Gruppuso, A., Gudmundsson, J. E., Hamann, J., Hansen, F. K., Hanson, D., Harrison, D. L., Helou, G., Henrot-Versill, S., Hernndez-Monteagudo, C., Herranz, D., Hildebrandt, S. R., Hivon, E., Hobson, M., Holmes, W. A., Hornstrup, A., Hovest, W., Huang, Z., Huffenberger, K. M., Hurier, G., Jaffe, A. H., Jaffe, T. R., Jones, W. C., Juvela, M., Keihnen, E., Keskitalo, R., Kisner, T. S., Kneissl, R., Knoche, J., Knox, L., Kunz, M., Kurki-Suonio, H., Lagache, G., Lhteenmki, A., Lamarre, J.-M., Lasenby, A., Lattanzi, M., Lawrence, C. R., Leahy, J. P., Leonardi, R., Lesgourgues, J., Levrier, F., Lewis, A., Liguori, M., Lilje, P. B., Linden-Vrnle, M., Lpez-Caniego, M., Lubin, P. M., Macas-Prez, J. F., Maggio, G., Maino, D., Mandolesi, N., Mangilli, A., Marchini, A., Maris, M., Martin, P. G., Martinelli, M., Martnez-Gonzlez, E., Masi, S., Matarrese, S., McGehee, P., Meinhold, P. R., Melchiorri, A., Melin, J.-B., Mendes, L., Mennella, A., Migliaccio, M., Millea, M., Mitra, S., Miville-Deschnes, M.-A., Moneti, A., Montier, L., Morgante, G., Mortlock, D., Moss, A., Munshi, D., Murphy, J. A., Naselsky, P., Nati, F., Natoli, P., Netterfield, C. B., Nrgaard-Nielsen, H. U., Noviello, F., Novikov, D., Novikov, I., Oxborrow, C. A., Paci, F., Pagano, L., Pajot, F., Paladini, R., Paoletti, D., Partridge, B., Pasian, F., Patanchon, G., Pearson, T. J., Perdereau, O., Perotto, L., Perrotta, F., Pettorino, V., Piacentini, F., Piat, M., Pierpaoli, E., Pietrobon, D., Plaszczynski, S., Pointecouteau, E., Polenta, G., Popa, L., Pratt, G. W., Przeau, G., Prunet, S., Puget, J.-L., Rachen, J. P., Reach, W. T., Rebolo, R., Reinecke, M., Remazeilles, M., Renault, C., Renzi, A., Ristorcelli, I., Rocha, G., Rosset, C., Rossetti, M., Roudier, G., Rouill dOrfeuil, B., Rowan-Robinson, M., Rubio-Martn, J. A., Rusholme, B., Said, N., Salvatelli, V., Salvati, L., Sandri, M., Santos, D., Savelainen, M., Savini, G., Scott, D., Seiffert, M. D., Serra, P., Shellard, E. P. S., Spencer, L. D., Spinelli, M., Stolyarov, V., Stompor, R., Sudiwala, R., Sunyaev, R., Sutton, D., Suur-Uski, A.-S., Sygnet, J.-F., Tauber, J. A., Terenzi, L., Toffolatti, L., Tomasi, M., Tristram, M., Trombetti, T., Tucci, M., Tuovinen, J., Trler, M., Umana, G., Valenziano, L., Valiviita, J., Van Tent, F., Vielva, P., Villa, F., Wade, L. A., Wandelt, B. D., Wehus, I. K., White, M., White, S. D. M., Wilkinson, A., Yvon, D., Zacchei, A., and Zonca, A. Planck 2015 results - xiii. cosmological parameters. *A&A*, 594:A13, 2016. xiii, 10, 11

[26] M. Milgrom. A Modification of the Newtonian Dynamics - Implications for Galaxy Systems. ApJ, 270:384, July 1983. 12

[27] M. Milgrom. A modification of the Newtonian dynamics - Implications for galaxies. ApJ, 270:371–389, July 1983. 12

[28] M. Milgrom. A modification of the Newtonian dynamics as a possible alternative to the hidden mass hypothesis. ApJ, 270:365–370, July 1983. 12

[29] J. Bekenstein and M. Milgrom. Does the missing mass problem signal the breakdown of Newtonian gravity? ApJ, 286:7–14, November 1984. 12

[30] J. D. Bekenstein. The missing light puzzle: a hint about gravitation? In K. S. Thorne, editor, *Proceedings of the 2nd Canadian Conference on General Relativity and Relativistic Astrophysics*, pages 68–104, 1988. 12

[31] J. D. Bekenstein. An alternative to the dark matter paradigm: relativistic MOND gravitation. *ArXiv Astrophysics e-prints*, December 2004. 12

[32] C. Kraus, B. Bornschein, L. Bornschein, J. Bonn, B. Flatt, A. Kovalik, B. Ostrick, E. W. Otten, J. P. Schall, T. Thümmler, and C. Weinheimer. Final results from phase II of the Mainz neutrino mass searchin tritium $\{\beta\}$ decay. *European Physical Journal C*, 40:447–468, April 2005. 12

[33] D. Parno and Katrin Collaboration. The KATRIN Neutrino Mass Experiment. In *APS Meeting Abstracts*, January 2017. 12

[34] D. Clowe, M. Bradač, A. H. Gonzalez, M. Markevitch, S. W. Randall, C. Jones, and D. Zaritsky. A Direct Empirical Proof of the Existence of Dark Matter. ApJ, 648:L109–L113, September 2006. 13

[35] P. Hut. Limits on masses and number of neutral weakly interacting particles. *Physics Letters A*, 69:85–88, July 1977. 13

[36] B. W. Lee and S. Weinberg. Cosmological lower bound on heavy-neutrino masses. *Physical Review Letters*, 39:165–168, July 1977. 13

[37] B. Paczynski. Gravitational microlensing by the galactic halo. ApJ, 304:1–5, May 1986. 15

[38] K. Griest. Galactic microlensing as a method of detecting massive compact halo objects. ApJ, 366:412–421, January 1991. 15

[39] C. Alcock, R. A. Allsman, D. R. Alves, T. S. Axelrod, A. C. Becker, D. P. Bennett, K. H. Cook, N. Dalal, A. J. Drake, K. C. Freeman, M. Geha, K. Griest, M. J. Lehner, S. L. Marshall, D. Minniti, C. A. Nelson, B. A. Peterson, P. Popowski, M. R. Pratt, P. J. Quinn, C. W. Stubbs, W. Sutherland, A. B. Tomaney, T. Vandehei, and D. Welch. The MACHO Project: Microlensing Results from 5.7 Years of Large Magellanic Cloud Observations. ApJ, 542:281–307, October 2000. 15

[40] P. Tisserand, L. Le Guillou, C. Afonso, J. N. Albert, J. Andersen, R. Ansari, É. Aubourg, P. Bareyre, J. P. Beaulieu, X. Charlot, C. Coutures, R. Ferlet, P. Fouqué, J. F. Glicenstein, B. Goldman, A. Gould, D. Graff, M. Gros, J. Haissinski, C. Hamadache, J. de Kat, T. Lasserre, É. Lesquoy, C. Loup, C. Magneville, J. B. Marquette, É. Maurice, A. Maury, A. Milsztajn, M. Moniez,

N. Palanque-Delabrouille, O. Perdereau, Y. R. Rahal, J. Rich, M. Spiro, A. Vidal-Madjar, L. Vigroux, S. Zylberajch, and EROS-2 Collaboration. Limits on the Macho content of the Galactic Halo from the EROS-2 Survey of the Magellanic Clouds. A&A, 469:387–404, July 2007. 15

[41] G. Steigman and M. S. Turner. Cosmological constraints on the properties of weakly interacting massive particles. *Nuclear Physics B*, 253:375–386, 1985. 15

[42] M. Srednicki, R. Watkins, and K. A. Olive. Calculations of relic densities in the early universe. *Nuclear Physics B*, 310:693–713, December 1988. 15

[43] P. Gondolo and G. Gelmini. Cosmic abundances of stable particles: improved analysis. *Nuclear Physics B*, 360:145–179, August 1991. 15

[44] Wendy Freedman. The expansion rate of the universe. *Astronomy & Geophysics*, 43(1):1.10–1.13, 2002. 16

[45] Dan Hooper. The dawn of the lhc era: Particle dark matter. *World Scientific*, pages 709–764, 2012. xiii, 17

[46] Jonathan L. Feng. Dark matter candidates from particle physics and methods of detection. *Annual Review of Astronomy and Astrophysics*, 48(1):495–545, 2010. 16

[47] J. E. Gunn and J. R. Gott, III. On the Infall of Matter Into Clusters of Galaxies and Some Effects on Their Evolution. ApJ, 176:1, August 1972. 18

[48] J. F. Navarro, C. S. Frenk, and S. D. M. White. A Universal Density Profile from Hierarchical Clustering. ApJ, 490:493–508, December 1997. 19

[49] D. Merritt, A. W. Graham, B. Moore, J. Diemand, and B. Terzić. Empirical Models for Dark Matter Halos. I. Nonparametric Construction of Density Profiles and Comparison with Parametric Models. AJ, 132:2685–2700, December 2006. 19

[50] J. D. Lewin and P. F. Smith. Review of mathematics, numerical factors, and corrections for dark matter experiments based on elastic nuclear recoil. *Astroparticle Physics*, 6:87–112, December 1996. xviii, 19, 22, 57

[51] A. Boehle, A. M. Ghez, R. Schödel, L. Meyer, S. Yelda, S. Albers, G. D. Martinez, E. E. Becklin, T. Do, J. R. Lu, K. Matthews, M. R. Morris, B. Sitarski, and G. Witzel. An Improved Distance and Mass Estimate for Sgr A* from a Multistar Orbit Analysis. ApJ, 830:17, October 2016. 19

[52] Jim Alexander et al. Dark Sectors 2016 Workshop: Community Report. In *Dark Sectors 2016 Workshop: Community Report*, 2016. 19, 20

[53] Lawrence J. Hall, Karsten Jedamzik, John March-Russell, and Stephen M. West. Freeze-in production of fimp dark matter. *Journal of High Energy Physics*, 2010(3):80, Mar 2010. 19

[54] Rouven Essig, Jeremy Mardon, and Tomer Volansky. Direct detection of sub-gev dark matter. *Phys. Rev. D*, 85:076007, Apr 2012. 19

[55] C. Bhm and P. Fayet. Scalar dark matter candidates. *Nuclear Physics B*, 683(1):219 – 263, 2004. 19

[56] C. Bœhm, P. Fayet, and J. Silk. Light and heavy dark matter particles. *Phys. Rev. D*, 69:101302, May 2004. 19

[57] Dan Hooper and Kathryn M. Zurek. Natural supersymmetric model with mev dark matter. *Phys. Rev. D*, 77:087302, Apr 2008. 19

[58] Steve Ritz et al. Building for Discovery: Strategic Plan for U.S. Particle Physics in the Global Context. 2014. 20

[59] David E. Kaplan, Markus A. Luty, and Kathryn M. Zurek. Asymmetric dark matter. *Phys. Rev. D*, 79:115016, Jun 2009. 20

[60] Adam Falkowski, Joshua T. Ruderman, and Tomer Volansky. Asymmetric dark matter from leptogenesis. *Journal of High Energy Physics*, 2011(5):106, May 2011. 20

[61] Nicols Bernal, Matti Heikinheimo, Tommi Tenkanen, Kimmo Tuominen, and Ville Vaskonen. The dawn of fimp dark matter: A review of models and constraints. *International Journal of Modern Physics A*, 32(27):1730023, 2017. 20

[62] Yonit Hochberg, Eric Kuflik, Tomer Volansky, and Jay G. Wacker. Mechanism for thermal relic dark matter of strongly interacting massive particles. *Phys. Rev. Lett.*, 113:171301, Oct 2014. 20

[63] Yonit Hochberg, Yonatan Kahn, Mariangela Lisanti, Christopher G. Tully, and Kathryn M. Zurek. Directional detection of dark matter with two-dimensional targets. *Physics Letters B*, 772:239 – 246, 2017. 20

[64] A. Drukier and L. Stodolsky. Principles and applications of a neutral-current detector for neutrino physics and astronomy. Phys. Rev. D, 30:2295–2309, December 1984. 20

[65] M. W. Goodman and E. Witten. Detectability of certain dark-matter candidates. Phys. Rev. D, 31:3059–3063, June 1985. 20

[66] P. Cushman, C. Galbiati, D. N. McKinsey, H. Robertson, T. M. P. Tait, D. Bauer, A. Borgland, B. Cabrera, F. Calaprice, J. Cooley, T. Empl, R. Essig, E. Figueroa-Feliciano, R. Gaitskell, S. Golwala, J. Hall, R. Hill, A. Hime, E. Hoppe, L. Hsu, E. Hungerford, R. Jacobsen, M. Kelsey, R. F. Lang, W. H. Lippincott, B. Loer, S. Luitz, V. Mandic, J. Mardon, J. Maricic, R. Maruyama, R. Mahapatra, H. Nelson, J. Orrell, K. Palladino, E. Pantic, R. Partridge, A. Ryd, T. Saab, B. Sadoulet, R. Schnee, W. Shepherd, A. Sonnenschein, P. Sorensen, M. Szydagis, T. Volansky, M. Witherell, D. Wright, and K. Zurek. Snowmass CF1 Summary: WIMP Dark Matter Direct Detection. *ArXiv e-prints*, October 2013. xiv, 21

[67] A. Kurylov and M. Kamionkowski. Generalized analysis of the direct weakly interacting massive particle searches. Phys. Rev. D, 69(6):063503, March 2004. 22

[68] R. Agnese, A. J. Anderson, T. Aramaki, I. Arnquist, W. Baker, D. Barker, R. Basu Thakur, D. A. Bauer, A. Borgland, M. A. Bowles, P. L. Brink, R. Bunker, B. Cabrera, D. O. Caldwell, R. Calkins, C. Cartaro, D. G. Cerdeño, H. Chagani, Y. Chen, J. Cooley, B. Cornell, P. Cushman, M. Daal, P. C. F. Di Stefano, T. Doughty, L. Esteban, S. Fallows, E. Figueroa-Feliciano, M. Fritts, G. Gerbier, M. Ghaith, G. L. Godfrey, S. R. Golwala, J. Hall, H. R. Harris, T. Hofer, D. Holmgren, Z. Hong, E. Hoppe, L. Hsu, M. E. Huber, V. Iyer, D. Jardin, A. Jastram, M. H. Kelsey, A. Kennedy, A. Kubik, N. A. Kurinsky, A. Leder, B. Loer, E. Lopez Asamar, P. Lukens, R. Mahapatra, V. Mandic, N. Mast, N. Mirabolfathi, R. A. Moffatt, J. D. Morales Mendoza, J. L. Orrell, S. M. Oser, K. Page, W. A. Page, R. Partridge, M. Pepin, A. Phipps, S. Poudel, M. Pyle, H. Qiu, W. Rau, P. Redl, A. Reisetter, A. Roberts, A. E. Robinson, H. E. Rogers, T. Saab, B. Sadoulet, J. Sander, K. Schneck, R. W. Schnee, B. Serfass, D. Speller, M. Stein, J. Street, H. A. Tanaka, D. Toback, R. Underwood, A. N. Villano, B. von Krosigk, B. Welliver, J. S. Wilson, D. H. Wright, S. Yellin, J. J. Yen, B. A. Young, X. Zhang, and X. Zhao. Projected sensitivity of the supercdms snolab experiment. *Phys. Rev. D*, 95:082002, Apr 2017. xvii, xviii, xix, xxvi, 24, 51, 54, 57, 62, 64, 69, 71, 98, 128, 155

[69] E. Aprile, J. Aalbers, F. Agostini, M. Alfonsi, F. D. Amaro, M. Anthony, L. Arazi, F. Arneodo, C. Balan, P. Barrow, L. Baudis, B. Bauermeister, T. Berger, P. Breur, A. Breskin, A. Brown, E. Brown, S. Bruenner, G. Bruno, R. Budnik, L. Bütikofer, J. M. R. Cardoso, M. Cervantes, D. Cichon, D. Coderre, A. P. Colijn, J. Conrad, H. Contreras, J. P. Cussonneau, M. P. Decowski, P. de Perio, P. Di Gangi, A. Di Giovanni, E. Duchovni, S. Fattori, A. D. Ferella, A. Fieguth, D. Franco, W. Fulgione, M. Galloway, M. Garbini, C. Geis, L. W. Goetzke, Z. Greene, C. Grignon, E. Gross, W. Hampel, C. Hasterok, R. Itay, F. Kaether, B. Kaminsky, G. Kessler, A. Kish, H. Landsman, R. F. Lang, D. Lellouch, L. Levinson, M. Le Calloch, C. Levy, S. Lindemann, M. Lindner, J. A. M. Lopes, A. Lyashenko, S. Macmullin, A. Manfredini, T. Marrodán Undagoitia, J. Masbou, F. V. Massoli, D. Mayani, A. J. Melgarejo Fernandez, Y. Meng, M. Messina, K. Micheneau, B. Miguez, A. Molinario, M. Murra, J. Naganoma, U. Oberlack, S. E. A. Orrigo, P. Pakarha, B. Pelssers, R. Persiani, F. Piastra, J. Pienaar, G. Plante, N. Priel, L. Rauch, S. Reichard, C. Reuter, A. Rizzo, S. Rosendahl, N. Rupp, J. M. F. dos Santos, G. Sartorelli, M. Scheibelhut, S. Schindler, J. Schreiner, M. Schumann, L. Scotto Lavina, M. Selvi, P. Shagin, H. Simgen, A. Stein, D. Thers, A. Tiseni, G. Trinchero, C. Tunnell, M. von Sivers, R. Wall, H. Wang, M. Weber, Y. Wei, C. Weinheimer, J. Wulf, and Y. Zhang. Physics reach of the XENON1T dark matter experiment. J. Cosmology Astropart. Phys., 4:027, April 2016. 24

[70] C. Amole, M. Ardid, D. M. Asner, D. Baxter, E. Behnke, P. Bhattacharjee, H. Borsodi, M. Bou-Cabo, S. J. Brice, D. Broemmelsiek, K. Clark, J. I. Collar, P. S. Cooper, M. Crisler, C. E. Dahl, S. Daley, M. Das, F. Debris, N. Dhungana, J. Farine, I. Felis, R. Filgas, M. Fines-Neuschild, F. Girard, G. Giroux, M. Hai, J. Hall,

O. Harris, C. M. Jackson, M. Jin, C. B. Krauss, M. Lafrenière, M. Laurin, I. Lawson, I. Levine, W. H. Lippincott, E. Mann, J. P. Martin, D. Maurya, P. Mitra, R. Neilson, A. J. Noble, A. Plante, R. B. Podviianiuk, S. Priya, A. E. Robinson, M. Ruschman, O. Scallon, S. Seth, A. Sonnenschein, N. Starinski, I. Štekl, E. Vázquez-Jáuregui, J. Wells, U. Wichoski, V. Zacek, J. Zhang, and PICO Collaboration. Dark Matter Search Results from the PICO-2L C_3F_8 Bubble Chamber. *Physical Review Letters*, 114(23):231302, June 2015. 24

[71] C. Amole, M. Ardid, D. M. Asner, D. Baxter, E. Behnke, P. Bhattacharjee, H. Borsodi, M. Bou-Cabo, S. J. Brice, D. Broemmelsiek, K. Clark, J. I. Collar, P. S. Cooper, M. Crisler, C. E. Dahl, S. Daley, M. Das, F. Debris, N. Dhungana, S. Fallows, J. Farine, I. Felis, R. Filgas, F. Girard, G. Giroux, A. Grandison, M. Hai, J. Hall, O. Harris, M. Jin, C. B. Krauss, M. Lafrenière, M. Laurin, I. Lawson, I. Levine, W. H. Lippincott, E. Mann, D. Maurya, P. Mitra, R. Neilson, A. J. Noble, A. Plante, R. B. Podviianiuk, S. Priya, E. Ramberg, A. E. Robinson, R. Rucinski, M. Ruschman, O. Scallon, S. Seth, P. Simon, A. Sonnenschein, I. Štekl, E. Vázquez-Jáuregui, J. Wells, U. Wichoski, V. Zacek, J. Zhang, I. A. Shkrob, and PICO Collaboration. Dark matter search results from the PICO-60 CF_3 I bubble chamber. Phys. Rev. D, 93(5):052014, March 2016. xiv, 24, 28

[72] M. D. Cervantes. *Dedicated searches for leptophilic dark matter with XENON100 detector*. PhD thesis, Purdue University, 2016. 24

[73] E. Armengaud, Q. Arnaud, C. Augier, A. Benoît, A. Benoît, L. Bergé, T. Bergmann, J. Billard, J. Blümer, T. de Boissière, G. Bres, A. Broniatowski, V. Brudanin, P. Camus, A. Cazes, M. Chapellier, F. Charlieux, L. Dumoulin, K. Eitel, D. Filosofov, N. Foerster, N. Fourches, G. Garde, J. Gascon, G. Gerbier, A. Giuliani, M. Grollier, M. Gros, L. Hehn, S. Hervé, G. Heuermann, V. Humbert, M. De Jésus, Y. Jin, S. Jokisch, A. Juillard, C. Kéfélian, M. Kleifges, V. Kozlov, H. Kraus, V. A. Kudryavtsev, H. Le-Sueur, J. Lin, M. Mancuso, S. Marnieros, A. Menshikov, X.-F. Navick, C. Nones, E. Olivieri, P. Pari, B. Paul, M.-C. Piro, D. V. Poda, E. Queguiner, M. Robinson, H. Rodenas, S. Rozov, V. Sanglard, B. Schmidt, S. Scorza, B. Siebenborn, D. Tcherniakhovski, L. Vagneron, M. Weber, E. Yakushev, and X. Zhang. Constraints on low-mass WIMPs from the EDELWEISS-III dark matter search. J. Cosmology Astropart. Phys., 5:019, May 2016. 24

[74] C. Savage, A. Scaffidi, M. White, and A. G. Williams. LUX likelihood and limits on spin-independent and spin-dependent WIMP couplings with LUXCalc. Phys. Rev. D, 92(10):103519, November 2015. 24

[75] D. S. Akerib, H. M. Araújo, X. Bai, A. J. Bailey, J. Balajthy, P. Beltrame, E. P. Bernard, A. Bernstein, T. P. Biesiadzinski, E. M. Boulton, A. Bradley, R. Bramante, S. B. Cahn, M. C. Carmona-Benitez, C. Chan, J. J. Chapman, A. A. Chiller, C. Chiller, A. Currie, J. E. Cutter, T. J. R. Davison, L. de Viveiros, A. Dobi, J. E. Y. Dobson, E. Druszkiewicz, B. N. Edwards, C. H. Faham, S. Fiorucci, R. J. Gaitskell, V. M. Gehman, C. Ghag, K. R. Gibson, M. G. D. Gilchriese, C. R. Hall, M. Hanhardt, S. J. Haselschwardt, S. A. Hertel, D. P. Hogan, M. Horn, D. Q. Huang,

C. M. Ignarra, M. Ihm, R. G. Jacobsen, W. Ji, K. Kazkaz, D. Khaitan, R. Knoche, N. A. Larsen, C. Lee, B. G. Lenardo, K. T. Lesko, A. Lindote, M. I. Lopes, D. C. Malling, A. Manalaysay, R. L. Mannino, M. F. Marzioni, D. N. McKinsey, D.-M. Mei, J. Mock, M. Moongweluwan, J. A. Morad, A. S. J. Murphy, C. Nehrkorn, H. N. Nelson, F. Neves, K. O'Sullivan, K. C. Oliver-Mallory, R. A. Ott, K. J. Palladino, M. Pangilinan, E. K. Pease, P. Phelps, L. Reichhart, C. Rhyne, S. Shaw, T. A. Shutt, C. Silva, V. N. Solovov, P. Sorensen, S. Stephenson, T. J. Sumner, M. Szydagis, D. J. Taylor, W. Taylor, B. P. Tennyson, P. A. Terman, D. R. Tiedt, W. H. To, M. Tripathi, L. Tvrznikova, S. Uvarov, J. R. Verbus, R. C. Webb, J. T. White, T. J. Whitis, M. S. Witherell, F. L. H. Wolfs, K. Yazdani, S. K. Young, C. Zhang, and LUX Collaboration. Results on the Spin-Dependent Scattering of Weakly Interacting Massive Particles on Nucleons from the Run 3 Data of the LUX Experiment. *Physical Review Letters*, 116(16):161302, April 2016. xviii, 24, 57

[76] M. Szydagis, for the LUX Collaboration, and the LZ Collaboration. The Present and Future of Searching for Dark Matter with LUX and LZ. *ArXiv e-prints*, November 2016. xxiv, 24, 158

[77] G. Angloher, A. Bento, C. Bucci, L. Canonica, X. Defay, A. Erb, F. von Feilitzsch, N. Ferreiro Iachellini, P. Gorla, A. Gütlein, D. Hauff, J. Jochum, M. Kiefer, H. Kluck, H. Kraus, J. C. Lanfranchi, J. Loebell, A. Münster, C. Pagliarone, F. Petricca, W. Potzel, F. Pröbst, F. Reindl, K. Schäffner, J. Schieck, S. Schönert, W. Seidel, L. Stodolsky, C. Strandhagen, R. Strauss, A. Tanzke, H. H. Trinh Thi, C. Türkoğlu, M. Uffinger, A. Ulrich, I. Usherov, S. Wawoczny, M. Willers, M. Wüstrich, and A. Zöller. Results on light dark matter particles with a low-threshold cresst-ii detector. *The European Physical Journal C*, 76(1):25, 2016. xiv, xv, xviii, xxiv, 24, 28, 29, 57, 158

[78] LAURA BAUDIS. Dark matter searches. *International Journal of Modern Physics A*, 21(08n09):1925–1937, 2006. 24

[79] GIANFRANCO BERTONE and DAVID MERRITT. Dark matter dynamics and indirect detection. *Modern Physics Letters A*, 20(14):1021–1036, 2005. 24

[80] M. Ackermann, A. Albert, B. Anderson, L. Baldini, J. Ballet, G. Barbiellini, D. Bastieri, K. Bechtol, R. Bellazzini, E. Bissaldi, E. D. Bloom, E. Bonamente, A. Bouvier, T. J. Brandt, J. Bregeon, M. Brigida, P. Bruel, R. Buehler, S. Buson, G. A. Caliandro, R. A. Cameron, M. Caragiulo, P. A. Caraveo, C. Cecchi, E. Charles, A. Chekhtman, J. Chiang, S. Ciprini, R. Claus, J. Cohen-Tanugi, J. Conrad, F. D'Ammando, A. de Angelis, C. D. Dermer, S. W. Digel, E. do Couto e Silva, P. S. Drell, A. Drlica-Wagner, R. Essig, C. Favuzzi, E. C. Ferrara, A. Franckowiak, Y. Fukazawa, S. Funk, P. Fusco, F. Gargano, D. Gasparrini, N. Giglietto, M. Giroletti, G. Godfrey, G. A. Gomez-Vargas, I. A. Grenier, S. Guiriec, M. Gustafsson, M. Hayashida, E. Hays, J. Hewitt, R. E. Hughes, T. Jogler, T. Kamae, J. Knödlseder, D. Kocevski, M. Kuss, S. Larsson, L. Latronico, M. Llena Garde, F. Longo, F. Loparco, M. N. Lovellette, P. Lubrano, G. Martinez, M. Mayer, M. N. Mazziotta, P. F. Michelson, W. Mitthumsiri, T. Mizuno, A. A.

Moiseev, M. E. Monzani, A. Morselli, I. V. Moskalenko, S. Murgia, R. Nemmen, E. Nuss, T. Ohsugi, E. Orlando, J. F. Ormes, J. S. Perkins, F. Piron, G. Pivato, T. A. Porter, S. Rainò, R. Rando, M. Razzano, S. Razzaque, A. Reimer, O. Reimer, S. Ritz, M. Sánchez-Conde, N. Sehgal, C. Sgrò, E. J. Siskind, P. Spinelli, L. Strigari, D. J. Suson, H. Tajima, H. Takahashi, J. B. Thayer, L. Tibaldo, M. Tinivella, D. F. Torres, Y. Uchiyama, T. L. Usher, J. Vandenbroucke, G. Vianello, V. Vitale, M. Werner, B. L. Winer, K. S. Wood, M. Wood, G. Zaharijas, and S. Zimmer. Dark matter constraints from observations of 25 milky way satellite galaxies with the fermi large area telescope. *Phys. Rev. D*, 89:042001, Feb 2014. 24

[81] M. Ackermann, M. Ajello, A. Allafort, L. Baldini, J. Ballet, G. Barbiellini, D. Bastieri, K. Bechtol, R. Bellazzini, R.D. Blandford, E.D. Bloom, E. Bonamente, A.W. Borgland, A. Bouvier, T.J. Brandt, J. Bregeon, M. Brigida, P. Bruel, R. Buehler, S. Buson, G.A. Caliandro, R.A. Cameron, P.A. Caraveo, S. Carrigan, J.M. Casandjian, C. Cecchi, E. Charles, A. Chekhtman, C.C. Cheung, J. Chiang, S. Ciprini, R. Claus, J. Cohen-Tanugi, L.R. Cominsky, J. Conrad, A. de Angelis, F. de Palma, E. do Couto e Silva, P.S. Drell, A. Drlica-Wagner, R. Dubois, D. Dumora, Y. Edmonds, C. Farnier, C. Favuzzi, S.J. Fegan, M. Frailis, Y. Fukazawa, P. Fusco, F. Gargano, D. Gasparrini, N. Gehrels, S. Germani, N. Giglietto, F. Giordano, T. Glanzman, G. Godfrey, I.A. Grenier, S. Guiriec, M. Gustafsson, A.K. Harding, M. Hayashida, D. Horan, R.E. Hughes, T.E. Jeltema, G. Jhannesson, A S. Johnson, W.N. Johnson, T. Kamae, H. Katagiri, J. Kataoka, J. Kndlseder, M. Kuss, J. Lande, L. Latronico, S.-H. Lee, M. Llena Garde, F. Longo, F. Loparco, M.N. Lovellette, P. Lubrano, G.M. Madejski, A. Makeev, M.N. Mazziotta, P.F. Michelson, W. Mitthumsiri, T. Mizuno, A.A. Moiseev, C. Monte, M.E. Monzani, A. Morselli, I.V. Moskalenko, S. Murgia, P.L. Nolan, J.P. Norris, E. Nuss, M. Ohno, T. Ohsugi, N. Omodei, E. Orlando, J.F. Ormes, J.H. Panetta, M. Pepe, M. Pesce-Rollins, F. Piron, T.A. Porter, S. Profumo, S. Rain, M. Razzano, T. Reposeur, S. Ritz, A.Y. Rodriguez, M. Roth, H.F.-W. Sadrozinski, A. Sander, J.D. Scargle, C. Sgr, E.J. Siskind, P.D. Smith, G. Spandre, P. Spinelli, J.-L. Starck, M.S. Strickman, D.J. Suson, H. Takahashi, T. Tanaka, J.B. Thayer, J.G. Thayer, L. Tibaldo, D.F. Torres, G. Tosti, T.L. Usher, V. Vasileiou, V. Vitale, A.P. Waite, P. Wang, B.L. Winer, K.S. Wood, Z. Yang, T. Ylinen, and M. Ziegler. Constraints on dark matter annihilation in clusters of galaxies with the fermi large area telescope. *Journal of Cosmology and Astroparticle Physics*, 2010(05):025, 2010. 24

[82] M. Aguilar, G. Alberti, B. Alpat, A. Alvino, G. Ambrosi, K. Andeen, H. Anderhub, L. Arruda, P. Azzarello, A. Bachlechner, F. Barao, B. Baret, A. Barrau, L. Barrin, A. Bartoloni, L. Basara, A. Basili, L. Batalha, J. Bates, R. Battiston, J. Bazo, R. Becker, U. Becker, M. Behlmann, B. Beischer, J. Berdugo, P. Berges, B. Bertucci, G. Bigongiari, A. Biland, V. Bindi, S. Bizzaglia, G. Boella, W. de Boer, K. Bollweg, J. Bolmont, B. Borgia, S. Borsini, M. J. Boschini, G. Boudoul, M. Bourquin, P. Brun, M. Buénerd, J. Burger, W. Burger, F. Cadoux, X. D. Cai, M. Capell, D. Casadei, J. Casaus, V. Cascioli, G. Castellini, I. Cernuda, F. Cervelli, M. J. Chae, Y. H. Chang, A. I. Chen, C. R. Chen, H. Chen, G. M. Cheng, H. S. Chen, L. Cheng, N. Chernoplyiokov, A. Chikanian, E. Choumilov, V. Choutko, C. H. Chung,

C. Clark, R. Clavero, G. Coignet, V. Commichau, C. Consolandi, A. Contin, C. Corti, M. T. Costado Dios, B. Coste, D. Crespo, Z. Cui, M. Dai, C. Delgado, S. Della Torre, B. Demirkoz, P. Dennett, L. Derome, S. Di Falco, X. H. Diao, A. Diago, L. Djambazov, C. Díaz, P. von Doetinchem, W. J. Du, J. M. Dubois, R. Duperay, M. Duranti, D. D'Urso, A. Egorov, A. Eline, F. J. Eppling, T. Eronen, J. van Es, H. Esser, A. Falvard, E. Fiandrini, A. Fiasson, E. Finch, P. Fisher, K. Flood, R. Foglio, M. Fohey, S. Fopp, N. Fouque, Y. Galaktionov, M. Gallilee, L. Gallin-Martel, G. Gallucci, B. García, J. García, R. García-López, L. García-Tabares, C. Gargiulo, H. Gast, I. Gebauer, S. Gentile, M. Gervasi, W. Gillard, F. Giovacchini, L. Girard, P. Goglov, J. Gong, C. Goy-Henningsen, D. Grandi, M. Graziani, A. Grechko, A. Gross, I. Guerri, C. de la Guía, K. H. Guo, M. Habiby, S. Haino, F. Hauler, Z. H. He, M. Heil, J. Heilig, R. Hermel, H. Hofer, Z. C. Huang, W. Hungerford, M. Incagli, M. Ionica, A. Jacholkowska, W. Y. Jang, H. Jinchi, M. Jongmanns, L. Journet, L. Jungermann, W. Karpinski, G. N. Kim, K. S. Kim, Th. Kirn, R. Kossakowski, A. Koulemzine, O. Kounina, A. Kounine, V. Koutsenko, M. S. Krafczyk, E. Laudi, G. Laurenti, C. Lauritzen, A. Lebedev, M. W. Lee, S. C. Lee, C. Leluc, H. León Vargas, V. Lepareur, J. Q. Li, Q. Li, T. X. Li, W. Li, Z. H. Li, P. Lipari, C. H. Lin, D. Liu, H. Liu, T. Lomtadze, Y. S. Lu, S. Lucidi, K. Lübelsmeyer, J. Z. Luo, W. Lustermann, S. Lv, J. Madsen, R. Majka, A. Malinin, C. Mañá, J. Marín, T. Martin, G. Martínez, F. Masciocchi, N. Masi, D. Maurin, A. McInturff, P. McIntyre, A. Menchaca-Rocha, Q. Meng, M. Menichelli, I. Mereu, M. Millinger, D. C. Mo, M. Molina, P. Mott, A. Mujunen, S. Natale, P. Nemeth, J. Q. Ni, N. Nikonov, F. Nozzoli, P. Nunes, A. Obermeier, S. Oh, A. Oliva, F. Palmonari, C. Palomares, M. Paniccia, A. Papi, W. H. Park, M. Pauluzzi, F. Pauss, A. Pauw, E. Pedreschi, S. Pensotti, R. Pereira, E. Perrin, G. Pessina, G. Pierschel, F. Pilo, A. Piluso, C. Pizzolotto, V. Plyaskin, J. Pochon, M. Pohl, V. Poireau, S. Porter, J. Pouxe, A. Putze, L. Quadrani, X. N. Qi, P. G. Rancoita, D. Rapin, Z. L. Ren, J. S. Ricol, E. Riihonen, I. Rodríguez, U. Roeser, S. Rosier-Lees, L. Rossi, A. Rozhkov, D. Rozza, A. Sabellek, R. Sagdeev, J. Sandweiss, B. Santos, P. Saouter, M. Sarchioni, S. Schael, D. Schinzel, M. Schmanau, G. Schwering, A. Schulz von Dratzig, G. Scolieri, E. S. Seo, B. S. Shan, J. Y. Shi, Y. M. Shi, T. Siedenburg, R. Siedling, D. Son, F. Spada, F. Spinella, M. Steuer, K. Stiff, W. Sun, W. H. Sun, X. H. Sun, M. Tacconi, C. P. Tang, X. W. Tang, Z. C. Tang, L. Tao, J. Tassan-Viol, Samuel C. C. Ting, S. M. Ting, C. Titus, N. Tomassetti, F. Toral, J. Torsti, J. R. Tsai, J. C. Tutt, J. Ulbricht, T. Urban, V. Vagelli, E. Valente, C. Vannini, E. Valtonen, M. Vargas Trevino, S. Vaurynovich, M. Vecchi, M. Vergain, B. Verlaat, C. Vescovi, J. P. Vialle, G. Viertel, G. Volpini, D. Wang, N. H. Wang, Q. L. Wang, R. S. Wang, X. Wang, Z. X. Wang, W. Wallraff, Z. L. Weng, M. Willenbrock, M. Wlochal, H. Wu, K. Y. Wu, Z. S. Wu, W. J. Xiao, S. Xie, R. Q. Xiong, G. M. Xin, N. S. Xu, W. Xu, Q. Yan, J. Yang, M. Yang, Q. H. Ye, H. Yi, Y. J. Yu, Z. Q. Yu, S. Zeissler, J. G. Zhang, Z. Zhang, M. M. Zhang, Z. M. Zheng, H. L. Zhuang, V. Zhukov, A. Zichichi, P. Zuccon, and C. Zurbach. First result from the alpha magnetic spectrometer on the international space station: Precision measurement of the positron fraction in primary cosmic rays of 0.5˘350 gev. *Phys. Rev. Lett.*, 110:141102, Apr 2013. 24, 25

[83] M. Aguilar, D. Aisa, B. Alpat, A. Alvino, G. Ambrosi, K. Andeen, L. Arruda, N. Attig, P. Azzarello, A. Bachlechner, F. Barao, A. Barrau, L. Barrin, A. Bartoloni, L. Basara, M. Battarbee, R. Battiston, J. Bazo, U. Becker, M. Behlmann, B. Beischer, J. Berdugo, B. Bertucci, G. Bigongiari, V. Bindi, S. Bizzaglia, M. Bizzarri, G. Boella, W. de Boer, K. Bollweg, V. Bonnivard, B. Borgia, S. Borsini, M. J. Boschini, M. Bourquin, J. Burger, F. Cadoux, X. D. Cai, M. Capell, S. Caroff, J. Casaus, V. Cascioli, G. Castellini, I. Cernuda, F. Cervelli, M. J. Chae, Y. H. Chang, A. I. Chen, H. Chen, G. M. Cheng, H. S. Chen, L. Cheng, A. Chikanian, H. Y. Chou, E. Choumilov, V. Choutko, C. H. Chung, C. Clark, R. Clavero, G. Coignet, C. Consolandi, A. Contin, C. Corti, B. Coste, M. Crispoltoni, Z. Cui, M. Dai, C. Delgado, S. Della Torre, M. B. Demirköz, L. Derome, S. Di Falco, L. Di Masso, F. Dimiccoli, C. Díaz, P. von Doetinchem, F. Donnini, W. J. Du, M. Duranti, D. D'Urso, A. Eline, F. J. Eppling, T. Eronen, Y. Y. Fan, L. Farnesini, J. Feng, E. Fiandrini, A. Fiasson, E. Finch, P. Fisher, Y. Galaktionov, G. Gallucci, B. García, R. García-López, C. Gargiulo, H. Gast, I. Gebauer, M. Gervasi, A. Ghelfi, W. Gillard, F. Giovacchini, P. Goglov, J. Gong, C. Goy, V. Grabski, D. Grandi, M. Graziani, C. Guandalini, I. Guerri, K. H. Guo, M. Habiby, S. Haino, K. C. Han, Z. H. He, M. Heil, J. Hoffman, T. H. Hsieh, Z. C. Huang, C. Huh, M. Incagli, M. Ionica, W. Y. Jang, H. Jinchi, K. Kanishev, G. N. Kim, K. S. Kim, Th. Kirn, R. Kossakowski, O. Kounina, A. Kounine, V. Koutsenko, M. S. Krafczyk, S. Kunz, G. La Vacca, E. Laudi, G. Laurenti, I. Lazzizzera, A. Lebedev, H. T. Lee, S. C. Lee, C. Leluc, H. L. Li, J. Q. Li, Q. Li, Q. Li, T. X. Li, W. Li, Y. Li, Z. H. Li, Z. Y. Li, S. Lim, C. H. Lin, P. Lipari, T. Lippert, D. Liu, H. Liu, T. Lomtadze, M. J. Lu, Y. S. Lu, K. Luebelsmeyer, F. Luo, J. Z. Luo, S. S. Lv, R. Majka, A. Malinin, C. Mañá, J. Marín, T. Martin, G. Martínez, N. Masi, D. Maurin, A. Menchaca-Rocha, Q. Meng, D. C. Mo, L. Morescalchi, P. Mott, M. Müller, J. Q. Ni, N. Nikonov, F. Nozzoli, P. Nunes, A. Obermeier, A. Oliva, M. Orcinha, F. Palmonari, C. Palomares, M. Paniccia, A. Papi, M. Pauluzzi, E. Pedreschi, S. Pensotti, R. Pereira, F. Pilo, A. Piluso, C. Pizzolotto, V. Plyaskin, M. Pohl, V. Poireau, E. Postaci, A. Putze, L. Quadrani, X. M. Qi, T. Räihä, P. G. Rancoita, D. Rapin, J. S. Ricol, I. Rodríguez, S. Rosier-Lees, A. Rozhkov, D. Rozza, R. Sagdeev, J. Sandweiss, P. Saouter, C. Sbarra, S. Schael, S. M. Schmidt, D. Schuckardt, A. Schulz von Dratzig, G. Schwering, G. Scolieri, E. S. Seo, B. S. Shan, Y. H. Shan, J. Y. Shi, X. Y. Shi, Y. M. Shi, T. Siedenburg, D. Son, F. Spada, F. Spinella, W. Sun, W. H. Sun, M. Tacconi, C. P. Tang, X. W. Tang, Z. C. Tang, L. Tao, D. Tescaro, Samuel C. C. Ting, S. M. Ting, N. Tomassetti, J. Torsti, C. Türkoğlu, T. Urban, V. Vagelli, E. Valente, C. Vannini, E. Valtonen, S. Vaurynovich, M. Vecchi, M. Velasco, J. P. Vialle, L. Q. Wang, Q. L. Wang, R. S. Wang, X. Wang, Z. X. Wang, Z. L. Weng, K. Whitman, J. Wienkenhöver, H. Wu, X. Xia, M. Xie, S. Xie, R. Q. Xiong, G. M. Xin, N. S. Xu, W. Xu, Q. Yan, J. Yang, M. Yang, Q. H. Ye, H. Yi, Y. J. Yu, Z. Q. Yu, S. Zeissler, J. H. Zhang, M. T. Zhang, X. B. Zhang, Z. Zhang, Z. M. Zheng, H. L. Zhuang, V. Zhukov, A. Zichichi, N. Zimmermann, P. Zuccon, and C. Zurbach. Precision measurement of the $(e^+ + e^-)$ flux in primary cosmic rays from 0.5 gev to 1 tev with the alpha magnetic spectrometer on the international space station. *Phys. Rev. Lett.*, 113:221102, Nov 2014. 24

[84] Leila Ali Cavasonza, Henning Gast, Michael Krmer, Mathieu Pellen, and Stefan Schael. Constraints on leptophilic dark matter from the ams-02 experiment. *The Astrophysical Journal*, 839(1):36, 2017. 25

[85] Timothy Cohen, Kohta Murase, Nicholas L. Rodd, Benjamin R. Safdi, and Yotam Soreq. γ-ray constraints on decaying dark matter and implications for icecube. *Phys. Rev. Lett.*, 119:021102, Jul 2017. 25

[86] Galle Giesen, Mathieu Boudaud, Yoann Gnolini, Vivian Poulin, Marco Cirelli, Pierre Salati, and Pasquale D. Serpico. Ams-02 antiprotons, at last! secondary astrophysical component and immediate implications for dark matter. *Journal of Cosmology and Astroparticle Physics*, 2015(09):023, 2015. 25

[87] Alejandro Ibarra, Anna S. Lamperstorfer, and Joseph Silk. Dark matter annihilations and decays after the ams-02 positron measurements. *Phys. Rev. D*, 89:063539, Mar 2014. 25

[88] Gert Htsi, Andi Hektor, and Martti Raidal. Implications of the fermi-lat diffuse gamma-ray measurements on annihilating or decaying dark matter. *Journal of Cosmology and Astroparticle Physics*, 2010(07):008, 2010. 25

[89] M. Ackermann, M. Ajello, W. B. Atwood, L. Baldini, G. Barbiellini, D. Bastieri, K. Bechtol, R. Bellazzini, R. D. Blandford, E. D. Bloom, E. Bonamente, A. W. Borgland, E. Bottacini, T. J. Brandt, J. Bregeon, M. Brigida, P. Bruel, R. Buehler, S. Buson, G. A. Caliandro, R. A. Cameron, P. A. Caraveo, J. M. Casandjian, C. Cecchi, E. Charles, A. Chekhtman, J. Chiang, S. Ciprini, R. Claus, J. Cohen-Tanugi, J. Conrad, A. Cuoco, S. Cutini, F. DAmmando, A. de Angelis, F. de Palma, C. D. Dermer, E. do Couto e Silva, P. S. Drell, A. Drlica-Wagner, L. Falletti, C. Favuzzi, S. J. Fegan, W. B. Focke, Y. Fukazawa, S. Funk, P. Fusco, F. Gargano, D. Gasparrini, S. Germani, N. Giglietto, F. Giordano, M. Giroletti, T. Glanzman, G. Godfrey, I. A. Grenier, S. Guiriec, M. Gustafsson, D. Hadasch, M. Hayashida, D. Horan, R. E. Hughes, M. S. Jackson, T. Jogler, G. Jhannesson, A. S. Johnson, T. Kamae, J. Kndlseder, M. Kuss, J. Lande, L. Latronico, A. M. Lionetto, M. Llena Garde, F. Longo, F. Loparco, B. Lott, M. N. Lovellette, P. Lubrano, M. N. Mazziotta, J. E. McEnery, J. Mehault, P. F. Michelson, W. Mitthumsiri, T. Mizuno, A. A. Moiseev, C. Monte, M. E. Monzani, A. Morselli, I. V. Moskalenko, S. Murgia, M. Naumann-Godo, J. P. Norris, E. Nuss, T. Ohsugi, M. Orienti, E. Orlando, J. F. Ormes, D. Paneque, J. H. Panetta, M. Pesce-Rollins, M. Pierbattista, F. Piron, G. Pivato, H. Poon, S. Rain, R. Rando, M. Razzano, S. Razzaque, A. Reimer, O. Reimer, C. Romoli, C. Sbarra, J. D. Scargle, C. Sgr, E. J. Siskind, G. Spandre, P. Spinelli, ukasz Stawarz, A. W. Strong, D. J. Suson, H. Tajima, H. Takahashi, T. Tanaka, J. G. Thayer, J. B. Thayer, L. Tibaldo, M. Tinivella, G. Tosti, E. Troja, T. L. Usher, J. Vandenbroucke, V. Vasileiou, G. Vianello, V. Vitale, A. P. Waite, E. Wallace, K. S. Wood, M. Wood, Z. Yang, G. Zaharijas, and S. Zimmer. Constraints on the galactic halo dark matter from fermi-lat diffuse measurements. *The Astrophysical Journal*, 761(2):91, 2012. 25

[90] *The Pierre Auger Observatory: Contributions to the 34th International Cosmic Ray Conference (ICRC 2015)*, 2015. 25

[91] D Kang, W D Apel, J C Arteaga-Velzquez, K Bekk, M Bertaina, J Blmer, H Bozdog, I M Brancus, E Cantoni, A Chiavassa, F Cossavella, K Daumiller, V de Souza, F Di Pierro, P Doll, R Engel, Z Feng, D Fuhrmann, A Gherghel-Lascu, H J Gils, R Glasstetter, C Grupen, A Haungs, D Heck, J R Hrandel, D Huber, T Huege, K H Kampert, H O Klages, K Link, P uczak, H J Mathes, H J Mayer, J Milke, B Mitrica, C Morello, J Oehlschlger, S Ostapchenko, N Palmieri, M Petcu, T Pierog, H Rebel, M Roth, H Schieler, S Schoo, F Schrder, O Sima, G Toma, G C Trinchero, H Ulrich, A Weindl, J Wochele, and J Zabierowski. A limit on the diffuse gamma-rays measured with kascade-grande. *Journal of Physics: Conference Series*, 632(1):012013, 2015. 25

[92] M. C. Chantell, C. E. Covault, J. W. Cronin, B. E. Fick, L. F. Fortson, J. W. Fowler, K. D. Green, B. J. Newport, R. A. Ong, S. Oser, M. A. Catanese, M. A. K. Glasmacher, J. Matthews, D. F. Nitz, D. Sinclair, J. C. van der Velde, and D. B. Kieda. Limits on the isotropic diffuse flux of ultrahigh energy γ radiation. *Phys. Rev. Lett.*, 79:1805–1808, Sep 1997. 25

[93] Andrea Albert. Investigating dark matter with cosmic gamma rays. In *Searching for Dark Matter with Cosmic Gamma Rays*, 2053-2571, pages 3–1 to 3–15. Morgan & Claypool Publishers, 2016. xiv, 25

[94] Kwei-Chou Yang. Search for scalar dark matter via pseudoscalar portal interactions in light of the galactic center gamma-ray excess. *Phys. Rev. D*, 97:023025, Jan 2018. 26

[95] David Curtin, Rouven Essig, Stefania Gori, Prerit Jaiswal, Andrey Katz, Tao Liu, Zhen Liu, David McKeen, Jessie Shelton, Matthew Strassler, Ze'ev Surujon, Brock Tweedie, and Yi-Ming Zhong. Exotic decays of the 125 gev higgs boson. *Phys. Rev. D*, 90:075004, Oct 2014. 26

[96] Anna Shcherbakova and ATLAS collaboration. Search for dark matter with the atlas detector at the lhc. *Journal of Physics: Conference Series*, 798(1):012100, 2017. 26

[97] CMS Collaboration. Search for dark matter and large extra dimensions in pp collisions yielding a photon and missing transverse energy. *Phys. Rev. Lett.*, 108:261803, Jun 2012. 26

[98] Basudeb Dasgupta, Joachim Kopp, and Pedro Schwaller. Photons, photon jets, and dark photons at 750gev and beyond. *The European Physical Journal C*, 76(5):277, May 2016. 26

[99] Search for exotic decays of a higgs boson into undetectable particles and one or more photons. *Physics Letters B*, 753:363 – 388, 2016. 26

[100] Hyun Min Lee and Min-Seok Seo. Communication with simp dark mesons via z-portal. *Physics Letters B*, 748:316 – 322, 2015. 26

[101] R. Agnese, A. J. Anderson, M. Asai, D. Balakishiyeva, R. Basu Thakur, D. A. Bauer, J. Billard, A. Borgland, M. A. Bowles, D. Brandt, P. L. Brink, R. Bunker, B. Cabrera, D. O. Caldwell, D. G. Cerdeno, H. Chagani, J. Cooley, B. Cornell, C. H. Crewdson, P. Cushman, M. Daal, P. C. F. Di Stefano, T. Doughty, L. Esteban, S. Fallows, E. Figueroa-Feliciano, G. L. Godfrey, S. R. Golwala, J. Hall, H. R. Harris, S. A. Hertel, T. Hofer, D. Holmgren, L. Hsu, M. E. Huber, A. Jastram, O. Kamaev, B. Kara, M. H. Kelsey, A. Kennedy, M. Kiveni, K. Koch, B. Loer, E. Lopez Asamar, R. Mahapatra, V. Mandic, C. Martinez, K. A. McCarthy, N. Mirabolfathi, R. A. Moffatt, D. C. Moore, P. Nadeau, R. H. Nelson, K. Page, R. Partridge, M. Pepin, A. Phipps, K. Prasad, M. Pyle, H. Qiu, W. Rau, P. Redl, A. Reisetter, Y. Ricci, T. Saab, B. Sadoulet, J. Sander, K. Schneck, R. W. Schnee, S. Scorza, B. Serfass, B. Shank, D. Speller, A. N. Villano, B. Welliver, D. H. Wright, S. Yellin, J. J. Yen, B. A. Young, and J. Zhang. Search for low-mass weakly interacting massive particles using voltage-assisted calorimetric ionization detection in the supercdms experiment. *Phys. Rev. Lett.*, 112:041302, Jan 2014. 26

[102] R. Agnese, A. J. Anderson, T. Aralis, T. Aramaki, I. J. Arnquist, W. Baker, D. Balakishiyeva, D. Barker, R. Basu Thakur, D. A. Bauer, T. Binder, M. A. Bowles, P. L. Brink, R. Bunker, B. Cabrera, D. O. Caldwell, R. Calkins, C. Cartaro, D. G. Cerdeño, Y. Chang, H. Chagani, Y. Chen, J. Cooley, B. Cornell, P. Cushman, M. Daal, P. C. F. Di Stefano, T. Doughty, L. Esteban, E. Fascione, E. Figueroa-Feliciano, M. Fritts, G. Gerbier, M. Ghaith, G. L. Godfrey, S. R. Golwala, J. Hall, H. R. Harris, Z. Hong, E. W. Hoppe, L. Hsu, M. E. Huber, V. Iyer, D. Jardin, A. Jastram, C. Jena, M. H. Kelsey, A. Kennedy, A. Kubik, N. A. Kurinsky, A. Leder, B. Loer, E. Lopez Asamar, P. Lukens, D. MacDonell, R. Mahapatra, V. Mandic, N. Mast, E. H. Miller, N. Mirabolfathi, R. A. Moffatt, B. Mohanty, J. D. Morales Mendoza, J. Nelson, J. L. Orrell, S. M. Oser, K. Page, W. A. Page, R. Partridge, M. Pepin, M. Peñalver Martinez, A. Phipps, S. Poudel, M. Pyle, H. Qiu, W. Rau, P. Redl, A. Reisetter, T. Reynolds, A. Roberts, A. E. Robinson, H. E. Rogers, T. Saab, B. Sadoulet, J. Sander, K. Schneck, R. W. Schnee, S. Scorza, K. Senapati, B. Serfass, D. Speller, M. Stein, J. Street, H. A. Tanaka, D. Toback, R. Underwood, A. N. Villano, B. von Krosigk, B. Welliver, J. S. Wilson, M. J. Wilson, D. H. Wright, S. Yellin, J. J. Yen, B. A. Young, X. Zhang, and X. Zhao. Low-mass dark matter search with cdmslite. *Phys. Rev. D*, 97:022002, Jan 2018. xv, 26, 29

[103] R. Agnese, T. Aramaki, I. J. Arnquist, W. Baker, D. Balakishiyeva, S. Banik, D. Barker, R. Basu Thakur, D. A. Bauer, T. Binder, M. A. Bowles, P. L. Brink, R. Bunker, B. Cabrera, D. O. Caldwell, R. Calkins, C. Cartaro, D. G. Cerdeño, Y. Chang, Y. Chen, J. Cooley, B. Cornell, P. Cushman, M. Daal, P. C. F. Di Stefano, T. Doughty, E. Fascione, E. Figueroa-Feliciano, M. Fritts, G. Gerbier, R. Germond, M. Ghaith, G. L. Godfrey, S. R. Golwala, J. Hall, H. R. Harris, Z. Hong, E. W. Hoppe, L. Hsu, M. E. Huber, V. Iyer, D. Jardin, A. Jastram, C. Jena, M. H. Kelsey, A. Kennedy, A. Kubik, N. A. Kurinsky, B. Loer, E. Lopez Asamar, P. Lukens, D. MacDonell, R. Mahapatra, V. Mandic, N. Mast, E. H. Miller, N. Mirabolfathi, B. Mohanty, J. D. Morales Mendoza, J. Nelson, J. L. Orrell, S. M. Oser, K. Page,

W. A. Page, R. Partridge, M. Penalver Martinez, M. Pepin, A. Phipps, S. Poudel, M. Pyle, H. Qiu, W. Rau, P. Redl, A. Reisetter, T. Reynolds, A. Roberts, A. E. Robinson, H. E. Rogers, T. Saab, B. Sadoulet, J. Sander, K. Schneck, R. W. Schnee, S. Scorza, K. Senapati, B. Serfass, D. Speller, M. Stein, J. Street, H. A. Tanaka, D. Toback, R. Underwood, A. N. Villano, B. von Krosigk, B. Welliver, J. S. Wilson, M. J. Wilson, D. H. Wright, S. Yellin, J. J. Yen, B. A. Young, X. Zhang, and X. Zhao. Results from the super cryogenic dark matter search experiment at soudan. *Phys. Rev. Lett.*, 120:061802, Feb 2018. xiv, 26, 28, 70

[104] R. Agnese, Z. Ahmed, A. J. Anderson, S. Arrenberg, D. Balakishiyeva, R. Basu Thakur, D. A. Bauer, J. Billard, A. Borgland, D. Brandt, P. L. Brink, T. Bruch, R. Bunker, B. Cabrera, D. O. Caldwell, D. G. Cerdeno, H. Chagani, J. Cooley, B. Cornell, C. H. Crewdson, P. Cushman, M. Daal, F. Dejongh, E. do Couto e Silva, T. Doughty, L. Esteban, S. Fallows, E. Figueroa-Feliciano, J. Filippini, J. Fox, M. Fritts, G. L. Godfrey, S. R. Golwala, J. Hall, R. H. Harris, S. A. Hertel, T. Hofer, D. Holmgren, L. Hsu, M. E. Huber, A. Jastram, O. Kamaev, B. Kara, M. H. Kelsey, A. Kennedy, P. Kim, M. Kiveni, K. Koch, M. Kos, S. W. Leman, B. Loer, E. Lopez Asamar, R. Mahapatra, V. Mandic, C. Martinez, K. A. McCarthy, N. Mirabolfathi, R. A. Moffatt, D. C. Moore, P. Nadeau, R. H. Nelson, K. Page, R. Partridge, M. Pepin, A. Phipps, K. Prasad, M. Pyle, H. Qiu, W. Rau, P. Redl, A. Reisetter, Y. Ricci, T. Saab, B. Sadoulet, J. Sander, K. Schneck, R. W. Schnee, S. Scorza, B. Serfass, B. Shank, D. Speller, K. M. Sundqvist, A. N. Villano, B. Welliver, D. H. Wright, S. Yellin, J. J. Yen, J. Yoo, B. A. Young, and J. Zhang. Silicon detector dark matter results from the final exposure of cdms ii. *Phys. Rev. Lett.*, 111:251301, Dec 2013. xiv, 28

[105] C. Savage, G. Gelmini, P. Gondolo, and K. Freese. Compatibility of dama/libra dark matter detection with other searches. *Journal of Cosmology and Astroparticle Physics*, 2009(04):010, 2009. xiv, 28

[106] R. Agnese, A. J. Anderson, T. Aramaki, M. Asai, W. Baker, D. Balakishiyeva, D. Barker, R. Basu Thakur, D. A. Bauer, J. Billard, A. Borgland, M. A. Bowles, P. L. Brink, R. Bunker, B. Cabrera, D. O. Caldwell, R. Calkins, D. G. Cerdeno, H. Chagani, Y. Chen, J. Cooley, B. Cornell, P. Cushman, M. Daal, P. C. F. Di Stefano, T. Doughty, L. Esteban, S. Fallows, E. Figueroa-Feliciano, M. Ghaith, G. L. Godfrey, S. R. Golwala, J. Hall, H. R. Harris, T. Hofer, D. Holmgren, L. Hsu, M. E. Huber, D. Jardin, A. Jastram, O. Kamaev, B. Kara, M. H. Kelsey, A. Kennedy, A. Leder, B. Loer, E. Lopez Asamar, P. Lukens, R. Mahapatra, V. Mandic, N. Mast, N. Mirabolfathi, R. A. Moffatt, J. D. Morales Mendoza, S. M. Oser, K. Page, W. A. Page, R. Partridge, M. Pepin, A. Phipps, K. Prasad, M. Pyle, H. Qiu, W. Rau, P. Redl, A. Reisetter, Y. Ricci, A. Roberts, H. E. Rogers, T. Saab, B. Sadoulet, J. Sander, K. Schneck, R. W. Schnee, S. Scorza, B. Serfass, B. Shank, D. Speller, D. Toback, R. Underwood, S. Upadhyayula, A. N. Villano, B. Welliver, J. S. Wilson, D. H. Wright, S. Yellin, J. J. Yen, B. A. Young, and J. Zhang. New results from the search for low-mass weakly interacting massive particles with the cdms low ionization threshold experiment. *Phys. Rev. Lett.*, 116:071301, Feb 2016. xiv, xv, 28, 29

[107] E. Armengaud, C. Augier, A. Benot, L. Berg, J. Blmer, A. Broniatowski, V. Brudanin, B. Censier, G. Chardin, M. Chapellier, F. Charlieux, P. Coulter, G.A. Cox, X. Defay, M. De Jesus, Y. Dolgorouki, J. Domange, L. Dumoulin, K. Eitel, D. Filosofov, N. Fourches, J. Gascon, G. Gerbier, J. Gironnet, M. Gros, S. Henry, S. Herv, A. Juillard, H. Kluck, V. Kozlov, H. Kraus, V.A. Kudryavtsev, P. Loaiza, S. Marnieros, X.-F. Navick, C. Nones, E. Olivieri, P. Pari, L. Pattavina, B. Paul, M. Robinson, S. Rozov, V. Sanglard, B. Schmidt, S. Scorza, S. Semikh, A.S. Torrento-Coello, L. Vagneron, M.-A. Verdier, R.J. Walker, and E. Yakushev. Final results of the edelweiss-ii wimp search using a 4-kg array of cryogenic germanium detectors with interleaved electrodes. *Physics Letters B*, 702(5):329 – 335, 2011. xiv, 28

[108] R. Agnese, A. J. Anderson, M. Asai, D. Balakishiyeva, R. Basu Thakur, D. A. Bauer, J. Beaty, J. Billard, A. Borgland, M. A. Bowles, D. Brandt, P. L. Brink, R. Bunker, B. Cabrera, D. O. Caldwell, D. G. Cerdeno, H. Chagani, Y. Chen, M. Cherry, J. Cooley, B. Cornell, C. H. Crewdson, P. Cushman, M. Daal, D. DeVaney, P. C. F. Di Stefano, E. Do Couto E Silva, T. Doughty, L. Esteban, S. Fallows, E. Figueroa-Feliciano, G. L. Godfrey, S. R. Golwala, J. Hall, S. Hansen, H. R. Harris, S. A. Hertel, B. A. Hines, T. Hofer, D. Holmgren, L. Hsu, M. E. Huber, A. Jastram, O. Kamaev, B. Kara, M. H. Kelsey, S. Kenany, A. Kennedy, M. Kiveni, K. Koch, A. Leder, B. Loer, E. Lopez Asamar, R. Mahapatra, V. Mandic, C. Martinez, K. A. McCarthy, N. Mirabolfathi, R. A. Moffatt, R. H. Nelson, L. Novak, K. Page, R. Partridge, M. Pepin, A. Phipps, M. Platt, K. Prasad, M. Pyle, H. Qiu, W. Rau, P. Redl, A. Reisetter, R. W. Resch, Y. Ricci, M. Ruschman, T. Saab, B. Sadoulet, J. Sander, R. L. Schmitt, K. Schneck, R. W. Schnee, S. Scorza, D. N. Seitz, B. Serfass, B. Shank, D. Speller, A. Tomada, S. Upadhyayula, A. N. Villano, B. Welliver, D. H. Wright, S. Yellin, J. J. Yen, B. A. Young, and J. Zhang. Search for low-mass weakly interacting massive particles with supercdms. *Phys. Rev. Lett.*, 112:241302, Jun 2014. xiv, xv, xviii, xxiv, 28, 29, 57, 158

[109] P. Agnes, L. Agostino, I. F. M. Albuquerque, T. Alexander, A. K. Alton, K. Arisaka, H. O. Back, B. Baldin, K. Biery, G. Bonfini, M. Bossa, B. Bottino, A. Brigatti, J. Brodsky, F. Budano, S. Bussino, M. Cadeddu, L. Cadonati, M. Cadoni, F. Calaprice, N. Canci, A. Candela, H. Cao, M. Cariello, M. Carlini, S. Catalanotti, P. Cavalcante, A. Chepurnov, A. G. Cocco, G. Covone, L. Crippa, D. D'Angelo, M. D'Incecco, S. Davini, S. De Cecco, M. De Deo, M. De Vincenzi, A. Derbin, A. Devoto, F. Di Eusanio, G. Di Pietro, E. Edkins, A. Empl, A. Fan, G. Fiorillo, K. Fomenko, G. Forster, D. Franco, F. Gabriele, C. Galbiati, C. Giganti, A. M. Goretti, F. Granato, L. Grandi, M. Gromov, M. Guan, Y. Guardincerri, B. R. Hackett, J. Hall, K. Herner, P. H. Humble, E. V. Hungerford, Al. Ianni, An. Ianni, I. James, C. Jollet, K. Keeter, C. L. Kendziora, V. Kobychev, G. Koh, D. Korablev, G. Korga, A. Kubankin, X. Li, M. Lissia, P. Lombardi, S. Luitz, Y. Ma, I. N. Machulin, A. Mandarano, S. M. Mari, J. Maricic, L. Marini, C. J. Martoff, A. Meregaglia, P. D. Meyers, T. Miletic, R. Milincic, D. Montanari, A. Monte, M. Montuschi, M. Monzani, P. Mosteiro, B. J. Mount, V. N. Muratova, P. Musico, J. Napolitano, A. Nelson, S. Odrowski, M. Orsini, F. Ortica, L. Pagani,

M. Pallavicini, E. Pantic, S. Parmeggiano, K. Pelczar, N. Pelliccia, S. Perasso, A. Pocar, S. Pordes, D. A. Pugachev, H. Qian, K. Randle, G. Ranucci, A. Razeto, B. Reinhold, A. L. Renshaw, A. Romani, B. Rossi, N. Rossi, D. Rountree, D. Sablone, P. Saggese, R. Saldanha, W. Sands, S. Sangiorgio, C. Savarese, E. Segreto, D. A. Semenov, E. Shields, P. N. Singh, M. D. Skorokhvatov, O. Smirnov, A. Sotnikov, C. Stanford, Y. Suvorov, R. Tartaglia, J. Tatarowicz, G. Testera, A. Tonazzo, P. Trinchese, E. V. Unzhakov, A. Vishneva, B. Vogelaar, M. Wada, S. Walker, H. Wang, Y. Wang, A. W. Watson, S. Westerdale, J. Wilhelmi, M. M. Wojcik, X. Xiang, J. Xu, C. Yang, J. Yoo, S. Zavatarelli, A. Zec, W. Zhong, C. Zhu, and G. Zuzel. Results from the first use of low radioactivity argon in a dark matter search. *Phys. Rev. D*, 93:081101, Apr 2016. xiv, 28

[110] E. Armengaud, C. Augier, A. Benoît, L. Bergé, T. Bergmann, J. Blümer, A. Broniatowski, V. Brudanin, B. Censier, M. Chapellier, F. Charlieux, F. Couëdo, P. Coulter, G. A. Cox, J. Domange, A. A. Drillien, L. Dumoulin, K. Eitel, D. Filosofov, N. Fourches, J. Gascon, G. Gerbier, J. Gironnet, M. Gros, S. Henry, G. Heuermann, S. Hervé, A. Juillard, M. Kleifges, H. Kluck, V. Kozlov, H. Kraus, V. A. Kudryavtsev, H. Le Sueur, P. Loaiza, S. Marnieros, A. Menshikov, X-F. Navick, C. Nones, E. Olivieri, P. Pari, B. Paul, M. Robinson, S. Rozov, V. Sanglard, B. Schmidt, B. Siebenborn, D. Tcherniakhovski, A. S. Torrento-Coello, L. Vagneron, R. J. Walker, M. Weber, E. Yakushev, and X. Zhang. Search for low-mass wimps with edelweiss-ii heat-and-ionization detectors. *Phys. Rev. D*, 86:051701, Sep 2012. xiv, 28

[111] R. Agnese, A. J. Anderson, M. Asai, D. Balakishiyeva, D. Barker, R. Basu Thakur, D. A. Bauer, J. Billard, A. Borgland, M. A. Bowles, D. Brandt, P. L. Brink, R. Bunker, B. Cabrera, D. O. Caldwell, R. Calkins, D. G. Cerdeño, H. Chagani, Y. Chen, J. Cooley, B. Cornell, C. H. Crewdson, P. Cushman, M. Daal, P. C. F. Di Stefano, T. Doughty, L. Esteban, S. Fallows, E. Figueroa-Feliciano, G. L. Godfrey, S. R. Golwala, J. Hall, H. R. Harris, S. A. Hertel, T. Hofer, D. Holmgren, L. Hsu, M. E. Huber, D. Jardin, A. Jastram, O. Kamaev, B. Kara, M. H. Kelsey, A. Kennedy, M. Kiveni, K. Koch, A. Leder, B. Loer, E. Lopez Asamar, P. Lukens, R. Mahapatra, V. Mandic, K. A. McCarthy, N. Mirabolfathi, R. A. Moffatt, S. M. Oser, K. Page, W. A. Page, R. Partridge, M. Pepin, A. Phipps, K. Prasad, M. Pyle, H. Qiu, W. Rau, P. Redl, A. Reisetter, Y. Ricci, H. E. Rogers, T. Saab, B. Sadoulet, J. Sander, K. Schneck, R. W. Schnee, S. Scorza, B. Serfass, B. Shank, D. Speller, D. Toback, S. Upadhyayula, A. N. Villano, B. Welliver, J. S. Wilson, D. H. Wright, X. Yang, S. Yellin, J. J. Yen, B. A. Young, and J. Zhang. Improved wimp-search reach of the cdms ii germanium data. *Phys. Rev. D*, 92:072003, Oct 2015. xiv, 28

[112] Andi Tan, Mengjiao Xiao, Xiangyi Cui, Xun Chen, Yunhua Chen, Deqing Fang, Changbo Fu, Karl Giboni, Franco Giuliani, Haowei Gong, Xuyuan Guo, Ke Han, Shouyang Hu, Xingtao Huang, Xiangdong Ji, Yonglin Ju, Siao Lei, Shaoli Li, Xiaomei Li, Xinglong Li, Hao Liang, Qing Lin, Huaxuan Liu, Jianglai Liu, Wolfgang Lorenzon, Yugang Ma, Yajun Mao, Kaixuan Ni, Xiangxiang Ren, Michael Schubnell, Manbin Shen, Fang Shi, Hongwei Wang, Jimin Wang, Meng Wang, Qiuhong Wang, Siguang Wang, Xuming Wang, Zhou Wang, Shiyong Wu, Xiang Xiao, Pengwei Xie,

Binbin Yan, Yong Yang, Jianfeng Yue, Xionghui Zeng, Hongguang Zhang, Hua Zhang, Huanqiao Zhang, Tao Zhang, Li Zhao, Jing Zhou, Ning Zhou, and Xiaopeng Zhou. Dark matter results from first 98.7 days of data from the pandax-ii experiment. *Phys. Rev. Lett.*, 117:121303, Sep 2016. xiv, xv, 28, 29

[113] D. S. Akerib, S. Alsum, H. M. Araújo, X. Bai, A. J. Bailey, J. Balajthy, P. Beltrame, E. P. Bernard, A. Bernstein, T. P. Biesiadzinski, E. M. Boulton, R. Bramante, P. Brás, D. Byram, S. B. Cahn, M. C. Carmona-Benitez, C. Chan, A. A. Chiller, C. Chiller, A. Currie, J. E. Cutter, T. J. R. Davison, A. Dobi, J. E. Y. Dobson, E. Druszkiewicz, B. N. Edwards, C. H. Faham, S. Fiorucci, R. J. Gaitskell, V. M. Gehman, C. Ghag, K. R. Gibson, M. G. D. Gilchriese, C. R. Hall, M. Hanhardt, S. J. Haselschwardt, S. A. Hertel, D. P. Hogan, M. Horn, D. Q. Huang, C. M. Ignarra, M. Ihm, R. G. Jacobsen, W. Ji, K. Kamdin, K. Kazkaz, D. Khaitan, R. Knoche, N. A. Larsen, C. Lee, B. G. Lenardo, K. T. Lesko, A. Lindote, M. I. Lopes, A. Manalaysay, R. L. Mannino, M. F. Marzioni, D. N. McKinsey, D.-M. Mei, J. Mock, M. Moongweluwan, J. A. Morad, A. St. J. Murphy, C. Nehrkorn, H. N. Nelson, F. Neves, K. O'Sullivan, K. C. Oliver-Mallory, K. J. Palladino, E. K. Pease, P. Phelps, L. Reichhart, C. Rhyne, S. Shaw, T. A. Shutt, C. Silva, M. Solmaz, V. N. Solovov, P. Sorensen, S. Stephenson, T. J. Sumner, M. Szydagis, D. J. Taylor, W. C. Taylor, B. P. Tennyson, P. A. Terman, D. R. Tiedt, W. H. To, M. Tripathi, L. Tvrznikova, S. Uvarov, J. R. Verbus, R. C. Webb, J. T. White, T. J. Whitis, M. S. Witherell, F. L. H. Wolfs, J. Xu, K. Yazdani, S. K. Young, and C. Zhang. Results from a search for dark matter in the complete lux exposure. *Phys. Rev. Lett.*, 118:021303, Jan 2017. xiv, xxiv, 28, 158

[114] E. Aprile, J. Aalbers, F. Agostini, M. Alfonsi, F. D. Amaro, M. Anthony, F. Arneodo, P. Barrow, L. Baudis, B. Bauermeister, M. L. Benabderrahmane, T. Berger, P. A. Breur, A. Brown, A. Brown, E. Brown, S. Bruenner, G. Bruno, R. Budnik, L. Bütikofer, J. Calvén, J. M. R. Cardoso, M. Cervantes, D. Cichon, D. Coderre, A. P. Colijn, J. Conrad, J. P. Cussonneau, M. P. Decowski, P. de Perio, P. Di Gangi, A. Di Giovanni, S. Diglio, G. Eurin, J. Fei, A. D. Ferella, A. Fieguth, W. Fulgione, A. Gallo Rosso, M. Galloway, F. Gao, M. Garbini, R. Gardner, C. Geis, L. W. Goetzke, L. Grandi, Z. Greene, C. Grignon, C. Hasterok, E. Hogenbirk, J. Howlett, R. Itay, B. Kaminsky, S. Kazama, G. Kessler, A. Kish, H. Landsman, R. F. Lang, D. Lellouch, L. Levinson, Q. Lin, S. Lindemann, M. Lindner, F. Lombardi, J. A. M. Lopes, A. Manfredini, I. Mariş, T. Marrodán Undagoitia, J. Masbou, F. V. Massoli, D. Masson, D. Mayani, M. Messina, K. Micheneau, A. Molinario, K. Morå, M. Murra, J. Naganoma, K. Ni, U. Oberlack, P. Pakarha, B. Pelssers, R. Persiani, F. Piastra, J. Pienaar, V. Pizzella, M.-C. Piro, G. Plante, N. Priel, L. Rauch, S. Reichard, C. Reuter, B. Riedel, A. Rizzo, S. Rosendahl, N. Rupp, R. Saldanha, J. M. F. dos Santos, G. Sartorelli, M. Scheibelhut, S. Schindler, J. Schreiner, M. Schumann, L. Scotto Lavina, M. Selvi, P. Shagin, E. Shockley, M. Silva, H. Simgen, M. v. Sivers, A. Stein, S. Thapa, D. Thers, A. Tiseni, G. Trinchero, C. Tunnell, M. Vargas, N. Upole, H. Wang, Z. Wang, Y. Wei, C. Weinheimer, J. Wulf, J. Ye, Y. Zhang, and T. Zhu. First dark matter search results from the xenon1t experiment. *Phys. Rev. Lett.*, 119:181301, Oct 2017. xiv, 28

[115] P.N. Luke, J. Beeman, F.S. Goulding, S.E. Labov, and E.H. Silver. Calorimetric ionization detector. *Nuclear Instruments and Methods in Physics Research Section A: Accelerators, Spectrometers, Detectors and Associated Equipment*, 289(3):406 – 409, 1990. 27

[116] G. Wang. Phonon emission in germanium and silicon by electrons and holes in applied electric field at low temperature. *Journal of Applied Physics*, 107(9):094504, 2010. 27

[117] J. Lindhard, V. Nielsen, M. Scharff, and P.V. Thomsen. Integral equations governing radiation effects. (notes on atomic collisions, iii). *Kgl. Danske Videnskab., Selskab. Mat. Fys. Medd.*, Vol: 33: No. 10, Jan 1963. 30

[118] R. Agnese, A. J. Anderson, T. Aramaki, W. Baker, D. Balakishiyeva, S. Banik, D. Barker, R. Basu Thakur, D. A. Bauer, T. Binder, A. Borgland, M. A. Bowles, P. L. Brink, R. Bunker, B. Cabrera, D. O. Caldwell, R. Calkins, C. Cartaro, D. G. Cerdeno, H. Chagani, Y. Chang, Y. Chen, J. Cooley, B. Cornell, P. Cushman, M. Daal, T. Doughty, E. M. Dragowsky, L. Esteban, S. Fallows, E. Fascione, E. Figueroa-Feliciano, M. Fritts, G. Gerbier, R. Germond, M. Ghaith, G. L. Godfrey, S. R. Golwala, J. Hall, H. R. Harris, D. Holmgren, Z. Hong, L. Hsu, M. E. Huber, V. Iyer, D. Jardin, A. Jastram, C. Jena, M. H. Kelsey, A. Kennedy, A. Kubik, N. A. Kurinsky, A. Leder, E. Lopez Asamar, P. Lukens, D. MacDonell, R. Mahapatra, V. Mandic, N. Mast, K. A. McCarthy, E. H. Miller, N. Mirabolfathi, R. A. Moffatt, B. Mohanty, D. Moore, J. D. Morales Mendoza, J. Nelson, S. M. Oser, K. Page, W. A. Page, R. Partridge, M. Penalver Martinez, M. Pepin, A. Phipps, S. Poudel, M. Pyle, H. Qiu, W. Rau, P. Redl, A. Reisetter, A. Roberts, A. E. Robinson, T. Saab, B. Sadoulet, J. Sander, K. Schneck, R. W. Schnee, S. Scorza, K. Senapati, B. Serfass, D. Speller, P. C. F. Di Stefano, M. Stein, J. Street, H. A. Tanaka, D. Toback, R. Underwood, A. N. Villano, B. von Krosigk, B. Welliver, J. S. Wilson, M. J. Wilson, D. H. Wright, S. Yellin, J. J. Yen, B. A. Young, X. Zhang, and X. Zhao. Nuclear-recoil energy scale in CDMS II silicon dark-matter detectors. *ArXiv e-prints*, March 2018. 30

[119] A. E. Chavarria, J. I. Collar, J. R. Peña, P. Privitera, A. E. Robinson, B. Scholz, C. Sengul, J. Zhou, J. Estrada, F. Izraelevitch, J. Tiffenberg, J. R. T. de Mello Neto, and D. Torres Machado. Measurement of the ionization produced by sub-kev silicon nuclear recoils in a ccd dark matter detector. *Phys. Rev. D*, 94:082007, Oct 2016. 30

[120] J. Frenkel. Über die wärmebewegung in festen und flüssigen körpern. *Zeitschrift für Physik*, 35(8):652–669, Aug 1926. 30, 126, 128

[121] Geant4 physics reference manual. *(Unpublished)*, 10.3, 2016. xv, 33, 34, 128

[122] G. Wentzel. Zwei bemerkungen uber die zerstreuung korpuskularer strahlen als beugungserscheinung. *Z. Phys.*, 40:590–593, 1926. 33

[123] Claude Leroy and P. G. Rancoita. *Principles of radiation interaction in matter and detection*. World Scientific, 2 edition, 2009. 33, 128

[124] E. Holmström, A. Kuronen, and K. Nordlund. Threshold defect production in silicon determined by density functional theory molecular dynamics simulations. *Phys. Rev. B*, 78:045202, Jul 2008. xv, 34

[125] K. Nordlund, J. Wallenius, and L. Malerba. Molecular dynamics simulations of threshold displacement energies in fe. *Nuclear Instruments and Methods in Physics Research Section B: Beam Interactions with Materials and Atoms*, 246(2):322 – 332, 2006. 34, 154

[126] L. Malerba and J. M. Perlado. Basic mechanisms of atomic displacement production in cubic silicon carbide: A molecular dynamics study. Phys. Rev. B, 65(4):045202, January 2002. 35, 155

[127] Frank H. Stillinger and Thomas A. Weber. Computer simulation of local order in condensed phases of silicon. *Phys. Rev. B*, 31:5262–5271, Apr 1985. 35, 101, 155

[128] L Pizzagalli, J Godet, J Gunol, S Brochard, E Holmstrom, K Nordlund, and T Albaret. A new parametrization of the stillingerweber potential for an improved description of defects and plasticity of silicon. *Journal of Physics: Condensed Matter*, 25(5):055801, 2013. 35, 101, 155

[129] Matthew Stein. A fast, parallel algorithm for distant-dependent calculation of crystal properties. *Computer Physics Communications*, 221:273 – 281, 2017. 36, 162

[130] Fedja Kadribasic, Nader Mirabolfathi, Kai Nordlund, Andrea E. Sand, Eero Holmström, and Flyura Djurabekova. Directional sensitivity in light-mass dark matter searches with single-electron-resolution ionization detectors. *Phys. Rev. Lett.*, 120:111301, Mar 2018. xxv, 36, 154, 157, 159, 162

[131] Anonymous. Minutes of the. *Phys. Rev.*, 86:637–662, May 1952. 37

[132] W. Kohn and N. Rostoker. Solution of the schrödinger equation in periodic lattices with an application to metallic lithium. *Phys. Rev.*, 94:1111–1120, Jun 1954. 37

[133] Vavilov, Smirnov, Galkin, Spitsyn, and Patskevich. *J. Tech. Phys. U.S.S.R.*, 26:1865, 1956. 37, 128

[134] N.A. Vitovskii, D. Mustafakulov, and A.P. Chekmareva. *Fiz. Tekh. Poluprovodn.*, 11:1747, 1977. 37, 128

[135] Kejian Ding and Hans C. Andersen. Molecular-dynamics simulation of amorphous germanium. *Phys. Rev. B*, 34:6987–6991, Nov 1986. 37, 128

[136] V.V. Emtsev, T.V. Mashovets, and V.V. Mikhnovich. *Fiz. Tekh. Poluprovodn.*, 26:20, 1992. 37, 128

[137] K. Nordlund, M. Ghaly, R. S. Averback, M. Caturla, T. Diaz de la Rubia, and J. Tarus. Defect production in collision cascades in elemental semiconductors and fcc metals. *Phys. Rev. B*, 57:7556–7570, Apr 1998. 37, 128

[138] Jos M Soler, Emilio Artacho, Julian D Gale, Alberto Garca, Javier Junquera, Pablo Ordejn, and Daniel Snchez-Portal. The siesta method for ab initio order- n materials simulation. *Journal of Physics: Condensed Matter*, 14(11):2745, 2002. 37, 128

[139] E Holmstrm, K Nordlund, and A Kuronen. Threshold defect production in germanium determined by density functional theory molecular dynamics simulations. *Physica Scripta*, 81(3):035601, 2010. 37, 128, 154

[140] D. S. Akerib, M. S. Armel-Funkhouser, M. J. Attisha, C. N. Bailey, L. Baudis, D. A. Bauer, P. L. Brink, R. Bunker, B. Cabrera, D. O. Caldwell, C. L. Chang, M. B. Crisler, P. Cushman, M. Daal, R. Dixon, M. R. Dragowsky, D. D. Driscoll, L. Duong, R. Ferril, J. Filippini, R. J. Gaitskell, R. Hennings-Yeomans, D. Holmgren, M. E. Huber, S. Kamat, A. Lu, R. Mahapatra, V. Mandic, J. M. Martinis, P. Meunier, N. Mirabolfathi, H. Nelson, R. Nelson, R. W. Ogburn, T. A. Perera, M. C. Perillo Issac, E. Ramberg, W. Rau, A. Reisetter, R. R. Ross, T. Saab, B. Sadoulet, J. Sander, C. Savage, R. W. Schnee, D. N. Seitz, B. Serfass, K. M. Sundqvist, J-P. F. Thompson, G. Wang, S. Yellin, and B. A. Young. Exclusion limits on the wimp-nucleon cross section from the first run of the cryogenic dark matter search in the soudan underground laboratory. *Phys. Rev. D*, 72:052009, Sep 2005. xv, 38, 39, 40, 47

[141] R. Agnese, A. J. Anderson, D. Balakishiyeva, R. Basu Thakur, D. A. Bauer, A. Borgland, D. Brandt, P. L. Brink, R. Bunker, B. Cabrera, D. O. Caldwell, D. G. Cerdeno, H. Chagani, M. Cherry, J. Cooley, B. Cornell, C. H. Crewdson, P. Cushman, M. Daal, P. C. F. Di Stefano, E. Do Couto E Silva, T. Doughty, L. Esteban, S. Fallows, E. Figueroa-Feliciano, J. Fox, M. Fritts, G. L. Godfrey, S. R. Golwala, J. Hall, H. R. Harris, J. Hasi, S. A. Hertel, B. A. Hines, T. Hofer, D. Holmgren, L. Hsu, M. E. Huber, A. Jastram, O. Kamaev, B. Kara, M. H. Kelsey, S. A. Kenany, A. Kennedy, C. J. Kenney, M. Kiveni, K. Koch, B. Loer, E. Lopez Asamar, R. Mahapatra, V. Mandic, C. Martinez, K. A. McCarthy, N. Mirabolfathi, R. A. Moffatt, D. C. Moore, P. Nadeau, R. H. Nelson, L. Novak, K. Page, R. Partridge, M. Pepin, A. Phipps, K. Prasad, M. Pyle, H. Qiu, R. Radpour, W. Rau, P. Redl, A. Reisetter, R. W. Resch, Y. Ricci, T. Saab, B. Sadoulet, J. Sander, R. Schmitt, K. Schneck, R. W. Schnee, S. Scorza, D. Seitz, B. Serfass, B. Shank, D. Speller, A. Tomada, A. N. Villano, B. Welliver, D. H. Wright, S. Yellin, J. J. Yen, B. A. Young, and J. Zhang. Demonstration of surface electron rejection with interleaved germanium detectors for dark matter searches. *Applied Physics Letters*, 103(16):164105, 2013. xvi, xix, xxii, 38, 44, 46, 66, 67, 130, 151

[142] J D. Taylor, Daniel Akerib, Peter Barnes, Jr, P A. Luft, R R. Ross, B Sadoulet, R V. Schafer, S White, and R C. Wolgast. Low radioactivity cryostat system for a 20mk particle detector. 41:1971–1978, 01 1996. 39

[143] D. S. Akerib, J. Alvaro-Dean, M. S. Armel, M. J. Attisha, L. Baudis, D. A. Bauer, A. I. Bolozdynya, P. L. Brink, R. Bunker, B. Cabrera, D. O. Caldwell, J. P. Castle, C. L. Chang, R. M. Clarke, M. B. Crisler, P. Cushman, A. K. Davies, R. Dixon, D. D. Driscoll, L. Duong, J. Emes, R. Ferril, R. J. Gaitskell, S. R. Golwala,

M. Haldeman, J. Hellmig, M. Hennessey, D. Holmgren, M. E. Huber, S. Kamat, M. Kurylowicz, A. Lu, R. Mahapatra, V. Mandic, J. M. Martinis, P. Meunier, N. Mirabolfathi, S. W. Nam, H. Nelson, R. Nelson, R. W. Ogburn, J. Perales, T. A. Perera, M. C. Perillo Isaac, W. Rau, A. Reisetter, R. R. Ross, T. Saab, B. Sadoulet, J. Sander, C. Savage, R. W. Schnee, D. N. Seitz, T. A. Shutt, G. Smith, A. L. Spadafora, J.-P. F. Thompson, A. Tomada, G. Wang, S. Yellin, and B. A. Young. New results from the cryogenic dark matter search experiment. *Phys. Rev. D*, 68:082002, Oct 2003. 42

[144] I. Antcheva, M. Ballintijn, B. Bellenot, M. Biskup, R. Brun, N. Buncic, Ph. Canal, D. Casadei, O. Couet, V. Fine, L. Franco, G. Ganis, A. Gheata, D. Gonzalez Maline, M. Goto, J. Iwaszkiewicz, A. Kreshuk, D. Marcos Segura, R. Maunder, L. Moneta, A. Naumann, E. Offermann, V. Onuchin, S. Panacek, F. Rademakers, P. Russo, and M. Tadel. Root a c++ framework for petabyte data storage, statistical analysis and visualization. *Computer Physics Communications*, 180(12):2499 – 2512, 2009. 40 YEARS OF CPC: A celebratory issue focused on quality software for high performance, grid and novel computing architectures. 48, 129

[145] F. Duncan, A.J. Noble, and D. Sinclair. The construction and anticipated science of snolab. *Annual Review of Nuclear and Particle Science*, 60(1):163–180, 2010. 51

[146] A. J. Noble. SNOLab: An international facility for low background particle astrophysics experiments. New A Rev., 49:311–313, May 2005. 51, 61

[147] I.T. Lawson. SNOLAB-STR-2007-003: Analysis of Rock Samples from the New Laboratory. *(unpublished)*, Dec 2007. xxvi, 53, 63, 72, 97

[148] B.T. Cleveland and I.T. Lawson. SNOLAB-STR-2012-004: Measurement with Ge detector of vacuum dirt from SNOLAB floors. *(unpublished)*, May 2012. 53, 72, 97

[149] P. N. Luke. Voltageassisted calorimetric ionization detector. *Journal of Applied Physics*, 64(12):6858–6860, 1988. 53

[150] B. S. Neganov and V. N. Trofimov. Colorimetric method measuring ionizing radiation. *Otkryt. Izobret.*, 146:215, 1985. 53

[151] M. Pyle, D. A. Bauer, B. Cabrera, J. Hall, R. W. Schnee, R. BasuThakur, and S. Yellin. Low-mass wimp sensitivity and statistical discrimination of electron and nuclear recoils by varying luke-neganov phonon gain in semiconductor detectors. *Journal of Low Temperature Physics*, 167(5):1081–1086, Jun 2012. 55

[152] R. Agnese, A. J. Anderson, M. Asai, D. Balakishiyeva, R. Basu Thakur, D. A. Bauer, J. Beaty, J. Billard, A. Borgland, M. A. Bowles, D. Brandt, P. L. Brink, R. Bunker, B. Cabrera, D. O. Caldwell, D. G. Cerdeno, H. Chagani, Y. Chen, M. Cherry, J. Cooley, B. Cornell, C. H. Crewdson, P. Cushman, M. Daal, D. DeVaney, P. C. F. Di Stefano, E. D. C. E. Silva, T. Doughty, L. Esteban, S. Fallows, E. Figueroa-Feliciano, G. L. Godfrey, S. R. Golwala, J. Hall, S. Hansen, H. R. Harris, S. A. Hertel, B. A. Hines, T. Hofer, D. Holmgren, L. Hsu, M. E. Huber, A. Jastram,

O. Kamaev, B. Kara, M. H. Kelsey, S. Kenany, A. Kennedy, M. Kiveni, K. Koch, A. Leder, B. Loer, E. Lopez Asamar, R. Mahapatra, V. Mandic, C. Martinez, K. A. McCarthy, N. Mirabolfathi, R. A. Moffatt, R. H. Nelson, L. Novak, K. Page, R. Partridge, M. Pepin, A. Phipps, M. Platt, K. Prasad, M. Pyle, H. Qiu, W. Rau, P. Redl, A. Reisetter, R. W. Resch, Y. Ricci, M. Ruschman, T. Saab, B. Sadoulet, J. Sander, R. L. Schmitt, K. Schneck, R. W. Schnee, S. Scorza, D. N. Seitz, B. Serfass, B. Shank, D. Speller, A. Tomada, S. Upadhyayula, A. N. Villano, B. Welliver, D. H. Wright, S. Yellin, J. J. Yen, B. A. Young, J. Zhang, and SuperCDMS Collaboration. Search for Low-Mass Weakly Interacting Massive Particles with SuperCDMS. *Physical Review Letters*, 112(24):241302, June 2014. xviii, xxiv, 57, 158

[153] F. Ruppin, J. Billard, E. Figueroa-Feliciano, and L. Strigari. Complementarity of dark matter detectors in light of the neutrino background. *Phys. Rev. D*, 90:083510, Oct 2014. xviii, xxiv, 57, 158

[154] P. M. Bauleo and J. Rodríguez Martino. The dawn of the particle astronomy era in ultra-high-energy cosmic rays. Nature, 458:847–851, April 2009. 59

[155] Sergei V Troitsky. Cosmic particles with energies above 10 19ev: a brief summary of results. *Physics-Uspekhi*, 56(3):304, 2013. 59

[156] R. A. Millikan and G. H. Cameron. High Frequency Rays of Cosmic Origin III. Measurements in Snow-Fed Lakes at High Altitudes. *Physical Review*, 28:851–868, November 1926. 59

[157] Jian-Ping Cheng, Ke-Jun Kang, Jian-Min Li, Jin Li, Yuan-Jing Li, Qian Yue, Zhi Zeng, Yun-Hua Chen, Shi-Yong Wu, Xiang-Dong Ji, and Henry T. Wong. The china jinping underground laboratory and its early science. *Annual Review of Nuclear and Particle Science*, 67(1):231–251, 2017. xviii, 60

[158] D.-M. Mei and A. Hime. Muon-induced background study for underground laboratories. Phys. Rev. D, 73(5):053004, March 2006. 61

[159] S. Agostinelli, J. Allison, K. Amako, J. Apostolakis, H. Araujo, P. Arce, M. Asai, D. Axen, S. Banerjee, G. Barrand, F. Behner, L. Bellagamba, J. Boudreau, L. Broglia, A. Brunengo, H. Burkhardt, S. Chauvie, J. Chuma, R. Chytracek, G. Cooperman, G. Cosmo, P. Degtyarenko, A. Dell'Acqua, G. Depaola, D. Dietrich, R. Enami, A. Feliciello, C. Ferguson, H. Fesefeldt, G. Folger, F. Foppiano, A. Forti, S. Garelli, S. Giani, R. Giannitrapani, D. Gibin, J.J. Gmez Cadenas, I. Gonzlez, G. Gracia Abril, G. Greeniaus, W. Greiner, V. Grichine, A. Grossheim, S. Guatelli, P. Gumplinger, R. Hamatsu, K. Hashimoto, H. Hasui, A. Heikkinen, A. Howard, V. Ivanchenko, A. Johnson, F.W. Jones, J. Kallenbach, N. Kanaya, M. Kawabata, Y. Kawabata, M. Kawaguti, S. Kelner, P. Kent, A. Kimura, T. Kodama, R. Kokoulin, M. Kossov, H. Kurashige, E. Lamanna, T. Lampn, V. Lara, V. Lefebure, F. Lei, M. Liendl, W. Lockman, F. Longo, S. Magni, M. Maire, E. Medernach, K. Minamimoto, P. Mora de Freitas, Y. Morita, K. Murakami,

M. Nagamatu, R. Nartallo, P. Nieminen, T. Nishimura, K. Ohtsubo, M. Okamura, S. O'Neale, Y. Oohata, K. Paech, J. Perl, A. Pfeiffer, M.G. Pia, F. Ranjard, A. Rybin, S. Sadilov, E. Di Salvo, G. Santin, T. Sasaki, N. Savvas, Y. Sawada, S. Scherer, S. Sei, V. Sirotenko, D. Smith, N. Starkov, H. Stoecker, J. Sulkimo, M. Takahata, S. Tanaka, E. Tcherniaev, E. Safai Tehrani, M. Tropeano, P. Truscott, H. Uno, L. Urban, P. Urban, M. Verderi, A. Walkden, W. Wander, H. Weber, J.P. Wellisch, T. Wenaus, D.C. Williams, D. Wright, T. Yamada, H. Yoshida, and D. Zschiesche. Geant4a simulation toolkit. *Nuclear Instruments and Methods in Physics Research Section A: Accelerators, Spectrometers, Detectors and Associated Equipment*, 506(3):250 – 303, 2003. 61

[160] J. Allison, K. Amako, J. Apostolakis, H. Araujo, P. Arce Dubois, M. Asai, G. Barrand, R. Capra, S. Chauvie, R. Chytracek, G. A. P. Cirrone, G. Cooperman, G. Cosmo, G. Cuttone, G. G. Daquino, M. Donszelmann, M. Dressel, G. Folger, F. Foppiano, J. Generowicz, V. Grichine, S. Guatelli, P. Gumplinger, A. Heikkinen, I. Hrivnacova, A. Howard, S. Incerti, V. Ivanchenko, T. Johnson, F. Jones, T. Koi, R. Kokoulin, M. Kossov, H. Kurashige, V. Lara, S. Larsson, F. Lei, O. Link, F. Longo, M. Maire, A. Mantero, B. Mascialino, I. McLaren, P. Mendez Lorenzo, K. Minamimoto, K. Murakami, P. Nieminen, L. Pandola, S. Parlati, L. Peralta, J. Perl, A. Pfeiffer, M. G. Pia, A. Ribon, P. Rodrigues, G. Russo, S. Sadilov, G. Santin, T. Sasaki, D. Smith, N. Starkov, S. Tanaka, E. Tcherniaev, B. Tome, A. Trindade, P. Truscott, L. Urban, M. Verderi, A. Walkden, J. P. Wellisch, D. C. Williams, D. Wright, and H. Yoshida. Geant4 developments and applications. *IEEE Transactions on Nuclear Science*, 53(1):270–278, Feb 2006. 61

[161] J. Allison, K. Amako, J. Apostolakis, P. Arce, M. Asai, T. Aso, E. Bagli, A. Bagulya, S. Banerjee, G. Barrand, B.R. Beck, A.G. Bogdanov, D. Brandt, J.M.C. Brown, H. Burkhardt, Ph. Canal, D. Cano-Ott, S. Chauvie, K. Cho, G.A.P. Cirrone, G. Cooperman, M.A. Corts-Giraldo, G. Cosmo, G. Cuttone, G. Depaola, L. Desorgher, X. Dong, A. Dotti, V.D. Elvira, G. Folger, Z. Francis, A. Galoyan, L. Garnier, M. Gayer, K.L. Genser, V.M. Grichine, S. Guatelli, P. Guye, P. Gumplinger, A.S. Howard, I. Hivnov, S. Hwang, S. Incerti, A. Ivanchenko, V.N. Ivanchenko, F.W. Jones, S.Y. Jun, P. Kaitaniemi, N. Karakatsanis, M. Karamitros, M. Kelsey, A. Kimura, T. Koi, H. Kurashige, A. Lechner, S.B. Lee, F. Longo, M. Maire, D. Mancusi, A. Mantero, E. Mendoza, B. Morgan, K. Murakami, T. Nikitina, L. Pandola, P. Paprocki, J. Perl, I. Petrovi, M.G. Pia, W. Pokorski, J.M. Quesada, M. Raine, M.A. Reis, A. Ribon, A. Risti Fira, F. Romano, G. Russo, G. Santin, T. Sasaki, D. Sawkey, J.I. Shin, I.I. Strakovsky, A. Taborda, S. Tanaka, B. Tom, T. Toshito, H.N. Tran, P.R. Truscott, L. Urban, V. Uzhinsky, J.M. Verbeke, M. Verderi, B.L. Wendt, H. Wenzel, D.H. Wright, D.M. Wright, T. Yamashita, J. Yarba, and H. Yoshida. Recent developments in geant4. *Nuclear Instruments and Methods in Physics Research Section A: Accelerators, Spectrometers, Detectors and Associated Equipment*, 835:186 – 225, 2016. 61

[162] J. J. Back and Y. A. Ramachers. ACTIVIA: Calculation of isotope production cross-sections and yields. *Nuclear Instruments and Methods in Physics Research A*, 586:286–294, February 2008. 61

[163] C. Zhang, D.-M. Mei, V. A. Kudryavtsev, and S. Fiorucci. Cosmogenic activation of materials used in rare event search experiments. *Astroparticle Physics*, 84:62–69, November 2016. xviii, 61, 62

[164] J.C. Loach, J. Cooley, G.A. Cox, Z. Li, K.D. Nguyen, and A.W.P. Poon. A database for storing the results of material radiopurity measurements. *Nuclear Instruments and Methods in Physics Research Section A: Accelerators, Spectrometers, Detectors and Associated Equipment*, 839:6 – 11, 2016. 63, 64

[165] E. Aprile, K. Arisaka, F. Arneodo, A. Askin, L. Baudis, A. Behrens, K. Bokeloh, E. Brown, J.M.R. Cardoso, B. Choi, D. Cline, S. Fattori, A.D. Ferella, K.L. Giboni, A. Kish, C.W. Lam, J. Lamblin, R.F. Lang, K.E. Lim, J.A.M. Lopes, T. Marrodn Undagoitia, Y. Mei, A.J. Melgarejo Fernandez, K. Ni, U. Oberlack, S.E.A. Orrigo, E. Pantic, G. Plante, A.C.C. Ribeiro, R. Santorelli, J.M.F. dos Santos, M. Schumann, P. Shagin, A. Teymourian, D. Thers, E. Tziaferi, H. Wang, C. Weinheimer, M. Laubenstein, and S. Nisi. Material screening and selection for xenon100. *Astroparticle Physics*, 35(2):43 – 49, 2011. 64

[166] C. Arpesella, H.O. Back, M. Balata, T. Beau, G. Bellini, J. Benziger, S. Bonetti, A. Brigatti, C. Buck, B. Caccianiga, L. Cadonati, F. Calaprice, G. Cecchet, M. Chen, O. Dadoun, D. D'Angelo, A. De Bari, A. de Bellefon, E. De Haas, H. de Kerret, A. Derbin, M. Deutsch, A. Di Credico, F. Elisei, A. Etenko, F. von Feilitzsch, R. Fernholz, R. Ford, D. Franco, B. Freudiger, C. Galbiati, F. Gatti, S. Gazzana, M.G. Giammarchi, D. Giugni, M. Gger-Neff, T. Goldbrunner, A. Golubchikov, A. Goretti, C. Grieb, C. Hagner, T. Hagner, W. Hampel, E. Harding, F.X. Hartmann, R. von Hentig, G. Heusser, M. Hult, A. Ianni, A.M. Ianni, J. Kiko, T. Kirsten, M. Khler, G. Korga, G. Korschinek, Y. Kozlov, D. Kryn, P. LaMarche, M. Laubenstein, C. Lendvai, F. Loeser, P. Lombardi, K. McCarty, I. Machulin, S. Malvezzi, J. Maneira, I. Manno, G. Manuzio, A. Martemianov, F. Masetti, U. Mazzucato, E. Meroni, L. Miramonti, M.E. Monzani, P. Musico, H. Neder, L. Niedermeier, S. Nisi, L. Oberauer, M. Obolensky, F. Ortica, M. Pallavicini, L. Papp, L. Perasso, A. Pocar, R.S. Raghavan, G. Ranucci, W. Rau, A. Razeto, E. Resconi, T. Riedel, A. Sabelnikov, C. Salvo, R. Scardaoni, S. Schnert, K.H. Schuhbeck, T. Shutt, H. Simgen, A. Sonnenschein, O. Smirnov, A. Sotnikov, M. Skorokhvatov, S. Sukhotin, V. Tarasenkov, R. Tartaglia, G. Testera, P.R. Trincherini, V. Vyrodov, R.B. Vogelaar, D. Vignaud, S. Vitale, M. Wjcik, O. Zaimidoroga, and G. Zuzel. Measurements of extremely low radioactivity levels in borexino. *Astroparticle Physics*, 18(1):1 – 25, 2002. 64

[167] SNOLAB User's Handbook Revision 2. *(unpublished)*, 2006. xviii, 63, 64, 72, 83

[168] J. F. Ziegler, M. D. Ziegler, and J. P. Biersack. SRIM - The stopping and range of ions in matter (2010). *Nuclear Instruments and Methods in Physics Research B*, 268:1818–1823, June 2010. 66, 90, 136, 154

[169] Devendra Lal, Edward D. Goldberg, and Minoru Koide. Cosmic-ray-produced silicon-32 in nature. *Science*, 131(3397):332–337, 1960. 68

[170] P. Becker, H.-J. Pohl, H. Riemann, and N. Abrosimov. Enrichment of silicon for a better kilogram. *physica status solidi (a)*, 207(1):49–66, 2010. 68

[171] R. Plaga. Silicon for ultra-low-level detectors and 32si. *Nuclear Instruments and Methods in Physics Research Section A: Accelerators, Spectrometers, Detectors and Associated Equipment*, 309(3):598 – 599, 1991. 68

[172] A. Aguilar-Arevalo, D. Amidei, X. Bertou, D. Bole, M. Butner, G. Cancelo, A. Castaeda Vzquez, A.E. Chavarria, J.R.T. de Mello Neto, S. Dixon, J.C. D'Olivo, J. Estrada, G. Fernandez Moroni, K.P. Hernndez Torres, F. Izraelevitch, A. Kavner, B. Kilminster, I. Lawson, J. Liao, M. Lpez, J. Molina, G. Moreno-Granados, J. Pena, P. Privitera, Y. Sarkis, V. Scarpine, T. Schwarz, M. Sofo Haro, J. Tiffenberg, D. Torres Machado, F. Trillaud, X. You, and J. Zhou. Measurement of radioactive contamination in the high-resistivity silicon ccds of the damic experiment. *Journal of Instrumentation*, 10(08):P08014, 2015. 68

[173] P. Jagam and J.J. Simpson. SNO-STR-95-050: Deposition Rates of U and Th by NAA of Witness Plates. *(unpublished)*, Nov 1995. 72

[174] Coursey, J.S., Schwab, D.J., Tsai, J.J., and Dragoset, R.A. (2015), Atomic Weights and Isotopic Compositions (version 4.1). [Online] Available: http://physics.nist.gov/Comp [2017, March, 20]. National Institute of Standards and Technology, Gaithersburg, MD. 81

[175] W. B. Wilson, R. T. Perry, E. F. Shores, W. S. Charlton, Theodore A. Parish, G. P. Estes, T. H. Brown, Edward D. Arthur, Michael Bozoian, T. R. England, and et al. *SOURCES 4C: a code for calculating ([alpha],n), spontaneous fission, and delayed neutron sources and spectra.* Jan 2002. 81

[176] VITO TOMASELLO and VITALY A. KUDRYAVTSEV. *CALCULATION OF NEUTRON YIELD FROM RADIOACTIVITY IN MATERIALS RELEVANT TO DARK MATTER SEARCHES*, pages 537–541. WORLD SCIENTIFIC, 2012. 81

[177] Enomoto Shanshiro. *Neutrino Geophysics and Observation of Geo-Neutrinos at KamLAND*. PhD thesis, Tohoku University, 2005. xx, 82

[178] M. Wjcik and G. Zuzel. Radon permeability through nylon at various humidities used in the borexino experiment. *Nuclear Instruments and Methods in Physics Research Section A: Accelerators, Spectrometers, Detectors and Associated Equipment*, 524(1):355 – 365, 2004. 85

[179] H Bateman. Solution of a system of differential equations occurring in the theory of radioactive transformations. *Proc. Cambridge Phil. Soc.*, 15:423–427, 1910. 86

[180] The xia ultra-lo 1800 users manual. http://www.xia.com/UltraLo/index.html. Accessed 5 January 2018. xxi, 91

[181] Wolfgang Rau. Measurement of radon diffusion in polyethylene based on alpha detection. *Nuclear Instruments and Methods in Physics Research Section A: Accelerators, Spectrometers, Detectors and Associated Equipment*, 664(1):65 – 70, 2012. 95

[182] United Nations. *Sources and effects of ionizing radiation : United Nations Scientific Committee on the Effects of Atomic Radiation : UNSCEAR 2000 report to the General Assembly, with scientific annexes*. United Nations New York, 2000. 97

[183] J. E. Jones and A. E. Ingham. On the calculation of certain crystal potential constants, and on the cubic crystal of least potential energy. *Proceedings of the Royal Society of London A: Mathematical, Physical and Engineering Sciences*, 107(744):636–653, 1925. 101, 103

[184] R. A. Buckingham. The classical equation of state of gaseous helium, neon and argon. *Proceedings of the Royal Society of London A: Mathematical, Physical and Engineering Sciences*, 168(933):264–283, 1938. 101

[185] Zi Jian, Zhang Kaiming, and Xie Xide. Modification of stillinger-weber potentials for si and ge. *Phys. Rev. B*, 41:12915–12918, Jun 1990. 101

[186] Maria Timonova, Beyong-Joo Lee, and Barend J. Thijsse. Sputter erosion of si(001) using a new silicon meam potential and different thermostats. *Nuclear Instruments and Methods in Physics Research Section B: Beam Interactions with Materials and Atoms*, 255(1):195 – 201, 2007. Computer Simulation of Radiation Effects in Solids. 101

[187] R.L.C. Vink, G.T. Barkema, W.F. van der Weg, and Normand Mousseau. Fitting the stillingerweber potential to amorphous silicon. *Journal of Non-Crystalline Solids*, 282(2):248 – 255, 2001. 101

[188] W. Kahan. Pracniques: Further remarks on reducing truncation errors. *Commun. ACM*, 8(1):40–, January 1965. 102

[189] Peter Schwerdtfeger, Nicola Gaston, Robert P. Krawczyk, Ralf Tonner, and Gloria E. Moyano. Extension of the lennard-jones potential: Theoretical investigations into rare-gas clusters and crystal lattices of he, ne, ar, and kr using many-body interaction expansions. *Phys. Rev. B*, 73:064112, Feb 2006. 103, 104, 124

[190] Duane C. Wallace and Janice L. Patrick. Stability of crystal lattices. *Phys. Rev.*, 137:A152–A160, Jan 1965. 103, 104, 124

[191] Satish Balay, Shrirang Abhyankar, Mark F. Adams, Jed Brown, Peter Brune, Kris Buschelman, Lisandro Dalcin, Victor Eijkhout, William D. Gropp, Dinesh Kaushik, Matthew G. Knepley, Lois Curfman McInnes, Karl Rupp, Barry F. Smith, Stefano Zampini, Hong Zhang, and Hong Zhang. PETSc Web page. http://www.mcs.anl.gov/petsc, 2016. 104

[192] Ewing Lusk, Nathan Doss, and Anthony Skjellum. A high-performance, portable implementation of the mpi message passing interface standard. *Parallel Computing*, 22:789–828, 1996. 108

[193] P. Redl. Accurate Simulations of Pb Recoils in SuperCDMS. *Journal of Low Temperature Physics*, 176:937–942, September 2014. 128, 140

[194] David Freedman and Persi Diaconis. On the histogram as a density estimator:l2 theory. *Zeitschrift für Wahrscheinlichkeitstheorie und Verwandte Gebiete*, 57(4):453–476, Dec 1981. 143

[195] I. Lazanu and S. Lazanu. Kinetics of defects in low temperature semiconductor detectors and direct dark matter search. *Romanian Reports in Physics*, 62:309–318, 2010. 154

[196] G. H. Kinchin and R. S. Pease. REVIEW ARTICLES: The Displacement of Atoms in Solids by Radiation. *Reports on Progress in Physics*, 18:1–51, January 1955. 154

[197] M.J. Norgett, M.T. Robinson, and I.M. Torrens. A proposed method of calculating displacement dose rates. *Nuclear Engineering and Design*, 33(1):50 – 54, 1975. 154

[198] D Bodlaki, H Yamamoto, D.H Waldeck, and E Borguet. Ambient stability of chemically passivated germanium interfaces. *Surface Science*, 543(1):63 – 74, 2003. 154

[199] Siti Kudnie Sahari, Hideki Murakami, Tomohiro Fujioka, Tatsuya Bando, Akio Ohta, Katsunori Makihara, Seiichiro Higashi, and Seiichi Miyazaki. Native oxidation growth on ge(111) and (100) surfaces. *Japanese Journal of Applied Physics*, 50(4S):04DA12, 2011. 154

[200] R. K. Romani, P. L. Brink, B. Cabrera, M. Cherry, T. Howarth, N. Kurinsky, R. A. Moffatt, R. Partridge, F. Ponce, M. Pyle, A. Tomada, S. Yellin, J. J. Yen, and B. A. Young. Thermal detection of single e-h pairs in a biased silicon crystal detector. *Applied Physics Letters*, 112(4):043501, 2018. 155

[201] Matthew Stein, Dan Bauer, Ray Bunker, Rob Calkins, Jodi Cooley, Ben Loer, and Silvia Scorza. Radon daughter plate-out measurements at snolab for polyethylene and copper. *Nuclear Instruments and Methods in Physics Research Section A: Accelerators, Spectrometers, Detectors and Associated Equipment*, 880:92 – 97, 2018. 161

[202] W. Jacobi. Activity and potential alpha-energy of 222radon and 220radon-daughters in different air atmospheres. *Health physics*, 22(5):441 – 450, 1958. 162

[203] S. R. Golwala. Ph.D. thesis. *University of California, Berkeley*, 2000. 163

[204] F. Zwicky. On the Masses of Nebulae and of Clusters of Nebulae. ApJ, 86:217, October 1937.

[205] H. C. van de Hulst, E. Raimond, and H. van Woerden. Rotation and density distribution of the Andromeda nebula derived from observations of the 21-cm line. Bull. Astron. Inst. Netherlands, 14:1, November 1957.

[206] Astronomical history of radio kootwijk. http://radiokootwijk.nu/sterrenwacht/. Accessed 5 April 2017.

[207] N. Thonnard, V. C. Rubin, W. K. Ford, Jr., and M. S. Roberts. Radial velocities of spiral galaxies determined from 21-cm neutral hydrogen observations. AJ, 83:1564–1565, December 1978.

[208] G. Battaglia, A. Helmi, H. Morrison, P. Harding, E. W. Olszewski, M. Mateo, K. C. Freeman, J. Norris, and S. A. Shectman. The radial velocity dispersion profile of the Galactic halo: constraining the density profile of the dark halo of the Milky Way. MNRAS, 364:433–442, December 2005.

[209] D. R. Tovey, R. J. Gaitskell, P. Gondolo, Y. Ramachers, and L. Roszkowski. A new model-independent method for extracting spin-dependent cross section limits from dark matter searches. *Physics Letters B*, 488:17–26, August 2000.

[210] W. C. Haxton, K. A. Philpott, R. Holtz, P. Long, and J. F. Wilkerson. Arguments for a "US Kamioka": SNOLab and its implications for North American underground science planning. *Nuclear Instruments and Methods in Physics Research A*, 570:414–436, January 2007.

[211] GERALD L. POLLACK. The solid state of rare gases. *Rev. Mod. Phys.*, 36:748–791, Jul 1964.

[212] R. Agnese, A. J. Anderson, T. Aramaki, I. Arnquist, W. Baker, D. Barker, R. Basu Thakur, D. A. Bauer, A. Borgland, M. A. Bowles, P. L. Brink, R. Bunker, B. Cabrera, D. O. Caldwell, R. Calkins, C. Cartaro, D. G. Cerdeño, H. Chagani, Y. Chen, J. Cooley, B. Cornell, P. Cushman, M. Daal, P. C. F. Di Stefano, T. Doughty, L. Esteban, S. Fallows, E. Figueroa-Feliciano, M. Fritts, G. Gerbier, M. Ghaith, G. L. Godfrey, S. R. Golwala, J. Hall, H. R. Harris, T. Hofer, D. Holmgren, Z. Hong, E. Hoppe, L. Hsu, M. E. Huber, V. Iyer, D. Jardin, A. Jastram, M. H. Kelsey, A. Kennedy, A. Kubik, N. A. Kurinsky, A. Leder, B. Loer, E. Lopez Asamar, P. Lukens, R. Mahapatra, V. Mandic, N. Mast, N. Mirabolfathi, R. A. Moffatt, J. D. Morales Mendoza, J. L. Orrell, S. M. Oser, K. Page, W. A. Page, R. Partridge, M. Pepin, A. Phipps, S. Poudel, M. Pyle, H. Qiu, W. Rau, P. Redl, A. Reisetter, A. Roberts, A. E. Robinson, H. E. Rogers, T. Saab, B. Sadoulet, J. Sander, K. Schneck, R. W. Schnee, B. Serfass, D. Speller, M. Stein, J. Street, H. A. Tanaka, D. Toback, R. Underwood, A. N. Villano, B. von Krosigk, B. Welliver, J. S. Wilson, D. H. Wright, S. Yellin, J. J. Yen, B. A. Young, X. Zhang, and X. Zhao.

Projected sensitivity of the supercdms snolab experiment. *Phys. Rev. D*, 95:082002, Apr 2017.

[213] R.S. Hager and E.C. Seltzer. Internal conversion tables part i: K-, l-, m-shell conversion coefficients for z=30 to z=103. *Nuclear Data Sheets. Section A*, 4(1):1 – 11, 1968.

[214] K-, l-, m-shell internal conversion coefficients z = 30 to z = 103. *Nuclear Data Sheets. Section A*, 4(1):13 – 235, 1968.

[215] R.S. Hager and E.C. Seltzer. Internal conversion tables part iii: Coefficients for the analysis of penetration effects in internal conversion and e0 internal conversion. *Nuclear Data Sheets. Section A*, 6(1):1 – 127, 1969.

[216] M.B. Lewis. Nuclear data sheets for a = 210. *Nuclear Data Sheets*, 5(6):631 – 663, 1971.

[217] Marcus H. Mendenhall and Robert A. Weller. An algorithm for computing screened coulomb scattering in geant4. *Nuclear Instruments and Methods in Physics Research Section B: Beam Interactions with Materials and Atoms*, 227(3):420 – 430, 2005.

[218] G.P. Yost, R.M. Barnett, I. Hinchliffe, G.R. Lynch, A. Rittenberg, R.R. Ross, M. Suzuki, T.G. Trippe, C.G. Wohl, B. Armstrong, G.S. Wagman, F.C. Porter, L. Montanet, M. Aguilar-Benitez, J.J. Hernandez, G. Conforto, R.L. Crawford, K.R. Schubert, M. Roos, N.A. Trnqvist, G. Hhler, K. Hagiwara, S. Kawabata, D.M. Manley, K.A. Olive, K.G. Hayes, R.H. Schindler, B. Cabrera, R.E. Shrock, R.A. Eichler, L.D. Roper, and W.P. Trower. Review of particle properties. *Physics Letters B*, 204(Supplement C):1, 1988.

[219] The CDMS II Collaboration. Dark matter search results from the cdms ii experiment. *Science*, 327(5973):1619–1621, 2010.

[220] D. Abrams, D. S. Akerib, M. S. Armel-Funkhouser, L. Baudis, D. A. Bauer, A. Bolozdynya, P. L. Brink, R. Bunker, B. Cabrera, D. O. Caldwell, J. P. Castle, C. L. Chang, R. M. Clarke, M. B. Crisler, R. Dixon, D. Driscoll, S. Eichblatt, R. J. Gaitskell, S. R. Golwala, E. E. Haller, J. Hellmig, D. Holmgren, M. E. Huber, S. Kamat, A. Lu, V. Mandic, J. M. Martinis, P. Meunier, S. W. Nam, H. Nelson, T. A. Perera, M. C. Perillo Isaac, W. Rau, R. R. Ross, T. Saab, B. Sadoulet, J. Sander, R. W. Schnee, T. Shutt, A. Smith, A. H. Sonnenschein, A. L. Spadafora, G. Wang, S. Yellin, and B. A. Young. Exclusion limits on the wimp-nucleon cross section from the cryogenic dark matter search. *Phys. Rev. D*, 66:122003, Dec 2002.

[221] J. R. Primack, D. Seckel, and B. Sadoulet. Detection of cosmic dark matter. *Annual Review of Nuclear and Particle Science*, 38(1):751–807, 1988.

[222] R. Bernabei, P. Belli, V. Landoni, F. Montecchia, Nicolantonio W. Di, A. Incicchitti, D. Prosperi, C. Bacci, Dai C.J., Ding L.K., H.H. Kuang, J.M. Ma, M. Angelone, P. Bastistoni, and M. Pillon. New limits on wimp search with large-mass

low-radioactivity nai(tl) set-up at gran sasso. *Physics Letters B*, 389(4):757 – 766, 1996.

[223] Z. Ahmed, D. S. Akerib, S. Arrenberg, M. J. Attisha, C. N. Bailey, L. Baudis, D. A. Bauer, J. Beaty, P. L. Brink, T. Bruch, R. Bunker, S. Burke, B. Cabrera, D. O. Caldwell, J. Cooley, P. Cushman, F. DeJongh, M. R. Dragowsky, L. Duong, J. Emes, E. Figueroa-Feliciano, J. Filippini, M. Fritts, R. J. Gaitskell, S. R. Golwala, D. R. Grant, J. Hall, R. Hennings-Yeomans, S. Hertel, D. Holmgren, M. E. Huber, R. Mahapatra, V. Mandic, K. A. McCarthy, N. Mirabolfathi, H. Nelson, L. Novak, R. W. Ogburn, M. Pyle, X. Qiu, E. Ramberg, W. Rau, A. Reisetter, T. Saab, B. Sadoulet, J. Sander, R. Schmitt, R. W. Schnee, D. N. Seitz, B. Serfass, A. Sirois, K. M. Sundqvist, M. Tarka, A. Tomada, G. Wang, S. Yellin, J. Yoo, and B. A. Young. Search for weakly interacting massive particles with the first five-tower data from the cryogenic dark matter search at the soudan underground laboratory. *Phys. Rev. Lett.*, 102:011301, Jan 2009.

[224] E. Aprile, L. Baudis, B. Choi, K. L. Giboni, K. Lim, A. Manalaysay, M. E. Monzani, G. Plante, R. Santorelli, and M. Yamashita. New measurement of the relative scintillation efficiency of xenon nuclear recoils below 10 kev. *Phys. Rev. C*, 79:045807, Apr 2009.

[225] V. N. Lebedenko, H. M. Araújo, E. J. Barnes, A. Bewick, R. Cashmore, V. Chepel, A. Currie, D. Davidge, J. Dawson, T. Durkin, B. Edwards, C. Ghag, M. Horn, A. S. Howard, A. J. Hughes, W. G. Jones, M. Joshi, G. E. Kalmus, A. G. Kovalenko, A. Lindote, I. Liubarsky, M. I. Lopes, R. Lüscher, P. Majewski, A. St. J. Murphy, F. Neves, J. Pinto da Cunha, R. Preece, J. J. Quenby, P. R. Scovell, C. Silva, V. N. Solovov, N. J. T. Smith, P. F. Smith, V. N. Stekhanov, T. J. Sumner, C. Thorne, and R. J. Walker. Results from the first science run of the zeplin-iii dark matter search experiment. *Phys. Rev. D*, 80:052010, Sep 2009.

[226] John Ellis, Keith A. Olive, Yudi Santoso, and Vassilis C. Spanos. Supersymmetric dark matter in light of wmap. *Physics Letters B*, 565:176 – 182, 2003.

[227] Leszek Roszkowski, Roberto Ruiz de Austri, and Roberto Trotta. Implications for the constrained mssm from a new prediction for b s . *Journal of High Energy Physics*, 2007(07):075, 2007.

[228] Ionel Lazanu, Magdalena Lidia Ciurea, and Sorina Lazanu. Analysis of defect formation in semiconductor cryogenic bolometric detectors created by heavy dark matter. *Astroparticle Physics*, 44:9 – 14, 2013.

[229] M. Pyle, B. Serfass, P. L. Brink, B. Cabrera, M. Cherry, N. Mirabolfathi, L. Novak, B. Sadoulet, D. Seitz, K. M. Sundqvist, A. Tomada, J. J. Yen, and B. A. Young. Surface electron rejection from ge detector with interleaved charge and phonon channels. *AIP Conference Proceedings*, 1185(1):223–226, 2009.

[230] P. Ehrhart and H. Zillgen. Vacancies and interstitial atoms in e-irradiated germanium. *Journal of Applied Physics*, 85(7):3503–3511, 1999.

[231] V.V. Emtsev, T.V. Mashovets, and V.V. Mikhnovich. Frenkel pairs in germanium and silicon. *Soviet Physics - Semiconductors*, 26(1):12 – 25, 1992.

[232] Ronald Knief. *Nuclear Energy Technology*. Harpercollins College Div, 1936.

[233] J. H. Quick. The turbo-encabulator in industry. *Students' Quarterly Journal*, 25(99):184, March 1955.

[234] S.I. Raider, R. Flitsch, and M.J. Palmer. Oxide growth on etched silicon in air at room temperature. *Journal of the Electrochemical Society*, 122(3):413 – 418, 1975.

[235] M. Morita, T. Ohmi, E. Hasegawa, M. Kawakami, and M. Ohwada. Growth of native oxide on a silicon surface. *Journal of Applied Physics*, 68(3):1272–1281, 1990.